KU LEUVEN

ARENBERG DOCTORAL SCHOOL
Faculty of Science

TURUN
YLIOPISTO
UNIVERSITY
OF TURKU

Multi-scale modelling of energetic particle dynamics and radio signatures in coronal and heliospheric plasmas

Edin Husidic

Supervisors:
Prof Stefaan Poedts
Prof Rami Vainio
(University of Turku)
Prof Nicolas Wijsen

Dissertation presented in partial fulfillment of the requirements for the degree of
Doctor of Science (PhD): Mathematics (KU Leuven)
and the degree of
Doctor of Philosophy: Physics (University of Turku)

October 2025

KU Leuven

Faculty of Science
Department of Mathematics
Mathematics
Doctoral Programme in Science

Multi-scale modelling of energetic particle dynamics and radio signatures in coronal and heliospheric plasmas

Edin HUSIDIC

Examination committee at KU Leuven:
Prof Stefan Van Aelst, chair
Prof Stefaan Poedts, supervisor
Prof Rami Vainio, supervisor
(University of Turku)
Prof Nicolas Wijsen, supervisor
Prof Jasmina Magdalenić-Zhukov
Prof Jon Sundqvist
Dr Nina Dresing
(University of Turku)
Prof Kamen Kozarev
(Bulgarian Academy of Sciences)
Dr Igor Sokolov
(University of Michigan)

Dissertation presented in partial fulfillment of the requirements for the degree of
Doctor of Science (PhD): Mathematics (KU Leuven)
and the degree of
Doctor of Philosophy: Physics (University of Turku)

October 2025

Uitgegeven in eigen beheer, Edin Husidic, Celestijnenlaan 200B, B-3001 Leuven (Belgium)

Generative AI assistance tools were merely used for language assistance (e.g. abstract translations, grammar and spelling checks, and style improvements). The text/code/images in this thesis are my own (unless otherwise specified). The use of generative AI complied with the KU Leuven and University of Turku guidelines, and appropriate references have been added. I have reviewed and edited the content as needed and I take full responsibility for the content of the thesis.

University of Turku

Faculty of Science
Department of Physics and Astronomy
Physics
Doctoral Programme in Exact Sciences

Supervised by

Prof Rami Vainio, Department of Physics and Astronomy, University of Turku, Turku, Finland
Prof Stefan Poedts, Department of Mathematics, Centre for Mathematical Plasma-Astrophysics, KU Leuven, Leuven, Belgium
Prof Nicolas Wijsen, Department of Mathematics, Campus Kulak Kortrijk, KU Leuven, Leuven, Belgium

Reviewed by

Prof Kamen Kozarev, Institute of Astronomy and National Astronomical Observatory, Bulgarian Academy of Sciences, Sofia, Bulgaria
Dr Igor Sokolov, Department of Climate and Space, University of Michigan, Ann Arbor, Michigan, USA

Opponent

Dr Frederic Effenberger, Institute for Theoretical Physics IV, Ruhr-University Bochum, Bochum, Germany

Abstract

Solar Energetic Particles (SEPs) accelerated during space weather events such as solar flares, Coronal Mass Ejections (CMEs), and corotating interaction regions, can reach energies up to several GeV per nucleon for ions and several tens MeV for electrons, thereby posing significant risks to satellites, astronauts, and ground-based systems. Understanding SEP acceleration and transport, along with their associated radio signatures, is crucial for enhancing space weather forecasts and mitigation strategies.

This thesis presents, in three stages, a novel, physics-based framework to simulate the acceleration, transport, and radio emission of SEPs in realistic solar wind and coronal environments. Building on an earlier implementation in which the MagnetoHydroDynamic (MHD) model *EUHFORIA* has been coupled with the focused transport code *PARADISE*, we first replace *EUHFORIA* with the more advanced inner heliospheric solar wind MHD code *Icarus*, which supports localised grid refinements and higher shock resolutions via adaptive mesh refinement. Next, to study SEP and CME dynamics below 0.1 au, the framework is extended into the corona using the *COCONUT* MHD model. Finally, we integrate the *Ultimate Fast Gyrosynchrotron Codes* to compute radio emission from energetic electrons trapped in a CME flux rope.

Applications for each stage demonstrate significant advances in modelling particle dynamics in both the corona and heliosphere. The framework enables realistic simulations of particle acceleration at finely resolved shocks, investigation of particle confinement and escape in low-coronal magnetic flux ropes, and direct linkage of these processes to observable type IV radio emission, offering valuable diagnostic capabilities for CME magnetic fields and SEP properties near the Sun. Moreover, the integration of coronal and heliospheric domains represents a key step towards global-scale simulations of CME and SEP events from the solar surface to Earth's orbit and beyond, supporting future efforts to untangle the complex, interconnected processes governing space plasmas.

Beknopte samenvatting

Zonne-energetische deeltjes (SEP's), versneld tijdens ruimteweergebeurtenissen zoals zonnevlammen, coronale massa-ejecties (CME's) en coroterende interactieregio's, kunnen energieën bereiken tot enkele GeV per nucleon voor ionen en enkele tientallen MeV voor elektronen. Hierdoor vormen zij een aanzienlijk risico voor satellieten, astronauten en systemen op aarde. Inzicht in de versnelling en het transport van SEP's, evenals in hun bijbehorende radiosignalen, is cruciaal voor het verbeteren van ruimteweersvoorspellingen en het ontwikkelen van mitigatiestrategieën.

Dit proefschrift presenteert, in drie stappen, een nieuw, op natuurkundige principes gebaseerd model om de versnelling, het transport en de radio-emissie van SEP's te simuleren in realistische zonnewind- en coronale omgevingen. Voortbouwend op een eerdere implementatie waarin het magnetohydrodynamische (MHD) model *EUHFORIA* werd gekoppeld aan de gefocuste transportcode *PARADISE*, vervangen we eerst *EUHFORIA* door het meer geavanceerde, helioferische zonnewind-MHD-code *Icarus*, die lokale roosterverfijning en hogere schokresolutie ondersteunt via adaptieve roosterverfijning. Vervolgens wordt, om de dynamica van SEP's en CME's onder 0,1 au te bestuderen, het model uitgebreid naar de corona met het *COCONUT* MHD-model. Ten slotte integreren we de *Ultimate Fast Gyrosynchrotron Codes* om radio-emissie te berekenen van energetische elektronen die vastzitten in de magnetische fluxbuis van een CME.

Toepassingen voor elke stap tonen aanzienlijke vooruitgang in het modelleren van deeltjesdynamica in zowel de corona als de heliosfeer. Het model maakt realistische simulaties mogelijk van deeltjesversnelling aan fijn opgeloste schokken, onderzoek naar opsluiting en ontsnapping van deeltjes in laag-coronale magnetische fluxbuizen, en directe koppeling van deze processen aan waarneembare type IV-radio-emissie. Dit biedt waardevolle diagnostische mogelijkheden voor CME-magnetische velden en SEP-eigenschappen nabij de zon. Bovendien vormt de integratie van coronale en heliosferische domeinen

een belangrijke stap richting grootschalige simulaties van CME- en SEP-gebeurtenissen vanaf het zonneoppervlak tot aan de baan van de aarde en daarbuiten, ter ondersteuning van toekomstige inspanningen om de complexe, onderling verbonden processen die ruimteplasma's beheersen, te ontrafelen.

Tiivistelmä

Auringon suurienergiaiset hiukkaset (SEP:t) muodostavat merkittävän riskin satelliiteille, astronauteille ja joillekin maanpinnan teknisille järjestelmille. SEP:t kiihtyvät suuriin energioihin muiden avaruussääilmiöiden kuten auringonpurkausten, koronan massapurkausten (CME:t) ja aurinkotuulen vuorovaikutusalueiden yhteydessä. Hiukkasten maksimienergiat ovat useita gigaelektronivoltteja/nukleoni ionien tapauksessa ja useita kymmeniä megaelektronivoltteja elektronien tapauksessa. SEP:ien kiihdytyksen ja kuljetuksen sekä niihin liittyvien radiohavaintojen ymmärtäminen on ratkaisevan tärkeää avaruussäänennusteiden ja torjuntastrategioiden parantamiseksi.

Tässä väitöskirjassa esitellään uusi, fysiikkaan perustuva integroitu mallikokoelma SEP:ien kiihtymisen, kuljetuksen ja radioemission simuloimiseksi realistisissa aurinkotuulen ja koronan olosuhteissa. Uusi mallikokoelma perustuu olemassa olevaan toteutuksen, jossa magnetohydrodynaminen (MHD) *EUHFORIA*-malli on yhdistetty SEP-kuljetusmalliin *PARADISE*. Uudessa mallissa korvaamme ensin *EUHFORIA*:n kehittyneemmällä sisäheliofäärin aurinkotuuli-MHD-koodilla *Icarus*, joka tukee paikallista hilan tarkennusta ja mahdollistaa korkeamman shokkiaaltoresoluution adaptiivisen hilan tarkennuksen avulla. Seuraavaksi mallikokoelmaa laajennetaan Auringon koronan alueelle käyttäen MHD-mallia *COCONUT* CME- ja SEP-dynamiikan tutkimiseksi heliosentrisen etäisyyden 0,1 au alapuolella, jonne *EUHFORIA* ja *Icarus* eivät ulotu. Lopuksi integroimme mallikokoelmaan *Ultimate Fast Gyrosynchrotron Codes* -koodit CME:n magneettisen fluxiköyden kenttään vangittuna olevien suurienergiaisten elektronien radioemission laskemista varten.

Kunkin vaiheen sovellukset osoittavat merkittäviä edistysaskeleita hiukkasdynamiikan mallintamisessa sekä koronassa että ulompana heliosfäärissä. Mallikokoelma mahdollistaa realistiset simulaatiot hiukkasten kiihtymisestä hienojakoisesti ratkaistuissa shokkiaaltorintamissa, hiukkasten vangitsemisen ja karkaamisen tutkimisen matalan koronan magneettisissa vuoköysissä sekä näiden prosessien suoran liittämisen havaittavaan Auringon tyypin IV radioemissioon.

Tämä tarjoaa arvokkaita diagnostisia mahdollisuuksia CME:n magneettikenttien ja SEP:ien ominaisuuksien analysointiin lähellä Aurinkoa. Lisäksi korona- ja heliosfäärialueiden integrointi edustaa tärkeää askelta kohti globaalin mittakaavan CME- ja SEP-tapahtumien simulointia Auringon pinnalta Maan radalle ja sen ulkopuolelle, tukien tulevia pyrkimyksiä selvittää avaruusplasmoja hallitsevien monimutkaisten, toisiinsa kytkeytyneiden prosessien luonnetta.

For Amalie Emmy Husidic.

May no struggle ever extinguish the spring in your heart
and your desire to discover the secrets of the universe.

Acknowledgements

I am writing these acknowledgements as my PhD journey comes to an end. It has been an exciting and formative period, filled with research discoveries, continuous learning, inspiring collaborations, and opportunities to attend conferences, summer schools, and workshops across the world. I would like to thank everyone who contributed to the success of this project and to the many wonderful experiences along the way.

First and foremost, I would like to thank my three supervisors, Prof Stefaan Poedts, Prof Rami Vainio (University of Turku), and Prof Nicolas Wijsen, for the opportunity to pursue this double PhD. Stefaan has been an inspiring and supportive mentor whose enthusiasm for the project was a constant motivation. His impressive expertise and broad perspective helped me grow as a researcher and encouraged independent thinking. I am especially grateful for the freedom he gave us to pursue ideas, explore new directions, attend postgraduate lectures, and engage with the wider scientific community through conferences, summer schools, and workshops.

No less thanks are due to Rami, who has been an inspiring and motivating guide throughout the project, both remotely and during my research stay in Turku. The regular modelling team meetings there were especially valuable, allowing for in-depth discussions on solar energetic particles. His ability to interpret simulation results, relate them to observations, and anticipate potential issues in our setups was always extremely helpful.

Last but not least, I would like to express my sincere thanks to Nicolas, who was not only my supervisor but also my closest collaborator. Working with his original PARADISE code and further developing it gave me extensive experience in coding, debugging, and maintaining large scientific software. Our weekly discussions on energetic particles, transport theory, and numerical modelling were always educative and inspiring. Particularly valuable was his intuition in knowing when to trust physics-based numerical models and when to remain sceptical, and his ability to connect simulation results with the behaviour of

real plasmas and particles.

I would like to express my gratitude to Dr Immanuel Christopher Jebaraj, whom I met during my stay in Turku and began collaborating with. I am very grateful to him for introducing me to the fascinating field of solar radio bursts, for our many insightful discussions about type IV bursts and open problems in the field, for his valuable input to our collaborative paper, and for drawing my attention to classic Soviet literature, which remain a remarkably rich source of knowledge in space plasma physics.

I would also like to thank my collaborators on the publications. Dr Tinatin Baratashvili kindly introduced me to the Icarus code and assisted during debugging. Dr Michaela Brchnelova introduced me to the COCONUT code and suggested using cell-connectivity information for particle tracing on its unstructured grid. Dr Luis Linan provided me with initial COCONUT CME simulations and later helped me set up the updated version. Special thanks go to Dr Angelos Vourlidas (Johns Hopkins University Applied Physics Laboratory) for collaborating on our synthetic gyrosynchrotron emission modelling and for valuable comments and criticism that greatly improved the publication.

I also thank Dr Nina Dresing (University of Turku) and Prof Jon Sundqvist, members of my supervisory and examination committees, for their valuable feedback during the milestone meetings and their comments on the thesis. I am likewise grateful to Prof Stefan Van Aelst for serving as chair of the committee, and to Prof Jasmina-Magdalenić-Zhukov, member of the examination committee, for her constructive remarks and insightful discussions during the defence and in earlier scientific exchanges.

My sincere gratitude goes to Prof Kamen Kozarev (Bulgarian Academy of Sciences) and Dr Igor Sokolov (University of Michigan) for examining my PhD thesis at the University of Turku, for also participating in the examination committee in Leuven, and for their valuable comments and insights. I also thank Dr Frederic Effenberger for agreeing to act as my opponent in the defence in Turku.

I warmly thank all members of the CmPA in Leuven for the pleasant and inspiring working atmosphere. I am grateful to Prof Rony Keppens and Prof Fabio Bacchini for our discussions on the MPI-AMRVAC framework. Special thanks go to my office and team colleagus—Angelos, Antonio, Anwesha, Ephrem, Guiseppe, Luca, Myrthe, Panagiotis, Roger, and others for their support. I also thank Prof Rozina Chaudhary (Lahore College for Women University) for many stimulating discussions during her stay in Leuven and for kindly inviting me to give a talk at a conference.

I would also like to thank the team at the University of Turku, particularly the

members of the modelling meetings—Dr Aleksandr Afanasiev, PhD candidate Seve Nyberg, and Dr Laura Vuorinen—for insightful discussions. Special thanks go to Seve for handling the organisation of my PhD defence in Turku.

I feel truly fortunate to have pursued a double PhD within the SWATNet project. My sincere thanks go to the organisers, including Prof Emilia Kilpua (coordinator), Prof Teresa Barata, Prof Dario Del Moro, Prof Alexander Nindos, and Dr Anastasiya Boiko, for creating such an inspiring and educational framework. The many workshops, summer schools, and annual meetings were scientifically invaluable, extended my transferable skills, and were personally enriching, offering the opportunity to meet the organisers and my wonderful great SWATNet PhD colleagues, including Andreas, Augustin, Guilherme, Grégoire, Lidiya, and Shreeyesh.

As part of SWATNet, I also undertook a one-month research stay at the Gyula Solar Observatory in Gyula, Hungary. I am sincerely grateful to Prof Robertus von Fay-Siebenburgen and Dr Marianna B. Korsós for their kind help and support during my stay. I also thank my colleague Guilherme for sharing that month at the observatory—I greatly appreciated our time in the tower, our discussions on science, philosophy, and life, and the unhealthy number of dinners we had at the Skorpio pizzeria.

As another part of SWATNet, I completed a three-month industrial internship at Space Applications Services in Sint-Stevens-Woluwe, Belgium. I thank Matthieu Melcot and Dr Carla Jacobs for their supervision and introducing me to the exciting field of machine learning.

I would also like to express my deepest gratitude to my former mentors at the Ruhr-University Bochum—Prof Marian Lazar, PD Dr Horst Fichtner, and Dr Klaus Scherer—with whom I stayed in contact and met at conferences throughout my PhD. I am especially thankful for the opportunity to work as a research assistant in their group during the two years between my master's degree and the start of the PhD, contributing to first- and co-authored publications and to teaching activities. Special thanks go to Marian for helping me undertake a traineeship at KU Leuven and for giving me insight into the advanced numerical modelling conducted at the CmPA. It was also Marian who redirected my research interest from plasma waves and instabilities towards particle transport theory, which ultimately inspired me to pursue this PhD.

Beyond academia, I thank my family and friends for their constant support and for providing balance alongside my scientific work. I am deeply grateful to my parents and sister for their help during my stay in Belgium, and to my dear friends Simon Kirchhoff and Patrick Gawliczek for their encouragement. Special thanks go to my brother and moral hero, Zissis Tsakiridis, for always

supporting and believing in me.

Last but certainly not least, I owe immense thanks to my lovely wife, Julia, who took on many daily tasks and responsibilities, allowing me to focus on my research and studies, especially while writing this thesis. She even put her own career on hold so that I could dedicate myself fully to science—something I will always owe her for. During my PhD, our daughter, Amalie Emmy, was born. The many late evenings spent writing computer code with calm music playing and Emmy sleeping beside me will remain some of my most vivid memories of this journey.

Edin Husidic

List of Symbols

$\hbar$	Reduced Planck constant ($= h/(2\,\pi) \approx 1.055 \times 10^{-34}$ J s)
c	Speed of light in vacuum ($= 299,792,458\,\mathrm{m\,s^{-1}}$)
$R_\odot$	Solar radius ($\approx 6.957 \times 10^8$ m)
au	Astronomical unit ($\approx 1.496 \times 10^{11}\,\mathrm{m} \approx 215\,R_\odot$)
α	Pitch angle
α_ω	Net absorption coefficient
$\alpha_{\omega\mathrm{A}}$	Stimulated absorption coefficient
$\alpha_{\omega\mathrm{S}}$	Stimulated emission coefficient
β	Speed normalised to vacuum light speed
$\boldsymbol{\kappa}_\perp$	Cross-field diffusion tensor
$\delta(x)$	Dirac delta distribution of argument x
ϵ	Dielectric tensor (reduces to identity in the cold-plasma limit)
ϵ_{tot}	Total dielectric tensor (including conductivity contributions)
η_ω	Emissivity of spontaneous emission
$\eta_{\omega\mathrm{A}}$	Emissivity of stimulated absorption
$\eta_{\omega\mathrm{S}}$	Emissivity of stimulated emission
γ	Lorentz factor
Γ_i^ν	Coefficient in current density component $i \in \{x, y, z\}$ and harmonic ν
$\kappa_\perp$	Cross-field diffusion coefficient

Λ	Dispersion tensor
λ	Adjugate of the dispersion tensor Λ
λ_{w}	Wavelength of electromagnetic radiation
$\lambda_{\parallel}$	Parallel mean free path length
$\lambda_{\perp}$	Perpendicular mean free path length
μ	Pitch angle cosine
ν	Harmonic number
Ω	Gyrofrequency
ω	Angular frequency
$\omega^{\dagger}$	Plasma frequency squared divided by angular frequency squared
$\omega_{\mathrm{p}\varsigma}$	Plasma frequency of particle species ς
Ω_{s}	Solid angle
ϕ	Azimuthal angle
σ	Conductivity tensor
Θ	Temperature
θ	Viewing (or emission) angle
$\tilde{\Omega}$	Relativistic gyrofrequency
ε	Sign of a charge
ς	Particle species
$\hat{\mathbf{k}}$	Direction unit wave vector
$\mathbf{B}$	Magnetic field vector
$\mathbf{b}$	Magnetic field directional unit vector
$\mathbf{D}$	Electric displacement field
$\mathbf{E}$	Electric field vector
$\mathbf{e}$	Normalised polarisation vector
$\mathbf{j}$	Electric current density

$\mathbf{k}$	Wave vector
$\mathbf{p}$	Momentum
$\mathbf{p}'$	Momentum after photon emission
$\mathbf{r}$	Positional vector
$\mathbf{v}$	Velocity
$\mathcal{D}$	Green's function
$\mathcal{I}$	Identity matrix
$\mathcal{K}$	Longitudinal component of the polarisation vector
$\mathcal{L}$	Determinant of the dispersion tensor Λ
$\mathcal{R}$	Particle rigidity
$\mathcal{T}$	Transverse component of the polarisation vector
$\tilde{z}$	Argument of the Bessel function of first kind J_ν
A	Area
B	Magnetic field magnitude
D	Stix parameter
$D_{\mu\mu}$	Pitch angle diffusion coefficient
E	Energy
f	Particle distribution function
f_ω	Oscillation frequency (as opposed to angular frequency)
I_ω	Specific intensity
j	Electric current density magnitude
$J_\nu(\tilde{z})$	Bessel function of first kind of argument $\tilde{z}$
j_ω	Emission coefficient
$j_\pm$	Transverse current density components in a polarisation basis
k	Magnitude of the wave vector, also known as wave number
k_z	Parallel wave vector component

L	Stix parameter
m	Mass
N	Number of particles
n	Refractive index
n_e	Electron number density
n_L	Landau quantum number
P	Stix parameter
p	Momentum magnitude
P_avg	Average power
q	Electric charge
$q_\perp$	Transverse canonical momentum (quantum number)
q_z	Longitudinal canonical momentum (quantum number)
R	Stix parameter
r	Radial distance
R_g	Gyroradius (in CGS units)
r_g	Gyroradius (in SI units)
S	Stix parameter
T	Time interval (or period)
t	Time (instantaneous)
v	Speed
$v_\pm$	Transverse velocity components in a polarisation basis
W	Electromagnetic energy density
$w_{q_z,n_\mathrm{L},\nu}$	Spontaneous emission probability
∇	Vector differential operator with respect to position
$\parallel$	Denotes parallel component with respect to the magnetic field
$\perp$	Denotes perpendicular component with respect to the magnetic field
x, y	Cartesian coordinates perpendicular to the magnetic field
z	Cartesian coordinate parallel to the magnetic field

List of Abbreviations

1D One-Dimensional. 113, 170

2D Two-Dimensional. xxviii, 73, 76, 77, 80, 109, 128

3D Three-Dimensional. xxxi, 18, 19, 21, 24, 66, 67, 76, 80, 84, 94, 105, 113, 114, 143, 150, 156

AAH Altar-Appleton-Hartree. 33, 34, 63, 180–183

ACE Advanced Composition Explorer. 7

AI Artificial Intelligence. 17, 212

AIA Atmospheric Imaging Assembly. xxvii, 6, 7

AMR Adaptive Mesh Refinement. xxviii, xxix, 19, 20, 66, 72–75, 81, 82, 84, 86, 88–90, 93–98, 151, 154

AR Active Region. xxvii, 6–8, 10, 16, 34

au astronomical unit. i, iii, v, xxviii–xxx, 4, 7, 12, 18, 19, 24, 30, 66, 67, 74, 81, 82, 84–97, 99–102, 104, 105, 110, 113, 117, 126

AWSoM Alfvén Wave-driven Solar atmosphere Model. 101

BATS-R-US Block-Adaptive-Tree Solar Wind Roe-type Upwind Scheme. 84

CFD CrossField Diffusion. xxix–xxxi, 28, 30, 87, 99, 100, 102, 104–109, 111, 112, 116, 117, 126, 150, 152, 155

CGS Centimetre-Gram-Second. xvi, 20, 21, 119, 157

CH Coronal Hole. xxvii, 6–8, 67

CIR Corotating Interaction Region. xxviii, 3, 9, 12, 18, 20, 29, 81–86, 88, 89, 92, 93, 97, 98, 151, 154

CME Coronal Mass Ejection. i, iii–vi, xxvii, xxx–xxxiii, 1, 3, 4, 9–20, 29, 31, 34, 64, 66, 68, 69, 71, 82, 98–104, 106, 108, 111, 114, 116, 117, 119–126, 129–136, 138, 139, 141, 143–146, 152–155, 160

COCONUT COolfluid COroNal UnsTructured. i, iii, v, xxviii, xxx, xxxi, 19–21, 25, 26, 29, 47, 65, 67, 68, 70, 71, 76, 77, 80, 99, 101–103, 111–117, 119, 123–125, 143, 146, 149–152, 154, 155

COOLFluiD Computational Object-Oriented Libraries for Fluid Dynamics. 19, 67

CORHEL CORona-HELiosphere. 98, 101

CR Cosmic Ray. 12, 101

DSA Diffusive Shock Acceleration. 12–14, 83, 91, 92, 94, 151

ECMI Electron Cyclotron Maser Instability. 150

ENA Energetic Neutral hydrogen Atom. 156

EPREM Energetic Particle Radiation Environment Module. 84, 98, 101

ESA European Space Agency. xxvii, 2, 7

ESP Energetic Storm Particle. 12

EUHFORIA EUropean Heliospheric FORecasting Information Asset. i, iii, v, xxviii, xxix, 18, 20, 29, 65–67, 69, 72, 74, 76, 80–82, 84, 85, 88–94, 96–99, 101, 111–113, 117, 149–152, 154

EUV Extreme UltraViolet. 3, 6, 7, 9

FD Forbush Decrease. 101, 116

FRi3D Flux Rope in 3D. 66

FTE Focused Transport Equation. 19, 21, 28, 29, 69, 70, 72, 86, 87, 99, 102, 104, 108, 116, 125, 126, 150

FVM Finite Volume Method. 66, 67

GLE Ground Level Enhancement. 12, 13, 15

GMS Geomagnetic Storm. 1–3, 16, 17, 19, 82

GNSS Global Navigation Satellite System. 3

GOES Geostationary Operational Environmental Satellite. 10

GONG Global Oscillation Network Group. 67

GS GyroSynchrotron. 16, 19, 21, 31–34, 63, 64, 70, 71, 80, 119–123, 125, 129, 131, 132, 134, 135, 137–141, 143–147, 149–155, 158, 160, 164, 166, 175

HCS Heliospheric Current Sheet. 9, 154

HEEQ Heliocentric Earth Equatorial. 66, 90

HLL Harten-Lax-van-Leer. 88, 97, 154

HMI Helioseismic and Magnetic Imager. 7, 67, 71, 102, 124, 143

ICME Interplanetary Coronal Mass Ejection. 11

IMAP Interstellar Mapping and Acceleration Probe. 156

IMF Interplanetary Magnetic Field. 9

iPATH improved Particle Acceleration and Transport. 101

KH Kelvin-Helmholtz. 96

LOFAR LOw-Frequency ARray. 146

LOS Lines Of Sight. 80, 125, 126, 132, 134, 135, 137–139, 145, 153, 160

LTE Local Thermodynamic Equilibrium. 161

M-FLAMPA Multiple-Field-Line-Advection Model for Particle Acceleration. 101

MAS Magnetohydrodynamic Algorithm outside a Sphere. 101

MFP Mean Free Path. 30, 87, 94, 100, 102, 104, 105, 116, 126, 152

MFR Magnetic Flux Rope. xxviii, xxx, xxxi, 11, 32, 68, 69, 71, 100–103, 105–109, 112, 114, 116, 117, 119, 123–125, 129–132, 134, 135, 137–139, 143, 145, 146, 152

MHD Magnetohydrodynamics. i, iii, v, 4, 18, 19, 21, 23–25, 29, 47, 66–68, 70–72, 74, 76, 80, 84, 90, 94, 95, 98, 99, 101, 102, 105, 113, 115, 119, 123, 124, 128, 143, 144, 146, 150–152, 156, 168

ML Machine Learning. 17, 149, 212

MPI-AMRVAC Message Passing Interface - Adaptive Mesh Refinement Versatile Advection Code. xxviii, 18, 24, 25, 66, 72–74, 81, 88, 90, 94, 97, 152

MR Magnetic Reconnection. 2, 6, 8, 10, 11, 14, 101, 103, 105, 107, 116, 150, 155

NASA National Aeronautics and Space Administration. 7, 156

PARADISE PArticle Radiation Asset Directed at Interplanetary Space Exploration. i, iii, v, xxix, xxxi, 18–21, 28, 29, 65, 69–74, 76, 77, 80, 81, 84–88, 90, 92–94, 96–99, 101, 102, 104, 111–113, 115–117, 119, 123–125, 128, 129, 143, 146, 149–155

PDE Partial Differential Equation. 113

PDF Particle Distribution Function. 22, 23

PSP Parker Solar Probe. 7, 15, 67, 100, 101, 116, 117, 146, 152, 154–156

rRKD relativistic Regularised Kappa Distribution. 128

RTE Radiative Transfer Equation. 32, 34–37, 64, 151, 160

SA Stochastic Acceleration. 12, 14, 83

SDA Shock Drift Acceleration. 14, 83

SDE Stochastic Differential Equation. 70

SDO Solar Dynamics Observatory. 7, 124

SEP Solar Energetic Particle. i, iii–vi, xxvii, 1, 3, 12–17, 19, 30, 82–84, 86, 87, 98–101, 116, 117, 119, 120, 143, 152, 156

SEPMOD Solar Energetic Particle MODel. 84

sfu solar flux unit. 131

SI Systéme International d'unités. xvi, 20, 21, 77, 81, 99

SIR Stream Interaction Region. 3

SOHO SOlar and Heliospheric Observatory. 122

SolO Solar Orbiter. 7, 15, 154–156

SRB Solar Radio Burst. xxviii, 15, 17, 19, 119

STAT Solar particle event Threat Assessment Tool. 101

TD Titov–Démoulin. xxviii, 68, 69, 99, 102, 109, 116, 117, 119, 123, 124, 130

TVDLF Total Variation Diminishing Lax-Friedrichs. 88, 93, 97, 151

UFGSC Ultimate Fast GyroSynchrotron Code. 19, 20, 32, 63, 65, 70, 71, 80, 119, 123, 125, 128, 143, 145, 146, 149, 150, 152, 155, 160

WSA Wang-Sheeley-Arge. 67

Contents

Abstract i

Beknopte samenvatting iii

Tiivistelmä v

Acknowledgements ix

List of Abbreviations xxi

Contents xxiii

List of Figures xxvii

List of Tables xxxiii

1 Introduction 1
- 1.1 Space weather . . . 1
- 1.2 The Sun as driver of space weather . . . 4
  - 1.2.1 Solar magnetic field . . . 4
  - 1.2.2 Solar corona . . . 5
  - 1.2.3 Solar wind . . . 7
  - 1.2.4 Solar flares and CMEs . . . 9
- 1.3 Energetic particles in the heliosphere . . . 11
- 1.4 Solar radio activity . . . 15
- 1.5 Motivation and outline . . . 17

2 Theoretical and mathematical framework for plasma and radiation modelling 21
- 2.1 The ideal MHD equations . . . 21
- 2.2 Focused transport equation . . . 27
- 2.3 Gyrosynchrotron emission . . . 31

2.3.1 Radiative transfer equation . . . 35
2.3.2 General expressions for emission and absorption coefficients 36
2.3.3 Semi-classical description of emissivity . . . 39
2.3.4 Classical derivation of time-averaged radiated power . . 40
2.3.5 Current density vector in Fourier space . . . 46
2.3.6 Derivation of the spontaneous emission probability . . . 52
2.3.7 Constructing the spontaneous emission probability . . . 53
2.3.8 Emissivity formula in cold plasma limit . . . 60
2.3.9 Final expressions for GS emission and absorption coefficients 63

3 Numerical framework and model integration 65
3.1 Numerical models . . . 65
3.1.1 EUHFORIA . . . 66
3.1.2 Icarus . . . 66
3.1.3 COCONUT . . . 67
3.1.4 PARADISE . . . 69
3.1.5 Ultimate Fast GS Codes . . . 70
3.2 Block-based grid . . . 72
3.3 Unstructured grid . . . 76

4 Modelling energetic particle dynamics in the heliosphere 81
4.1 Background and motivation . . . 82
4.2 Numerical setup . . . 85
4.3 Simulation results . . . 90
4.3.1 Validating the Icarus-PARADISE model . . . 90
4.3.2 Application of AMR . . . 94
4.4 Summary and discussion . . . 96

5 Modelling energetic particle dynamics in the solar corona 99
5.1 Background and motivation . . . 100
5.2 Numerical setup . . . 102
5.3 Simulation results . . . 104
5.3.1 Simulations without CFD . . . 105
5.3.2 CFD with a constant perpendicular MFP length . . . 105
5.3.3 CFD with a Larmor radius-dependent perpendicular MFP length . . . 108
5.4 Supplementary modelling notes . . . 111
5.4.1 A note on the CFD models . . . 111
5.4.2 Interpolating unstructured COCONUT to a structured grid 111
5.4.3 A note on numerical diffusion . . . 113
5.5 Summary and discussion . . . 116

6 Modelling gyrosynchrotron emission in the solar corona 119

6.1 Background and motivation . . . 120
6.2 Numerical setup . . . 124
6.3 Simulation results . . . 129
6.4 Summary and discussion . . . 143

7 Conclusions **149**
7.1 Summary and discussion . . . 149
7.2 Outlook . . . 153

A Appendix **157**
A.1 Validity of the straight-line transport approximation of radio waves 157
A.2 Derivation of Einstein-like relations . . . 161
A.3 Momentum-space expansion of the distribution function . . . 163
A.4 On the spontaneous emission probability in quantum mechanical terms . . . 166
A.5 Energy density in electromagnetic fields . . . 168
A.6 Mathematical identities involving the adjugate tensor λ_{ij} . . . 170
A.7 Inhomogeneous wave equation . . . 172
A.8 Particle motion . . . 173
A.9 Regularisation of products of Dirac delta distributions . . . 175
A.10 Cold plasma dispersion relation . . . 177
A.11 Altar-Appleton-Hartree approximations . . . 180

Bibliography **185**

Curriculum Vitae **211**

List of Figures

1.1 Illustration of space weather effects on space-based and ground-based technologies, as well as human health. Credit: European Space Agency (ESA)/Science Office. 2

1.2 Sunspot area diagrams from solar cycles 12 to 23. The top panel shows the distribution of relative sunspot area in equal-area latitude stripes. The bottom panel shows the average daily sunspot area. Adapted from Hathaway (2015). 5

1.3 Solar coronal structures. Panel a) shows an AIA image of the Sun at 193 Ångström (Å; 1 Å = 0.1 nm) wavelength, observed on 26 March 2017. The red arrow points to an AR, the blue arrow to a CH, and the white arrow to a quiet-Sun region. Credit: Helioviewer (helioviewer.org). Panel b) shows a white-light image of the Sun during a total solar eclipse from 1 August 2008. The red arrow marks a helmet streamer. Credit: Miroslav Druckmüller (www.zam.fme.vutbr.cz/ druck/eclipse/). 6

1.4 Sketch of the origin of the solar wind and its propagation into interplanetary space. Credit: Richard Woo, Shadia Habbal and Tom Dunne (www.americanscientist.org/article/the-origin-of-the-solar-wind). 8

1.5 Classical three-part CME model. The white-light image of a CME shows the three standard parts: core, cavity, and bright front. Adapted from Riley et al. (2008) and Klein (2018). . . . 10

1.6 Schematic diagram of typical energy spectra of oxygen nuclei from various heliospheric particle populations. Adapted from Stone et al. (1998) and Lee et al. (2012). 12

1.7 Historical two-class picture for SEP events. Panels a) and b) show schematic representations of a gradual and an impulsive SEP event, respectively. Panels c) and d) illustrate corresponding observed intensity-time profiles. Adapted from Reames (1999) and Desai & Giacalone (2016). 13

1.8 Schematic diagram of frequency-time profiles showing the relative positions of SRBs of types I–V. The frequency and duration ranges are illustrative and do not capture the full range observed in SRBs. In particular, type I and type IV can extend well beyond the displayed range, up to several GHz (see references in the main text). Adapted from Shamsuddin et al. (2023). 15

3.1 Schematic illustration of the TD MFR model, showing a thin flux rope placed between the two polarities of a locally bipolar region. The coordinate system with origin O and axes x, y, and z is located in the centre of the flux rope. The variables and functionality are addressed in the main text. Adapted from Titov et al. (2014). 68
3.2 Illustration of the modelling chain for the generation of synthetic radio spectra. 71
3.3 Block indexing in *MPI-AMRVAC* on a 2D example grid. Colours denote AMR levels (blue: level 1, yellow: level 2, red: level 3). Each block has the index that would logically follow, if the entire grid was on its AMR level (see main text). Inspired by Keppens et al. (2012). 73
3.4 Illustration of the AMR nesting and communication between blocks. Using AMR likely requires blocks of some level L to communicate both to coarse blocks (level $L-1$) and further refined blocks (level $L+1$). Inspired by Keppens et al. (2012). 75
3.5 Illustrations of the cell structure and cell connectivity in *COCONUT*. Panel a) shows the shape of a single cell with triangular faces and rectangular sides. Adapted from Brchnelova et al. (2022). Panel b) illustrates the cell connection in *COCONUT* exploited for the particle tracer and derivative computation algorithms. Adapted from Lani (2009). 77

4.1 Schematic illustration of a CIR in the solar wind reference frame. The grey shaded area indicates the compression region, while the red and blue curves illustrate the forward and reverse shock waves, respectively. Arrows of the same colour show the corresponding propagation directions. Adapted from Pizzo (1978). 83
4.2 Contour plot (latitude versus longitude) of the radial solar wind velocity component at the inner boundary (0.1 au or 21.5 $R_\odot$) both for *Icarus* and *EUHFORIA*. 85
4.3 Contour plots of key solar wind parameters in the ecliptic plane from 0.1 au to 2 au obtained from the *Icarus* simulation. Panel a) shows the radial component of the solar wind velocity, while panel b) displays the solar wind velocity divergence. 86

4.4 Illustration of CFD effects on particle intensity distributions obtained with *PARADISE* from 0.12 au to 2 au in the ecliptic plane. Panel a) shows the particle intensities 48 h after particle injection in the energy channel 980–1230 keV without CFD. Panel b) displays the corresponding results with CFD included. . . . 87
4.5 Comparison of solar wind parameters between *Icarus* and *EUHFORIA*. The plots show the magnetic field magnitude (top panel), the solar wind speed (middle panel), and the solar wind particle number density (bottom panel) as functions of longitude ϕ at a radial distance $r = 1$ au and colatitude $\theta = 90°$. *Icarus* results are shown as blue solid lines, and *EUHFORIA* results as red dashed lines. 89
4.6 Longitudinal profiles of particle intensities and solar wind parameters at $r = 1$ au and $\theta = 90°$. The top panel shows particle intensities, with different colours corresponding to the energy channels listed in the legend below. The middle and bottom panels display the solar wind speed and solar wind particle number density, respectively. In all panels, solid lines indicate *EUHFORIA*-based results, while dotted lines refer to those obtained with the *Icarus* wind. 91
4.7 Longitudinal profiles of particle intensities and solar wind parameters at $r = 1.5$ au and $\theta = 90°$. The top panel shows particle intensities, with different colours corresponding to the energy channels listed in the legend below. The middle and bottom panels display the solar wind speed and solar wind particle number density, respectively. In all panels, solid lines indicate *EUHFORIA*-based results, while dotted lines refer to those obtained with the *Icarus* wind. 93
4.8 Longitudinal profiles of particle intensities and solar wind parameters observed at $r = 1.8$ au and $\theta = 90°$, illustrating the effects of AMR. Panels a) through e) correspond to AMR levels 1 through 5, respectively. In each panel, the top subpanel shows the particle intensities, while the middle and bottom subpanels display the solar wind speed and particle number density, respectively. 95
4.9 Intensity-energy plots illustrating the effects of AMR. The four panels show the peak particle intensities across energy channels at the reverse shock, sampled at $r = 0.5$ au (panel a), $r = 1$ au (panel b), $r = 1.5$ au (panel c), and $r = 1.8$ au (panel d). 96
4.10 Cutouts of contour plots showing the radial component of the solar wind velocity. Panel a) displays the high-speed stream refined at AMR level 1, panel b) at AMR level 5. 97

5.1 Visualisation of the flux rope CME modelled with *COCONUT*. The three panels show the evolved flux rope at different times: $t = 0.48\,\mathrm{h}$ (panel a), $t = 1.53\,\mathrm{h}$ (panel b), and $t = 3.06\,\mathrm{h}$ (panel c). The sphere of radius $1\,R_\odot$ represents the Sun, with the mapped radial magnetic field component on its surface. The sphere and MFR are colour-coded by magnetic polarity: red indicates positive polarity, blue indicates negative polarity, and white corresponds to zero values. Black lines illustrate a sample of the global magnetic field. 103

5.2 Time-lapse of particle propagation in the flux rope without CFD. Panels a) through d) show particle intensity contours at $t = 0.48\,\mathrm{h}$, $1.53\,\mathrm{h}$, $3.06\,\mathrm{h}$, and $4.5\,\mathrm{h}$, respectively, plotted together with the MFR. The sphere of 1 $R_\odot$ with the mapped radial magnetic field component symbolises the Sun. 106

5.3 Time-lapse of particle propagation in a MFR using the CFD approach with a constant $\lambda_\perp$. Panels a) through c) in the top row show the results for $\lambda_\perp = 2.15 \times 10^{-2}\,R_\odot$; panels d) through f) in the middle row correspond to $\lambda_\perp = 1.075 \times 10^{-2}\,R_\odot$; and panels g) through i) in the bottom row show results for $\lambda_\perp = 2.15 \times 10^{-3}\,R_\odot$. The three columns represent simulation times of 1.53 h, 3.06 h, and 4.5 h, respectively. The colour bar for the particle intensities from Fig. 5.2 also applies here. 107

5.4 Time-lapse of particle propagation in a MFR using the CFD approach with a $\lambda_\perp$ that is a function of the Larmor radius. Panels a) through c) in the top row show the results for $\chi = 10$; panels d) through f) in the middle row correspond to $\chi = 5$, and panels g) through i) in the bottom row show the results for $\chi = 1$. The three columns represent simulation times 1.53 h, 3.06 h, and 4.5 h, respectively. The colour bar for the particle intensities from Fig. 5.2 also applies here. 109

5.5 Particle intensities integrated over the first ~ 6.5 hours at the outer boundary ($21.5\,R_\odot$), shown in the θ-ϕ plane, illustrating particle escape from the flux rope. The top row shows results for the Larmor radius-dependent $\lambda_\perp$: $\chi = 10$ (panel a), $\chi = 5$ (panel b), and $\chi = 1$ (panel c). The bottom row shows results using a constant $\lambda_\perp$: $\lambda_\perp = 2.15 \times 10^{-2}\,R_\odot$ (panel d), $\lambda_\perp = 1.075 \times 10^{-2}\,R_\odot$ au (panel e), and $2.15 \times 10^{-3}\,R_\odot$ (panel f). . . 110

5.6 Contour plots comparing the parameters of the two CFD approaches. Panel a) shows the Larmor radius-dependent $\lambda_\perp$ in the case of $\chi = 5$ (corresponding to the results in the middle row of Fig. 5.4), while panel b) illustrates values of χ based on a constant $\lambda_\perp = 1.075 \times 10^{-2}\, R_\odot$ (corresponding to the results in the middle row of Fig. 5.3). Both panels show the contours in the two planes perpendicular to the MFR at $t = 3.06$ h. 112
5.7 Comparison of unstructured *COCONUT* to *COCONUT* interpolated onto a structured grid. Panels a) and c) show 3D plots of particle intensity contours and the MFR on the (original) unstructured *COCONUT* grid, while panels b) and d) show the results on the interpolated structured grid. The top two panels correspond to $t = 1.04$ h, and the bottom two panels to $t = 2.01$ h. 114
5.8 Illustration of numerical diffusion effects using *COCONUT-PARADISE*. Panels a) through c) show a *COCONUT* snapshot at $t = 1.77$ h from simulations with an output interval of approximately 5, 15, and 20 minutes, respectively, and a minimal timestep of $\Delta t_{\min} = 10^{-4}$ s within *PARADISE*. Panel d) uses a simulation with an output interval of 5 min but $\Delta t_{\min} = 5$ s. . 115

6.1 Dynamic radio spectrum of a type IV radio burst detected by the Sagamore Hill Solar Radio Observatory on 24 September 2011. Adapted from Kumari (2022). 121
6.2 Positions of the virtual spacecraft and their respective viewing fields. The black cube represents the spacecraft, while the violet area illustrates the field of view. Some representative lines of sight are included. 127
6.3 Comparing the distribution function tails of the background and the injected electron distribution. The particle distribution function (PDF) is plotted as a red solid graph, while the background rRKD with $\kappa = 8$ and $\xi = 0.001$ is plotted as a blue dashed graph. 128
6.4 Synthetic radio spectra for the CME case with $\zeta = 30$. The panels in the left column show the observed radio emission from the injection spectrum with $\delta = 2$ seen from the three spacecraft locations, while the panels in the right column contain the radio emission from the injection spectrum with $\delta = 3$. 133
6.5 Synthetic radio spectra for the CME case with $\zeta = 70$. The panels in the left column show the observed radio emission from the injection spectrum with $\delta = 2$ seen from the three spacecraft locations, while the panels in the right column contain the radio emission from the injection spectrum with $\delta = 3$. 136

6.6 Comparing the weighted mean magnetic field strength over time for different observer positions and CME cases. For calculating the weighted average $\overline{B}$, we used the electron distribution of the $\delta = 2$ case. Each curve corresponds to a specific vantage point (halo, edge-on, face-on) and CME case ($\zeta = 30$, $\zeta = 70$). 139
6.7 Radio spectra with the peak intensity drifts from the simulation results and those calculated from theory. Exemplary, the drift of the peak intensity from higher to lower frequencies with time is shown for the case $\zeta = 30$, $\delta = 2$ (left panel), and $\zeta = 70$, $\delta = 2$ (right panel), both seen from the halo view. The black dotted curve shows the peak intensities from the simulation results, while the dark-red dashed curve shows the theoretical peak intensities calculated with Eq. (6.3). 141
6.8 Intensity curves as a function of frequency for a single time. The panels in the left column show the emission spectra in the case $\zeta = 30$ of the electrons injected with spectral indices $\delta = 2$ (black solid line) and $\delta = 3$ (red dashed line). In contrast, the right column depicts the equivalent results in the case $\zeta = 70$. Vertical lines mark the roll-over (or peak) frequencies. All spectra were recorded approximately 32 minutes into the simulation, which is about 3 minutes after the injection of the electrons. 142

List of Tables

6.1 Observer geometry and parameter combinations in the simulation setup. 126
6.2 Frequency drift rates, R_{drift}, estimated over the first ~ 30 minutes after electron injection, and peak intensities for the different simulation configurations. 130
6.3 Peak intensity ratios across observer positions, spectral indices, and CME cases. 134

1 Introduction

This chapter discusses key aspects of solar physics relevant to this thesis, highlighting how the complex and dynamic interplay of solar activity and its manifestations drives space weather phenomena. Beyond scientific curiosity, understanding these processes is of growing practical relevance for the safety of technology and human activity in space. Section 1.1 defines space weather and highlights its implications for modern society and technological systems. Section 1.2 then provides an overview of the Sun's role as the source of space weather, including its magnetic activity, solar wind, and eruptive phenomena such as Coronal Mass Ejections (CMEs) and solar flares. Solar Energetic Particles (SEPs) and solar radio activity are addressed in Sections 1.3 and 1.4, respectively. Finally, Section 1.5 concludes this chapter by motivating the research presented in this thesis and outlining its structure.

1.1 Space weather

Often described as an ordinary star among the countless other stars in the universe, the Sun remains uniquely important for humans, as its constant stream of energy makes life on Earth possible. Despite humanity's millennia-long fascination with the Sun, it was only in the mid-19th century that awareness of the connection between the dynamics of the Sun and its effects on the near-Earth space environment and conditions on the ground began to grow, notably with the historical Carrington Event. On 1 September 1859, Carrington (1859) and Hodgson (1859) independently observed and reported an increased number of sunspots and a sudden bright flash of white light on the solar disk. Within the following day, the most intense GeoMagnetic Storm (GMS) ever recorded led to widespread auroral sightings and caused major disruptions to telegraph

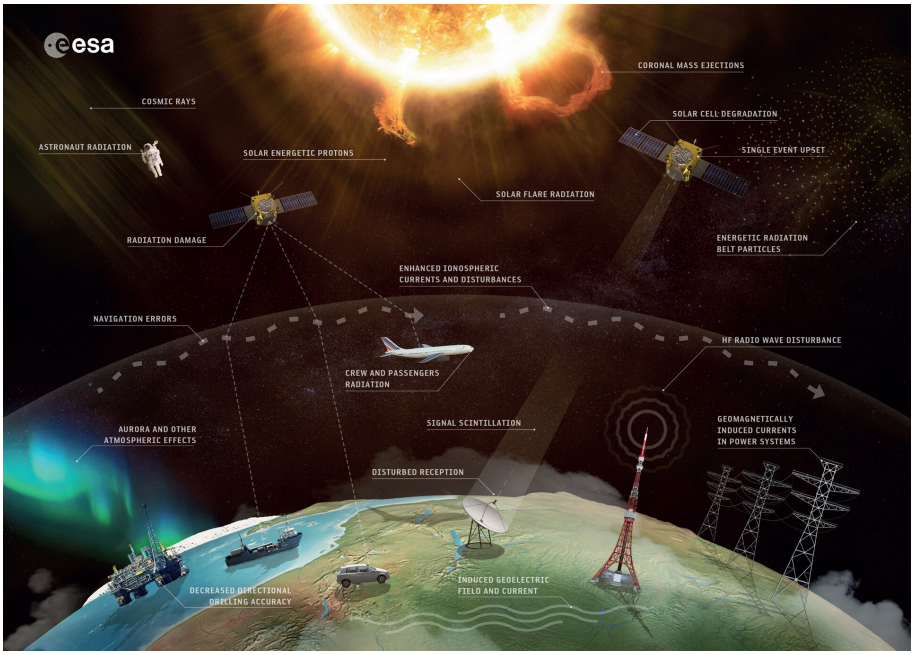

Figure 1.1. Illustration of space weather effects on space-based and ground-based technologies, as well as human health. Credit: European Space Agency (ESA)/Science Office.

systems across Europe and North America (e.g. Tsurutani et al. 2003, Hudson 2021, and references therein). GMSs are defined as temporary disturbances of the terrestrial magnetosphere driven by enhanced solar activity.

In the decades since the Carrington Event, it has become clear that solar magnetic activity is a primary driver of changing conditions in interplanetary space. This domain is now collectively known as space weather (Temmer, 2021). Solar magnetic activity encompasses the generation and evolution of the solar magnetic field and associated electric currents. Energy stored in the magnetic field can be released through processes such as Magnetic Reconnection (MR), which may lead to plasma heating, particle acceleration, and macroscopic plasma flows (Verscharen et al., 2019; Lysenko et al., 2020). Modern society, with its dependence on satellite-based communication and navigation systems, its need for the continuous operation of power grids, and its growing activity in manned and unmanned space exploration, is becoming increasingly vulnerable to harsh space weather events.

Figure 1.1 illustrates a selection of space weather sources and sectors they

impact. Among the most prominent drivers of space weather are CMEs, which are large expulsions of plasma and magnetic field from the solar corona (Howard, 2006; Gopalswamy, 2016). As they travel through interplanetary space, CMEs may strike Earth and trigger GMSs. During such encounters, the intrinsic magnetic field of the CME can interact and reconnect with the terrestrial magnetic field, thus injecting charged particles into the upper atmosphere. These particles may induce electric currents in ground-based conductors, potentially accelerating corrosion in steel pipelines, and disrupting power grid infrastructure (Hapgood, 2011; Cannon et al., 2013). Another important source of geomagnetic disturbances involves Corotating Interaction Regions (CIRs) or Stream Interaction Regions (SIRs[1]), which are persistent solar wind structures that form where the fast and slow solar wind streams interact (Richardson, 2018). CIRs are discussed in more detail in Chapter 4, where their formation, structure, and geoeffective potential are described.

Often, CMEs are accompanied by intense bursts of electromagnetic radiation called solar flares (CMEs and flares are discussed in more detail in Section 1.2.4). During powerful solar flares, X-ray and Extreme UltraViolet (EUV) radiation can be emitted, disturbing Earth's ionosphere and affecting the Global Navigation Satellite System (GNSS) and communication systems (Cannon et al., 2013; Schrijver et al., 2015). Additionally, charged particles can be accelerated at the fronts of shock waves, either driven by fast CMEs or formed in CIRs, as well as in reconnection regions at solar flare sites. These particles are known as SEPs, and consist of electrons, protons, and heavier ions (SEPs are discussed in more detail in Section 1.3). High-energy SEPs can damage satellite electronics and pose a significant radiation hazard to astronauts and passengers on high-altitude flights, potentially causing tissue damage and increasing long-term cancer risk (Chancellor et al., 2014; Knipp, 2017; Rees et al., 2023).

Other historical GMSs approaching the Carrington Event's intensity include the New York Railroad Superstorm of May 1921 (Love et al., 2019) and the March 1989 storm that triggered a major blackout in Quebec, Canada (Bolduc, 2002). Economic estimates of a Carrington-like storm reach up to the order of $\sim 10^{12}$ US dollars (National Research Council, 2008; Eastwood et al., 2017). Estimates for the likelihood of such an event include one occurrence every 250 years (Cannon et al., 2013), or a 12% chance of occurrence within the next decade (Riley, 2012), although such probabilities are difficult to constrain due to the limited dataset of extreme events (Vennerstrom et al., 2016). Nevertheless, recorded superstorms illustrate the socio-economic impacts of space weather,

[1]Some authors (e.g. Jian et al. 2006; Richardson 2018; Allen et al. 2020) reserve the term CIR for interaction regions with lifetimes exceeding one solar rotation, while referring to events of shorter duration as SIRs. In this thesis, such a distinction is not relevant, and we use CIRs in a general sense.

highlighting the urgent need to deepen our understanding of the underlying physical processes through sophisticated, physics-based numerical models and to develop reliable forecasting tools that enable timely protective measures.

1.2 The Sun as driver of space weather

At an average distance of 1 astronomical unit (au; $149,597,870,700\,\mathrm{m} \approx 215\,R_\odot$, where $R_\odot$ denotes the solar radius) from Earth, the Sun is a nearly perfect sphere of hot plasma with an equatorial radius of $R_\odot \approx 6.957 \times 10^8$ m (Stix, 2002). Its proximity makes the Sun and its heliosphere a unique natural laboratory, enabling in-situ measurements of space plasma properties and processes, the testing of theoretical models, and serving as a reference for understanding other stars.

1.2.1 Solar magnetic field

The Sun's complex and dynamic magnetic field is a primary driver of space weather phenomena. It governs coronal structures, provides the energy for eruptive events such as CMEs and solar flares, and shapes the large-scale structure of the heliosphere. It is widely accepted that the solar magnetic field is generated and sustained by a MagnetoHydroDynamic (MHD) dynamo operating in the Sun's interior (Charbonneau, 2014). This dynamo is thought to arise from the interaction of convective flows and differential rotation (i.e. the faster rotation of the equator compared to the poles) in the Sun's electrically conducting plasma. These motions twist and stretch magnetic field lines, converting kinetic energy into magnetic energy (Tobias, 2002). In this process, differential rotation leads to the conversion of a poloidal field into a more toroidal field (termed the Ω-effect), while helical convective motions regenerate the poloidal field (termed the α-effect), describing the so-called α-Ω-dynamo model (Kallenrode, 2001; Tobias, 2002).

One of the most prominent characteristics of solar magnetism is its variability. Approximately every 11 years, the global magnetic polarity reverses in what is known as the Schwabe cycle. This cycle modulates the occurrence of sunspots, solar flares, and CMEs. It begins and ends with a low level of solar activity, known as the solar minimum, characterised by fewer sunspots and eruptive events. In contrast, the solar maximum, which occurs in the middle of a Schwabe cycle, shows significantly enhanced magnetic activity (Aschwanden, 2005; Hathaway, 2015). Figure 1.2 illustrates these characteristics: the top

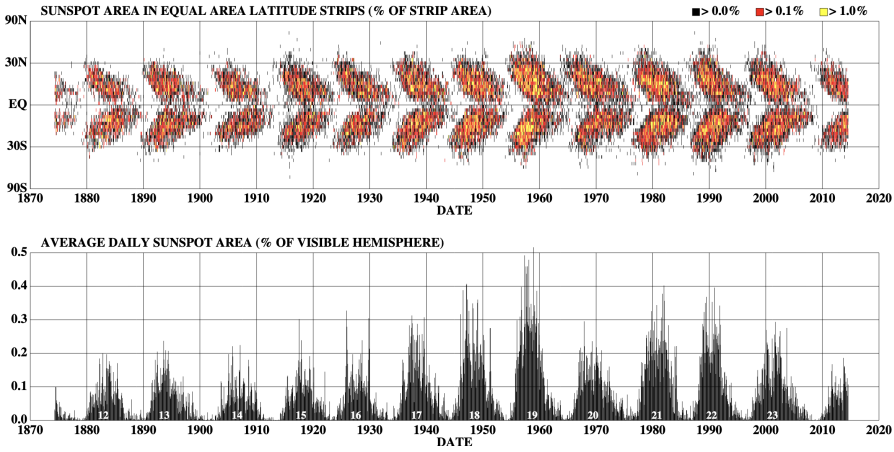

Figure 1.2. Sunspot area diagrams from solar cycles 12 to 23. The top panel shows the distribution of relative sunspot area in equal-area latitude stripes. The bottom panel shows the average daily sunspot area. Adapted from Hathaway (2015).

panel shows the latitude-time distribution of sunspots, revealing their drift towards the equator during each cycle, while the bottom panel displays the variability of daily sunspot areas over time (Hathaway, 2015).

Despite advances in observations and modelling, the detailed mechanisms underlying the generation and evolution of the solar magnetic field remain poorly understood. Solar dynamo modelling efforts face significant challenges due to the non-linear, turbulent nature of interior plasma flows (Fan, 2021), and the wide range of spatial and temporal scales involved (Tobias, 2002). Competing dynamo models, the role of subsurface shear layers such as the tachocline, and the exact nature of the processes regenerating poloidal field components are all topics of ongoing investigation (Sheeley, 2005; Parker, 2009; Charbonneau, 2014, 2020).

1.2.2 Solar corona

The solar atmosphere is composed of multiple layers, characterised by distinct plasma properties, such as particle number density and temperature. Above the solar surface, known as the photosphere, lie the chromosphere and transition region, where temperatures rise steeply from about 5700 K to several hundred thousand kelvin (Kallenrode, 2001). These layers are followed by the corona, the outermost part of the Sun's atmosphere, where temperatures exceed 10^6 K

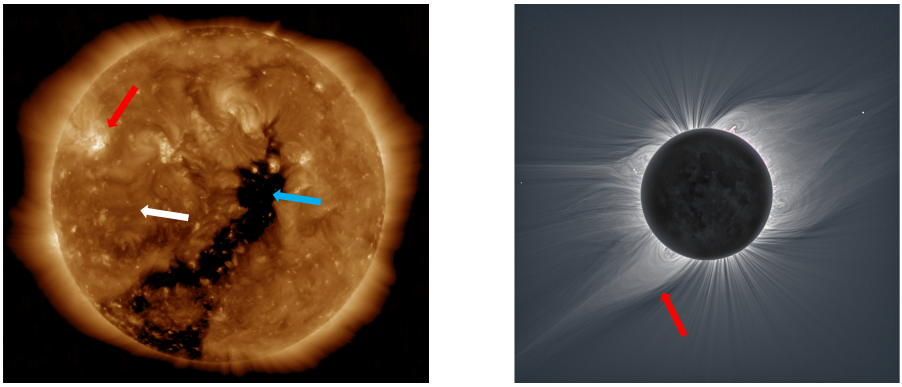

(a) EUV view of the Sun **(b)** White-light image of a solar eclipse

Figure 1.3. Solar coronal structures. Panel a) shows an AIA image of the Sun at 193 Ångström (Å; 1 Å = 0.1 nm) wavelength, observed on 26 March 2017. The red arrow points to an AR, the blue arrow to a CH, and the white arrow to a quiet-Sun region. Credit: Helioviewer (helioviewer.org). Panel b) shows a white-light image of the Sun during a total solar eclipse from 1 August 2008. The red arrow marks a helmet streamer. Credit: Miroslav Druckmüller (www.zam.fme.vutbr.cz/ druck/eclipse/).

(Aschwanden, 2005). The cause for this immense temperature increase remains an open problem, while proposed mechanisms include plasma wave heating and MR (e.g. Sakurai 2017; Cranmer & Winebarger 2019). The particle number density in the corona typically varies from $\sim 10^{11}$ cm^{-3} in flare loops, through $\sim 10^{9}$ cm^{-3} at the coronal base, to $\sim 10^{6}$ cm^{-3} in the upper corona (Aschwanden, 2005).

The corona is a highly dynamic and magnetically structured environment that includes Active Regions (ARs), quiet-Sun areas, Coronal Holes (CHs), and helmet streamers, all of which play a key role in shaping the solar wind. The plasma-β parameter ($\beta_{\rm pl}$), which denotes the ratio of thermal pressure to magnetic pressure, is commonly used to characterise different regions in the solar atmosphere. While the photosphere and lower chromosphere exhibit $\beta_{\rm pl} > 1$, values drop below unity in the corona, indicating that the plasma dynamics are governed by the magnetic field, and rise above one again beyond the corona (Gary, 2001).

Figure 1.3 illustrates these coronal features using both EUV imaging (panel a) and white-light eclipse observations (panel b). ARs, often associated with sunspots, are characterised by closed, complex magnetic field lines, and are sites of intense emission in EUV and X-ray wavelengths. Quiet-Sun regions exist outside ARs and have a weaker and more stable closed magnetic field

topology. While the strongest magnetic fields with up to 3000 G are found in sunspots, ARs have an average field strength of a few hundred G (Aschwanden, 2005), and the quiet Sun only about 1–4 G (Yang et al., 2020). CHs are regions of open magnetic field lines and are typically found in the pole regions during solar minima. However, during solar maxima, they can also appear at mid-latitudes and even across the equator. In this context, open field lines refer to magnetic field lines that extend to 'infinity' or close only after spanning vast distances through the heliosphere. Finally, helmet streamers are large, long-lived structures that superimpose sunspots and ARs. The lower part of the helmet streamers consists of magnetic field lines forming a helmet-shaped cusp located typically at heliocentric distances of 2.5 $R_\odot$ (Lee et al., 2021), while their narrow, elongated upper parts, rooted in opposite-polarity regions, extend outwards into the heliosphere, potentially enabling plasma outflow (Aschwanden, 2005; Lee et al., 2021). In contrast, so-called pseudo-streamers form at lower heliocentric distances, typically around 1.25 $R_\odot$, and have their elongated parts rooted in regions of the same magnetic polarity (Wang et al., 2007).

Traditionally, our knowledge of the corona relied on remote sensing from spacecraft such as the Solar Dynamics Observatory (SDO) with the Helioseismic and Magnetic Imager (HMI) on board to obtain line-of-sight magnetograms (Scherrer et al., 2012), and the Atmospheric Imaging Assembly (AIA) taking EUV images and providing information about the different layers in the solar atmosphere (Lemen et al., 2012). With the launches of the spacecraft Parker Solar Probe (PSP) in 2018 (Fox et al., 2016) operated by the National Aeronautics and Space Administration (NASA), and Solar Orbiter (SolO) in 2020 (Müller et al., 2020) operated by ESA and NASA, in-situ measurements of heliospheric and coronal plasmas in unprecedented proximity to the Sun became accessible.

1.2.3 Solar wind

The solar wind is a continuous, supersonic outflow of charged particles from the Sun's corona (Parker, 1958; Noyes, 1982) that fills the heliosphere and extends up to a distance of about 120 au, where its pressure is balanced by that of the local interstellar medium (Richardson et al., 2022). Composed primarily of electrons and protons, along with minor fractions of heavier ions, the solar wind has typical proton and electron number densities of about 3 cm^{-3} and temperatures around 10^5 K at Earth's orbit (Geiss et al., 1995; Baumjohann & Treumann, 1996; Kallenrode, 2001; Verscharen et al., 2019).

In-situ measurements of the solar wind by spacecraft such as the Advanced Composition Explorer (ACE; McComas et al. 1998) and the Ulysses spacecraft

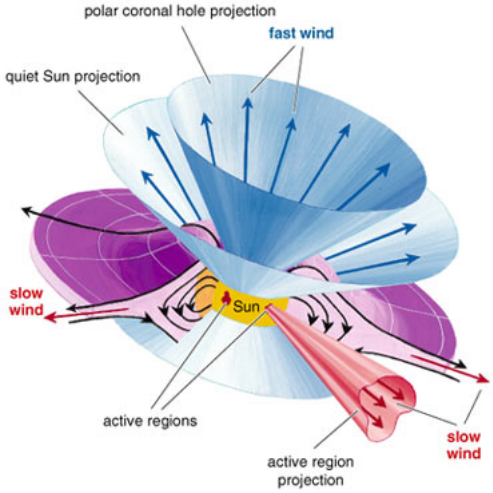

Figure 1.4. Sketch of the origin of the solar wind and its propagation into interplanetary space. Credit: Richard Woo, Shadia Habbal and Tom Dunne (www.americanscientist.org/article/the-origin-of-the-solar-wind).

(Bame et al., 1992) motivated the division of the solar wind into two fundamental components of different characteristics: a denser, more variable and turbulent component with a typical flow speed of 250–400 $\mathrm{km\,s^{-1}}$ called the slow solar wind, and a less dense, less variable component with a typical flow speed of 500–800 $\mathrm{km\,s^{-1}}$ called the fast solar wind (see Schwenn 2006 and references therein). This classification also reflects differences in their source regions on the Sun, illustrated in Fig. 1.4, though the precise source and acceleration mechanisms of the solar wind remain only partially understood (e.g. Cranmer et al. 2017 and references therein). The fast wind is believed to originate from the low-density, magnetically open CHs where the plasma escapes freely (He et al., 2010; Cranmer et al., 2017; Stansby et al., 2021). In contrast, the origin of the slow solar wind is linked to coronal streamers and ARs that lie under closed magnetic field lines, and the plasma escapes during MR processes (He et al., 2010; Antiochos et al., 2011). Some authors have also proposed that quiet-Sun regions may contribute to both the fast and slow solar wind (e.g. Woo & Habbal 2000; Feldman et al. 2005; He et al. 2007, 2010).

Owing to its dilute nature, the solar wind is weakly collisional near the Sun and becomes essentially collisionless in interplanetary space (Marsch, 2006). Due to the lack of (frequent) collisions, most particle populations cannot maintain isotropic or Maxwellian velocity distributions, as evidenced by frequent in-situ measurements (Maksimovic et al., 2005; Zouganelis et al., 2005; Marsch, 2006;

Scherer et al., 2022). The measured particle distributions are best described by the family of kappa distributions (Vasyliunas 1968; Pierrard & Lazar 2010; for a contemporary overview, see Lazar & Fichtner 2021), which comprise a thermal or Maxwellian core, and a superthermal halo characterised by enhanced high-energy tails. Often, solar wind electron distributions also contain a suprathermal strahl component, consisting of energetic electrons streaming focused along the magnetic field direction (Maksimovic et al., 2005; Lazar et al., 2017).

Due to the high conductivity of the solar wind, the solar magnetic field is essentially frozen into the plasma flow and dragged with the solar wind out into the heliosphere (Kallenrode, 2001). This is a consequence of Alfvén's theorem stating that in a perfectly conducting fluid (i.e. with zero resistivity), the magnetic field lines are frozen into the plasma flow (Alfvén, 1943, 1950; Goedbloed et al., 2019). As the Sun rotates, the dragged-out field lines become wound up to form an Archimedean or Parker spiral (Parker, 1958; Kallenrode, 2001), which provides a good approximation when the solar wind is averaged over long periods. In reality, the Interplanetary Magnetic Field (IMF) is much more complex due to the highly turbulent solar wind flow. The IMF is further distorted by interactions between the slow and fast solar wind (e.g. CIRs) and by transient structures such as CMEs (Borovsky, 2008; Balogh & Erdõs, 2013; Owens & Forsyth, 2013; Zhao et al., 2025). At Earth's orbit, the magnetic field magnitude has dropped to 3–5 nT (Kallenrode, 2001; Verscharen et al., 2019).

A prominent structure in the heliosphere is the Heliospheric Current Sheet (HCS). This large, wavy structure originates in the corona, a few solar radii above the photosphere, and arises due to the solar wind outflow and solar rotation. It separates regions of oppositely directed magnetic field lines of the IMF, and, following Ampére's law, a sheet-like electric current is maintained along the boundary. The HCS is a dynamic structure and strongly influenced by the solar cycle, being more warped and dynamic during solar maximum, while more planar and stable during solar minimum (Wilcox et al., 1980; Hoeksema et al., 1983; Khabarova et al., 2021; Pezzi et al., 2021).

1.2.4 Solar flares and CMEs

Two of the most violent manifestations of solar magnetic activity are solar flares and CMEs, both generally understood to be powered by the release of stored magnetic energy into the solar atmosphere.

Solar flares are brief, intense bursts of electromagnetic radiation spanning a broad spectrum from radio waves to gamma rays (Schwenn, 2006; Fletcher et al., 2011; Benz, 2017). Most commonly observed in soft X-rays and EUV, solar flares

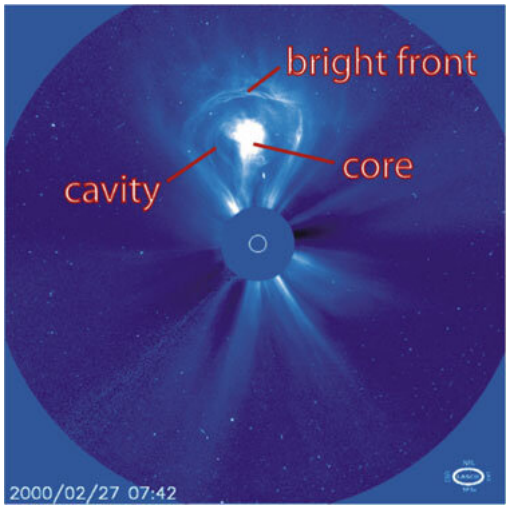

Figure 1.5. Classical three-part CME model. The white-light image of a CME shows the three standard parts: core, cavity, and bright front. Adapted from Riley et al. (2008) and Klein (2018).

typically occur in ARs. Their frequency and intensity vary with the solar cycle and correlate with sunspot activity (Hathaway, 2015). Flares are commonly believed to be caused by MR in the solar corona, rapidly converting magnetic energy into energetic particles, heat, and radiation (Shibata et al., 1995; Shibata & Magara, 2011; Priest, 2014; Lysenko et al., 2020). Commonly, solar flares are classified according to their peak soft X-ray flux in the 1–8 Å band, as measured by the Geostationary Operational Environmental Satellites (GOESs), and labelled by the letters A ($< 10^{-7}$ W m^{-2}), B, C, M, and X ($\geq 10^{-4}$ W m^{-2}). Each flare class represents an increase in the X-ray flux by a factor of 10 and is linearly subdivided from 1 to 9 (Hudson, 2011; Fletcher et al., 2011). M- and especially X-class flares are of primary interest due to their potential to significantly disturb Earth's magnetosphere and ionosphere (see Sect. 1.1), whereas A- and B-class flares are generally considered insufficient to notably affect Earth (Temmer, 2021; Grodji et al., 2021). C-class flares, although typically not geoeffective, can nevertheless produce substantial heating and magnetic restructuring in the solar atmosphere (Yadav et al., 2021; Bajnoková et al., 2025).

In contrast, CMEs involve the large-scale expulsion of solar plasma and magnetic flux into interplanetary space, often (but not always) associated with flares. Typically, CMEs consist of $\sim 10^{11}$–10^{13} kg of plasma ejected with speeds up to 3000 km s^{-1} (Vourlidas et al., 2010; Lamy et al., 2019; Temmer, 2021).

Figure 1.5 illustrates the standard three-part CME structure observed in white-light coronagraph images: i) a bright core often associated with solar filament or prominence material; ii) a surrounding dark cavity region containing a Magnetic Flux Rope[2] (MFR) with lower density; and iii) an outer bright leading edge formed by compressed plasma ahead of the eruption (Riley et al., 2008; Klein, 2018). The eruption is generally thought to be triggered by an instability in an MFR, which may pre-exist or form during the eruption. As the MFR rises, MR occurs beneath it in a vertical current sheet. In cases where the eruption speed exceeds the local Alfvén speed[3], a shock wave forms ahead of the CME (Chen, 2011). The Alfvén speed represents the propagation speed of disturbances along magnetic field lines, and is defined as

$$v_{\mathrm{A}} = \frac{B}{\sqrt{\mu_0\,\rho}}\,, \tag{1.1}$$

where B is the magnitude of the background magnetic field, ρ the mass density, and μ_0 the vacuum permeability.

Whether all CMEs follow this standard model or multiple CME classes exist, remains a subject of ongoing debate (see Temmer 2021 and references therein). Moreover, some authors distinguish between CMEs observed remotely near the Sun and Interplanetary CMEs (ICMEs) observed in situ by spacecraft (Bothmer & Mrotzek, 2017; Temmer, 2021).

1.3 Energetic particles in the heliosphere

Energetic particle populations are ubiquitous in the corona and heliosphere. These particles originate from solar, interplanetary, or extrasolar sources and play a significant role in space weather. They are typically classified according to their acceleration source. Figure 1.6 presents a schematic overview of typical intensity-energy spectra of various particle populations in the heliosphere. The solar wind dominates the intensity spectrum, but is significantly less energetic than the other shown populations, with typical proton energies around 1 keV and electron energies between 0.01–0.1 keV (Mewaldt et al., 2001; Boldyrev et al., 2020). For energetic particles of solar and heliospheric origin, the energy range spans from $\sim$ 1 keV to several GeV per nucleon (Lee et al., 2012). If

[2]An MFR is a twisted and strongly sheared magnetic field believed to be present in CMEs. In the later sections, the terms MFR and CME are used interchangeably.

[3]Strictly speaking, a shock forms when the eruption speed exceeds the local fast magnetosonic speed, which depends on the Alfvén speed, the sound speed, and the wave propagation angle relative to the magnetic field. In the lower corona, however, the Alfvén speed typically dominates (Morton et al., 2015) and provides a good approximation.

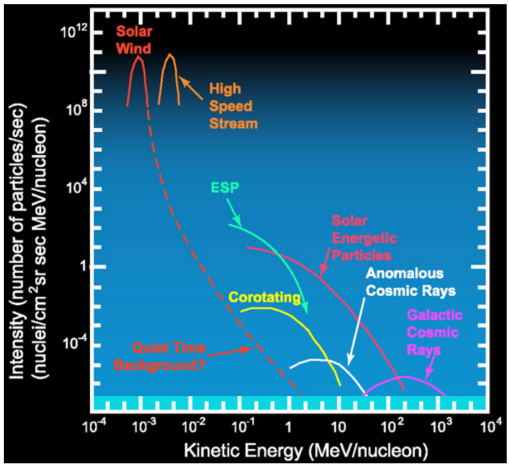

Figure 1.6. Schematic diagram of typical energy spectra of oxygen nuclei from various heliospheric particle populations. Adapted from Stone et al. (1998) and Lee et al. (2012).

galactic and extragalactic Cosmic Rays (CRs) are also included, the particle energy range extends to nearly 1 ZeV (Pierre Auger Collaboration et al., 2017), albeit at much lower intensities.

In the context of space weather, particularly relevant particle populations include Energetic Storm Particles (ESPs), ions associated with CIRs, and SEPs. ESPs are high-intensity ions observed near interplanetary shocks driven by fast CMEs, where particles are thought to be accelerated by Diffusive Shock Acceleration (DSA; a form of first-order Fermi acceleration) in combination with enhanced turbulence (Reames, 1999; Vainio et al., 2014; Wijsen et al., 2022). Similarly, CIR-associated shocks can accelerate ions, especially beyond 2–3 au, through DSA (Fisk & Lee, 1980) or Stochastic Acceleration (SA; i.e. second-order Fermi acceleration) enabled by turbulent conditions (Fermi, 1949; Tsubouchi, 2017).

SEPs are accelerated close to the Sun and span energies from a few keV per nucleon to several GeV per nucleon in the case of ions, and up to tens MeV for electrons (Reames, 2021). Various acceleration mechanisms have been proposed (see paragraphs below), but there is still no consensus in the scientific community about the exact acceleration mechanisms for SEPs (Petrosian, 2016; Perri et al., 2022b). Since the 1940s, ground-based observations have identified intense SEP events via Ground Level Enhancements (GLEs) caused by relativistic particles entering Earth's atmosphere (Forbush, 1946; Meyer et al., 1956; Kuwabara et al., 2006; Gopalswamy et al., 2012). Due to their temporal coincidence with

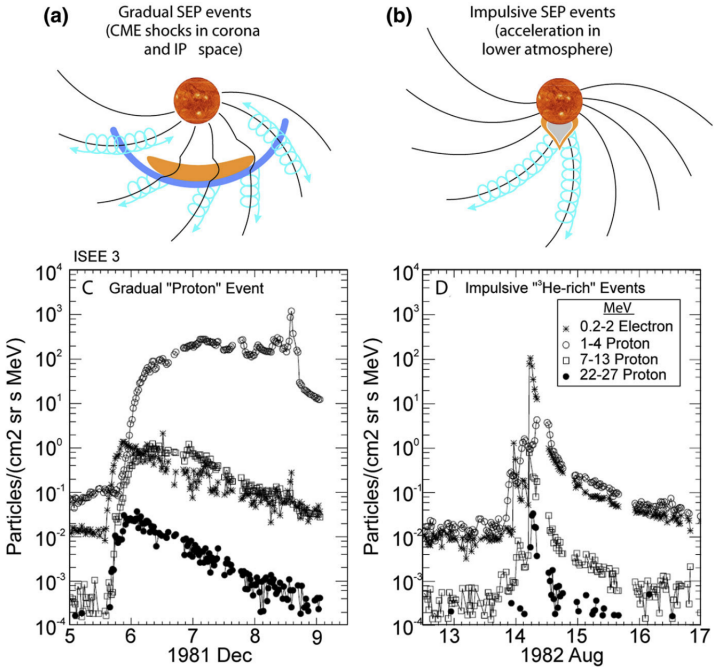

Figure 1.7. Historical two-class picture for SEP events. Panels a) and b) show schematic representations of a gradual and an impulsive SEP event, respectively. Panels c) and d) illustrate corresponding observed intensity-time profiles. Adapted from Reames (1999) and Desai & Giacalone (2016).

GLEs, solar flares were long believed to be the primary source of SEPs (e.g. Gosling 1993 and references therein). In contrast, other observed SEP events closely associated with type II radio bursts (Wild et al. 1963; see Section 1.4) and CMEs (Kahler et al., 1978) suggested CME-driven shocks as an additional source of SEP generation. Historically, this led to a classification of SEP events into two types, gradual and impulsive events, which not only differ in source region and mechanism of acceleration, but also in properties, duration, and composition (see Desai & Giacalone 2016, Reames 2021, and references therein).

Gradual SEP events are associated with sufficiently fast CMEs driving shock waves in the corona and interplanetary space. It is believed that SEPs (mainly protons and heavier ions) are accelerated primarily through DSA (Axford et al., 1977; Krymskii, 1977; Bell, 1978a,b; Blandford & Ostriker, 1978), where particles gain energy by repeatedly crossing the shock front and scattering off magnetic turbulence on either side. Further extensions of DSA theory include the effects of gradient and curvature drifts near shocks (Jokipii, 1982) and the strong

impact of shock obliquity and diffusion anisotropy on acceleration efficiency (Jokipii, 1987). Depending on factors such as shock geometry, turbulence levels, and the presence (or absence) of seed populations, DSA may be accompanied by Shock Drift Acceleration (SDA; Sonnerup 1969; Decker & Vlahos 1985; Ball & Melrose 2001; Vainio & Afanasiev 2018) and SA (Petrosian & Liu, 2004; Petrosian, 2012). These factors also influence whether a given CME produces an associated SEP event (Verkhoglyadova et al., 2015). In this context, the exact nature, drivers, and evolution of turbulence in the solar corona and heliosphere remain active topics of debate (e.g. Matthaeus & Velli 2011; Cranmer et al. 2015; Verscharen et al. 2019).

Figure 1.7 presents schematics of gradual and impulsive SEP events in panels a) and b), respectively, while panels c) and d) show typical corresponding observed time-intensity profiles. As panel a) illustrates, during gradual events, SEPs are accelerated at the fronts of shock waves. Since the CME-driven shock wave extends longitudinally across a wide range, multiple observers may be magnetically connected to the SEP source region. As the CME is propagating through interplanetary space and continuously accelerating particles, gradual SEP events typically last several days (panel c) and observations indicate enhanced abundances of protons and associations with type II radio bursts (Reames, 1999; Cliver, 2000). Since protons and heavier ions can be accelerated from a few MeV up to several hundreds of MeV per nucleon in large gradual SEP events, these events are of particular interest in space weather research due to the potential danger for astronauts and spacecraft (Reames, 2021; Temmer, 2021).

In contrast, impulsive SEP events occur at solar flare sites, where MR occurs. SA mechanisms are the primary explanation proposed for the associated SEPs, including resonant wave-particle interactions (Temerin & Roth, 1992; Roth & Temerin, 1997) and first-order Fermi acceleration in collapsing magnetic islands (Drake et al., 2013, 2009). Panel b) of Fig. 1.7 indicates that, in contrast to the gradual case, impulsive SEP events are spatially more confined, and therefore, often only observers magnetically well-connected to the solar flare site may observe the event. Since solar flares and the underlying MR processes last minutes to a few hours, impulsive SEP events have a shorter duration compared to gradual SEP events and typically last up to several hours. Furthermore, observations show impulsive SEP events to be rich in electrons and connected to type III radio bursts (Reames, 1999, 2021). The associated SEPs typically reach energies from a few hundred keV up to several MeV per nucleon (Reames, 2021).

While the two-class picture of SEP events is still employed, it should be noted that the largest SEP events involve contributions from both flare and CME shock acceleration (Kallenrode, 2003; Cane et al., 2010). Furthermore, recent missions,

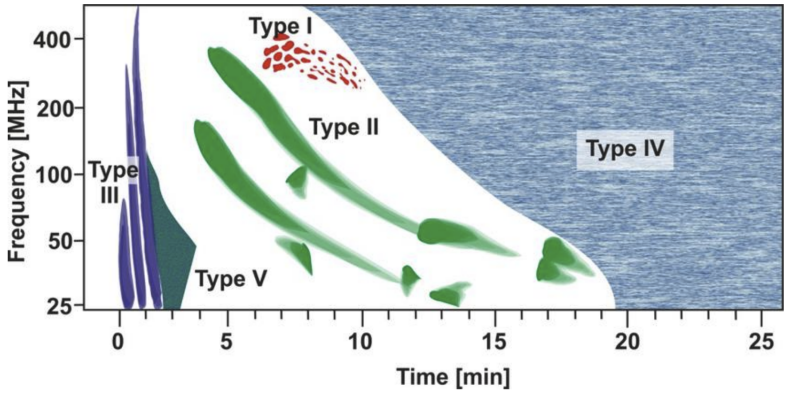

Figure 1.8. Schematic diagram of frequency-time profiles showing the relative positions of SRBs of types I–V. The frequency and duration ranges are illustrative and do not capture the full range observed in SRBs. In particular, type I and type IV can extend well beyond the displayed range, up to several GHz (see references in the main text). Adapted from Shamsuddin et al. (2023).

such as SolO and PSP, provide valuable in-situ data at closer distances to the Sun, helping improve our understanding of SEP properties and acceleration mechanisms, and complementing Earth-based GLE data and remote sensing (Paouris et al., 2023; Cohen et al., 2024).

1.4 Solar radio activity

The Sun emits electromagnetic radiation across the full spectrum, from radio waves to gamma rays. Each wavelength probes different heights and physical processes in the solar atmosphere (Aschwanden, 2005). Especially during and after solar flares and CMEs, the solar atmosphere is a rich source for radio emission, which is closely linked to space weather phenomena (Pick, 2004; Schwenn, 2006; Temmer, 2021; White, 2024). Distinct Solar Radio Bursts (SRBs) in the solar emission continuum are labelled as type I–V (Wild & McCready, 1950; Wild, 1950a,b; Wild et al., 1959), each corresponding to distinct plasma processes and solar phenomena (Kundu, 1965; Zheleznyakov, 1970).

Figure 1.8 presents a schematic illustration of the relative positions of the main SRB types I–V, along with their typical frequency ranges and durations. These ranges are not absolute, and actual observed values can extend well beyond

the illustrated scales. Type I bursts, also called noise storms, consist of short, narrowband bursts often superimposed on a continuum background, observed primarily over ARs and typically spanning the 40–400 MHz range. Individual bursts typically last 1–20 s (Melrose, 2017), while storms can persist up to a few hours (Nindos et al., 2008). These events are not directly linked to flares or CMEs, and thus are of limited relevance to space weather. The leading emission model involves energetic electrons trapped in coronal loops, exciting Langmuir waves that convert to radio waves (Melrose, 1980). However, details of this process remain debated (e.g. Melrose 2017 and references therein).

Type II bursts are slow-drifting emissions in frequency, with drift rates ranging from $\sim 10^2$ kHz/s to under 1 MHz/s (Kumari et al., 2023; Ndacyayisenga et al., 2024), and usually appearing in harmonic pairs as elongated lanes in the radio emission spectrum. They last from a few minutes to an hour, typically in the range of a few hundred MHz, but possibly down to kHz at greater distances from the Sun (Cane & Erickson, 2005). Type II bursts are believed to be generated by accelerated electrons at CME-driven shock waves, producing plasma emissions at the plasma frequency and its second harmonic (Chernov & Fomichev, 2021). Because of their close link to CMEs, type II bursts are important for identifying shock formation and forecasting related space weather effects such as SEP events and GMSs (Cairns et al., 2003; Schwenn, 2006; Temmer, 2021).

Type III bursts are fast frequency-drifting events, with drift rates ranging from a few MHz/s up to $\sim 10^2$ MHz/s (Reid & Kontar, 2018; Zhang et al., 2018). They occur when flare-accelerated electrons propagate along open magnetic field lines into the heliosphere, generating Langmuir waves that convert to radio emission. These events can appear as isolated events (with a duration of a few seconds), in groups (with a duration of a few minutes), or as storms (with durations of minutes to hours). Type III bursts often include an underlying continuum (Cane et al., 2002; Reid & Ratcliffe, 2014) and are typically covering a wide frequency range from GHz down to a few kHz. Due to their connection to energetic electron escape, they are widely used in space weather monitoring and forecasting (Reames, 2013).

Type IV bursts are broadband radio continua that are observed during or after solar flares and CMEs, usually following type II and III bursts (Fokker, 1963; Pick & Vilmer, 2008; White, 2024). They typically last from minutes to over an hour and may involve multiple emission mechanisms, including GyroSynchrotron (GS) emission (Dulk, 1973; Bastian et al., 2001; Vasanth et al., 2016, 2019), plasma emission (Gary et al., 1985; Bastian et al., 2001; Morosan et al., 2019), and potentially maser processes (Winglee & Dulk, 1986; Chernov et al., 1998). Type IV bursts are of particular interest in space weather as they can provide insight into magnetic field strengths within CMEs near the Sun (Bastian et al., 2001; Maia et al., 2007; Bain et al., 2014; Carley et al., 2017) and trapped

populations of energetic electrons (Morosan et al., 2020; Temmer, 2021). Their complex morphology (Pick, 1986) and debated origins are discussed in detail in Chapter 6.

Finally, type V bursts are smooth, continuum-like emissions that typically follow type III bursts, lasting for a few minutes. They occur in a similar frequency range as type III bursts, but extend further to lower frequencies (Dulk et al., 1980). Believed to result from the same electron beams as type III bursts (Warwick, 1967), the emission is likely due to continued plasma emission (Zheleznyakov & Zaitsev, 1968) or possibly electron cyclotron maser mechanisms (e.g. Tang et al. 2013 and references therein). Though less studied, type V bursts can extend the diagnostic reach of type III events.

1.5 Motivation and outline

In this chapter, we outlined the modern understanding of the Sun and the heliosphere as dynamic environments hosting a wide variety of (often violent) plasma processes and structures. These include solar flares, CMEs, and associated SEPs, all of which influence the near-Earth space environment and are key drivers of space weather. With modern society's growing dependence on satellites, alongside ambitions for interplanetary space exploration and long-term human presence in space, improving our ability to understand and forecast space weather phenomena is becoming increasingly important.

We also demonstrated that, despite significant progress in observations, many fundamental questions remain unanswered, such as those concerning particle acceleration, energy transport, and the mechanisms underlying SRBs. Observational approaches are constrained by the immense financial and logistical demands of constructing, launching, and operating spacecraft. Moreover, the vast range of spatial, temporal, and energy scales across which plasma processes occur in the corona and heliosphere, poses significant challenges for instrumentation alone.

To address these challenges, two complementary approaches have been increasingly employed in recent space weather research: Artificial Intelligence (AI), particularly models using Machine Learning (ML), and physics-based numerical simulations. ML models have shown promise in tasks such as solar flare prediction (Bobra & Couvidat, 2015), CME detection (Bobra & Ilonidis, 2016), and GMS forecasting (Tan et al., 2018), benefiting from rapid operation and the ability to extract complex, non-linear patterns from large datasets.

However, these models suffer from their black-box nature, limited interpretability, and sensitivity to the quality of training data and biases.

In contrast, physics-based numerical models are derived from fundamental physical laws, offering physically interpretable results. These models typically focus on specific regions (e.g. the solar corona or inner heliosphere) or particular processes (e.g. solar wind evolution or energetic particle transport), allowing for systematic parameter control. By coupling different models, a coherent and multi-scale picture of space plasma environments and processes can be achieved.

This thesis aims to develop an advanced numerical modelling framework to study the acceleration, transport, and observational signatures of energetic particles in complex coronal and heliospheric environments. The work builds on the framework of the solar wind and CME evolution and propagation model EUropean Heliospheric FORecasting and Information Asset (*EUHFORIA*; Pomoell & Poedts 2018), and the particle acceleration and transport code PArticle Radiation Asset Directed at Interplanetary Space Exploration (*PARADISE*; Wijsen 2020).

Both models have been successfully applied in multiple studies of observed space weather events (e.g. Scolini et al. 2019, 2020; Wijsen et al. 2022, 2023; Maharana et al. 2023). Despite its strengths, the MHD model *EUHFORIA*, which provides the necessary backgrounds for particle transport simulations in *PARADISE*, comes with several limitations, including a uniform equidistant grid, the exclusion of the corona, and challenges in modelling shocks with sufficient accuracy.

To achieve our goal, we advance the existing *EUHFORIA*-*PARADISE* model in three stages.

1. In general, shocks in MHD simulations appear as discontinuities smeared out by numerical diffusion (or artificial viscosity). Since key particle acceleration mechanisms occur on small spatial scales, modelling shocks at sufficiently high resolution is essential. Due to *EUHFORIA*'s uniform grid nature, higher shock resolutions require global grid refinement, which significantly increases computational cost. To overcome this, in the first stage, we introduce the advanced *Icarus*-*PARADISE* model by incorporating the *Icarus* code. Similar to *EUHFORIA*, *Icarus* (Verbeke et al., 2022), part of the Message Passing Interface - Adaptive Mesh Refinement Versatile Advection Code (*MPI-AMRVAC*; Keppens et al. 2023; Baratashvili et al. 2025), is a 3D ideal MHD code that models the global solar wind, including transient structures such as CMEs and CIRs, from 0.1 au onwards. However, unlike *EUHFORIA*, *MPI-AMRVAC* offers advanced techniques, including solution-Adaptive Mesh Refinement

(AMR) and grid stretching, which enable higher local resolutions and result in more efficient and accurate simulations.

2. Modelling CMEs and energetic particles only from 0.1 au onwards ignores many important physical processes already occurring in the solar corona, including CME evolution (Wang et al., 2014), shock formation (Mann et al., 2003), or SEP acceleration in flare regions or at the fronts of CME-driven shock waves (Reames, 1999; Desai & Giacalone, 2016). Therefore, in the second stage, we introduce the novel *COCONUT-PARADISE* model by incorporating the *COOLFluiD* COroNal UnsTructured (*COCONUT*) code. *COCONUT*, part of the Computational Object-Oriented Libraries for Fluid Dynamics (*COOLFluiD*; Lani 2009) platform, is a 3D ideal MHD model that generates coronal background configurations for the energetic particle simulations in *PARADISE*, potentially containing CMEs modelled as flux ropes.

3. As outlined in Section 1.4, SRBs play an essential role in space weather research, for instance, functioning as precursors to CME and SEP events observed near Earth, as well as to GMSs (Schwenn, 2006; Klein et al., 2018). In this context, type IV bursts are particularly interesting due to their potential to diagnose CME magnetic field strengths from their spectra containing GS emission. For this reason, in the third stage, we extend the *COCONUT-PARADISE* model by integrating the Ultimate Fast GS Codes (*UFGSC*s; Kuznetsov & Fleishman 2021) into the modelling chain, allowing the computation of synthetic type IV spectra containing GS and synchrotron emission.

The structure of this thesis is as follows. Chapter 2 provides the theoretical background relevant to the later chapters. Section 2.1 describes the concept of ideal MHD that is used for modelling background environments such as the corona and the inner-heliospheric solar wind. Section 2.2 then presents the Focused Transport Equation (FTE), which governs the acceleration and propagation of energetic particles. Finally, Section 2.3 outlines the theory behind synchrotron and GS emission, including a detailed derivation of the GS emission and absorption coefficients.

Chapter 3 discusses the numerical developments in the *PARADISE* code. All numerical models used are briefly described in Section 3.1. In Section 3.2, the necessary adaptations for working with *Icarus*'s block-based grids are described, including support for AMR and stretched grids. The modifications required to handle unstructured meshes, enabling particle propagation through coronal configurations obtained with the *COCONUT* model, are described in Section 3.3.

Chapters 4 to 6 introduce the newly developed coupled models by showing first applications. Chapter 4 presents the *Icarus*-*PARADISE* model and showcases a theoretical study of particle acceleration and transport at a CIR. This includes the validation of the new model by reproducing results from the *EUHFORIA*-*PARADISE* model, as well as a demonstration of AMR application to the shock regions of the CIR.

Chapter 5 then illustrates the *COCONUT*-*PARADISE* model and focuses on theoretical studies of particle transport in the corona in the presence of a CME. Particle dynamics within the CME flux rope, both with and without perpendicular diffusion, are analysed, thereby exploring particle confinement and escape from CME flux ropes.

Finally, Chapter 6 illustrates the extension of the *COCONUT*-*PARADISE* framework with the introduction of the *UFGSC*s to simulate radio signatures produced by energetic electrons. The impact of different CME properties, electron injections, and observer geometry on the synthetic radio spectra is investigated.

The thesis concludes in Chapter 7 with a summary and discussion of the previous chapters (Section 7.1), and an outlook on potential future developments and applications of the established modelling framework (Section 7.2).

Throughout this thesis, physical quantities and equations are expressed in the unit system used in the source work or relevant to the underlying numerical model. In particular, Section 2.2 and Chapters 4 and 5 are based on Systéme International d'unités (SI). In contrast, Sections 2.1 and 2.3, Chapter 6, and Appendix A use the Centimetre-Gram-Second (CGS) unit system, also known as Gaussian units. Chapter 3 is presented in a unit-independent manner. For consistency, numerical values of physical, astronomical, and mathematical constants are given in SI units where applicable in the symbol list at the front of this thesis, which contains important symbols and variables used throughout the thesis, limited to those appearing frequently or in multiple sections.

2

Theoretical and mathematical framework for plasma and radiation modelling

This chapter[1] presents the theoretical background behind the numerical models utilised in Chapters 4–6. *Icarus* and *COCONUT* generate inner heliospheric solar wind and coronal plasma configurations, respectively, by solving the set of 3D ideal MHD equations, which are discussed in Section 2.1. The evolution of energetic particle distributions is governed by the FTE and solved by *PARADISE* in a stochastic manner. The FTE accounts both for macroscopic effects due to large-scale motion in the solar wind and microscopic effects arising from interactions with magnetic field fluctuations, outlined in Section 2.2. Finally, to compute GS emission intensities, the emission and absorption coefficients must be calculated, whose complete derivation is provided in Section 2.3. Since Section 2.3 is very technical, readers primarily interested in the application and results may wish to proceed directly to Chapter 3 (discussion about the numerical models) or Chapter 4 (first model application), and return to Section 2.3 for reference as needed.

2.1 The ideal MHD equations

In the current view of the universe, it is estimated that 99.9% of normal (visible) matter exists in a plasma state (Kallenrode, 2001), with the solar corona and solar wind being no exception. Chen (2016) provides a helpful definition for

[1] Sections 2.1 and 2.3 are based on CGS units, while Section 2.2 uses SI units.

a plasma: "*A plasma is a quasineutral gas of charged and neutral particles which exhibits collective behaviour.*" Typically, three criteria must be satisfied for this: i) the Debye length λ_D must be much smaller than the characteristic length scale of the plasma system, ensuring quasi-neutrality on macroscopic scales; ii) the number of particles within a Debye sphere must be large, enabling collective behaviour; iii) the average time between collisions with neutral atoms exceeds the timescale of plasma oscillations, allowing for electromagnetic forces to dominate (Chen, 2016).

Plasmas are primarily characterised by their particle number density and temperature, spanning more than 30 orders of magnitude in density and over 10 in temperature (Kallenrode, 2001). These vast ranges motivate different approaches for their mathematical description. For modelling large-scale environments such as the solar corona and the heliosphere, a (macroscopic) fluid approach is typically employed. This treats the plasma as a conducting fluid, neglecting single-particle motion while accounting for collective plasma behaviour and describing it in terms of macroscopic quantities. In the most general multi-fluid picture, each particle species is defined as a separate fluid, allowing for distinct behaviour of lighter electrons and heavier ions (Baumjohann & Treumann, 1996; Goedbloed et al., 2019).

The multi-fluid equations and associated macroscopic variables can be derived from (mesoscopic) plasma kinetic theory. In this statistical approach, the evolution of a Particle Distribution Function (PDF) $f_\varsigma(\mathbf{r}, \mathbf{v}, t)$ is considered for a particle species ς, defined in six-dimensional phase-space $(\mathbf{r}, \mathbf{v})$, where $\mathbf{r}$ denotes position, $\mathbf{v}$ velocity, and t time. The PDF is defined such that

$$\mathrm{d}N_\varsigma = f_\varsigma(\mathbf{r}, \mathbf{v}, t)\, \mathrm{d}^3 r\, \mathrm{d}^3 v \tag{2.1}$$

gives the number of particles inside the phase-space volume element $\mathrm{d}^3 r\, \mathrm{d}^3 v$ at time t.

The evolution of the PDF is governed by the kinetic equation

$$\frac{\partial f_\varsigma}{\partial t} + \mathbf{v} \cdot \nabla f_\varsigma + \frac{q_\varsigma}{m_\varsigma}(\mathbf{E} + \mathbf{v} \times \mathbf{B}) \cdot \nabla_\mathbf{v} f_\varsigma = \begin{cases} \left(\frac{\partial f_\varsigma}{\partial t}\right)_\mathrm{coll}, \\ 0\,. \end{cases} \tag{2.2}$$

Here, q_ς and m_ς denote the particle's charge and mass, $\mathbf{E}$ and $\mathbf{B}$ are the electric and magnetic fields, and ∇ and $\nabla_\mathbf{v}$ denote gradients with respect to position and velocity, respectively. The collision term $(\partial f_\varsigma / \partial t)_\mathrm{coll}$ describes the net change of f_ς due to collisions. When (binary) collisions are significant, the collision term is retained, and Eq. (2.2) is referred to as the Boltzmann equation. In space plasmas that are effectively collisionless, the collision term can be neglected, thereby reducing Eq. (2.2) to the Vlasov equation (Baumjohann & Treumann, 1996; Chen, 2016).

Macroscopic plasma variables are obtained by taking velocity moments of the PDF. The i-th moment $\mathcal{M}_i$ is defined as

$$\mathcal{M}_i = \int \mathrm{d}^3 v \, f_\varsigma(\mathbf{r}, \mathbf{v}, t) \, \mathbf{v}^i \,, \tag{2.3}$$

where the zeroth, first, and second moments yield the average particle number density, bulk velocity, and temperature (or energy), respectively[2]. The macroscopic fluid equations for space plasmas are derived by taking velocity moments of the Vlasov equation, as defined in Eq. (2.3). The first three moments yield the continuity, momentum, and energy equations. These are coupled with Maxwell's equations and a form of Ohm's law to describe the evolution of the electric and magnetic fields (Baumjohann & Treumann, 1996; Goedbloed et al., 2019). Furthermore, this procedure generates an infinite hierarchy of moments, where each order introduces a higher-order variable, so a closure relation is required to truncate the hierarchy at some point (typically after the first two or three moments).

Under certain conditions, the multi-fluid equations can be approximated by a single-fluid description. In particular, a two-fluid model that treats electrons and protons separately can be combined into a single-fluid framework, leading to the (resistive) MHD approach. These conditions include quasi-neutrality between the particle species, a common bulk velocity and temperature, non-relativistic particle and wave speeds, neglecting the displacement current in Ampére's law, characteristic length scales that are much larger than the particle gyroradii, and characteristic time scales much longer than the inverse of the gyrofrequencies and plasma frequencies, such that microscopic processes are averaged out. To derive the MHD description of plasmas, macroscopic one-fluid variables are defined as linear combinations of species-specific quantities, such as mass or charge density. These new variables enable the combination of the separated fluid equations into a combined set of single-fluid equations (Goedbloed et al., 2019).

To further simplify the resistive MHD equations and obtain the ideal MHD limit, it is assumed that the plasma behaves as a perfect conductor. This leads to setting the resistivity to zero (or, equivalently, assuming infinite conductivity), which eliminates the resistive term from a generalised form of Ohm's law. As a consequence, magnetic field lines become frozen into the plasma and are advected with the flow (see Section 1.2.3). The magnetic Reynolds number, $R_\mathrm{m} \coloneqq U_0 \, L_0 / \eta_\mathrm{m}$, quantifies how strongly a plasma flow is coupled to the magnetic field, where U_0 is the characteristic flow speed, L_0 is the characteristic

[2]For $i \geq 2$, depending on the context, $\mathbf{v}^i$ denotes successive scalar or dyadic (outer) products, thereby yielding scalars or tensors of order two or higher (see appendix in Scherer et al. 2019).

length scale, and $\eta_{\rm m}$ is the magnetic diffusivity. If $R_{\rm m} \ll 1$, magnetic diffusion dominates, while $R_{\rm m} \gg 1$ corresponds to the advection-dominated regime, where the magnetic field is effectively frozen into the plasma and ideal MHD applies (Goedbloed et al., 2019).

For modelling large-scale solar wind backgrounds from 0.1 au up to 2 au and beyond, *Icarus* solves the 3D ideal MHD equations in the form (Verbeke et al., 2022)

$$\frac{\partial \rho}{\partial t} + \nabla \cdot (\rho\, \mathbf{U}_{\rm sw}) = 0\,, \tag{2.4}$$

$$\frac{\partial (\rho\, \mathbf{U}_{\rm sw})}{\partial t} + \nabla \cdot (\rho\, \mathbf{v}\mathbf{v} + p_{\rm tot}\, \mathcal{I} - \mathbf{B}\mathbf{B}) = \rho\, \mathbf{g} + \mathbf{F}_{\rm in}\,, \tag{2.5}$$

$$\frac{\partial \mathcal{E}}{\partial t} + \nabla \cdot [\mathcal{E}\, \mathbf{U}_{\rm sw} + p_{\rm tot}\, \mathbf{U}_{\rm sw} - \mathbf{B}(\mathbf{B} \cdot \mathbf{U}_{\rm sw})] = \rho\, \mathbf{U}_{\rm sw} \cdot \mathbf{g} + \mathbf{U}_{\rm sw} \cdot \mathbf{F}_{\rm in}\,, \tag{2.6}$$

$$\frac{\partial \mathbf{B}}{\partial t} + \nabla \cdot (\mathbf{U}_{\rm sw}\mathbf{B} - \mathbf{B}\mathbf{U}_{\rm sw}) = \mathbf{0}\,, \tag{2.7}$$

complemented by the solenoidal constraint in Eq. (A.43). Here, ρ, $\mathbf{U}_{\rm sw}$, $\mathcal{E}$, and $\mathcal{I}$ denote the mass density, solar wind bulk velocity, total energy density, and identity tensor, respectively. The total pressure $p_{\rm tot}$, gravitational acceleration $\mathbf{g}$, and inertial force density $\mathbf{F}_{\rm in}$ are given by

$$p_{\rm tot} = (\gamma_{\rm ad} - 1)\left(\mathcal{E} - \rho\frac{\mathbf{U}_{\rm sw}^2}{2} - \frac{\mathbf{B}^2}{2}\right) + \frac{\mathbf{B}^2}{2}\,, \tag{2.8}$$

$$\mathbf{g} = -\frac{G\, M_\odot}{r^2}\, \mathbf{e}_{\rm r}\,, \tag{2.9}$$

$$\mathbf{F}_{\rm in} = \rho(\mathbf{\Omega}_{\rm rot} \times \mathbf{r}) \times \mathbf{\Omega}_{\rm rot} + 2\,\rho\,(\mathbf{U}_{\rm sw} \times \mathbf{\Omega}_{\rm rot})\,. \tag{2.10}$$

In Eq. (2.8), $\gamma_{\rm ad}$ is the adiabatic index. In Eq. (2.9), G is the gravitational constant, $M_\odot$ the solar mass, r the radial distance, and $\mathbf{e}_{\rm r}$ the radial unit vector. Equation (2.10) expresses the sum of the centrifugal and Coriolis forces, where $\mathbf{\Omega}_{\rm rot}$ is the Sun's angular velocity. The inertial forces are included since *Icarus* solves the ideal MHD equations in a frame corotating with the Sun.

MPI-AMRVAC supports both constrained transport that enforces $\nabla \cdot \mathbf{B} = 0$ exactly, and divergence-cleaning approaches that tolerate small local deviations from zero, which are subsequently removed (Keppens et al., 2023). In the work presented in Chapter 4, we adopt the latter method, implementing the Hodge–Helmholtz projection technique, also known as elliptic divergence cleaning (see Brackbill & Barnes 1980 and Teunissen & Keppens 2019 for details).

This approach supplements the ideal MHD equations with two additional equations,

$$\nabla \cdot \nabla\Phi = \nabla \cdot \mathbf{B}_{\text{old}}\,, \tag{2.11}$$

$$\mathbf{B}_{\text{new}} = \mathbf{B}_{\text{old}} - \nabla\Phi\,, \tag{2.12}$$

where Φ is a scalar potential, and $\mathbf{B}_{\text{old}}$ and $\mathbf{B}_{\text{new}}$ denote the magnetic field before and after the divergence cleaning, respectively. Thus, Poisson's equation (Eq. 2.11) is solved for $\nabla\Phi$, which is then used in Eq. (2.12) to correct the magnetic field. *MPI-AMRVAC* also includes other methods to control the magnetic field divergence (see Keppens et al. 2023 for a detailed list with references).

The *COCONUT* model solves a similar set of equations as Eqs. (2.4)–(2.7), formulated also in conservative form but including several important modifications. The inertial force terms are set to $\mathbf{0}$. *COCONUT* also employs a divergence-cleaning method, albeit different from the one used in *MPI-AMRVAC*. In the approach in *COCONUT*, the left-hand side of the induction equation (Eq. 2.7) is extended by an additional term $+\mathcal{I}\tilde{\psi}$ involving the Lagrange multiplier $\tilde{\psi}$, while the set of equations solved in *COCONUT* is accompanied by the equation

$$\frac{\partial\tilde{\psi}}{\partial t} + U_{\text{ref}}^2\,\nabla \cdot \mathbf{B} = -\frac{\tilde{\psi}}{\tau}\,, \tag{2.13}$$

where the parameter τ has the dimension of time and can be interpreted as a damping scale. Equation (2.13) is included for numerical stability reasons, connecting the evolution equations to the solenoidal constraint (Eq. A.43) and moving divergence errors to the domain boundaries with the reference speed U_{ref}, while simultaneously damping them, controlled by the parameter τ (for details, see Dedner et al. 2002; Perri et al. 2022a, 2023). In Chapters 5 and 6, following Perri et al. (2022a) and Perri et al. (2023), we employ $\tau = \infty$ by setting the right-hand side of Eq. (2.13) to zero, so that divergence errors are only transported outwards, without explicit damping.

Furthermore, *COCONUT* exists in two versions, differing in their physical source terms. In Chapter 5, we employ a polytropic version of *COCONUT*, where the source term S_{th} (Eq. 2.14) containing any heating and radiation loss components, is set to zero. The adiabatic index is further fixed to $\gamma_{\text{ad}} = 1.05$, resulting in an almost isothermal plasma. Both versions use the ideal equation of state, $\rho\,\mathcal{E} = p_{\text{th}}/(\gamma_{\text{ad}} - 1)$, for closure, where p_{th} describes the thermal pressure. We note that while *COCONUT* expresses energy per unit mass and *Icarus* per unit volume, the units of Eq. (2.14) are consistent with Eq. (2.6) for *COCONUT*. In Chapter 6, we use an updated version of *COCONUT* (Baratashvili et al.,

2024), where the right-hand side of Eq. (2.6) is augmented by the source term

$$S_{\mathrm{th}} = -\nabla \cdot \mathbf{q} + Q_{\mathrm{rad}} + Q_{\mathrm{H}} \,. \tag{2.14}$$

Here, the first term describes thermal conduction with $\mathbf{q}$ being the heat flux vector, while Q_{rad} and Q_{H} are functions accounting for radiation losses and coronal heating, respectively. The heat flux is described differently depending on the heliocentric distance, following the approach by Mikić et al. (1999). For distances $r < 10\,R_\odot$, the plasma is assumed to be collisional, and the heat flux is modelled using the classical Spitzer-Haärm formulation

$$\mathbf{q}_{\mathrm{SH}} = -\mathcal{K}_{\parallel}\,(\mathbf{bb}) \cdot \nabla\Theta \,, \tag{2.15}$$

where $\mathbf{b}$ is the magnetic field unit vector, $\mathbf{bb}$ denotes the dyadic product of $\mathbf{b}$ with itself, Θ the temperature in units of K, and $\mathcal{K}_{\parallel} = 9 \times 10^{-7}\,\Theta^{5/2}$ the parallel thermal conductivity in units of erg cm^{-1} s^{-1} (Hollweg, 1978). For $r \geq 10\,R_\odot$, where the coronal plasma becomes effectively collisionless, the heat flux is described, following (Hollweg, 1976), as

$$\mathbf{q}_{\mathrm{H}} = \mathcal{G}\, n_{\mathrm{e}}\, k_{\mathrm{B}}\, \Theta\, \mathbf{U}_{\mathrm{sw}} \,, \tag{2.16}$$

where k_{B} is Boltzmann's constant, and $\mathcal{G}$ is a dimensionless parameter. Details on the determination of $\mathcal{G}$ are provided in Hollweg (1976).

Radiative losses in Eq. (2.14) are described by

$$Q_{\mathrm{rad}} = -n_{\mathrm{e}}\, n_{\mathrm{p}}\, \mathfrak{C}(\Theta) \,, \tag{2.17}$$

where n_{e} and n_{p} are the electron and proton number densities, respectively, and $\mathfrak{C}(\Theta)$ is a temperature-dependent radiative cooling function, whose detailed form is described in Rosner et al. (1978).

The coronal heating source term in Eq. (2.14) follows the empirical form proposed by Pevtsov et al. (2003) and Downs et al. (2010), given as

$$Q_{\mathrm{H}} = H_{\mathrm{s}}\, B\, \exp\left(-\frac{r - R_{\mathrm{s}}}{\lambda_{\mathrm{s}}}\right) \,, \tag{2.18}$$

where B is the magnetic field magnitude, H_{s} is the local heating rate at heliocentric distance R_{s}, and λ_{s} is the heating scale height. Following Linan et al. (2025), we adopt $H_{\mathrm{s}} = 4.9128 \times 10^{-7}\,\mathrm{erg\,cm^{-3}\,s^{-1}}$, $R_{\mathrm{s}} = 1\,R_\odot$, and $\lambda_{\mathrm{s}} = 0.7\,R_\odot$ in Chapter 6. Further details on the components of the source term S and some alternative expressions available in *COCONUT* can be found in Baratashvili et al. (2024) and Linan et al. (2025).

2.2 Focused transport equation

As discussed in Section 1.2.3, the solar wind streams out of the corona and fills the heliosphere. Due to its high conductivity, the solar magnetic field is frozen into the solar wind and dragged out by the charged particles into interplanetary space, forming a Parker spiral as the Sun rotates. As discussed in Section 1.3, various energetic particle populations are embedded in the collisionless and magnetised solar wind as they propagate through interplanetary space.

Ignoring gravity, the motion of the energetic particles is governed by the Newton-Lorentz equation (Eq. A.79), which represents the (microscopic) single-particle approach to describe plasma phenomena. Assuming a constant and uniform magnetic field, it can be shown that the charged particles describe a helical motion (see Appendix A.8). This motion is a superposition of a gyration around a magnetic field line with a velocity component perpendicular to the field line, and the motion of the centre of the gyration orbit (known as the guiding centre) with a velocity component parallel to the magnetic field (Boyd & Sanderson, 2003; Aran et al., 2018). In the presence of gravity, a curvature or gradient in the magnetic field, or an electric field (that is possibly time-dependent), drift motions of the guiding centre arise and superimpose the helical motion (Baumjohann & Treumann, 1996).

Using the single-particle approach, so-called adiabatic invariants can be derived, which are not absolute constants but quantities that change sufficiently slowly compared to the associated periodicities of particle motion, allowing them to be considered nearly constant. In this context, the conservation of the magnetic moment, defined as

$$\mu_{\mathrm{m}} = \frac{p_{\perp}^2}{2\,\gamma\,m\,B} = \frac{p^2\,\sin^2(\alpha)}{2\,\gamma\,m\,B}\,, \tag{2.19}$$

plays an important role. Here, $p_{\perp}$ is the perpendicular momentum component, p the momentum magnitude, and m the particle mass. The second variant of Eq. (2.19) contains the pitch angle α of the particle, defined as the angle formed by the particle's momentum vector and the magnetic field vector, $\tan(\alpha) = p_{\perp}/p_{\parallel}$, with the parallel momentum component $p_{\parallel}$.

The conservation of the magnetic moment and kinetic energy means that when a particle moves into a region with a weaker magnetic field, its pitch angle decreases. Furthermore, considering the first variant of Eq. (2.19), it also shows that $p_{\perp}$ decreases, but due to conservation of kinetic energy, $p_{\parallel}$ increases and the particle becomes increasingly ballistic. This process is called focusing and occurs when energetic particles move from the Sun outward into interplanetary space (Baumjohann & Treumann, 1996). Additionally,

a mirror force, $\mathbf{F}_{\mathrm{mirror}} = -\mu_{\mathrm{m}} \nabla_{\parallel} B$ (with $\nabla_{\parallel}$ being the directional gradient along the field), arises acting contrarily to the gradient. This means that if a particle moves into a region of a stronger magnetic field, its parallel speed can eventually become zero, and its direction is reflected, a phenomenon known as magnetic mirroring. It can be shown that only particles whose pitch angle satisfies $\sin(\alpha) > \sqrt{B/B_{\mathrm{m}}}$, where B_{m} is the maximum magnetic field strength encountered along the particle's trajectory (i.e. its individual mirror point), are reflected (Boyd & Sanderson, 2003).

The description of particle motion so far assumed an ideal Parker spiral magnetic field along which the particles propagate. In reality, the interplanetary magnetic field exhibits turbulent fluctuations that can interact with particles and scatter them in pitch angle space. Turbulence is understood here as "*seemingly random fluctuations containing some level of correlations or structures*" (van den Berg et al., 2020). Due to the stochastic nature of pitch angle diffusion, it is helpful to choose a statistical approach and describe energetic particles via their distribution function, whose evolution is governed by a transport equation.

To model the transport of energetic particles in the corona and inner heliosphere in this thesis, we employ the FTE. The FTE (Roelof, 1969; Skilling, 1971, 1975; Webb, 1985; Ruffolo, 1995; Isenberg, 1997; le Roux & Webb, 2009; Zank, 2014; Wijsen, 2020) is implemented in *PARADISE* in the form

$$\frac{\partial f}{\partial t} + \frac{\mathrm{d}\mathbf{r}}{\mathrm{d}t} \cdot \nabla f + \frac{\mathrm{d}\mu}{\mathrm{d}t}\frac{\partial f}{\partial \mu} + \frac{\mathrm{d}p}{\mathrm{d}t}\frac{\partial f}{\partial p} = \frac{\partial}{\partial \mu}\left(D_{\mu\mu}\frac{\partial f}{\partial \mu}\right) + \nabla \cdot (\boldsymbol{\kappa}_{\perp} \cdot \nabla f) \,, \quad (2.20)$$

where $f = f(\mathbf{r}, p, \mu, t)$ is the gyrotropic distribution function, $\mu = \cos\alpha$ is the cosine of the pitch angle, $D_{\mu\mu}$ denotes the pitch angle diffusion coefficient, and $\boldsymbol{\kappa}_{\perp}$ is the (spatial) CrossField Diffusion (CFD) tensor. The total derivatives of $\mathbf{r}$, μ, and p in Eq. (2.20) are given by

$$\frac{\mathrm{d}\mathbf{r}}{\mathrm{d}t} = \mathbf{U}_{\mathrm{sw}} + \mathbf{U}_{\mathrm{d}} + \mu\, v\, \mathbf{b} \,, \quad (2.21)$$

$$\frac{\mathrm{d}\mu}{\mathrm{d}t} = \frac{1-\mu^2}{2}\left(v\,\nabla\cdot\mathbf{b} + \mu\,\nabla\cdot\mathbf{U}_{\mathrm{sw}} - 3\,\mu\,\mathbf{bb} : \nabla\mathbf{U}_{\mathrm{sw}} - \frac{2}{v}\mathbf{b}\cdot\frac{\mathrm{d}\mathbf{U}_{\mathrm{sw}}}{\mathrm{d}t}\right) \,, \quad (2.22)$$

$$\frac{\mathrm{d}p}{\mathrm{d}t} = \left[\frac{1-3\,\mu^2}{2}\,(\mathbf{bb} : \nabla\mathbf{U}_{\mathrm{sw}}) - \frac{1-\mu^2}{2}\nabla\cdot\mathbf{U}_{\mathrm{sw}} - \frac{\mu}{v}\mathbf{b}\cdot\frac{\mathrm{d}\mathbf{U}_{\mathrm{sw}}}{\mathrm{d}t}\right] p \,. \quad (2.23)$$

The colon operator in Eqs. (2.22) and (2.23) denotes the Frobenius inner product

$$\mathbf{bb} : \nabla\mathbf{U}_{\mathrm{sw}} = b_i\, b_j\, \partial v_i / \partial x_j \,, \quad (2.24)$$

using Einstein's summation convention. The drift velocity $\mathbf{U}_{\mathrm{d}}$ in Eq. (2.21) accounts for particle drifts due to magnetic field gradients and curvature. It is

given by

$$\mathbf{U}_\mathrm{d} = \frac{v\,p}{q\,B}\left[\frac{1-\mu^2}{2\,B}\mathbf{b}\times\nabla B + \mu^2\,(\nabla\times\mathbf{b})_\perp\right], \tag{2.25}$$

with $(\nabla\times\mathbf{b})_\perp \coloneqq \nabla\times\mathbf{b} - (\mathbf{b}\cdot\nabla\times\mathbf{b})\,\mathbf{b}$ (Wijsen, 2020).

In Eq. (2.21), the three terms on the right-hand side describe convection with the solar wind, guiding centre drifts, and streaming along field lines, respectively. Equation (2.22) includes focusing and mirroring effects that the particle may experience, while Eq. (2.23) gives the changes of a particle's momentum. Typically, the middle term with the solar wind velocity divergence, $\nabla\cdot\mathbf{U}_\mathrm{sw}$, dominates in Eq. (2.23). Therefore, $\nabla\cdot\mathbf{U}_\mathrm{sw} > 0$ usually results in adiabatic deceleration, as it represents the expansion of the solar wind, and $\mathrm{d}p/\mathrm{d}t < 0$. Conversely, if the velocity divergence is negative, it describes regions of converging solar wind flow typical of shock or compression regions where particle acceleration occurs, and $\mathrm{d}p/\mathrm{d}t > 0$.

The FTE in Eqs. (2.20)–(2.23) is formulated in mixed coordinates, meaning that spatial coordinates are measured in an inertial frame fixed with respect to the Sun, while momentum magnitude and pitch angle are defined in the co-moving solar wind frame. This commonly used coordinate choice simplifies the description of pitch angle scattering and adiabatic energy changes, which are most naturally expressed in the turbulence rest frame, often assumed to coincide with the plasma rest frame. We note that Eqs. (2.20)–(2.23) neglect terms of order U_sw/c, where U_sw denotes the solar wind bulk speed and c the speed of light in vacuum. This approximation is justified, since $U_\mathrm{sw}/c \sim 10^{-3}$ under typical solar wind conditions. For a derivation of the FTE retaining higher-order terms in U_sw/c, see, for instance, Chapter 2 of Wijsen (2020) and references therein.

Global heliospheric MHD models, such as *EUHFORIA*, *Icarus*, and *COCONUT*, provide large-scale solar wind and coronal configurations, in which the global magnetic field generally follows a nominal Parker spiral unless disturbed by transient structures, such as CMEs and CIRs. However, even in the absence of such structures, the magnetic field exhibits turbulent fluctuations on small spatial and temporal scales. These fluctuations are not resolved by the MHD models but can play a significant role, for instance, by scattering energetic particles.

In *PARADISE*, diffusion processes are treated in a modular fashion, meaning that the diffusion terms in the FTE describing turbulence can be added, removed, or replaced. *PARADISE* includes different expressions for the pitch angle diffusion coefficient, derived under the assumptions of quasi-linear theory and magnetic slab turbulence (e.g. Jokipii 1966 and Jaekel & Schlickeiser 1992). In

this work, we use an expression similar to those of Agueda et al. (2008) and Agueda & Vainio (2013), given by

$$D_{\mu\mu} = D_0 \left(\frac{\mathcal{R}}{\mathcal{R}_0}\right)^{2-d} \left(\frac{|\mu|}{1+|\mu|} + \varpi\right)\left(1-\mu^2\right) . \tag{2.26}$$

Here, ϖ is a regularisation parameter used to smooth the resonance gap at $\mu = 0$ (e.g. Klimas & Sandri 1971; in this work, $\varpi = 0.048$), and d is the Kolmogorov spectral index (taken as $d = 5/3$ throughout this thesis). The scaling factor D_0 depends on the particle's rigidity $\mathcal{R}$ (defined here as $\mathcal{R} = p/q$), a reference rigidity $\mathcal{R}_0$ (in Chapters 4 and 5, the reference values are provided by a proton of 1 MeV energy), and a prescribed parallel MFP $\lambda_\parallel$, assumed constant in space (see Wijsen 2020 for details). In particular, in Chapter 4, we adopt $\lambda_\parallel = 0.3$ au, while in Chapters 5 and 6 we use $\lambda_\parallel = 0.1$ au. The diffusion coefficient $D_{\mu\mu}$ is related to the parallel MFP via (Hasselmann & Wibberenz, 1970)

$$\lambda_\parallel = \frac{3\,v}{8} \int_{-1}^{1} \frac{(1-\mu^2)^2}{D_{\mu\mu}}\,\mathrm{d}\mu\,, \tag{2.27}$$

from which D_0 can then be determined.

Besides pitch angle diffusion, we also consider CFD, represented by the diffusion tensor $\boldsymbol{\kappa}_\perp$. Spatial CFD has been proposed as a key mechanism to explain, for instance, SEP events observed by spacecraft that are not magnetically well connected to the particle source region (e.g. Klassen et al. 2015). To describe the CFD tensor in Eq. (2.20) we follow the approach of Zhang et al. (2009) and Wang et al. (2012), and assume it to be isotropic in the plane perpendicular to the magnetic field. The CFD tensor can then be written as

$$\boldsymbol{\kappa}_\perp = \kappa_\perp \left(\mathcal{I} - \mathbf{bb}\right) . \tag{2.28}$$

The scalar CFD coefficient $\kappa_\perp$ is related to the perpendicular MFP $\lambda_\perp$ via

$$\kappa_\perp = \lambda_\perp \frac{v}{3} . \tag{2.29}$$

In this thesis, two distinct approaches to modelling CFD are employed. The first (used in Chapters 4 and 5) assumes a constant value for $\lambda_\perp$, allowing a parametric study of its effect on particle transport. In the second approach (utilised in Chapter 5), $\lambda_\perp$ is made spatially and energetically dependent through its relation to $\lambda_\parallel$, a scaling parameter χ that is a measure of the ratio of $\lambda_\perp$ to $\lambda_\parallel$, and, the particle's maximum gyroradius, commonly referred to as the

Larmor radius,

$$r_{\mathrm{g}}(\mu) = \frac{m\,v}{|q|\,B}\sqrt{1-\mu^2}\,, \tag{2.30}$$

$$r_{\mathrm{L}} = r_{\mathrm{g}}(\mu = 0) = \frac{m\,v}{|q|\,B} = \frac{\mathcal{R}}{B}\,, \tag{2.31}$$

where r_{g} is the general expression of the gyroradius, and r_{L} can be expressed using the rigidity. This yields a modified expression for $\kappa_\perp$ (e.g. Dröge et al. 2010), reading after averaging over pitch angle ($\langle r_{\mathrm{g}}\rangle_\mu = \pi/4\, r_{\mathrm{L}}$),

$$\kappa_\perp = \underbrace{\frac{3}{4}\,\pi\,\chi\,\frac{r_{\mathrm{L}}}{r_{\mathrm{L0}}}\lambda_\parallel}_{=\,\lambda_\perp}\,v\,. \tag{2.32}$$

In Eq. (2.32), r_{L0} is a reference gyroradius defined by a chosen reference magnetic field strength B_0 and reference energy (see Chapter 5).

2.3 Gyrosynchrotron emission

As discussed in Section 1.4, radio emission from the solar atmosphere plays an important role in space weather research due to its connection to solar eruptive events and energetic particles. In this context, type IV radio bursts are of particular interest due to ongoing uncertainties regarding their emission mechanisms. Among the proposed candidates are GS and synchrotron emission. Both are produced by electrons spiralling along magnetic field lines. As an electron is accelerated, its electric field becomes distorted, generating a disturbance that propagates outwards as an electromagnetic wave, as described by Maxwell's equations (Willmott, 2019). A common classification[3] distinguishes between cyclotron emission produced by non-relativistic electrons, GS emission produced by mildly relativistic electrons, and synchrotron emission produced by ultra-relativistic electrons. However, these are not clear-cut regimes, since other factors, such as the magnetic field strength, also influence the emission characteristics, as shown in Chapter 6.

In the study presented in Chapter 6, we generated synthetic type IV spectra containing GS and synchrotron emission from electrons trapped in a CME

[3]Since all three types of emission originate from the same basic mechanism, that is, radiation by gyrating electrons, we occasionally use 'GS' as an umbrella term for brevity, and only distinguish cyclotron, GS, and synchrotron emission explicitly when the differences are physically relevant.

modelled as an MFR. Emission in such a magnetoactive plasma environment, that is, one with strong magnetic fields giving rise to distinct wave modes and large plasma and gyrofrequencies, is significantly more complex than the simple case of an electron spiralling in a vacuum (Ramaty, 1969).

In this section, we derive the equations used to compute the intensity of GS and synchrotron emission from electrons in a magnetoactive plasma. The required emission and absorption coefficients are obtained in full form as they are implemented in the *UFGSC*s by Fleishman & Kuznetsov (2010), which we use to compute synthetic radio spectra. The derivation builds on the foundational work of Eidman (1958, 1959); Wild et al. (1963); Liemohn (1965); Bekefi (1966); Sitenko & Kirochkin (1966); Mansfield (1967); Melrose (1968a,b); Ramaty (1969); Trulsen & Fejer (1970); Zheleznyakov (1970); Rybicki & Lightman (1986), with particular reference to the methods by Bekefi (1966), Melrose (1968a), Ramaty (1969), and Rybicki & Lightman (1986). Complementary derivations in the Appendix are mainly based on Bekefi (1966), Melrose (1968a), and Ramaty (1969), while the calculations related to the cold plasma dispersion relation refer to Stix (1962), Boyd & Sanderson (2003), and Goedbloed et al. (2019).

The following section presents a detailed derivation of the GS emission and absorption coefficients from first principles. Much of the foundational work dates back to the 1950s and 1960s, with some of its parts appearing in Soviet journals that are now difficult to access. Individual results are spread across several publications, occasionally contain confusing typographical errors, consider only the transverse or longitudinal component of the polarisation vector, and often omit non-trivial intermediate steps. To address these issues, we provide a transparent derivation, offering a complete and coherent calculation in one place.

To give an overview, we summarise the derivation as a roadmap of the required individual steps:

1. We aim to describe the evolution of a beam of radiation as it travels through space. In Section 2.3.1, we derive the macroscopic Radiative Transfer Equation (RTE), which includes an emission and an absorption coefficient. The specific form of these coefficients depends on the assumptions made about the radiating particles and the background plasma.

2. After identifying the emission and absorption coefficients as key to describing GS radiation, we derive general formulae to compute them in Section 2.3.2. Here, the emissivity emerges as the central quantity required to evaluate both coefficients.

3. To compute the emissivity, we adopt a semi-classical approach: the electron motion and background plasma are treated classically, while the radiation

is treated quantum mechanically via photon emission probabilities. In Section 2.3.3, we define the total radiated power and derive an expression for the emissivity involving the spontaneous emission probability.

4. Next, we derive an alternative expression for the radiated power using classical electrodynamics in Section 2.3.4. Equating the quantum and classical results allows us to extract the spontaneous emission probability and, hence, the full expression for the emissivity later in Section 2.3.6.

5. To evaluate the classical radiation formula from Section 2.3.4, we first need to derive an expression for the current density vector. Section 2.3.5 derives this vector in Fourier space, illustrating how the spiralling motion of electrons responsible for GS emission is incorporated.

6. With the current density vector in hand, we return in Section 2.3.6 to derive the complete expression for the spontaneous emission probability.

7. To complete the derivation of the emissivity, we identify expressions for particular quantities in the radiation formula in Section 2.3.7. Additionally, we incorporate the properties of the magnetoactive background plasma via the cold plasma dispersion relation.

8. With all required components established, we derive the full emissivity expression in Section 2.3.8, incorporating the Altar-Appleton-Hartree approximations (AAH) by only considering the contribution of the electrons in the Stix parameters.

9. Finally, using the explicit form of the emissivity, we return to the general formulae, derived in Section 2.3.2, to obtain the complete expressions for the GS emission and absorption coefficients.

For the derivation of the GS emission and absorption coefficients, we make the following assumptions:

- We consider only free-free transitions, that is, a free electron emits or absorbs radiation while remaining unbound after the interaction (Bekefi, 1966). Particle-particle collisions and other dissipative effects (e.g. thermal conduction or viscosity) are neglected. These assumptions are justified in the hot, highly ionised solar corona (Aschwanden, 2005), which is often considered weakly collisional. The particle gyroradii are much smaller than the collisional mean free path, and gyrofrequencies exceed collision frequencies (Braginskii, 1965; Marsch, 2006). The transition to an effectively collisionless regime is typically assumed to occur between 5 and 10 solar radii (Hollweg, 1978; Mikić et al., 1999; Marsch, 2006).

- The emission is treated as incoherent. The radiation is computed as arising from single-particle processes with random phases, neglecting collective effects. While coherent emission does occur in solar bursts (e.g. from type II and type III bursts; see Section 1.4), incoherent emission is frequently observed in the solar atmosphere (see Nindos 2020 and references therein).

- Photon energies and momenta are assumed to be much smaller than those of the emitting or absorbing electrons (Melrose, 1968a), justifying a semi-classical approach. Photon energies in the radio interval range from neV to μeV (e.g. Demtröder 2019), while mildly to ultra-relativistic electrons have keV to MeV energies. The radiation is modelled macroscopically using the RTE, neglecting scattering. This is justified under the assumption that plasma and magnetic field variations occur on scales much larger than the wavelength (Rybicki & Lightman, 1986). Scattering becomes important in strongly turbulent environments, for instance, near shocks (Murphy et al., 2021), or for high-energy processes such as Compton scattering (Bai & Ramaty, 1978). As discussed in Section 1.3, the turbulence level in the corona is not well constrained, and we assume weak turbulence.

- The background plasma is treated as cold, meaning that thermal motion is neglected in the dielectric response. This cold plasma approximation is valid when the phase speed of the wave greatly exceeds the thermal speed of the particles, and when the wave periods and lengths are large compared to particle gyroperiods and gyroradii, respectively. Additionally, the magnetic energy density must dominate over thermal energy density (e.g. Melrose 1968a; Ballai & Forgács-Dajka 2010).

- Small-amplitude electromagnetic perturbations are assumed, allowing the use of linear plasma theory. The radiation arises from resonant wave-particle interactions, but not from collective or non-linear effects such as induced emission (Melrose, 1968a).

- The derivation assumes a magnetoactive plasma with a strong ambient magnetic field, which permits wave mode splitting. Additionally, ray bending is assumed to be negligible, and the considered frequencies are sufficiently high for the emission to propagate through the coronal plasma, as discussed in Appendix A.1. GS emission is associated with ARs and CMEs, where strong magnetic fields dominate plasma dynamics (Ramaty & Lingenfelter, 1968; Melrose, 1968a; Ramaty, 1969; Lee et al., 2022).

- In the cold plasma description, with the AAH approximations incorporated, only electrons are considered, while ions are neglected due to their high inertia at radio frequencies. This is consistent with the assumption that GS emission is produced by free electrons in a collisionless environment.

2.3.1 Radiative transfer equation

We consider electromagnetic radiation originating from a distant source of characteristic size $L_{\rm sys} \gg \lambda_{\rm w}$, where $\lambda_{\rm w}$ is the wavelength of interest. In a pure vacuum, electromagnetic waves can be treated as rays that propagate along straight lines. However, in a magnetoionic medium such as the coronal plasma, the presence of a magnetic field and density gradients modifies the propagation. Rays can bend due to spatial variations in the refractive index, radiation can be suppressed at low frequencies below the local plasma cut-off, and polarisation can change due to Faraday rotation or coupling between the involved wave modes. In the present work, radiation transport is treated macroscopically as beams propagating along straight lines. In Appendix A.1, we discuss the conditions under which this approximation is valid in the context of this thesis. The evolution of such a beam is governed by the RTE, which incorporates changes in intensity due to emission, absorption, and potentially scattering processes (Rybicki & Lightman, 1986; Nindos, 2020). In this work, however, scattering is neglected, and only the total intensity (Stokes parameter I) is investigated in Chapter 6, while polarisation effects are left for future study.

The specific intensity $I_\omega = I_\omega(\mathbf{r}, \theta, \omega)$ is defined as energy per unit time, unit area, unit solid angle, and unit angular frequency. It depends on spatial location $\mathbf{r}$, viewing (or emission) angle θ, and angular frequency

$$\omega = 2\,\pi\, f_\omega\,, \tag{2.33}$$

where f_ω is the oscillation frequency. For brevity, we will refer to ω simply as the frequency. Then, the energy $\mathrm{d}E_{\rm rad}$ carried by radiation within frequency range $\mathrm{d}\omega$, passing through solid angle $\mathrm{d}\Omega_{\rm s}$ and area element $\mathrm{d}A$ over a time $\mathrm{d}t$, is given by

$$\mathrm{d}E_{\rm rad} = I_\omega\,\mathrm{d}t\,\mathrm{d}A\,\mathrm{d}\Omega_{\rm s}\,\mathrm{d}\omega\,. \tag{2.34}$$

To account for spontaneous emission in the medium, we define the emission coefficient j_ω with units of energy per unit time, per unit volume, per unit solid angle, and per unit frequency. It allows to write Eq. (2.34) as

$$\mathrm{d}E_{\rm rad} = j_\omega\,\mathrm{d}t\,\mathrm{d}V\,\mathrm{d}\Omega_{\rm s}\,\mathrm{d}\omega\,. \tag{2.35}$$

Using Eqs. (2.34) and (2.35), a beam that travels a distance $\mathrm{d}s$ through a volume element $\mathrm{d}V = \mathrm{d}A\,\mathrm{d}s$ experiences an intensity gain by

$$\frac{\mathrm{d}I_\omega}{\mathrm{d}s} = j_\omega\,. \tag{2.36}$$

In contrast, the radiation may be absorbed by electrons of particle number density n_e, with cross-section σ_ω representing their effective absorbing area. With the number of electrons in a volume element dV given by $n_\mathrm{e}\,\mathrm{d}A\,\mathrm{d}s$, and total absorption area calculated as $n_\mathrm{e}\,\mathrm{d}A\,\mathrm{d}s\,\sigma_\omega$, Eq. (2.34) yields for the absorbed specific intensity

$$\begin{aligned} -\mathrm{d}I_\omega\,\mathrm{d}t\,\mathrm{d}A\,\mathrm{d}\Omega_\mathrm{s}\,\mathrm{d}\omega &= I_\omega\,\mathrm{d}t\,(n_\mathrm{e}\,\mathrm{d}A\,\mathrm{d}s\,\sigma_\omega)\,\mathrm{d}\Omega_\mathrm{s}\,\mathrm{d}\omega \\ \Leftrightarrow \mathrm{d}I_\omega &= -n_\mathrm{e}\,\sigma_\omega\,I_\omega\,\mathrm{d}s \\ \Leftrightarrow \frac{\mathrm{d}I_\omega}{\mathrm{d}s} &= -\alpha_\omega\,I_\omega\,, \end{aligned} \tag{2.37}$$

where the minus sign is included by convention to denote a loss of energy. In the third line of Eq. (2.37), we define the absorption coefficient $\alpha_\omega \coloneqq n_\mathrm{e}\,\sigma_\omega$, with units of inverse length (Rybicki & Lightman, 1986).

Finally, combining the two processes from Eqs. (2.36) and (2.37) into one equation, we obtain the full form of the RTE, given as

$$\frac{\mathrm{d}I_\omega}{\mathrm{d}s} = j_\omega - \alpha_\omega\,I_\omega\,. \tag{2.38}$$

The primary objective now is to determine the emission and absorption coefficients, j_ω and α_ω, whose forms strongly depend on the involved physics, including the particle motion, the particle distribution function, and the electromagnetic properties and composition of the ambient medium.

2.3.2 General expressions for emission and absorption coefficients

With the RTE in Eq. (2.38) established, the next step is to derive general expressions from which the emission and absorption coefficients can be obtained. To achieve this, it is helpful to introduce the emissivity $\eta_\omega(\mathbf{r},\mathbf{p})$, defined as the differential rate at which an electron spontaneously radiates energy per unit solid angle, per unit time, and per unit frequency interval (Bekefi, 1966). In the following, we denote $\mathbf{p}$ as the initial momentum of the electron before emitting a photon, and $\mathbf{p}'$ as the state of the momentum after transitioning by emission[4].

Considering the number of electrons in momentum space per unit spatial volume, $\mathrm{d}\tilde{N} \coloneqq f(\mathbf{r},\mathbf{p})\,\mathrm{d}^3p$, the spontaneous emission rate by electrons in this momentum

[4]We note that different authors use varying conventions (e.g. Melrose 1968a compared to Bekefi 1966 and Ramaty 1969).

range is given by

$$\eta_\omega(\mathbf{r},\mathbf{p})\,\mathrm{d}\tilde{N}(\mathbf{r},\mathbf{p}) = \eta_\omega(\mathbf{r},\mathbf{p})\,f(\mathbf{r},\mathbf{p})\,\mathrm{d}^3p\,. \tag{2.39}$$

To obtain the total spontaneous emission (i.e. the total energy per unit volume, per unit time, per unit solid angle, and per unit frequency range), we integrate Eq. (2.39) over all electron momenta, yielding the emission coefficient[5]

$$j_\omega = \int \eta_\omega(\mathbf{r},\mathbf{p})\,f(\mathbf{r},\mathbf{p})\,\mathrm{d}^3p\,. \tag{2.40}$$

To derive an expression for the absorption coefficient, it is important to note two competing processes that both scale with I_ω: stimulated absorption (electron absorbs a photon and transitions from state $\mathbf{p}'$ to $\mathbf{p}$) and stimulated emission (electron is triggered by an incident photon to emit a second photon and transition from state $\mathbf{p}$ to $\mathbf{p}'$). We define $\eta_{\omega\mathrm{S}}(\mathbf{r},\mathbf{p})$ as the differential rate of stimulated emission by an electron per unit radiation intensity, per unit solid angle, and per unit frequency interval. Analogous to Eq. (2.39), the total rate of stimulated emission by $\mathrm{d}\tilde{N}(\mathbf{r},\mathbf{p})$ electrons per unit volume is

$$\eta_{\omega\mathrm{S}}(\mathbf{r},\mathbf{p})\,I_\omega(s)\,\mathrm{d}\tilde{N}(\mathbf{r},\mathbf{p}) = \eta_{\omega\mathrm{S}}(\mathbf{r},\mathbf{p})\,I_\omega(s)\,f(\mathbf{r},\mathbf{p})\,\mathrm{d}^3p\,, \tag{2.41}$$

and, the stimulated emission coefficient becomes

$$\alpha_{\omega\mathrm{S}} = \int \eta_{\omega\mathrm{S}}(\mathbf{r},\mathbf{p})\,f(\mathbf{r},\mathbf{p})\,\mathrm{d}^3p\,. \tag{2.42}$$

Similarly, defining $\eta_{\omega\mathrm{A}}(\mathbf{r},\mathbf{p}')$ as the differential rate of stimulated absorption by an electron per unit radiation intensity, per unit solid angle, and per unit frequency interval, the total rate of stimulated absorption by $\mathrm{d}\tilde{N}(\mathbf{r},\mathbf{p}')$ electrons per unit volume is

$$\eta_{\omega\mathrm{A}}(\mathbf{r},\mathbf{p}')\,I_\omega(s)\,\mathrm{d}\tilde{N}(\mathbf{r},\mathbf{p}') = \eta_{\omega\mathrm{A}}(\mathbf{r},\mathbf{p}')\,I_\omega(s)\,f(\mathbf{r},\mathbf{p}')\,\mathrm{d}^3p'\,, \tag{2.43}$$

which yields the stimulated absorption coefficient as

$$\alpha_{\omega\mathrm{A}} = \int \eta_{\omega\mathrm{A}}(\mathbf{r},\mathbf{p}')\,f(\mathbf{r},\mathbf{p}')\,\mathrm{d}^3p'\,. \tag{2.44}$$

However, Eq. (2.44) does not represent the absorption usually observable in practice (Bekefi, 1966). Instead, an observer would measure the difference between Eqs. (2.44) and (2.42). Hence, the effective absorption coefficient in the RTE is given by

$$\alpha_\omega = \int \eta_{\omega\mathrm{A}}(\mathbf{r},\mathbf{p}')\,f(\mathbf{r},\mathbf{p}')\,\mathrm{d}^3p' - \int \eta_{\omega\mathrm{S}}(\mathbf{r},\mathbf{p})\,f(\mathbf{r},\mathbf{p})\,\mathrm{d}^3p\,. \tag{2.45}$$

[5]Throughout this thesis, integrals without specified limits are assumed to extend from $-\infty$ to $+\infty$, unless stated otherwise.

Our goal is to re-express Eq. (2.45) in terms of $\eta_\omega(\mathbf{r},\mathbf{p})$ by establishing relations between $\eta_\omega(\mathbf{r},\mathbf{p})$, $\eta_{\omega\mathrm{S}}(\mathbf{r},\mathbf{p})$, and $\eta_{\omega\mathrm{A}}(\mathbf{r},\mathbf{p}')$. This can be accomplished using Einstein-like relations of the form

$$\eta_\omega(\mathbf{r},\mathbf{p}) = \frac{n^2\,\hbar\,\omega^3}{8\,\pi^3\,c^2}\eta_{\omega\mathrm{S}}(\mathbf{r},\mathbf{p})\,, \tag{2.46a}$$

$$\eta_{\omega\mathrm{A}}(\mathbf{r},\mathbf{p}')\mathrm{d}^3p' = \eta_{\omega\mathrm{S}}(\mathbf{r},\mathbf{p})\,\mathrm{d}^3p\,, \tag{2.46b}$$

where n is the refractive index, c is the speed of light in vacuum, and $\hbar = h/(2\,\pi)$ is the reduced Planck constant with h as the regular Planck constant. A detailed derivation of these relations is provided in Appendix A.2.

We first rearrange Eq. (2.46b) to isolate $\eta_{\omega\mathrm{A}}(\mathbf{r},\mathbf{p}')$, and substitute the result into the first integral of Eq. (2.45). This gives

$$\alpha_\omega = \int \eta_{\omega\mathrm{S}}(\mathbf{r},\mathbf{p})\,[f(\mathbf{r},\mathbf{p}') - f(\mathbf{r},\mathbf{p})]\,\mathrm{d}^3p\,. \tag{2.47}$$

Next, we rearrange Eq. (2.46a) to express $\eta_{\omega\mathrm{S}}(\mathbf{r},\mathbf{p})$ in terms of $\eta_\omega(\mathbf{r},\mathbf{p})$, and insert it into Eq. (2.47). This yields the net absorption coefficient in the form

$$\alpha_\omega = \frac{8\,\pi^3\,c^2}{n^2\,\hbar\,\omega^3}\int \eta_\omega(\mathbf{r},\mathbf{p})\,[f(\mathbf{r},\mathbf{p}') - f(\mathbf{r},\mathbf{p})]\,\mathrm{d}^3p\,. \tag{2.48}$$

Thus, α_ω represents the net loss (or gain) of energy from a beam of electromagnetic radiation and results from the imbalance between upward (stimulated absorption) and downward (stimulated emission) transitions.

Since the photon energy is assumed to be much smaller than the electron energy, the momentum change between states $\mathbf{p}$ and $\mathbf{p}'$ is also minimal. As a result, the corresponding distribution functions in Eq. (2.48) differ only slightly. This allows a Taylor expansion of their difference (Ramaty, 1969), yielding

$$f(\mathbf{r},\mathbf{p}') - f(\mathbf{r},\mathbf{p}) \approx -\frac{\hbar\,\omega}{p\,c} \times \left[\frac{\beta\,m^2\,c^2\,\gamma^2}{p}\frac{\partial f}{\partial p} + \frac{n\,\beta\,\cos(\theta)-\cos(\alpha)}{\beta\,\sin(\alpha)}\sqrt{1-\mu^2}\frac{\partial f}{\partial \mu}\right], \tag{2.49}$$

where $\beta = v/c$, $\gamma = (1-v^2/c^2)^{-1/2}$ is the Lorentz factor, α the pitch angle, and θ the emission angle (i.e. the angle between $\mathbf{B}$ and wave vector $\mathbf{k}$). A detailed derivation of the expansion in Eq. (2.49) is provided in Appendix A.3.

With the general expressions for the emission and absorption coefficients established in Eqs. (2.40) and (2.48), both formulated in terms of the emissivity η_ω, the next step is to work towards finding an explicit expression for η_ω.

2.3.3 Semi-classical description of emissivity

The emissivity introduced in Section 2.3.2 can be described using a semi-classical approach, in which the electron motion and the background plasma are treated using classical electrodynamics, while the emitted radiation is treated quantum mechanically as photons with energy $E_{\mathrm{ph}} = \hbar\,\omega$. In this framework, the spontaneous emission of radiation is associated with transitions between electron momentum states. These transitions occur with a differential probability rate $w_{\mathcal{S}}^{\mathcal{S}'}(\mathbf{k})$, defined per unit time and per unit wave vector volume, describing the likelihood that an electron in initial state $\mathcal{S}$ transitions to a final state $\mathcal{S}'$ by emitting a photon with wave vector $\mathbf{k}$. The probability also depends on the wave mode, as each mode is characterised by a distinct dispersion relation $\omega = \omega(\mathbf{k})$, polarisation, and propagation angle relative to the ambient magnetic field. This becomes clear in Section 2.3.8.

The total power P_{tot} radiated through a particular wave mode can be expressed as the sum over all final states $\mathcal{S}'$ and an integral over all photon wave vectors $\mathbf{k}$. For each transition, the emitted energy $\hbar\,\omega$ is multiplied by the probability of that transition $w_{\mathcal{S}}^{\mathcal{S}'}(\mathbf{k})$. This yields

$$\begin{aligned} P_{\mathrm{tot}} &= \sum_{\mathcal{S}'} \int \frac{\mathrm{d}^3 k}{(2\,\pi)^3} \hbar\,\omega(\mathbf{k})\, w_{\mathcal{S}}^{\mathcal{S}'}(\mathbf{k}) \\ &= \sum_{\nu=-\infty}^{\infty} \int \frac{\mathrm{d}^3 k}{(2\,\pi)^3} \hbar\,\omega(\mathbf{k})\, w_{q_z, n_{\mathrm{L}}, \nu}(\mathbf{k})\,. \end{aligned} \tag{2.50}$$

The factor $(2\,\pi)^3$ arises from Fourier transformation conventions. In the second line of Eq. (2.50), the sum is rephrased as a sum over cyclotron harmonics ν, where the transition probability $w_{\mathcal{S}}^{\mathcal{S}'}(\mathbf{k})$ is rewritten as $w_{q_z, n_{\mathrm{L}}, \nu}(\mathbf{k})$, with the quantum number q_z representing motion along the magnetic field, and n_{L} denoting the Landau quantum number of the harmonic oscillator. Appendix A.4 presents a justification for replacing the sum over states $\mathcal{S}'$ with a sum over harmonic numbers ν, while a full quantum mechanical derivation lies beyond the scope of this work (see Melrose 1968a and references therein for a detailed treatment).

Considering the different harmonics ν, we denote the emissivity by $\eta^{\nu}(\omega, \theta)$, expressed in terms of photon frequency ω and emission angle θ. This adopts a photon-based perspective, while the previous section describes the microscopic emissivity in terms of an electron's phase-space variables. From the definition and physical dimensions of the emissivity, the total radiated power can thus be

obtained by integrating over all frequencies and emission directions,

$$P_{\mathrm{tot}} = \sum_{\nu=-\infty}^{\infty} \int \mathrm{d}\omega \int \mathrm{d}\Omega \, \eta^{\nu}(\omega, \theta) \, . \tag{2.51}$$

Using the general definition of the refractive index,

$$n = \frac{k\,c}{\omega} \, , \tag{2.52}$$

and expressing the wave vector volume element d^3k in spherical coordinates, we can rewrite d^3k as

$$\begin{aligned} \mathrm{d}^3k &= k^2 \, \mathrm{d}k \, \mathrm{d}\Omega \\ &= \frac{n^2\,\omega^2}{c^2} \frac{\mathrm{d}k}{\mathrm{d}\omega} \mathrm{d}\omega \, \mathrm{d}\Omega \\ &= \frac{n^2\,\omega^2}{c^3} \frac{\partial(n\,\omega)}{\partial\omega} \, \mathrm{d}\omega \, \mathrm{d}\Omega \, , \end{aligned} \tag{2.53}$$

where, in the last line, we adopt the notation of partial derivatives to account for a more general case where the refractive index may depend on multiple variables. By substituting d^3k from Eq. (2.53) into Eq. (2.50), and comparing the integrand with Eq. (2.51), we identify the emissivity as

$$\eta^{\nu}(\omega, \theta) = \frac{n^2\,\hbar\,\omega^3}{(2\,\pi)^3\,c^3} \frac{\partial(n\,\omega)}{\partial\omega} \, w_{q_z, n_{\mathrm{L}}, \nu}(\mathbf{k}) \tag{2.54}$$

for a particular mode.

In the following sections, we derive an expression for the radiated power using classical electrodynamics, involving Fourier transformations and Maxwell's equations. By equating the (time-averaged) classical power expression with Eq. (2.50), we can identify the quantum probability term $w_{q_z, n_{\mathrm{L}}, \nu}(\mathbf{k})$, which, in turn, gives the complete form for the emissivity in Eq. (2.54). This matching of classical and quantum mechanical descriptions is justified under the present assumption of the classical limit, $\hbar\,\omega \ll E$, where E is the electron energy. In the context of radio emission, this condition is always satisfied (photon energies of neV to μeV compared to electron energies of keV to MeV).

2.3.4 Classical derivation of time-averaged radiated power

In this section, we derive an expression for the total (time-averaged) power radiated by an electron, using classical electrodynamics. To maintain the flow of

the derivation, supplementary steps and calculations are deferred to Appendix A, with references to the relevant sections and equations where appropriate. In the following, we switch between vector and index notation where convenient, and summation over repeated indices is implied.

We begin with the time derivative of the electromagnetic energy density W (see Appendix A.5 for its derivation), given by

$$\frac{\partial W}{\partial t} = -\nabla \cdot \mathbf{S} - \mathbf{j}(\mathbf{r}, t) \cdot \mathbf{E}(\mathbf{r}, t)\,, \tag{2.55}$$

where $\mathbf{j}$ is the electric current density, and $\mathbf{S}$ the Poynting vector. The total radiated power is obtained by integrating Eq. (2.55) over a volume V, giving

$$P_{\rm tot} = \int_V \frac{\partial W}{\partial t}\,\mathrm{d}^3 r = -\int_{\partial V} \mathbf{S} \cdot \mathrm{d}\mathbf{s} - \int_V \mathbf{j}(\mathbf{r}, t) \cdot \mathbf{E}(\mathbf{r}, t)\,\mathrm{d}^3 r\,, \tag{2.56}$$

where the divergence theorem $\int_V \nabla \cdot \mathbf{S}\,\mathrm{d}^3 r = \int_{\partial V} \mathbf{S} \cdot \mathrm{d}\mathbf{s}$ has been applied, with ∂V denoting the boundary surface of volume V. Assuming a sufficiently large integration volume that encompasses the near-field region, the fields vanish far away, and the surface integral in Eq. (2.56) can be neglected (Landau & Lifshitz, 1975). The expression then simplifies to

$$P_{\rm tot} = -\int \mathbf{j}(\mathbf{r}, t) \cdot \mathbf{E}(\mathbf{r}, t)\,\mathrm{d}^3 r\,. \tag{2.57}$$

Since $\mathbf{E}$ and $\mathbf{j}$ are oscillatory in time and we are interested in the net radiated power over many cycles, we take the time average of Eq. (2.57) over a long time interval T, which yields

$$P_{\rm avg} = -\lim_{T\to\infty} \frac{1}{T} \int_{-T/2}^{T/2} \mathrm{d}t \int \mathbf{j}(\mathbf{r}, t) \cdot \mathbf{E}(\mathbf{r}, t)\,\mathrm{d}^3 r\,. \tag{2.58}$$

Assuming wave-like variations for $\mathbf{j}$ and $\mathbf{E}$, we now express these quantities via their Fourier transforms. The forward and inverse Fourier transforms are defined by

$$\mathbf{F}(\mathbf{r}, t) = \int \frac{\mathrm{d}^3\mathrm{k}\,\mathrm{d}\omega}{(2\,\pi)^4} \mathbf{F}(\mathbf{k}, \omega)\, \exp[i(\mathbf{k} \cdot \mathbf{r} - \omega\, t)]\,, \tag{2.59}$$

$$\mathbf{F}(\mathbf{k}, \omega) = \int \mathrm{d}^3 r\,\mathrm{d}t\,\mathbf{F}(\mathbf{r}, t)\, \exp[-i(\mathbf{k} \cdot \mathbf{r} - \omega\, t)]\,, \tag{2.60}$$

which satisfy the standard symmetry property

$$\mathbf{F}(-\mathbf{k}, -\omega) = \mathbf{F}^*(\mathbf{k}, \omega)\,. \tag{2.61}$$

Substituting the Fourier representations into Eq. (2.58), we obtain

$$P_{\text{avg}} = -\lim_{T\to\infty}\frac{1}{T}\int_{-T/2}^{T/2}\mathrm{d}t\int\mathrm{d}^3r\int\frac{\mathrm{d}^3k\,\mathrm{d}\omega}{(2\,\pi)^4}\int\frac{\mathrm{d}^3k'\,\mathrm{d}\omega'}{(2\,\pi)^4}$$
$$\times\ \mathbf{j}(\mathbf{k}',\omega')\cdot\mathbf{E}(\mathbf{k},\omega)\,\exp\{i[(\mathbf{k}+\mathbf{k}')\cdot\mathbf{r}-(\omega+\omega')\,t]\}\,. \tag{2.62}$$

To solve the integrals over d^3r and $\mathrm{d}\omega$, we use the Fourier identity for the Dirac delta distribution δ (Boas, 2006),

$$\int_{-\infty}^{\infty}\mathrm{d}t\exp(\pm i\,\omega\,t) = 2\,\pi\,\delta(\omega)\,, \tag{2.63}$$

which exploits the even property of the delta distribution. With Eq. (2.63), we obtain for the spatial and temporal integrals in Eq. (2.62), respectively,

$$\int\mathrm{d}^3r\exp[i(\mathbf{k}+\mathbf{k}')\cdot\mathbf{r}] = (2\,\pi)^3\,\delta^{(3)}(\mathbf{k}+\mathbf{k}')\,, \tag{2.64}$$

$$\int_{-T/2}^{T/2}\mathrm{d}t\exp[-i(\omega+\omega')\,t] = 2\,\pi\,\delta_T(\omega+\omega')\,, \tag{2.65}$$

where in Eq. (2.65), δ_T is a time-broadened delta distribution valid as $T\to\infty$, which we cannot yet apply due to the prefactor $1/T$. The two delta distributions enforce $\mathbf{k}' = -\mathbf{k}$ and $\omega' = -\omega$, which allows us to substitute $\mathbf{j}(\mathbf{k}',\omega')\to\mathbf{j}(-\mathbf{k},-\omega) = \mathbf{j}^*(\mathbf{k},\omega)$ in Eq. (2.62). The remaining integrals over d^3k' and $\mathrm{d}\omega'$ collapse due to the delta constraints, so Eq. (2.62) reduces to

$$P_{\text{avg}} = -\lim_{T\to\infty}\frac{1}{T}\int\frac{\mathrm{d}^3k\,\mathrm{d}\omega}{(2\,\pi)^4}\mathbf{j}^*(\mathbf{k},\omega)\cdot\mathbf{E}(\mathbf{k},\omega)\,. \tag{2.66}$$

From the condition in Eq. (2.61), we know that positive and negative frequencies are physically equivalent. This allows us to split the integral over $\mathrm{d}\omega$ as

$$\int\mathrm{d}\omega\,\mathbf{j}^*(\mathbf{k},\omega)\cdot\mathbf{E}(\mathbf{k},\omega) = \int_{-\infty}^{0}\mathrm{d}\omega\,\mathbf{j}^*(\mathbf{k},\omega)\cdot\mathbf{E}(\mathbf{k},\omega)+\int_{0}^{\infty}\mathrm{d}\omega\,\mathbf{j}^*(\mathbf{k},\omega)\cdot\mathbf{E}(\mathbf{k},\omega)$$
$$=\int_{-\infty}^{0}(-\mathrm{d}\omega')\,\mathbf{j}(\mathbf{k},\omega)\cdot\mathbf{E}^*(\mathbf{k},\omega)+\int_{0}^{\infty}\mathrm{d}\omega\,\mathbf{j}^*(\mathbf{k},\omega)\cdot\mathbf{E}(\mathbf{k},\omega)$$
$$=\int_{0}^{\infty}\mathrm{d}\omega\ [\mathbf{j}^*(\mathbf{k},\omega)\cdot\mathbf{E}(\mathbf{k},\omega)+\mathbf{j}(\mathbf{k},\omega)\cdot\mathbf{E}^*(\mathbf{k},\omega)]\ , \tag{2.67}$$

where we substitute $\omega' = -\omega$, implying $\mathrm{d}\omega' = -\mathrm{d}\omega$, and account for the minus sign by adjusting the integration limits of the first integral. We can now rewrite Eq. (2.66) as[6]

$$\begin{aligned} P_{\mathrm{avg}} &= -\lim_{T\to\infty}\frac{1}{T}\frac{1}{(2\,\pi)^4}\int \mathrm{d}^3k \int_0^\infty \mathrm{d}\omega\ [\mathbf{j}^*(\mathbf{k},\omega)\cdot\mathbf{E}(\mathbf{k},\omega) + \mathbf{j}(\mathbf{k},\omega)\cdot\mathbf{E}^*(\mathbf{k},\omega)] \\ &= -\lim_{T\to\infty}\frac{1}{T}\frac{1}{(2\,\pi)^4}\int \mathrm{d}^3k \int_0^\infty \mathrm{d}\omega\, 2\,\mathrm{Re}[\mathbf{j}^*(\mathbf{k},\omega)\cdot\mathbf{E}(\mathbf{k},\omega)]. \end{aligned} \tag{2.68}$$

The next step is to find an expression for $\mathbf{E}$ in Eq. (2.68). To achieve this, we use the inhomogeneous dispersion relation

$$\Lambda_{ij}(\mathbf{k},\omega)E_j(\mathbf{k},\omega) = -\frac{i\,4\,\pi}{\omega}j_i(\mathbf{k},\omega)\,, \tag{2.69}$$

which is derived in Appendix A.7. The tensor Λ_{ij} is defined in Eq. (A.74). To solve for E_j in Eq. (2.69), we introduce a Green's function $\mathcal{D}_{ij}(\mathbf{k},\omega)$ that formally inverts $\Lambda_{ij}(\mathbf{k},\omega)$, such that

$$\mathcal{D}_{ij}\,\Lambda_{jl} = 4\,\pi\,\delta_{il} \tag{2.70}$$

is satisfied. Here, δ_{ij} is the Kronecker delta, and $\mathcal{D}_{ij}$ is effectively the matrix inverse of Λ_{ij}, scaled by a factor $4\,\pi$ for convenience, that is, $\mathcal{D} = 4\,\pi\,\Lambda^{-1}$. Multiplying Eq. (2.69) from the left side by $\mathcal{D}_{ki}$ yields

$$\mathcal{D}_{ki}\,\Lambda_{ij}\,E_j = -\frac{i\,4\,\pi}{\omega}\mathcal{D}_{ki}\,j_i\,. \tag{2.71}$$

Using the identity in Eq. (2.70), we rewrite Eq. (2.71) to

$$4\,\pi\,\delta_{kj}\,E_j = -\frac{i\,4\,\pi}{\omega}\mathcal{D}_{ki}\,j_i\,. \tag{2.72}$$

Contracting $\delta_{kj}\,E_j = E_k$ and reordering Eq. (2.72) gives

$$E_k = -\frac{i}{\omega}\mathcal{D}_{ki}\,j_i\,. \tag{2.73}$$

To express $\mathcal{D}_{ij}$ formally, we use the adjugate $\mathrm{adj}(\Lambda) \coloneqq \lambda_{ij}$ of Λ_{ij}, defined via the relation

$$\begin{aligned} \mathrm{adj}(\Lambda)\,\Lambda &= \mathcal{L}\,\mathcal{I}\,, \\ \lambda_{ij}\,\Lambda_{jl} &= \mathcal{L}\,\delta_{il}\,, \end{aligned} \tag{2.74}$$

[6] In the second line of Eq. (2.68), we recognise that the two terms inside the brackets are complex conjugates of each other, allowing the identity $Q + Q^* = 2\,\mathrm{Re}(Q)$ to be applied, where $Q = \mathbf{j}^*\cdot\mathbf{E}$.

where $\mathcal{L} \coloneqq \det(\Lambda)$ is the determinant of Λ, and $\mathcal{I}$ is the identity tensor. This gives the formal inverse

$$\Lambda^{-1} = \frac{1}{\mathcal{L}} \mathrm{adj}(\Lambda) \,. \tag{2.75}$$

Inserting this into $\mathcal{D} = 4\,\pi\,\Lambda^{-1}$ gives the Green's function as

$$\mathcal{D}_{ij} = 4\,\pi \frac{\lambda_{ij}}{\mathcal{L}} \,. \tag{2.76}$$

We note that Eq. (2.76) becomes singular at real frequencies satisfying the dispersion relation $\mathcal{L} = 0$. To correctly evaluate the frequency integral in Eq. (2.68), this singularity must be handled with care. We address it by imposing causal (retarded) boundary conditions through the substitution $\omega \to \omega + i\,\tilde{\sigma}$, where $\tilde{\sigma} > 0$ is infinitesimal. This ensures that the Green's function yields physically retarded fields, that is, fields generated by earlier currents. To proceed, we expand $\det(\Lambda)$ in the vicinity of a pole $\omega = \omega(\mathbf{k})$ as

$$\mathcal{L}(\mathbf{k}, \omega) \approx \left. \frac{\partial \mathcal{L}}{\partial \omega} \right|_{\omega = \omega(\mathbf{k})} [\omega - \omega(\mathbf{k})] \,, \tag{2.77}$$

and substitute this expansion into Eq. (2.76), while incorporating the complex frequency shift, to obtain

$$\mathcal{D}_{ij} = \frac{4\,\pi\,\lambda_{ij}}{\partial \mathcal{L}/\partial \omega} \frac{1}{\omega - \omega(\mathbf{k}) + i\,\tilde{\sigma}} \,. \tag{2.78}$$

To evaluate such singular integrals (once inserted into the power expression), we apply the Sokhotski–Plemelj formula (e.g. Weinberg 2005),

$$\lim_{\tilde{\sigma} \to 0^+} \frac{1}{\tilde{\omega} \pm i\,\tilde{\sigma}} = \mp i\,\pi\,\delta(\tilde{\omega}) + \mathcal{P}\left(\frac{1}{\tilde{\omega}}\right) \,, \tag{2.79}$$

where $\mathcal{P}$ denotes the Cauchy principal value. Comparing Eq. (2.79) to (2.78), we identify $\tilde{\omega} = \omega - \omega(\mathbf{k})$, and Eq. (2.78) becomes

$$\mathcal{D}_{ij} = \frac{4\,\pi\,\lambda_{ij}}{\partial \mathcal{L}/\partial \omega} \left\{ -i\,\pi\,\delta[(\omega - \omega(\mathbf{k})] + \mathcal{P}\left(\frac{1}{\omega - \omega(\mathbf{k})}\right) \right\} \,. \tag{2.80}$$

The real part of Eq. (2.80), involving the principal value, vanishes in the subsequent power calculation. This is because it represents time-symmetric contributions, which do not lead to a net energy gain or loss.

Returning to the integrand in Eq. (2.68), we now insert the expressions for the electric field from Eqs. (2.73) and the Green's function from (2.80), using only the imaginary part. The integrand becomes[7]

$$\begin{aligned}\mathrm{Re}\,[j_i^* \cdot E_i] &= \mathrm{Re}\left[-\frac{i}{\omega} j_i^*\, \mathcal{D}_{ij}\, j_j\right] \\ &= \mathrm{Im}\left[\frac{1}{\omega} j_i^*\, \mathcal{D}_{ij}\, j_j\right] \\ &= \mathrm{Im}\left\{-i\frac{4\,\pi^2}{\partial\mathcal{L}/\partial\omega}\delta[\omega-\omega(\mathbf{k})]\, j_i^*\, \lambda_{ij}\, j_j\right\} \\ &= -\frac{4\,\pi^2}{\partial\mathcal{L}/\partial\omega}\delta[\omega-\omega(\mathbf{k})]\, j_i^*\, \lambda_{ij}\, j_j\,. \end{aligned} \tag{2.81}$$

Substituting Eq. (2.81) into (2.68), we find the time-averaged total radiated power as

$$P_{\mathrm{avg}} = \lim_{T\to\infty} \frac{1}{2\,\pi^2\, T} \int \mathrm{d}^3k \int_0^\infty \frac{\mathrm{d}\omega}{\omega} \frac{\delta[\omega-\omega(\mathbf{k})]}{\partial\mathcal{L}/\partial\omega}\, j_i^*\, \lambda_{ij}\, j_j\,. \tag{2.82}$$

We now address the term $j_i^*\, \lambda_{ij}\, j_j$ in Eq. (2.82). Since we are evaluating this expression for the case $\mathcal{L} = 0$, we can apply the identity

$$\lambda_{ij} = \mathrm{tr}(\lambda)\, e_i\, e_j^*\,, \tag{2.83}$$

where $\mathrm{tr}(\lambda)$ is the trace of the adjugate matrix λ_{ij}, and $\mathbf{e}$ is the normalised polarisation vector (Eq. A.76) associated with the wave mode (Sitenko & Kirochkin, 1966; Melrose, 1968a). This identity is derived in Appendix A.6. Using Eq. (2.83), we can rewrite $j_i^*\, \lambda_{ij}\, j_j$ as

$$\begin{aligned} j_i^*\, \lambda_{ij}\, j_j &= \mathrm{tr}(\lambda)\, j_i^*\, e_i\, e_j^*\, j_j \\ &= \mathrm{tr}(\lambda)\, |e_i^*\, j_i|^2 \\ &= \mathrm{tr}(\lambda)\, |e_i\, j_i^*|^2\,. \end{aligned} \tag{2.84}$$

Here, we use in the second line that $j_i^*\, e_i = (e_i^*\, j_i)^*$, and that $e_j^*\, j_j = e_i^*\, j_i$ by relabelling the dummy index. In the third line, we exploit the fact that $|\tilde{a}^*|^2 = |\tilde{a}|^2$ for complex scalars $\tilde{a}$.

[7] In the second line of Eq. (2.81), we use the identity $\mathrm{Re}(-i\,z) = \mathrm{Im}(z)$ for any complex number z, which follows from $-i\,z = -i[\mathrm{Re}(z) + i\,\mathrm{Im}(z)] = \mathrm{Im}(z) - i\,\mathrm{Re}(z)$.

Furthermore, since the condition $\mathcal{L} = 0$ holds only at $\omega = \omega(\mathbf{k})$, we can write the delta distribution in Eq. (2.82) using the Dirac delta identity (Boas 2006; see also the more general case in Eq. 2.143), given by

$$\frac{\delta[\omega - \omega(\mathbf{k})]}{|\partial\mathcal{L}/\partial\omega|} = \delta(\mathcal{L})\,. \tag{2.85}$$

We also observe that for the radiated power $P_{\text{avg}} > 0$ in Eq. (2.82) with Eq. (2.84), $\text{tr}(\lambda)$ and $\partial\mathcal{L}/\partial\omega$ must be of the same sign. Hence,

$$\begin{aligned} \text{sign}[\text{tr}(\lambda)] &= \text{sign}(\partial\mathcal{L}/\partial\omega) \\ \Rightarrow \frac{\text{tr}(\lambda)\,\delta[\omega - \omega(\mathbf{k})]}{\partial\mathcal{L}/\partial\omega} &= \frac{|\text{tr}(\lambda)|\,\delta[\omega - \omega(\mathbf{k})]}{|\partial\mathcal{L}/\partial\omega|} \\ &= |\text{tr}(\lambda)|\,\delta(\mathcal{L})\,, \end{aligned} \tag{2.86}$$

ensuring that the integrand remains real and positive. Substituting Eqs. (2.84) and (2.86) into (2.82), we arrive at the expression for the power radiated by the electron, given by

$$P_{\text{avg}} = \lim_{T\to\infty} \frac{1}{2\,\pi^2\,T} \int \mathrm{d}^3k \int_0^\infty \frac{\mathrm{d}\omega}{\omega}\,\delta(\mathcal{L})\,|\text{tr}(\lambda)|\,|e_i\,j_i^*|^2. \tag{2.87}$$

To proceed, we require explicit expressions for the complex conjugate of the current density vector, $\mathbf{j}^*(\mathbf{k},\omega)$, and the normalised polarisation vector, $\mathbf{e}$. We begin with the current density in Section 2.3.5, and return to complete the evaluation of Eq. (2.87) in Section 2.3.6.

2.3.5 Current density vector in Fourier space

We now derive an explicit expression for the current density vector $\mathbf{j}$ and its complex conjugate, which is required for evaluating the power radiated by a single electron in the previous section. We begin with the definition of the current density vector for a point charge moving along a trajectory $\mathbf{r}$ with velocity $\mathbf{v}$, which reads

$$\mathbf{j}(\mathbf{r},t) = q\,\mathbf{v}(t)\,\delta[\mathbf{r} - \mathbf{r}(t)]\,, \tag{2.88}$$

where q is the charge of the particle. To obtain $\mathbf{j}(\mathbf{k}, \omega)$, we Fourier transform Eq. (2.88) using the inverse transform definition from Eq. (2.60), which yields

$$\begin{aligned}\mathbf{j}(\mathbf{k}, \omega) &= \int \mathrm{d}t \int \mathrm{d}^3 r\, \mathbf{j}(\mathbf{r}, t)\, \exp[-i(\mathbf{k}\cdot\mathbf{r} - \omega\, t)] \\ &= q \int \mathrm{d}t\, \mathbf{v}(t) \int \mathrm{d}^3 r\, \delta[\mathbf{r} - \mathbf{r}(t)]\, \exp[-i(\mathbf{k}\cdot\mathbf{r} - \omega\, t)]\,. \end{aligned} \tag{2.89}$$

We find the Fourier-transformed current density of a point charge q moving along a trajectory $\mathbf{r}(t)$ with velocity $\mathbf{v}(t)$ then as

$$\mathbf{j}(\mathbf{k}, \omega) = q \int \mathrm{d}t\, \mathbf{v}(t)\, \exp[-i(\mathbf{k}\cdot\mathbf{r}(t) - \omega\, t)]\,. \tag{2.90}$$

Next, we need to derive expressions for $\mathbf{v}(t)$ and $\mathbf{r}(t)$. To do this, we consider the motion of a charged particle in a uniform and constant magnetic field, which we take to point along the z-axis, that is, $\mathbf{B} = (0, 0, B)^{\mathrm{T}}$. While the coronal magnetic field is generally non-uniform and time-dependent (as is the case in the numerical simulations in Chapter 6), this simplification is commonly adopted and remains valid as long as the spatial and temporal variations of the background magnetic field occur on scales much larger than the electron's gyroradius and gyroperiod[8]. Under this assumption, the equations can be obtained from the Newton-Lorentz equation (A.79) by ignoring the electric field, and are derived in Appendix A.8, reading

$$\mathbf{r}(t) = [R_{\mathrm{g}}\, \sin(\varepsilon\, \tilde{\Omega}\, t), R_{\mathrm{g}}\, \cos(\varepsilon\, \tilde{\Omega}\, t), v_z\, t]^{\mathrm{T}}\,, \tag{2.91}$$

$$\mathbf{v}(t) = [\varepsilon\, v_\perp\, \cos(\varepsilon\, \tilde{\Omega}\, t), -\varepsilon\, v_\perp\, \sin(\varepsilon\, \tilde{\Omega}\, t), v_z]^{\mathrm{T}}\,. \tag{2.92}$$

Here, R_{g} (from Eq. A.94) is the gyroradius, ε (from Eq. A.82) denotes the sign of the charge, $\tilde{\Omega}$ (from Eq. A.84) is the relativistic variant of the regular gyrofrequency Ω (Eq. A.83), and $v_\perp$ and v_z are the perpendicular and parallel components (with respect to the background magnetic field) of the particle's velocity vector, respectively.

The wave vector in component form is given as

$$\mathbf{k} = [k_\perp \cos(\phi), k_\perp \sin(\phi), k_z]\,. \tag{2.93}$$

[8]For comparison, an electron with 1 MeV energy in a uniform magnetic field of 1 G has a Larmor radius of about 47 m and a gyroperiod of about 1 μs—both far below the spatial and temporal resolution of the MHD model *COCONUT* used in Chapter 6.

Using Eq. (2.93) and the gyroradius from Eq. (A.94), we evaluate the Fourier phase factor in Eq. (2.90) as

$$\begin{aligned}\mathbf{k}\cdot\mathbf{r}(t) &= k_\perp R_\mathrm{g}\,\sin(\varepsilon\,\tilde{\Omega}\,t)\,\cos(\phi) + k_\perp R_\mathrm{g}\,\cos(\varepsilon\,\tilde{\Omega}\,t)\,\sin(\phi) + k_z\,v_z\,t \\ &= k_\perp R_\mathrm{g}\,\sin(\phi+\varepsilon\,\tilde{\Omega}\,t) + k_z\,v_z\,t\,, \end{aligned} \tag{2.94}$$

where in the second line we use the trigonometric identity $\sin(\varphi_1+\varphi_2) = \sin(\varphi_1)\cos(\varphi_2)+\cos(\varphi_1)\sin(\varphi_2)$. To obtain the exponential phase factor in Eq. (2.94) in a linear form in ϕ and decomposed into harmonic components of the gyrofrequency, we rewrite it using Bessel functions of the first kind J_ν with argument $\tilde{z}$ via the Jacobi-Anger expansion (Abramowitz & Stegun, 1972), which reads

$$\exp[\pm i\,\tilde{z}\,\sin(\varphi)] = \sum_{\nu=-\infty}^{\infty} J_\nu(\tilde{z})\,\exp(\pm i\,\nu\,\varphi)\,. \tag{2.95}$$

Applying Eq. (2.95) with $\varphi = \phi+\varepsilon\,\tilde{\Omega}\,t$ and $\tilde{z} = k_\perp R_\mathrm{g}$, we obtain

$$\begin{aligned}\exp[-i\,\mathbf{k}\cdot\,\mathbf{r}(t)] &= \exp[-i\,k_\perp R_\mathrm{g}\,\sin(\phi+\varepsilon\,\tilde{\Omega}\,t)]\,\exp(-i\,k_z\,v_z\,t) \\ &= \sum_{\nu=-\infty}^{\infty} J_\nu(\tilde{z})\,\exp[-i\,\nu\,(\phi+\varepsilon\,\tilde{\Omega}\,t)]\,\exp(-i\,k_z\,v_z\,t)\,. \end{aligned} \tag{2.96}$$

It is convenient to express the transverse components in a circular (or polarisation) basis, corresponding to left- and right-handed helicity, by introducing the combinations

$$v_\pm(t) = v_x(t) \pm i\,\varepsilon\,v_y(t)\,, \tag{2.97}$$

$$j_\pm = j_x \pm i\,\varepsilon\,j_y\,. \tag{2.98}$$

Using the components of the velocity vector from Eq. (2.92), we can evaluate Eq. (2.97) as[9]

$$\begin{aligned} v_\pm &= v_\perp[\cos(\varepsilon\,\tilde{\Omega}\,t) \mp i\,\sin(\varepsilon\,\tilde{\Omega}\,t)] \\ &= v_\perp\,\exp(\mp i\,\varepsilon\,\tilde{\Omega}\,t)\,, \end{aligned} \tag{2.99}$$

where in the first line we exploit the even property of the cosine function, and in the second line we apply Euler's formula. Now we substitute Eqs. (2.96),

[9] We note that in Melrose 1968a the factor ε in the argument of the exponential function of Eq. (2.99) appears to be missing, and instead appears as a prefactor outside the exponential.

(2.98), and (2.99) into Eq. (2.90) to express the current components in Fourier space, yielding

$$j_{\pm}(\mathbf{k},\omega) = \sum_{\nu=-\infty}^{\infty} q\, v_{\perp} \exp(-i\,\nu\,\phi)\, J_{\nu}(z) \times \int \mathrm{d}t\, \exp\{i\,[\omega - (\nu \pm 1)\,\varepsilon\,\tilde{\Omega} - k_z\, v_z]\, t\}\,, \tag{2.100}$$

$$j_{z}(\mathbf{k},\omega) = \sum_{\nu=-\infty}^{\infty} q\, v_{z}\, \exp(-i\,\nu\,\phi)\, J_{\nu}(z) \times \int \mathrm{d}t\, \exp\{i\,[\omega - \nu\,\varepsilon\,\tilde{\Omega} - k_z\, v_z]\, t\}\,. \tag{2.101}$$

With the identity from Eq. (2.63) applied to the time integrals, and using a variable shift in Eq. (2.100) via $\nu' = \nu \pm 1 \Leftrightarrow \nu = \nu' \mp 1$, we find the expressions for the current density vector components[10]

$$j_{\pm}(\mathbf{k},\omega) = 2\,\pi\, q\, v_{\perp} \sum_{\nu=-\infty}^{\infty} \exp[-i\,(\nu \mp 1)\,\phi] \times J_{\nu\mp1}(\tilde{z})\,\delta(\omega - \nu\,\varepsilon\,\tilde{\Omega} - k_z\, v_z)\,, \tag{2.102}$$

$$j_{z}(\mathbf{k},\omega) = 2\,\pi\, q\, v_{z} \sum_{\nu=-\infty}^{\infty} \exp(-i\,\nu\,\phi) \times J_{\nu}(\tilde{z})\,\delta(\omega - \nu\,\varepsilon\,\tilde{\Omega} - k_z\, v_z)\,. \tag{2.103}$$

Equations (2.102)–(2.103) reflect the discrete harmonic structure of the current density spectrum, where each term contributes at a Doppler-shifted cyclotron frequency $\omega - \nu\,\varepsilon\,\tilde{\Omega} - k_z\, v_z$, selected by the delta distribution.

Since the x- and y-axes in the plane perpendicular to the magnetic field vector can be freely chosen, we orient the x-axis along the perpendicular wave vector component[11] $\mathbf{k}_{\perp}$, such that $k_x = k_{\perp}$, $\phi = 0$, and $k_y = 0$. This implies that $\exp(-i\,\nu\,\phi) = 1$, eliminating the exponential factor in Eq. (2.103). Then the

[10] We note that in Melrose 1968a, the argument of the Dirac delta distribution does not include the sign parameter ε next to $\tilde{\Omega}$, thereby deviating from the standard resonance condition $\omega - k_z\, v_z = \nu\,\Omega$ with signed gyrofrequency Ω.

[11] This choice differs from Melrose (1968a), where only $k_y = 0$ is imposed, allowing $\phi \in \{0, \pi\}$ and requiring sign-dependent expressions such as $\exp(i\,\phi) = \pm 1$.

expressions for the current density components are

$$j_{\pm}(\mathbf{k},\omega) = 2\,\pi\,q\,v_{\perp} \sum_{\nu=-\infty}^{\infty} J_{\nu\mp1}(\tilde{z})\,\delta(\omega - \nu\,\varepsilon\,\tilde{\Omega} - k_z\,v_z)\,, \tag{2.104}$$

$$j_z(\mathbf{k},\omega) = 2\,\pi\,q\,v_z \sum_{\nu=-\infty}^{\infty} J_{\nu}(\tilde{z})\,\delta(\omega - \nu\,\varepsilon\,\tilde{\Omega} - k_z\,v_z)\,. \tag{2.105}$$

Now, we transform back to Cartesian coordinates by calculating algebraic combinations of Eq. (2.98). We obtain j_x from $j_+ + j_-$, and j_y from $j_+ - j_-$, yielding

$$j_x = \frac{1}{2}(j_+ + j_-)\,, \tag{2.106}$$

$$j_y = -\frac{i\,\varepsilon}{2}(j_+ - j_-)\,. \tag{2.107}$$

To express j_x, j_y, and j_z in a unified Cartesian form j_i, we employ the Bessel recurrence relations (Boas, 2006)

$$J_{\nu-1}(\tilde{z}) + J_{\nu+1}(\tilde{z}) = \frac{2\,\nu}{\tilde{z}}\,J_{\nu}(\tilde{z})\,, \tag{2.108}$$

$$J_{\nu-1}(\tilde{z}) - J_{\nu+1}(\tilde{z}) = 2\,J'_{\nu}(\tilde{z})\,, \tag{2.109}$$

where $J'_{\nu}(\tilde{z}) \coloneqq \mathrm{d}/\mathrm{d}\tilde{z}\,[J(\tilde{z})]$ denotes the first derivative of the Bessel function of the first kind.

We then express the velocity components in terms of momenta using $E = \gamma\,m\,c^2$, giving

$$v_{\perp} = \frac{c^2}{E}p_{\perp}\,, \tag{2.110}$$

$$v_z = \frac{c^2}{E}p_z\,. \tag{2.111}$$

For the x-component of the current, we find

$$\begin{aligned} j_x &= \pi\, q\, v_\perp \sum_{\nu=-\infty}^{\infty} \left[J_{\nu-1}(\tilde{z}) + J_{\nu+1}(\tilde{z})\right] \delta(\omega - \nu\, \varepsilon\, \tilde{\Omega} - k_z\, v_z) \\ &= \frac{\pi\, q\, c^2}{E} \sum_{\nu=-\infty}^{\infty} \underbrace{\frac{2\, p_\perp\, \nu}{\tilde{z}}\, J_\nu(\tilde{z})}_{=:\Gamma_x^\nu}\, \delta(\omega - \nu\, \varepsilon\, \tilde{\Omega} - k_z\, v_z) \\ &= \frac{\pi\, q\, c^2}{E} \sum_{\nu=-\infty}^{\infty} \Gamma_x^\nu\, \delta(\omega - \nu\, \varepsilon\, \tilde{\Omega} - k_z\, v_z)\,. \end{aligned} \tag{2.112}$$

In the second line of Eq. (2.112), we use Eqs. (2.108) and (2.110), and in the third line we introduce a new variable Γ_x^ν. Similarly, for the y-component of the current density, we obtain

$$\begin{aligned} j_y &= -i\, \varepsilon\, \pi\, q\, v_\perp \sum_{\nu=-\infty}^{\infty} \left[J_{\nu-1}(\tilde{z}) - J_{\nu+1}(\tilde{z})\right] \delta(\omega - \nu\, \varepsilon\, \tilde{\Omega} - k_z\, v_z) \\ &= \frac{\pi\, q\, c^2}{E} \sum_{\nu=-\infty}^{\infty} \underbrace{\left[-2\, i\, \varepsilon\, p_\perp\, J'_\nu(\tilde{z})\right]}_{=:\Gamma_y^\nu}\, \delta(\omega - \nu\, \varepsilon\, \tilde{\Omega} - k_z\, v_z) \\ &= \frac{\pi\, q\, c^2}{E} \sum_{\nu=-\infty}^{\infty} \Gamma_y^\nu\, \delta(\omega - \nu\, \varepsilon\, \tilde{\Omega} - k_z\, v_z)\,, \end{aligned} \tag{2.113}$$

where we use Eqs. (2.109) and (2.110) in the second line, and in the third line introduce a new variable Γ_y^ν. Finally, beginning from Eq. (2.105), we derive the z-component of the current density as

$$\begin{aligned} j_z &= 2\, \pi\, q\, v_z \sum_{\nu=-\infty}^{\infty} J_\nu(\tilde{z})\, \delta(\omega - \nu\, \varepsilon\, \tilde{\Omega} - k_z\, v_z) \\ &= \frac{\pi\, q\, c^2}{E} \sum_{\nu=-\infty}^{\infty} \underbrace{2\, p_z\, J_\nu(\tilde{z})}_{=:\Gamma_z^\nu}\, \delta(\omega - \nu\, \varepsilon\, \tilde{\Omega} - k_z\, v_z) \\ &= \frac{\pi\, q\, c^2}{E} \sum_{\nu=-\infty}^{\infty} \Gamma_z^\nu\, \delta(\omega - \nu\, \varepsilon\, \tilde{\Omega} - k_z\, v_z)\,, \end{aligned} \tag{2.114}$$

where we use Eq. (2.111) in the second line, and introduce a new variable Γ_z^ν in the third line. We can now express all three components in the unified notation

$$j_i(\mathbf{k},\omega) = \frac{\pi\, q\, c^2}{E} \sum_{\nu=-\infty}^{\infty} \Gamma_i^\nu\, \delta(\omega - \nu\, \varepsilon\, \tilde{\Omega} - k_z\, v_z)\,, \tag{2.115}$$

with the coefficients

$$\Gamma_x^\nu = \frac{2\, p_\perp\, \nu}{\tilde{z}}\, J_\nu(\tilde{z})\,, \tag{2.116}$$

$$\Gamma_y^\nu = -i\, 2\, \varepsilon\, p_\perp\, J'_\nu(\tilde{z})\,, \tag{2.117}$$

$$\Gamma_z^\nu = 2\, p_z\, J_\nu(\tilde{z})\,. \tag{2.118}$$

To evaluate Eq. (2.87), we require the complex conjugate of Eq. (2.115), which reads

$$j_i^*(\mathbf{k},\omega) = \frac{\pi\, q\, c^2}{E} \sum_{\nu'=-\infty}^{\infty} \Gamma_i^{*\nu'}\, \delta(\omega - \nu'\, \varepsilon\, \tilde{\Omega} - k_z\, v_z)\,. \tag{2.119}$$

We denote the harmonic index in Eq. (2.119) as ν' to distinguish it from ν in the original term. Furthermore, using the relativistic gyrofrequency from Eq. (A.84) and the gyroradius from Eq. (A.94), we rewrite the Bessel argument as

$$\tilde{z} = k_\perp\, R_\mathrm{g} = \frac{k_\perp\, v_\perp}{\tilde{\Omega}} = \frac{k_\perp\, p_\perp}{m\, \Omega}\,. \tag{2.120}$$

Having now derived the complex conjugate of the current density vector, $\mathbf{j}^*(\mathbf{k},\omega)$, we are ready to proceed towards identifying the spontaneous emission probability in Section (2.3.6).

2.3.6 Derivation of the spontaneous emission probability

To derive an expression for the spontaneous emission probability $w_{q_z,n_\mathrm{L},\nu}(\mathbf{k})$ in Eq. (2.50), we first substitute the complex conjugate of the current density from Eq. (2.119) into the squared amplitude $|e_i\, j_i^*(\mathbf{k},\omega)|^2$ appearing in Eq. (2.87) to

find

$$|e_i\, j_i^*(\mathbf{k},\omega)|^2 = \left(\frac{\pi\, q\, c^2}{E}\right)^2 \sum_{\nu=-\infty}^{\infty} \sum_{\nu'=-\infty}^{\infty} (e_i\, \Gamma_i^{*\nu}) \left(e_j^*\, \Gamma_j^{\nu'}\right)$$
$$\times\ \delta(\omega - \nu\, \varepsilon\, \tilde{\Omega} - k_z\, v_z)\, \delta(\omega - \nu'\, \varepsilon\, \tilde{\Omega} - k_z\, v_z)\,. \tag{2.121}$$

The product of delta distributions in Eq. (2.121) is only non-zero when $\nu' = \nu$, since ω is fixed. Using an identity for coinciding δ functions, the product becomes

$$\sum_{\nu,\nu'} \delta(\omega - \nu\, \varepsilon\, \tilde{\Omega} - k_z\, v_z)\, \delta(\omega - \nu'\, \varepsilon\, \tilde{\Omega} - k_z\, v_z)$$
$$\longrightarrow \quad \frac{T}{2\,\pi} \sum_{\nu} \delta(\omega - \nu\, \varepsilon\, \tilde{\Omega} - k_z\, v_z)\,, \tag{2.122}$$

where we show the validity of Eq. (2.122) in Appendix A.9. This collapse of the sum removes the T-dependence in the prefactor, allowing us to take the limit $T \to \infty$. Substituting Eqs. (2.122) and (2.121) into Eq. (2.87) leads to the form

$$P_{\text{avg}} = \frac{q^2\, c^4}{4\,\pi\, E^2} \sum_{\nu=-\infty}^{\infty} \int \mathrm{d}^3\mathrm{k} \int \frac{\mathrm{d}\omega}{\omega} |\mathrm{tr}(\lambda)|$$
$$\times\ |e_i\, \Gamma_i^{*\nu}|^2\, \delta(\mathcal{L})\, \delta(\omega - \nu\, \varepsilon\, \tilde{\Omega} - k_z\, v_z)\,. \tag{2.123}$$

We are now able to identify the spontaneous emission probability $w_{q_z,n_\mathrm{L},\nu}(\mathbf{k})$ by comparing Eq. (2.123) to (2.50). This yields the probability as

$$w_{q_z,n_\mathrm{L},\nu}(\mathbf{k}) = \frac{2\,\pi^2\, q^2\, c^4}{\hbar\, E^2} \int_0^{\infty} \frac{\mathrm{d}\omega}{\omega^2} |\mathrm{tr}(\lambda)|$$
$$\times\ |e_i\, \Gamma_i^{*\nu}|^2\, \delta(\mathcal{L})\, \delta(\omega - \nu\, \varepsilon\, \tilde{\Omega} - k_z\, v_z)\,. \tag{2.124}$$

Before inserting Eq. (2.124) into (2.54) to get an expression for the emissivity, we first evaluate the remaining terms in the probability expression. This is carried out in Sections 2.3.7 and 2.3.8.

2.3.7 Constructing the spontaneous emission probability

To evaluate specific terms in the integrand of Eq. (2.124), we introduce assumptions about the background plasma. Here, we adopt the cold plasma

approximation, which neglects thermal motion and pressure effects. The relevant derivation is provided in Appendix A.10 and is based on the linearised version of the Newton-Lorentz equation (Eq. A.79) in combination with Maxwell's equations (Eqs. A.42–A.45). The resulting dielectric tensor takes the form

$$\epsilon_{ij}^{\mathrm{tot}} = \begin{pmatrix} S & -i\,D & 0 \\ i\,D & S & 0 \\ 0 & 0 & P \end{pmatrix}, \tag{2.125}$$

where the dimensionless variables R, L, S, D, and P are the so-called Stix parameters, defined as

$$R = 1 - \sum_{\varsigma} \frac{\omega_{\mathrm{p}\varsigma}^2}{\omega(\omega + \varepsilon_\varsigma\,\Omega_\varsigma)}\,, \tag{2.126}$$

$$L = 1 - \sum_{\varsigma} \frac{\omega_{\mathrm{p}\varsigma}^2}{\omega(\omega - \varepsilon_\varsigma\,\Omega_\varsigma)}\,, \tag{2.127}$$

$$S = \frac{1}{2}(R + L)\,, \tag{2.128}$$

$$D = \frac{1}{2}(R - L)\,, \tag{2.129}$$

$$P = 1 - \sum_{\varsigma} \frac{\omega_{\mathrm{p}\varsigma}^2}{\omega^2}\,. \tag{2.130}$$

The gyrofrequency and sign variable for the particular particle species are defined as

$$\Omega_\varsigma = \frac{|q_\varsigma|\,B}{m_\varsigma\,c}\,, \tag{2.131}$$

$$\varepsilon_\varsigma = \frac{q_\varsigma}{|q_\varsigma|}\,. \tag{2.132}$$

The Stix parameters depend on the plasma frequency (Eq. A.116) and gyrofrequency (Eq. 2.131) of the particle species involved. Inserting Eq. (2.125) into the wave equation (A.74) allows us to evaluate the elements of the dispersion tensor Λ_{ij}, which reads

$$\Lambda_{ij} = \begin{pmatrix} S - n^2\,\cos^2(\theta) & -i\,D & n^2\,\sin(\theta)\,\cos(\theta) \\ i\,D & S - n^2 & 0 \\ n^2\,\sin(\theta)\,\cos(\theta) & 0 & P - n^2\,\sin^2(\theta) \end{pmatrix}, \tag{2.133}$$

with refractive index n and photon emission angle θ.

Using the definition of the cofactor matrix, we write

$$C_{ij} = (-1)^{i+j} M_{ij} \,, \tag{2.134}$$

where M_{ij} denotes the corresponding minor of Λ. The elements of the adjugate matrix λ_{ij} of the dispersion tensor given in Eq. (2.133) are obtained by taking the transpose of the cofactor matrix, that is $\lambda_{ij} = C_{ji}$. The resulting components[12] are

$$\begin{aligned}
\lambda_{11} &= (S - n^2)[P - n^2 \sin^2(\theta)] \,, \\
\lambda_{12} &= i\, D[P - n^2 \sin^2(\theta)] \,, \\
\lambda_{13} &= -(S - n^2)\, n^2 \sin(\theta) \cos(\theta) \,, \\
\lambda_{21} &= -i\, D[P - n^2 \sin^2(\theta)] \,, \\
\lambda_{22} &= P\, S - n^2[S \sin^2(\theta) + P \cos^2(\theta)] \,, \\
\lambda_{23} &= i\, D\, n^2 \sin(\theta) \cos(\theta) \,, \\
\lambda_{31} &= -(S - n^2)\, n^2 \sin(\theta) \cos(\theta) \,, \\
\lambda_{32} &= -i\, D\, n^2 \sin(\theta) \cos(\theta) \,, \\
\lambda_{33} &= n^4 \cos^2(\theta) - S\, n^2[1 + \cos^2(\theta)] + RL \,.
\end{aligned} \tag{2.135}$$

Due to the Hermitian nature of the λ_{ij} tensor, it follows that $\lambda_{ij} = \lambda^*_{ji}$.

Next, we compute the determinant of Λ, denoted as $\mathcal{L} = \det(\Lambda)$. It can be computed, for instance, by developing Λ after the second row. This yields the intermediate result

$$\begin{aligned}
\mathcal{L} \coloneqq \det(\Lambda) = -i\, D \begin{vmatrix} -i\, D & n^2 \cos(\theta) \sin(\theta) \\ 0 & P - n^2 \sin^2(\theta) \end{vmatrix} \\
+ (S - n^2) \begin{vmatrix} S - n^2 \cos^2(\theta) & n^2 \cos(\theta) \sin(\theta) \\ n^2 \cos(\theta) \sin(\theta) & P - n^2 \sin^2(\theta) \end{vmatrix} \,.
\end{aligned} \tag{2.136}$$

[12] We note that Melrose (1968a) refers to λ as the cofactor matrix of Λ, omitting the transposition required to obtain the adjugate. Consequently, the signs of the off-diagonal elements λ_{12}, λ_{21}, λ_{23}, and λ_{32} are reversed compared to the true adjugate. Nevertheless, the final expressions for the transverse and longitudinal polarisation vector components in Eqs. (A.146) and (A.145), respectively, appear in Melrose (1968a) with the correct signs.

After evaluating the determinants and collecting terms with n^4, n^2, and those not containing a power of n, the determinant $\mathcal{L}$ can be expressed as a quadratic in n^2, reading

$$\mathcal{L} = \mathcal{A}\, n^4 - \mathcal{B}\, n^2 + \mathcal{C}\,, \tag{2.137}$$

with the corresponding coefficients defined as

$$\mathcal{A} = S\, \sin^2(\theta) + P\, \cos^2(\theta)\,, \tag{2.138}$$

$$\mathcal{B} = R\, L\, \sin^2(\theta) + P\, S[1 + \cos^2(\theta)]\,, \tag{2.139}$$

$$\mathcal{C} = L\, R\, P\,. \tag{2.140}$$

Solving the condition $\mathcal{L} = 0$ leads to two branches of solutions, given by

$$n^2 = n_\pm^2 = \frac{\mathcal{B} \pm \mathcal{F}}{2\,\mathcal{A}}\,, \tag{2.141}$$

with the discriminant

$$\begin{aligned} \mathcal{F}^2 &= \mathcal{B}^2 - 4\,\mathcal{A}\,\mathcal{C} \\ &= (R\,L - P\,S)^2 \sin^4(\theta) + 4\,D^2\,P^2\, \cos^2(\theta)\,. \end{aligned} \tag{2.142}$$

To evaluate the delta distribution $\delta(\mathcal{L})$ in the spontaneous emission probability of Eq. (2.124), we take Eq. (2.137) with the solution Eq. (2.141), and use the general identity for delta distributions of a function $g(x)$ with isolated roots x_i (Boas, 2006),

$$\delta[g(x)] = \sum_i \frac{\delta(x - x_i)}{|g'(x)|}\,, \tag{2.143}$$

applied at each x_i with $g(x_i) = 0$. In the current context, we have $x = n^2$, $g(x) = \mathcal{L}(n^2)$, and the two solutions of $\mathcal{L} = 0$ are n_+^2 and n_-^2 from Eq. (2.141). Substituting into the identity gives

$$\delta[\mathcal{L}(n^2)] = \frac{\delta(n^2 - n_+^2) + \delta(n^2 - n_-^2)}{|\partial\mathcal{L}/\partial n^2|}\,. \tag{2.144}$$

The two delta terms in Eq. (2.144) have a common denominator due to

$$\left|\frac{\partial\mathcal{L}}{\partial n^2}\right| = \left|2\,\mathcal{A}\,n_\pm^2 - \mathcal{B}\right| = |\pm\mathcal{F}| = \mathcal{F}\,. \tag{2.145}$$

These identities allow an evaluation of the delta distribution $\delta(\mathcal{L})$ in analytical or numerical calculations, ensuring that the wave dispersion constraint is satisfied.

To find a simplified expression for Eq. (2.145), we employ Jacobi's formula for derivatives of matrices (Magnus & Neudecker, 2019), which allows us to write the derivative of $\mathcal{L}$ as

$$\frac{\partial \mathcal{L}}{\partial n^2} = \mathrm{tr}\left(\mathrm{adj}(\Lambda) \cdot \frac{\partial \Lambda}{\partial n^2}\right) = \sum_{i,j} \lambda_{ij} \frac{\partial \Lambda_{ji}}{\partial n^2} \,. \tag{2.146}$$

Using this expression together with Eq. (2.133), we obtain[13]

$$\frac{\partial \mathcal{L}}{\partial n^2} = -\cos^2(\theta)\,\lambda_{11} - \lambda_{22} - \sin^2(\theta)\,\lambda_{33} + 2\,\sin(\theta)\,\cos(\theta)\,\lambda_{13} \,. \tag{2.147}$$

From the identity in Eq. (2.83), it follows that

$$\begin{aligned} \lambda_{ij}\,\lambda_{kl} &= \mathrm{tr}(\lambda)\, e_i\, e_j^*\, \mathrm{tr}(\lambda)\, e_k\, e_l^* \\ &= \mathrm{tr}(\lambda)\, e_i\, e_l^*\, \mathrm{tr}(\lambda)\, e_k\, e_j^* \\ &= \lambda_{il}\,\lambda_{kj} \,. \end{aligned} \tag{2.148}$$

Now, multiplying Eq. (2.147) by λ_{22}, and using the identity in Eqs. (2.148), we obtain

$$\left|\frac{\partial \mathcal{L}}{\partial n^2}\right| = \mathcal{F} = \frac{\left|[\cos(\theta)\,\lambda_{21} - \sin(\theta)\,\lambda_{23}]^2 - \lambda_{22}^2\right|}{|\lambda_{22}|} \,. \tag{2.149}$$

In the chosen coordinate system with the background magnetic field aligned with the z-axis, the polarisation vector components e_1 and e_3 couple through real coefficients, while the e_2 component appears only via the purely imaginary off-diagonal terms $\pm i\,D$ in the dispersion tensor (see Eq. 2.133). To satisfy the homogeneous wave equation (Eq. A.53) with real e_1 and e_3, the e_2 component must be purely imaginary so that its contributions can cancel against the real parts in the coupled equations. Given this pattern and the global phase freedom of the polarisation vector, we can always choose a basis in which

$$e_1^* = e_1, \quad e_2^* = -e_2 \quad e_3^* = e_3 \,, \tag{2.150}$$

that is, e_1 and e_3 are real, while e_2 is purely imaginary. The polarisation vector for any wave mode of interest can then be computed using the expression (Sitenko & Kirochkin, 1966)

$$e_i = \frac{\lambda_{ij}\, a_j}{\sqrt{\mathrm{tr}(\lambda)\, a_i^*\, \lambda_{ij}\, a_j}} \,, \tag{2.151}$$

[13] We note that the term $2\,\sin(\theta)\,\cos(\theta)\,\lambda_{13}$ in Eq. (2.147) is missing in Melrose (1968a).

where $\mathbf{a}$ is an auxiliary vector satisfying Eq. (2.150). The derivation of Eq. (2.151) is provided in Appendix A.6. Based on the previously chosen orientation of $\hat{\mathbf{k}}$, we define a convenient orthonormal basis as

$$\hat{\mathbf{a}} = (0, i, 0)^{\mathrm{T}}\,, \tag{2.152}$$

$$\hat{\mathbf{k}} = [\sin(\theta), 0, \cos(\theta)]^{\mathrm{T}}\,, \tag{2.153}$$

$$\hat{\boldsymbol{\tau}} = [\cos(\theta), 0, -\sin(\theta)]^{\mathrm{T}}\,. \tag{2.154}$$

By choosing the basis vector $\hat{\mathbf{a}} = (0, i, 0)^{\mathrm{T}}$, we obtain the simplified expression for the polarisation vector components as

$$e_i = \frac{i\,\lambda_{i2}}{\sqrt{\lambda_{22}\,\mathrm{tr}(\lambda)}}\,. \tag{2.155}$$

Since the basis vector $\hat{\mathbf{a}}$ has only one non-zero component, we have $\hat{a}_j = i\,\delta_{j2}$, and thus $\lambda_{ij}\,\hat{a}_j = i\,\lambda_{i2}$, while the denominator reads $\sqrt{\hat{a}^*_m\,\lambda_{mn}\,\hat{a}_n\,\mathrm{tr}(\lambda)} = \sqrt{(-i)\,\lambda_{22}\,i\,\mathrm{tr}(\lambda)} = \sqrt{\lambda_{22}\,\mathrm{tr}(\lambda)}$.

We now decompose the polarisation vector along the orthonormal basis formed by the vectors in Eqs. (2.152)–(2.154) by projecting the polarisation vector $\mathbf{e}$ onto the basis vectors $\hat{\mathbf{a}}$, $\hat{\mathbf{k}}$, and $\hat{\boldsymbol{\tau}}$. This gives the expression

$$\mathbf{e} = e_i\,\hat{k}_i\,\hat{\mathbf{k}} + e_i\,\hat{a}^*_i\,\hat{\mathbf{a}} + e_i\,\hat{\tau}_i\,\hat{\boldsymbol{\tau}}\,, \tag{2.156}$$

where the scalar projection coefficients are

$$\begin{aligned} e_i\,\hat{k}_i &= e_x\,\sin(\theta) + e_z\,\cos(\theta)\,,\\ e_i\,\hat{a}^*_i &= -i\,e_y\,,\\ e_i\,\hat{\tau}_i &= e_x\,\cos(\theta) - e_z\,\sin(\theta)\,. \end{aligned} \tag{2.157}$$

Combining these expressions with Eq. (2.155) yields the decomposition of the polarisation vector as

$$\begin{aligned} \mathbf{e} &= \frac{i\,\lambda_{12}\,\sin(\theta) + i\,\lambda_{32}\,\cos(\theta)}{\sqrt{\lambda_{22}\,\mathrm{tr}(\lambda)}}\hat{\mathbf{k}} + \frac{i\,(-i)\,\lambda_{22}}{\sqrt{\lambda_{22}\,\mathrm{tr}(\lambda)}}\hat{\mathbf{a}} + \frac{i\,\lambda_{12}\,\cos(\theta) - i\,\lambda_{32}\,\sin(\theta)}{\sqrt{\lambda_{22}\,\mathrm{tr}(\lambda)}}\,\hat{\boldsymbol{\tau}}\\ &= \sqrt{\frac{\lambda_{22}}{\mathrm{tr}(\lambda)}}\left(\frac{i\,\lambda_{12}\,\sin(\theta) + i\,\lambda_{32}\,\cos(\theta)}{\lambda_{22}}\hat{\mathbf{k}} + \hat{\mathbf{a}} + \frac{i\,\lambda_{12}\,\cos(\theta) - i\,\lambda_{32}\,\sin(\theta)}{\lambda_{22}}\,\hat{\boldsymbol{\tau}}\right)\\ &= \sqrt{\frac{\lambda_{22}}{\mathrm{tr}(\lambda)}}\left(\mathcal{K}\,\hat{\mathbf{k}} + \hat{\mathbf{a}} + \mathcal{T}\,\hat{\boldsymbol{\tau}}\right)\,, \end{aligned} \tag{2.158}$$

where in the third line, we define the coefficients

$$\mathcal{K} = \frac{i[\lambda_{12}\,\sin(\theta) + \lambda_{32}\,\cos(\theta)]}{\lambda_{22}} = \frac{D\,\sin(\theta)(n^2 - P)}{\lambda_{22}}\,, \tag{2.159}$$

$$\mathcal{T} = \frac{i[\lambda_{12}\,\cos(\theta) - \lambda_{32}\,\sin(\theta)]}{\lambda_{22}} = \frac{-D\,P\,\cos(\theta)}{\lambda_{22}}\,. \tag{2.160}$$

The second equal signs in Eqs. (2.159) and (2.159) result from inserting the explicit expressions for λ_{21} and λ_{23} given in Eq. (2.135).

We now recognise that Eq. (2.160) appears naturally in Eq. (2.149). Specifically, by inverting Eq. (2.149), multiplying both sides by $|\lambda_{22}|$, exploiting the Hermitian property $\lambda_{ij} = \lambda^*_{ji}$, and absorbing the imaginary unit i via a compensating minus sign in the squared term, we find

$$\begin{aligned}\frac{|\lambda_{22}|}{|\partial\mathcal{L}/\partial n^2|} &= \frac{|\lambda_{22}|^2}{|-\{i[\cos(\theta)\,\lambda_{21} - \sin(\theta)\,\lambda_{23}]\}^2 - \lambda_{22}^2|} \\ &= \frac{1}{|-\mathcal{T}^2 - 1|} \\ &= \frac{1}{\mathcal{T}^2 + 1}\,. \end{aligned} \tag{2.161}$$

Next, we address the quantity $|e_i\,\Gamma_i^{\nu *}|$, which appears in the integrand of Eq. (2.124). Using the decomposition of the polarisation vector in Eq. (2.158), we compute

$$\begin{aligned} e_i\,\Gamma_i^{\nu *} &= \sqrt{\frac{\lambda_{22}}{\mathrm{tr}(\lambda)}} \begin{pmatrix} \mathcal{K}\,\sin(\theta) + \mathcal{T}\,\cos(\theta) \\ i \\ \mathcal{K}\,\cos(\theta) - \mathcal{T}\,\sin(\theta) \end{pmatrix} \cdot \begin{pmatrix} \Gamma_x^{\nu *} \\ \Gamma_y^{\nu *} \\ \Gamma_z^{\nu *} \end{pmatrix} \\ &= \sqrt{\frac{\lambda_{22}}{\mathrm{tr}(\lambda)}} \{[\mathcal{K}\,\sin(\theta) + \mathcal{T}\,\cos(\theta)]\,\Gamma_x^{\nu *} + i\,\Gamma_y^{\nu *} + [\mathcal{K}\,\cos(\theta) - \mathcal{T}\,\sin(\theta)]\,\Gamma_z^{\nu *}\} \\ &= \sqrt{\frac{\lambda_{22}}{\mathrm{tr}(\lambda)}} (\mathfrak{a}\,\Gamma_x^{\nu} - i\,\Gamma_y^{\nu} + \mathfrak{b}\,\Gamma_z^{\nu})\,, \end{aligned} \tag{2.162}$$

where we define the scalar coefficients

$$\mathfrak{a} = \mathcal{K}\,\sin(\theta) + \mathcal{T}\,\cos(\theta)\,, \tag{2.163}$$

$$\mathfrak{b} = \mathcal{K}\,\cos(\theta) - \mathcal{T}\,\sin(\theta)\,. \tag{2.164}$$

Therefore, the relevant contraction appearing in the probability expression becomes

$$|\mathrm{tr}(\lambda)||e_i\,\Gamma_i^{\nu *}|^2 = |\lambda_{22}|\left|\mathfrak{a}\,\Gamma_x^\nu - i\,\Gamma_y^\nu + \mathfrak{b}\,\Gamma_z^\nu\right|^2 . \tag{2.165}$$

With all these derived expressions in hand, we now insert Eqs. (2.144), (2.161), and (2.165) into Eq. (2.124), yielding the spontaneous emission probability in the form

$$w_{q_z,n_\mathrm{L},\nu}(\mathbf{k}) = \frac{2\,\pi^2\,q^2\,c^4}{\hbar\,E^2}\int_0^\infty \frac{\mathrm{d}\omega}{\omega^2}\frac{\delta(n^2-n_+^2)+\delta(n^2-n_-^2)}{\mathcal{T}^2+1}$$
$$\times\,\delta(\omega-\nu\,\varepsilon\,\tilde{\Omega}-k_z\,v_z)\left|\mathfrak{a}\,\Gamma_x^\nu - i\,\Gamma_y^\nu + \mathfrak{b}\,\Gamma_z^\nu\right|^2 . \tag{2.166}$$

This expression incorporates both the wave dispersion relation and the polarisation structure of the emitted radiation. Before using it to derive the final form of the emissivity, Eq. (2.166) is further simplified by evaluating the frequency integral and the modulus squared bracket term in Section 2.3.8.

2.3.8 Emissivity formula in cold plasma limit

Equation (2.166) describes the total probability of spontaneous emission into any allowed wave mode. The two delta distributions select one of the two dispersion branches $n_\pm^2$, corresponding to the ordinary (O-mode) and extraordinary (X-mode) waves of the cold plasma dispersion relation. To isolate the contribution from a specific mode, we replace the sum of delta distributions with a single one, $\delta(n^2-n_\pm^2)$, and obtain the emission probability for a given mode by

$$w^\pm_{q_z,n_\mathrm{L},\nu}(\mathbf{k}) = \frac{2\,\pi^2\,q^2\,c^4}{\hbar\,E^2}\int_0^\infty \frac{\mathrm{d}\omega}{\omega^2}\frac{\delta(n^2-n_\pm^2)}{\mathcal{T}_\pm^2+1}$$
$$\times\,\delta(\omega-\nu\,\varepsilon\,\tilde{\Omega}-k_z\,v_z)\left|\mathfrak{a}_\pm\,\Gamma_x^\nu - i\,\Gamma_y^\nu + \mathfrak{b}_\pm\,\Gamma_z^\nu\right|^2 . \tag{2.167}$$

To evaluate the remaining integral over frequency in Eq. (2.167), we first use Eq. (2.52) to express n^2, note that $\delta(\varphi\,x) = \delta(x)/|\varphi|$ for any non-zero real constant φ, and then apply the delta distribution identity from Eq. (2.143). This allows us to compute the integral as

$$\int_0^\infty \frac{\mathrm{d}\omega}{\omega^2}\delta(n^2-n_\pm^2) = \int_0^\infty \mathrm{d}\omega\,\delta(k^2\,c^2-n_\pm^2\,\omega^2)$$

$$= \frac{1}{|\partial(n_\pm^2\,\omega^2)/\partial\omega|}\,. \tag{2.168}$$

Inserting Eq. (2.168) into Eq. (2.167), the spontaneous emission probability then simplifies to

$$w^{\pm}_{q_z,n_\mathrm{L},\nu}(\mathbf{k}) = \frac{2\,\pi^2\,q^2\,c^4}{\hbar\,E^2}\,\frac{\delta(\omega-\nu\,\varepsilon\,\tilde{\Omega}-k_z\,v_z)}{\mathcal{T}_\pm^2+1}\,\frac{\left|\mathfrak{a}_\pm\,\Gamma^\nu_x - i\,\Gamma^\nu_y + \mathfrak{b}_\pm\,\Gamma^\nu_z\right|^2}{|\partial(n_\pm^2\,\omega^2)/\partial\omega|}\,. \tag{2.169}$$

Lastly, substituting Eq. (2.169) into the general formula for the emissivity, Eq. (2.54), yields

$$\eta^\nu_\pm(\omega,\theta) = \frac{q^2\,n_\pm^2\,\omega^3\,c}{4\,\pi\,E^2}\,\frac{\partial(n_\pm\,\omega)/\partial\omega}{|\partial(n_\pm^2\,\omega^2)/\partial\omega|}\,\frac{\delta(\omega-\nu\,\varepsilon\,\tilde{\Omega}-k_z\,v_z)}{\mathcal{T}_\pm^2+1}$$
$$\times\left|\mathfrak{a}_\pm\,\Gamma^\nu_x - i\,\Gamma^\nu_y + \mathfrak{b}_\pm\,\Gamma^\nu_z\right|^2\,. \tag{2.170}$$

We now derive the final form of the emissivity in Eq. (2.170) by evaluating its remaining components. First, we define the dimensionless velocity parameters

$$\beta_\perp = \frac{v_\perp}{c}, \quad \beta_z = \frac{v_z}{c}\,. \tag{2.171}$$

Using Eq. (2.171) and the general definition of the refractive index from (2.52), we can rewrite the argument of the delta distribution in Eq. (2.170) as

$$k_z\,v_z = n_\pm\,\omega\,\beta_\parallel\,\cos(\theta)$$
$$\Rightarrow \delta(\omega-\nu\,\varepsilon\,\tilde{\Omega}-k_z\,v_z) = \delta\{\omega[1-n_\pm\,\beta_\parallel\,\cos(\theta)]-\nu\,\varepsilon\,\tilde{\Omega}\}\,. \tag{2.172}$$

Next, we consider the ratio of partial derivatives with respect to ω in Eq. (2.170) and simplify it to

$$\frac{\partial(n_\pm\,\omega)/\partial\omega}{|\partial(n_\pm\,\omega)^2/\partial\omega|} = \frac{\partial(n_\pm\,\omega)/\partial\omega}{2\,n_\pm\,\omega\,\partial(n_\pm\,\omega)/\partial\omega}$$
$$= \frac{1}{2\,n_\pm\,\omega}\,. \tag{2.173}$$

The absolute value in the denominator can be omitted here, as $n_\pm > 0$ for propagating modes in a cold plasma, and $\omega > 0$ for physical wave modes, ensuring the expression remains positive.

To evaluate the squared bracket term involving the Γ_i^ν-terms in Eq. (2.170), we insert the expressions from Eqs. (2.116)–(2.118) to find

$$\begin{aligned}\mathfrak{a}_\pm \Gamma_x^\nu - i\,\Gamma_y^\nu + \mathfrak{b}_\pm \Gamma_z^\nu &= 2\,\mathfrak{a}_\pm\, p_\perp \frac{\nu}{\tilde{z}} J_\nu(\tilde{z}) - 2\,\varepsilon\, p_\perp\, J_\nu'(\tilde{z}) + 2\,\mathfrak{b}_\pm\, p_z\, J_\nu(\tilde{z}) \\ &= 2\,p_\perp \left[\left(\mathfrak{a}_\pm \frac{\nu}{\tilde{z}} + \mathfrak{b}_\pm \frac{\beta_\parallel}{\beta_\perp}\right) J_\nu(\tilde{z}) - \varepsilon\, J_\nu'(\tilde{z})\right], \end{aligned} \tag{2.174}$$

where we use the relation $p_z/p_\perp = p_\parallel/p_\perp = \beta_\parallel/\beta_\perp$. Inserting Eqs. (2.172), (2.173), and (2.174) into Eq. (2.170), and substituting $E = \gamma\, m\, c^2$ and $p_\perp = \gamma\, m\, c\, \beta_\perp$, we obtain the final form of the emissivity as

$$\begin{aligned}\eta_\pm^\nu(\omega,\theta) = \frac{q^2\, n_\pm\, \omega^2\, \beta_\perp^2}{2\,\pi\, c} \frac{\delta\{\omega[1 - n_\pm\, \beta_\parallel\, \cos(\theta)] - \nu\,\varepsilon\,\tilde{\Omega}\}}{\mathcal{T}_\pm^2 + 1} \\ \times \left[\mathfrak{A}_\pm\, J_\nu(\tilde{z}_\pm) - \varepsilon\, J_\nu'(\tilde{z}_\pm)\right]^2, \end{aligned} \tag{2.175}$$

with the coefficient $\mathfrak{A}_\pm$ defined as

$$\mathfrak{A}_\pm := \mathfrak{a}_\pm \frac{\nu}{\tilde{z}_\pm} + \mathfrak{b}_\pm \frac{\beta_\parallel}{\beta_\perp}. \tag{2.176}$$

To make explicit that the Bessel functions contain the harmonic number ν in their argument, we reformulate the expression for the Bessel argument $\tilde{z}$. Setting the argument of the delta distribution in Eq. (2.175) to zero gives

$$\frac{\omega}{\varepsilon\,\tilde{\Omega}} = \frac{\nu}{1 - n_\pm\, \beta_\parallel\, \cos(\theta)}. \tag{2.177}$$

This relation allows us to rewrite the argument $\tilde{z}$ of the Bessel functions as

$$\begin{aligned}\tilde{z} &= \frac{k_\perp\, p_\perp}{m\,\Omega} \\ &= \frac{k\, \sin(\theta)\, \gamma\, m\, v\, \sin(\theta)}{m\,\Omega} \\ &= \frac{\omega\, n_\pm\, \beta_\perp\, \sin(\theta)\, E}{\Omega\, m\, c^2} \\ &= \frac{\omega}{\tilde{\Omega}} n_\pm\, \beta_\perp \sin(\theta) \\ &= \nu\,\varepsilon \frac{n_\pm\, \beta_\perp \sin(\theta)}{1 - n_\pm\, \beta_\parallel\, \cos(\theta)}. \end{aligned} \tag{2.178}$$

We note that, in practice, the sign parameter ε may be omitted when it appears in a product with the harmonic number ν (e.g. in Eq. 2.178 or in the delta distribution in Eq. 2.175 and earlier), since the latter already spans positive and negative integers, thereby effectively accounting for both charge signs (e.g. Fleishman & Kuznetsov 2010).

Additional simplified expressions for $n_{\pm}^2$, $\mathcal{T}_{\pm}$, $\mathcal{K}_{\pm}$, and $\mathfrak{A}_{\pm}$ can be obtained by applying the Altar-Appleton-Hartree (AAH) approximations to the Stix parameters. The AAH approximations, along with detailed derivations, are provided in Appendix A.11. In particular, we find for $\mathfrak{A}_{\pm}$ the expression

$$\mathfrak{A}_{\pm} = \mathcal{T}_{\pm} \left[\frac{\cos(\theta) - n_{\pm}\, \beta_{\parallel}}{n_{\pm}\, \beta_{\perp}\, \sin(\theta)} \right] + \frac{\mathcal{K}_{\pm}}{n_{\pm}\, \beta_{\perp}}\,, \tag{2.179}$$

which is required for expressing the emission and absorption coefficients in their final form.

2.3.9 Final expressions for GS emission and absorption coefficients

In this section, we derive the final expressions for the GS emission and absorption coefficients in a magnetoactive plasma. To obtain the GS emission coefficient, we insert Eq. (2.175) with (2.179) into Eq. (2.40) and sum over all harmonics. This yields the emission coefficient as

$$\begin{aligned} j_{\omega}^{\pm} = {} & \frac{q^2}{2\,\pi\,c} \frac{n_{\pm}\,\omega^2}{\mathcal{T}_{\pm}^2 + 1} \sum_{\nu=-\infty}^{\infty} \int \mathrm{d}^3 p\, f(\mathbf{r}, \mathbf{p}) \\ & \times \left\{ \frac{\mathcal{T}_{\pm}[\cos(\theta) - n_{\pm}\,\beta\,\mu] + \mathcal{K}_{\pm} \sin(\theta)}{n_{\pm}\, \sin(\theta)} J_{\nu}(\tilde{z}) - \varepsilon\,\beta\,\sqrt{1-\mu^2}\, J_{\nu}'(\tilde{z}) \right\}^2 \\ & \times \delta\{\omega[1 - n_{\pm}\,\beta\,\mu\,\cos(\theta)] - \nu\,\varepsilon\,\tilde{\Omega}\}\,. \end{aligned} \tag{2.180}$$

Here, we use the substitutions $\beta_{\perp} = \beta\,\sqrt{1-\mu^2}$ with $\mu = \cos(\phi)$ and $\sin(\phi) = \sqrt{1-\mu^2}$ following from the Pythagorean trigonometric identity, and we use $\beta_{\parallel} = \beta\,\cos(\phi)$.

To align with the expression given by Fleishman & Kuznetsov (2010), which is implemented in the *UFGSC*s, one must convert the angular frequency to the oscillation frequency using Eq. (2.33), and select the sign parameter as $\varepsilon = -1$. The conversion to oscillation frequency $f_{\omega} = \omega/(2\,\pi)$ introduces an additional factor of $2\,\pi$ inside the Dirac delta distribution. Specifically, the

identity $\delta(\varphi\, x) = \delta(x)/|\varphi|$ implies an additional factor $1/(2\,\pi)$ in the prefactor of $j_\omega^\pm$ when expressed in terms of oscillation frequency. This correction appears to be missing in Eq. (1a) in Fleishman & Kuznetsov (2010).

For the GS absorption coefficient, we insert Eq. (2.175) with Eq. (2.179) into Eq. (2.48). Furthermore, we replace the difference of distribution functions in Eq. (2.48) using Eq. (2.49). Then the absorption coefficient becomes

$$\begin{aligned}\alpha_\omega^\pm = &-\frac{4\,\pi^2\,q^2}{n_\pm\,(\mathcal{T}_\pm^2+1)}\sum_{\nu=\infty}^{\infty}\int \mathrm{d}^3p\\ &\times\left\{\frac{\mathcal{T}_\pm[\cos(\theta)-n_\pm\,\beta\,\mu]+\mathcal{K}_\pm\sin(\theta)}{n_\pm\,\sin(\theta)}J_\nu(\tilde{z})-\varepsilon\,\beta\,\sqrt{1-\mu^2}\,J_\nu'(\tilde{z})\right\}^2\\ &\times\frac{1}{\beta}\left[\frac{\partial f}{\partial p}+\frac{n_\pm\,\beta\,\cos(\theta)-\mu}{p}\frac{\partial f}{\partial \mu}\right]\,\delta\{\omega[1-n_\pm\,\beta\,\mu\,\cos(\theta)]-\nu\,\varepsilon\,\tilde{\Omega}\}\,, \quad (2.181)\end{aligned}$$

where we use $p = \beta\,\gamma\,m\,c$, and $f = f(\mathbf{r},\mathbf{p})$. Similar to the emission coefficient in Eq. (2.180), the version in Eq. (1b) in Fleishman & Kuznetsov (2010) is obtained by setting $\varepsilon = -1$ and converting ω to the oscillatory frequency. The factor $1/(2\,\pi)$ emerging from the frequency transformation in the delta distribution is not missing in Eq. (1b) in Fleishman & Kuznetsov (2010).

In conclusion, the specific intensity of GS emission can be determined, typically through numerical methods, by solving the RTE in Eq. (2.38) using the emission and absorption coefficients j_ω and α_ω from Eqs. (2.180) and (2.181), respectively. These expressions rely on the refractive indices $n_\pm$, given by Eq. (A.137); the longitudinal and transverse components of the polarisation vector, $\mathcal{K}_\pm$ and $\mathcal{T}_\pm$, from Eqs. (A.145) and (A.146), respectively; the variable Δ from Eq. (A.132) and $\omega^\dagger$ from Eq. (A.123), which enter the expressions for $n_\pm$, $\mathcal{T}_\pm$, and $\mathcal{K}_\pm$; and the Bessel function argument $\tilde{z}$, as given by Eq. (2.178). Together with values for the plasma and particle properties appearing in these expressions, these quantities fully determine the resulting GS intensity produced by electrons spiralling along the CME flux rope field lines under the considered assumptions and approximations.

3

Numerical framework and model integration

The model descriptions in Section 3.1 follow partially Husidic et al. (2024a), Husidic et al. (2024b), and Husidic et al. (2025). Parts of Section 3.2 follow Husidic et al. (2024a), while parts of Section 3.3 follow Husidic et al. (2024b).

In this chapter, we present the numerical models used in this work as well as some of the major modifications of the *PARADISE* transport code. Section 3.1 briefly describes the numerical models *EUHFORIA* (Section 3.1.1), *Icarus* (Section 3.1.2), *COCONUT* (Section 3.1.3), *PARADISE* (Section 3.1.4), and the *UFGSC*s (Section 3.1.5). Section 3.2 then discusses the main modifications made by the author to *PARADISE* to handle block-based grids such as those from *Icarus*. Section 3.3 then explains further updates introduced by the author to the transport code to enable operation on unstructured grids such as from *COCONUT*.

3.1 Numerical models

In the following, the main numerical models utilised in this thesis are briefly described, starting with *EUHFORIA*.

3.1.1 EUHFORIA

The physics-based forecasting tool *EUHFORIA* simulates the solar wind in the inner heliosphere from heliocentric distances $r = 0.1$ au onwards (Pomoell & Poedts, 2018). It consists of two components, a coronal and a heliospheric part. The coronal module (see Section 3.1.2) solely serves to derive inner boundary conditions at 0.1 au for the heliospheric module. *EUHFORIA*'s heliospheric module then incorporates the inner boundary conditions to solve the 3D ideal MHD equations using a second-order accurate semi-discrete Finite Volume Method (FVM) on a spherical grid to generate complex solar wind configurations extending to 2 au (default setting) and beyond. The scheme employs an approximate Riemann solver to compute intercell fluxes and enforces the solenoidal condition for the magnetic field (Eq. A.43) using a constrained transport method (Kissmann & Pomoell, 2012). Furthermore, the heliospheric module operates on a uniform, equidistant, monolithic grid, and employs Heliocentric Earth EQuatorial (HEEQ) coordinates with Earth fixed at longitude $\phi = 0°$.

EUHFORIA incorporates different models to simulate the propagation and evolution of CMEs. These models include: the default cone CME model (Pomoell & Poedts, 2018), where the CME is modelled as a hydrodynamic cloud (Zhao et al., 2002; Xie et al., 2004), being known for achieving accurate shock arrival times, but lacking an intrinsic CME magnetic field; the spheromak model (Verbeke et al., 2019; Scolini et al., 2019), where the CME is represented as a magnetised plasma structure with both toroidal and poloidal field components; and the Flux Rope in 3D (FRi3D) model (Isavnin, 2016; Maharana et al., 2022), where the CME is simulated as a flux rope, capturing more realistic CME geometry.

3.1.2 Icarus

The *Icarus* code (Verbeke et al., 2022; Baratashvili et al., 2022), which is based on the *MPI-AMRVAC* framework (Keppens et al., 2012; Porth et al., 2014; Xia et al., 2018; Keppens et al., 2023; Baratashvili et al., 2025), computes complex and realistic solar wind configurations targeting the inner heliosphere from $r = 0.1$ au onwards. In contrast to *EUHFORIA*, the 3D ideal MHD equations within *Icarus* are solved in a frame corotating with the Sun on a block-based grid using a FVM implemented via the *MPI-AMRVAC* framework, which offers various numerical schemes (Keppens et al., 2023). The *Icarus* grid can potentially be stretched in radial direction (Xia et al., 2018) and/or selectively refined via AMR (Baratashvili et al., 2022). Different CME models

are included in *Icarus* as well, including the *EUHFORIA*-like cone (Verbeke et al., 2022) and spheromak (Baratashvili & Poedts, 2024) models.

Similarly to *EUHFORIA*, the domain of *Icarus* is divided into a coronal and a heliospheric part by adopting *EUHFORIA*'s semi-empirical Wang-Sheeley-Arge (WSA) model (Wang & Sheeley, 1990; Arge et al., 2003) and using synoptic magnetograms by the Global Oscillation Network Group (GONG) to derive the inner boundary conditions for the heliospheric simulations. In the WSA model, the solar wind speed is derived from an empirical formula based on the magnetic flux tube expansion factor and the proximity to CH boundaries, using GONG magnetograms. Assuming a purely radial solar wind velocity at the inner boundary, the coronal module then uses this speed to derive magnetic field, particle number density, and temperature profiles at that location (for details, see Pomoell & Poedts 2018 and references therein). The division of domains with a separating line at 0.1 au is a common approach in MHD solar wind modelling, under the assumption that the solar wind becomes super-Alfvénic below this radius and is typically already faster than the fast magnetosonic speed at 0.1 au. However, recent observations by PSP suggest that the solar wind can still be sub-Alfvénic at distances beyond 0.1 au (Bandyopadhyay et al., 2022; Jiao et al., 2024). The block-based grid structure of *Icarus* is addressed in more detail in Section 3.2. Additional details about optional features of *Icarus* are described in Section 4.2.

3.1.3 COCONUT

The *COOLFluiD*-based *COCONUT* model solves the 3D ideal MHD equations in a time-implicit manner using an FVM (Perri et al., 2022a, 2023; Kuźma et al., 2023). The original motivation for developing *COCONUT* was to replace the semi-empirical WSA model in *EUHFORIA*. Unlike the WSA module, which only provides solar wind conditions at the outer coronal boundary, *COCONUT* self-consistently derives 3D configurations from the solar surface up to 25 solar radii (and potentially beyond). In the meantime, the model has been coupled both to *EUHFORIA* (Linan et al., 2025) and *Icarus* (Baratashvili et al., 2024) to provide inner boundary conditions for these inner-heliospheric wind models.

The inner boundary conditions for *COCONUT* are obtained from synoptic maps either from GONG or HMI. Using such magnetograms, a Dirichlet condition is derived from the radial magnetic field component and applied at the solar surface, while using zero-gradient conditions for the tangential magnetic field components, thereby minimising artificial currents near the surface. For the pressure and density, fixed Dirichlet conditions are applied, while the velocity

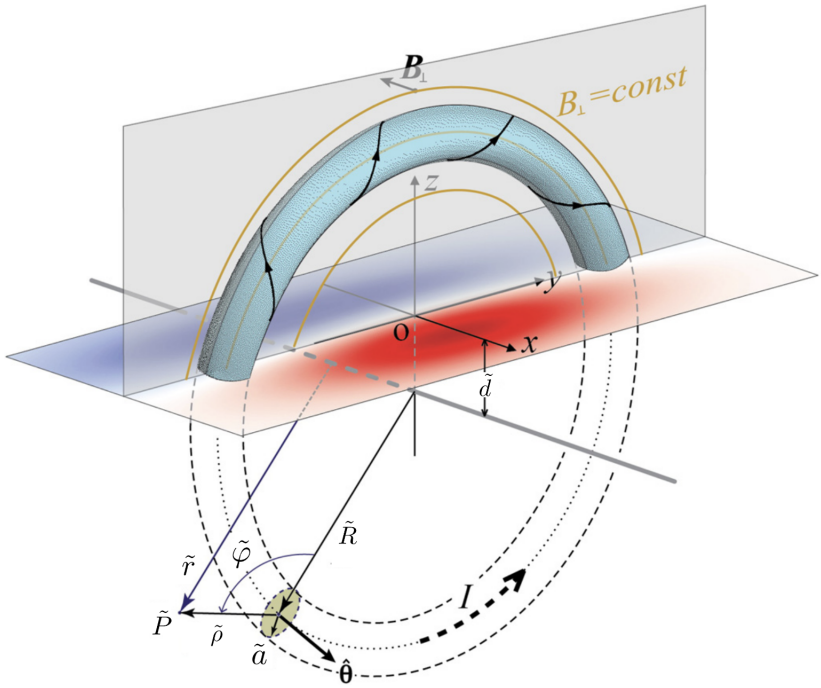

Figure 3.1. Schematic illustration of the TD MFR model, showing a thin flux rope placed between the two polarities of a locally bipolar region. The coordinate system with origin O and axes x, y, and z is located in the centre of the flux rope. The variables and functionality are addressed in the main text. Adapted from Titov et al. (2014).

at the solar surface is set to zero; nevertheless, a small outward flow emerges due to numerical effects (for details, see Perri et al. 2022a).

In this thesis, we employ two versions of the *COCONUT* model. The original version of *COCONUT* does not include any heating source terms in the MHD equations, but assumes polytropic processes with a reduced adiabatic index of $\gamma_{\mathrm{ad}} = 1.05$, thereby modelling an almost isothermal corona (Perri et al., 2022a). This version of *COCONUT* is employed in Chapter 5. A more recent update of *COCONUT* includes heating source terms to the MHD equations (Baratashvili et al., 2024) and employs an adiabatic index of $\gamma_{\mathrm{ad}} = 5/3$; this version is utilised in Chapter 6. Additional details about these terms are presented in Section 2.1.

COCONUT also incorporates CME modelling, including the Titov–Démoulin (TD) flux rope model (Titov & Démoulin, 1999; Titov et al., 2014; Linan et al.,

2023) and the regularised Biot-Savart law CME model (Titov et al., 2018; Guo et al., 2024); however, in Chapters 5 and 6, we employ only the former. The TD model is a semi-analytical force-free model designed to represent the magnetic structure of twisted flux ropes embedded in potential magnetic fields. Figure 3.1 shows a schematic illustration of the TD flux rope model with some of the important geometric parameters. A thin toroidal flux rope with minor and major radii $\tilde{a}$ and $\tilde{R}$, respectively, is placed between the polarities of a locally bipolar region on the solar surface, with half of the torus placed beneath the solar surface, thereby mimicking anchoring to the surface. The symmetry axis of the MFR oriented along the z-axis coincides with an iso-contour, where the perpendicular magnetic field component $B_\perp$ is constant. The centre of the toroidal axis is positioned at a height $\tilde{d}$. Furthermore, in Fig. 3.1, $\hat{\theta}$ denotes the unit vector tangential to the axis of the MFR, $\tilde{P}$ is a given point in space, and $\tilde{r}$ and $\tilde{a}$ are the distances from the toroidal and poloidal symmetry axes to $\tilde{P}$, respectively. The variable $\tilde{\varphi}$ denotes the angle between $\tilde{R}$ and $\tilde{\rho}$ (see Titov et al. 2014 for details).

The core field of the flux rope is generated by a ring current intensity I circulating within the flux rope that satisfies

$$I = \zeta\, I_{\mathrm{S}} \approx \zeta\, \frac{\tilde{R}\, B_{\mathrm{t}}}{\ln \frac{8\,\tilde{R}}{\tilde{a}} - \frac{3}{2} + \frac{I_{\mathrm{i}}}{2}}\,, \tag{3.1}$$

where I_{S} is the Shafranov intensity, ζ is a dimensionless parameter, B_{t} is the toroidal magnetic field component, and I_{i} is a dimensionless variable that characterises the radial distribution of the poloidal magnetic field inside the MFR. An eruptive behaviour of the TD flux rope is accomplished by setting $\zeta > 1$. In that case, the pressure of the resulting magnetic field from the ring current intensity I exceeds the magnetic pressure of the ambient coronal pressure (see Titov et al. 2014 and Linan et al. 2023 for details). Larger values of ζ generally correspond to a greater amount of free magnetic energy, resulting in more intense CMEs with higher injection speeds and stronger magnetic fields.

3.1.4 PARADISE

PARADISE is a particle acceleration and transport code that solves the FTE to propagate energetic particles as test particles through prescribed solar wind or coronal backgrounds, and outputs spatio-temporal particle intensity distributions. While initially using only the analytical Parker solar wind model or *EUHFORIA* to provide the necessary solar wind backgrounds for the particle transport simulations, *PARADISE* has been extended in the work of this thesis

to incorporate solar wind configurations from *Icarus* (see Chapter 4) and coronal MHD backgrounds from *COCONUT* (see Chapter 5).

The FTE from Eqs. (2.20)–(2.23) is solved in *PARADISE* in a stochastic manner by reformulating the FTE into an equivalent set of Stochastic Differential Equations (SDEs) using Itô calculus (Øksendal, 1995). Then, applying the Euler–Maruyama method, the SDEs are numerically integrated to update the position, momentum, and pitch angle of an individual energetic particle. The trajectories resulting from the calculations are not those of physical particles and do not follow real particles or their guiding centres. Instead, so-called pseudo-particles[1] are utilised that follow stochastic trajectories governed by the SDEs derived from the FTE. In this context, a pseudo-particle can be interpreted as '*the temporal evolution of an ensemble of real particles, or equivalently, the evolution of a phase-space density element*' (Strauss & Effenberger, 2017). The final intensities *PARADISE* outputs are derived by sampling the pseudo-particles in a five-dimensional (the three spatial coordinates, pitch angle, and energy) histogram to yield the differential intensities (for details, see Wijsen 2020).

The initial conditions, such as energy, pitch angle, or position, as well as the overall shape of the injected particle distributions, whether isotropic or anisotropic particle populations are considered, may be defined by the *PARADISE* user, including simple Gaussian distributions, pure power-law distributions, or more complex kappa distributions.

3.1.5 Ultimate Fast GS Codes

The *UFGSC*s contain a set of numerical schemes for calculating GS emission in the non-quantum regime, covering non-relativistic ($\gamma \approx 1$), mildly relativistic ($\gamma \gtrsim 1$), and ultra-relativistic ($\gamma \gg 1$) energy ranges (Kuznetsov & Fleishman, 2021). While an earlier version of these GS codes was limited to using idealised (i.e. analytically defined) distribution functions in energy and pitch angle cosine (Fleishman & Kuznetsov, 2010), the latest update (Kuznetsov & Fleishman, 2021) allows the use of arbitrarily shaped electron distributions defined on a mesh.

The *UFGSC*s were developed to circumvent the computationally demanding calculations of the exact equations for GS emission and absorption coefficients (Melrose, 1968a; Ramaty, 1969). To achieve this, Fleishman & Kuznetsov (2010) refined the fast numerical approximations introduced by Petrosian (1981) and Klein (1987), primarily by replacing the summation over cyclotron harmonics

[1] For simplicity, we refer to pseudo-particles as 'particles' throughout the remainder of the thesis.

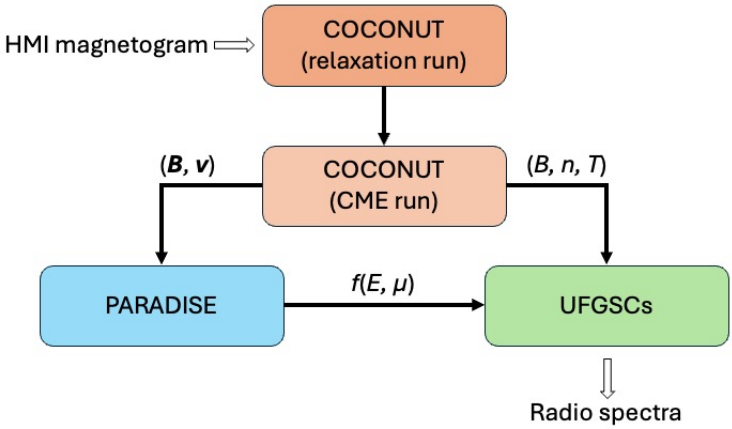

Figure 3.2. Illustration of the modelling chain for the generation of synthetic radio spectra.

with an integration over a corresponding continuous parameter, and including an approximate treatment of Bessel functions in Eqs. (2.180) and (2.181). In the current version, the code can operate in one of three modes: exact, continuous, or hybrid. In the hybrid mode, the user specifies a threshold frequency $f_{\omega 0} := \tilde{\eta}\,\Omega/(2\,\pi)$, where $\tilde{\eta}$ is a positive integer and Ω denotes the electron gyrofrequency (Eq. A.83). Below this threshold, the code employs the exact mode, while above, it switches to the continuous mode.

In Chapter 6, we present the coupling of *COCONUT*-*PARADISE* to the *UFGSC*s and include CME modelling. To provide a clearer overview of the involved modelling steps, Fig. 3.2 illustrates the modelling chain to generate synthetic radio spectra, represented as a flowchart. The process begins by computing a steady-state corona using *COCONUT* with an HMI magnetogram for the inner boundary conditions. The simulation is then restarted with a superimposed unstable MFR to represent the erupting CME. Next, *PARADISE* is utilised to evolve energetic electron distributions within the MHD environment. Finally, the synthetic GS emission is computed by providing the electron distributions from *PARADISE* and the plasma parameters from *COCONUT* as input to the *UFGSC*s.

3.2 Block-based grid

In the following, we describe some of the main modifications of *PARADISE* to couple it to *Icarus*. *PARADISE* employs a grid-free numerical approach for the propagation of energetic test particles. However, the input background solar wind or corona configurations required by *PARADISE* are provided on a numerical grid, containing parameters of the solar wind or coronal plasma. To integrate the set of equations constituting the FTE for a particular test particle, it becomes necessary to locate the particle on the numerical grid of the particular MHD model and determine the cells surrounding that location. Then, the various gradients are computed at the grid corners, and, along with the solar wind values, are interpolated to the particle's exact position inside the cell at each computational step.

In the original *EUHFORIA-PARADISE* framework (Wijsen et al., 2019a; Wijsen, 2020), *PARADISE* has been designed to locate particles and perform the described procedure on a monolithic grid potentially containing ghost cells, such as *EUHFORIA*'s uniform equidistant grid (Pomoell & Poedts, 2018), where the solar wind parameters are provided on one large rectangular and structured grid, consisting of rectangular cells of equal size. Through relatively simple algorithms, one can locate the 'lower left front' grid point of the current cell and gain automatically access to all the remaining grid points surrounding the particle, as well as the required grid points for the gradient computations.

In contrast to *EUHFORIA*'s monolithic grid structure, *Icarus* employs a block-based grid. The computational domain is also saved as a rectangular and structured grid consisting of rectangular cells, but these cells are organised into blocks (Keppens et al., 2012). An important feature of the *Icarus* grid is its potential application of AMR and/or grid stretching, where we first discuss the case with AMR. When AMR is applied, each refinement level subdivides a target block into eight smaller blocks by halving it along each coordinate direction. These refined blocks maintain the same number of cells as the original, but with half the cell size in each direction, thereby doubling the resolution. As higher levels of AMR are applied, these blocks with different AMR levels follow a strict nesting protocol, that is, two blocks touching each other either orthogonally or diagonally can never differ by more than one level of AMR (Nool & Keppens, 2002; Keppens et al., 2012).

Tracing particles on the *Icarus* grid requires algorithms that first locate the current particle in the block where it resides, and subsequently determine the grid corners surrounding the particle within that block. To achieve this, we exploit the indexing system used by *MPI-AMRVAC* for the blocks. The global

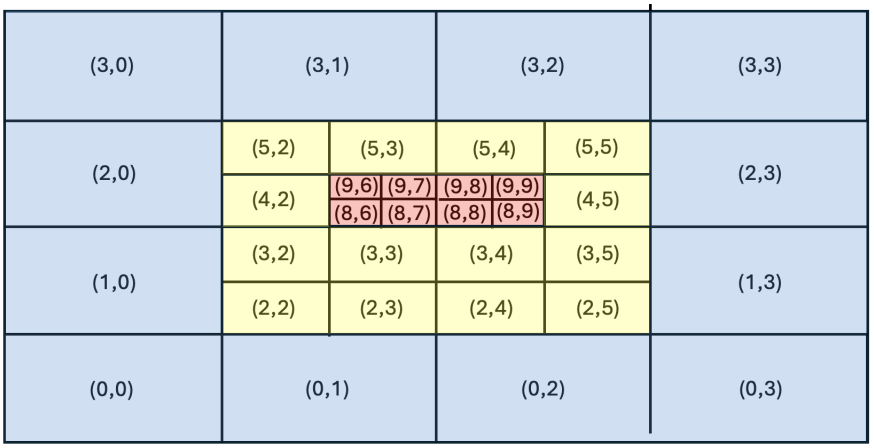

Figure 3.3. Block indexing in *MPI-AMRVAC* on a 2D example grid. Colours denote AMR levels (blue: level 1, yellow: level 2, red: level 3). Each block has the index that would logically follow, if the entire grid was on its AMR level (see main text). Inspired by Keppens et al. (2012).

block indices are designed in such a way that, per AMR level, each block has indices as if the entire grid were uniformly refined on the AMR level of that particular block. For instance, if the target block had AMR level 3, then its global indices would be as if the entire grid were refined to AMR level 3. Figure 3.3 illustrates this approach on a Two-Dimensional (2D) example grid. Blue, yellow, and red rectangles denote blocks on AMR levels 1, 2, and 3, respectively. Using zero-based indexing, we can see that, for instance, the bottom left yellow block has global index (2,2), because on the hypothetical uniform level-2 grid, there are two index steps to its left and two below it. The example in Fig. 3.3 also shows that blocks on different AMR levels can share the same global (i, j) pair, for instance, the blue and yellow blocks labelled (3,2) and (3,3).

To locate blocks efficiently, when preparing the *Icarus* input files for *PARADISE*, we create a list of unique numbers from the three global indices of each block on each AMR level, and locate the number within *PARADISE* using a binary search algorithm. The unique numbers are created using the Szudzik pairing function, which is a variant of the Rosenberg-Strong pairing function and more efficient than the standard Cantor pairing function (Szudzik, 2017). As the example in Fig. 3.3 illustrates, it is crucial to prepare unique block numbers on each AMR level separately, since the global block indices are only unique within the particular AMR level, but not across AMR levels (Keppens et al., 2012).

Once all cells are located, we perform a trilinear interpolation, similar to the *EUHFORIA*-case, of the solar wind parameters and spatial derivatives at the grid points to the actual particle location. For calculating spatial derivatives, we employ an alternating fourth-order uniform scheme, where the term 'alternating' refers to switching between different stencil formulas (central vs biased), depending on the proximity to the boundary. This allows derivative stencils to stay entirely within one block. Furthermore, since most timesteps in *PARADISE* do not exactly coincide with the timestamps of the *Icarus* snapshots, *PARADISE* loads the two nearest snapshots surrounding the current timestep and performs a linear interpolation in time. In the case of a steady-state solar wind, such as in Chapter 4, the static snapshot is rotated in *PARADISE* by an angle corresponding to the elapsed simulation time. This time-handling approach is also used for input from the other MHD models coupled to *PARADISE*.

A primary challenge in locating a particle on the *Icarus* grid arises from the block-based structure, especially when multiple levels of AMR are applied. When a particle is close to the boundary of a block, that is, when it is in some form outside the internal grid structure of the current block, communication between multiple neighbouring blocks becomes necessary to provide requisite data for numerical computations such as trilinear interpolation or finite volume differencing. This issue is illustrated in Fig. 3.4. In cases involving more than two levels of AMR, it becomes evident that a block of some level L must eventually communicate with either a so-called parent block of level $L-1$, or a so-called children block of level $L+1$. Communication between blocks of the same level occurs both with and without applied AMR (Keppens et al., 2012).

The solution of having ghost cells for each block (Keppens et al., 2012), as employed by the built-in particle tracer in *MPI-AMRVAC*, is not feasible for *PARADISE* due to the resulting significantly larger data files that would store these ghost cell values. As an initial alternative, we chose to individually address the various scenarios based on a particle's position relative to the numerical grid and acquire all necessary data from neighbouring blocks as needed. However, this case-by-case approach was later replaced by a more general and robust particle tracing routine, which now automatically identifies surrounding grid points, even when they reside in different block at different AMR levels.

Solar wind simulations of *Icarus* may involve large radial distances of 2 au and beyond. When using a uniform grid in *Icarus* (or other solar wind models such as *EUHFORIA*), due to the spherical grid and constant cell spacing in radial and angular directions, cells become elongated towards the outer boundary compared to the inner boundary. Furthermore, the resolution at the cells closer to the inner boundary might be more relevant. To address both issues, *MPI-AMRVAC* allows for grid stretching in the radial direction (Xia et al., 2018).

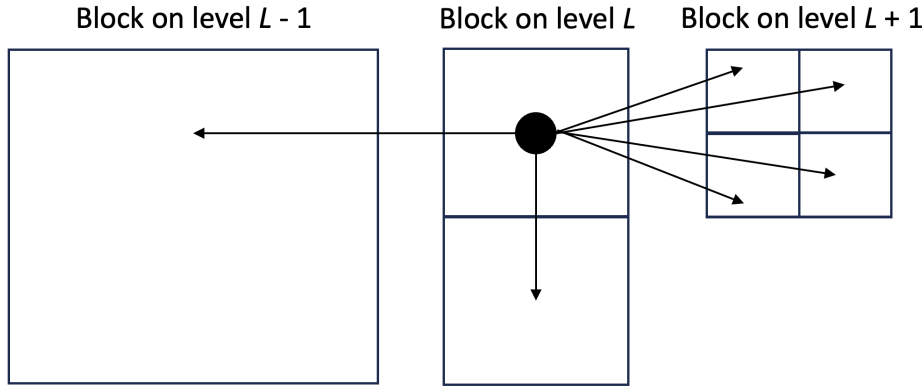

Figure 3.4. Illustration of the AMR nesting and communication between blocks. Using AMR likely requires blocks of some level L to communicate both to coarse blocks (level $L-1$) and further refined blocks (level $L+1$). Inspired by Keppens et al. (2012).

Then, the scaling factor needs to be calculated, which is determined via

$$q_{\mathrm{sf}} = \left(\frac{r_{\mathrm{out}}}{r_{\mathrm{in}}} \right)^{\frac{1}{N_{\mathrm{r}}}}, \tag{3.2}$$

with q_{sf} being the scaling factor, N_{r} the number of cells in radial direction, and r_{out} and r_{in} the radial coordinates at the outer and inner boundary, respectively. The scaling factor works such that from a given cell, the radial coordinate of the next cell is determined as $r_{i+1} = q_{\mathrm{sf}}\, r_i$, or in general, the i-th radial coordinate is given by

$$r_i = q_{\mathrm{sf}}^{i}\, r_{\mathrm{in}}. \tag{3.3}$$

When using stretched grids, the search algorithms for the colatitudinal and longitudinal indices of the grid corners encompassing the current particle remain the same, while the search algorithm[2] for the radial index is adjusted using Eq. (3.3).

When applying both AMR and grid stretching, it is essential to note that a refined block remains within the same radial range but contains twice as many cells per coordinate axis as its unrefined counterpart. For that reason, it is possible to obtain on each AMR level the particular scaling factor, where the

[2]The search algorithm can be generalised to support grid-stretching along the latitudinal or longitudinal axes as well.

scaling factor q^{sf}_{L+1} in the children block is

$$q^{\mathrm{sf}}_{L+1} = \sqrt{q^{\mathrm{sf}}_{L}}\,, \tag{3.4}$$

with q^{sf}_{L} being the scaling factor in the parent block (Xia et al., 2018).

3.3 Unstructured grid

Unlike *EUHFORIA* and *Icarus*, which incorporate a structured rectangular grid using spherical coordinates, *COCONUT* solves the 3D ideal MHD equations on an unstructured spherical grid using Cartesian coordinates. *COCONUT*'s grid consists of prism-shaped cells with equilateral triangular faces and rectangular lateral faces, with the cells being arranged in an onion-like shell structure and increasing in size with increasing heliocentric distance (for details, see Brchnelova et al. 2022). Panel a) of Fig. 3.5 illustrates the prism shape of a *COCONUT* cell. We note that the cell lengths in radial direction, that is, the point connections 1-4, 2-5, and 3-6 in panel a), are in general much smaller than the remaining edges.

Consequently, the approaches used to trace particles and compute gradients at grid points, as well as interpolate to a particle's exact location, which are employed for *EUHFORIA* and *Icarus*, are not suitable for *COCONUT*'s unstructured grid, necessitating alternative methods. For tracing particles and identifying surrounding grid points, we utilise the cell connectivity information present in the *COCONUT* files. For each cell, we have information both about the six grid points (or nodes) that make the cell (numbered from 1 to 6 in the left panel of Fig. 3.5) and the indices of all cells connected to it, where we use the definition of cell connectivity to share at least one node with a neighbouring cell. The coordinates and coronal plasma parameters of a cell are saved at its centre. Panel b) of Fig. 3.5 illustrates the principle of cell connectivity in a 2D example. The red dots mark cell centres, and the cyan-coloured cell is the located cell containing the particle. Then, all yellow-marked cells are connected cells, as they share at least one node with the located cell, and the cyan-marked and yellow-marked cells form a group of connected cells.

We may use this information to calculate at the very first computational step for a particular test particle the Euclidean distances between the initial particle location and all cell centres. The closest distance identifies the cell containing the particle. To save computational resources, we select timesteps in *PARADISE* that are sufficiently small, ensuring the particle never moves outside the current group of connected cells. This allows, in the subsequent computational steps,

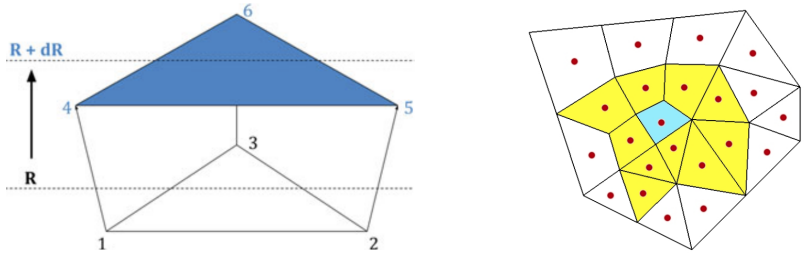

(a) Cell structure in *COCONUT*. **(b)** 2D illustration of cell connectivity.

Figure 3.5. Illustrations of the cell structure and cell connectivity in *COCONUT*. Panel a) shows the shape of a single cell with triangular faces and rectangular sides. Adapted from Brchnelova et al. (2022). Panel b) illustrates the cell connection in *COCONUT* exploited for the particle tracer and derivative computation algorithms. Adapted from Lani (2009).

to search only among the current group of connected cells for the cell centre closest to the particle position.

Once the cell containing the particle is located, we extract the coronal plasma parameters from the cell centres of all connected cells and linearly interpolate them to the particle's location, using the distances from the particle's location to the different cell centres as weights, normalised to the sum of all distances. The derivatives of the various quantities are also computed at the centres of all connected cells in the current group, and similarly linearly interpolated to the particle's exact location.

In the following, we aim to develop a framework for calculating gradients[3] on the *COCONUT* grid within *PARADISE*. Since *COCONUT*'s grid consists of an unstructured ordering of prism-shaped cells that increase in size with increasing radial distance, standard finite difference methods requiring neighbouring cells to be aligned on a line are not useful. Instead, we derive a formalism that uses the information of neighbouring cells and is based on a first-order Taylor approximation. The following formalism is similar to that in Lani (2009) and is derived here in more detail.

Let u be a function of position $\mathbf{x} = (x_1, x_2, x_3)^{\mathrm{T}}$. Then u_i is the function value at the centre of cell i. For each neighbouring cell u_j at cell centres j, we can approximate the values by a first-order Taylor expansion, yielding

$$u_j \approx u_i + \nabla u_i \cdot (\mathbf{x}_j - \mathbf{x}_i)\,, \tag{3.5}$$

[3]The mathematical formalism is unit-independent; however, in *PARADISE*, the relevant physical quantities are expressed in SI units.

with the differential operator $\nabla = (\partial/\partial x_1, \partial/\partial x_2, \partial/\partial x_3)$. We rearrange Eq. (3.5) to

$$u_j - u_i \approx \nabla u_i \cdot \Delta \mathbf{x}_j \,, \tag{3.6}$$

with $\Delta \mathbf{x}_j = \mathbf{x}_j - \mathbf{x}_i$ The equations for all N_i neighbours of the cell i can be collected in a vector-matrix form as

$$\begin{bmatrix} (\Delta x_1)_1 & (\Delta x_2)_1 & (\Delta x_3)_1 \\ (\Delta x_1)_2 & (\Delta x_2)_2 & (\Delta x_3)_2 \\ \vdots & \vdots & \vdots \\ (\Delta x_1)_{N_i} & (\Delta x_2)_{N_i} & (\Delta x_3)_{N_i} \end{bmatrix} \cdot \nabla u_i = \begin{bmatrix} (\Delta u)_1 \\ (\Delta u)_2 \\ \vdots \\ (\Delta u)_{N_i} \end{bmatrix} , \tag{3.7}$$

with $(\Delta u)_j = u_j - u_i$. To give closer cells more significance in the gradient computation, we calculate linear weights

$$w_j = \frac{1}{||\Delta \mathbf{x}_j||} \tag{3.8}$$

as the inverse of distances, and multiply each row of the matrix and the right-hand side vector by w_j, resulting in

$$\begin{aligned} [\mathbf{L}_{x_1} \quad \mathbf{L}_{x_2} \quad \mathbf{L}_{x_3}] \, \nabla u_i &= \mathbf{f}_u \\ \iff L \, \nabla u_i &= \mathbf{f}_u \,, \end{aligned} \tag{3.9}$$

where the matrix L is composed of column vectors

$$\mathbf{L}_{x_k} = [w_1(\Delta x_k)_1, w_2(\Delta x_k)_2, \ldots, w_{N_i}(\Delta x_k)_{N_i}]^{\mathrm{T}} \,, \tag{3.10}$$

and the right-hand side vector reads

$$\mathbf{f}_u = [w_1(\Delta u)_1, w_2(\Delta u)_2, \ldots, w_{N_i}(\Delta u)_{N_i}]^{\mathrm{T}} \,. \tag{3.11}$$

The system described in Eq. (3.9) is typically overdetermined, since there are three unknowns (the components of ∇u_i), but usually a system of $N_i > 3$ linear equations (one per neighbour of cell i), and thus there is no exact solution in general. In such cases, one seeks the best approximate solution by minimising the residual norm

$$\mathrm{Res}_{\min} = \min_{\nabla u_i} \| L \, \nabla u_i - \mathbf{f}_u \|^2 \,, \tag{3.12}$$

which describes a least squares problem. To solve Eq. (3.9) in a least squares sense (see Kong et al. 2020 for a proof), we multiply both sides from left by the transpose L^{T} of L to obtain a square matrix, yielding

$$L^{\mathrm{T}}\, L\, \nabla u_i = L^{\mathrm{T}}\, \mathbf{f}_u\,. \tag{3.13}$$

To isolate the unknown vector ∇u_i, we define the vector $\mathbf{f}_L \coloneqq L^{\mathrm{T}}\, \mathbf{f}_u$, and compute its components $(f_L)_k$ as

$$(f_L)_k = \sum_{l=1}^{N_i} L_{lk}\, (f_u)_l\,. \tag{3.14}$$

Furthermore, we define $G \coloneqq L^{\mathrm{T}}\, L$ and rewrite Eq. (3.13) as

$$G\, \nabla u_i = \mathbf{f}_L\,. \tag{3.15}$$

The inverse of G is given by[4]

$$G^{-1} = \frac{1}{\det(G)} \cdot \mathrm{adj}(G)\,. \tag{3.16}$$

Multiplying both sides of Eq. (3.13) by G^{-1} yields[5]

$$\begin{aligned} \nabla\, u_i = {} & \frac{1}{\det(G)} \\ & \times \begin{pmatrix} \det(M_{11}^G)\,(f_L)_1 - \det(M_{12}^G)\,(f_L)_2 + \det(M_{13}^G)\,(f_L)_3 \\ -\det(M_{12}^G)\,(f_L)_1 + \det(M_{22}^G)\,(f_L)_2 - \det(M_{23}^G)\,(f_L)_3 \\ \det(M_{13}^G)\,(f_L)_1 - \det(M_{23}^G)\,(f_L)_2 + \det(M_{33}^G)\,(f_L)_3 \end{pmatrix}, \end{aligned} \tag{3.17}$$

where we use only the upper triangle of the adjugate matrix, since G is symmetric and the corresponding minors satisfy $M_{ij}^G = M_{ji}^G$.

The selected stencil (i.e. the set of neighbouring cells used to approximate the derivative at a particular location) for the gradient calculations determines the number of rows in the system in Eq. (3.7), the geometry and conditioning of the matrix, the computational cost, and ultimately the accuracy and stability

[4]Equation (3.16) presents the analytical inverse of G. However, in future developments of the code, we will optimise this step by solving the system $G\, \nabla u_i = L^{\mathrm{T}}\, \mathbf{f}_u$ using more efficient and numerically stable methods, such as Cholesky or QR decomposition, rather than computing the matrix inverse explicitly.

[5]We note that in the literature, the signs of the minors are often not included in the formulation, but are taken into account in the numerical computation of the determinant (e.g. Yalim 2008; Lani 2009).

of the solution (see Lani 2009 and references therein). For instance, using many neighbouring cells can improve stability by overdetermining the system, but is also computationally more expensive. On the other hand, using a small stencil can be computationally inexpensive, but it also lowers the accuracy and robustness of the calculations. In our implementation in *PARADISE*, we define the reconstruction stencil as the set of all cells connected to the cell in which we desire to compute the gradient. This choice ensures accurate and robust gradient computations on unstructured grids, particularly in 3D. The sketch in panel b) of Fig. 3.5 illustrates this approach in 2D.

At the time of this writing, these procedures take significantly longer than those in the original *PARADISE* architecture. While we continue to improve the performance of *PARADISE* using the original *COCONUT* output, the author of this thesis has also created a code to interpolate the original unstructured *COCONUT* grid to a structured, rectangular *EUHFORIA*-like grid in spherical coordinates, allowing us to utilise the faster original *EUHFORIA*-*PARADISE* architecture. In Chapters 5 and 6, we employ the original unstructured *COCONUT*, and provide a comparison between the unstructured and interpolated structured grid in Section 5.4.2. While *COCONUT* itself has been benchmarked against other models and observations (Perri et al., 2022a, 2023; Kuźma et al., 2023), the interpolation of *COCONUT* to a *EUHFORIA*-like grid also serves as a test for the correct implementation of the unstructured grid handling in *PARADISE*.

For modelling GS emission with the *UFGSC*s, no additional modifications in the *COCONUT*-*PARADISE* framework were required. The coupling to the *UFGSC*s involved mainly additional separate codes to generate different virtual observer configurations, trace particles and extract solar wind parameters along Lines Of Sight (LOS), and to provide the MHD and particle data to the *UFGSC*s.

4

Modelling energetic particle dynamics in the heliosphere

Most of this chapter was published in "Energetic particle acceleration and transport with the novel Icarus+PARADISE *model", 2024b, J. Space Weather Space Clim., 14, 11 (Husidic et al., 2024a), and parts of the text and figures have been reproduced here directly. E. Husidic implemented the necessary modifications in the particle transport code* PARADISE *to work with* Icarus*, including the development of a particle tracer and algorithms for numerically calculating derivatives on a block-based AMR grid, as detailed in Section. 3.2. Furthermore, E. Husidic performed all the simulations, generated the data and figures, and drafted the complete original manuscript.*

Abstract. This chapter[1] presents the *Icarus-PARADISE* model and its initial application to simulate particle acceleration and transport at CIR shocks. *PARADISE* has been previously coupled to *EUHFORIA*, which computes solar wind conditions on a uniform grid. However, *EUHFORIA*'s lack of local grid refinement makes it computationally inefficient for resolving sharp structures such as shocks, which are critical regions for particle acceleration. To overcome this, *EUHFORIA* was replaced in this work within the *PARADISE* framework by the *MPI-AMRVAC*-based *Icarus* code. Besides constructing uniform grids, *Icarus* enables local mesh refinement through AMR, allowing higher resolution of shock regions without refining the entire domain. Prescribing the solar wind conditions at the inner boundary (0.1 au), we generated a background solar wind with two CIRs. We then injected monoenergetic protons at the forward and reverse shocks of one CIR, and tracked the evolution of the particles. First, we validated the new *Icarus-PARADISE* model by reproducing results previously obtained with *EUHFORIA-PARADISE*. Subsequently, we demonstrated the

[1]This chapter is based on SI units.

effect of increasing levels of AMR on shock resolution and particle intensities. Surpassing *EUHFORIA*'s resolution capabilities, we showed that higher AMR levels significantly enhanced particle acceleration, thereby yielding a more accurate capture of shock effects and highlighting the importance of spatial resolution in modelling energetic particle events.

4.1 Background and motivation

Space weather events increasingly affect modern societies across multiple socio-economic levels (Schrijver et al., 2014, 2015). In this context, CIRs play an important role as they can solely drive GMSs (Tsurutani et al., 1997; Richardson, 2018), accelerate energetic particles (Giacalone, 1999; Tsurutani et al., 1982; Richardson, 2018), and interact with CMEs in ways that enhance or otherwise modify the geoeffectiveness of CMEs (Chi et al., 2018; Wijsen et al., 2023). Additionally, CIRs regularly pass by spacecraft, thus making them valuable in-situ study cases (see Richardson 2004, Richardson 2018, and references within).

CIRs are large-scale, long-lived structures in interplanetary space that corotate with the Sun and can persist from weeks to months (e.g. Richardson 2004; Allen et al. 2020). They form when a fast solar wind stream overtakes a slower stream ahead, forming regions of compressed plasma, as illustrated by the shaded region in Fig. 4.1. Far beyond 1 au, a forward and a reverse shock can form if the compression is sufficiently strong, while at 1 au CIRs are typically bounded by two compression waves[2] (Richardson, 2018). The terms 'forward' and 'reverse' refer to the solar wind reference frame (Wijsen, 2020): the reverse shock (blue curve in Fig. 4.1) forms at the trailing edge and decelerates the fast wind, while the forward shock (red curve in Fig. 4.1) forms at the leading edge and accelerates the slow wind. In the frame corotating with the Sun, both shocks are essentially stationary and act to decelerate and deflect the flow, so the forward/reverse terminology is best understood as describing the expanding structure between them.

There is ongoing effort in understanding the acceleration and transport of protons and heavier ions in CIR regions. Despite decades of significant effort, there remains no consensus in the scientific community regarding the exact acceleration mechanisms for SEPs in general (Petrosian, 2016; Perri et al., 2022b), and various mechanisms have been proposed for acceleration at CIRs (e.g. Richardson 2004, Richardson 2018, and references therein). At CIR shocks,

[2]For simplicity, we use the term 'shock' to refer to both actual shocks and compression waves throughout this chapter, since the distinction is not relevant for the present study.

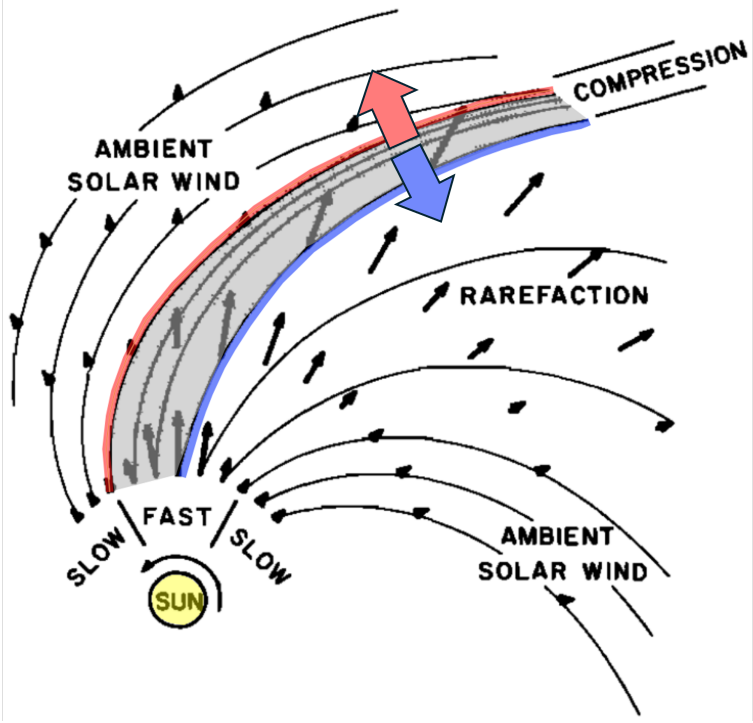

Figure 4.1. Schematic illustration of a CIR in the solar wind reference frame. The grey shaded area indicates the compression region, while the red and blue curves illustrate the forward and reverse shock waves, respectively. Arrows of the same colour show the corresponding propagation directions. Adapted from Pizzo (1978).

the most widely accepted mechanism is DSA (Desai & Giacalone, 2016; Vainio & Afanasiev, 2018). The DSA mechanism dominates at quasi-parallel shocks, where charged particles gain energy by repeatedly crossing the shock front and scattering off magnetic turbulence frozen into the plasma in both upstream and downstream regions. SDA may also contribute, particularly at quasi-perpendicular shocks, where particles gain energy via drift motions caused by magnetic field gradients near the shock. In addition, SA may occur in the presence of strong magnetic turbulence within the CIR structure, further energising particles through resonant wave-particle interactions between the SEPs and magnetic field fluctuations (Kallenrode, 2003; Vainio & Afanasiev, 2018). Observations show that the suprathermal particle intensity profiles recorded at CIRs typically form double-peaked intensity profiles, resulting from acceleration at both the forward and the reverse shocks (Smith & Wolfe, 1976; Richardson, 2018; Allen et al., 2021; Wijsen et al., 2021).

Over the past few decades, various simulation models have been developed to investigate SEP and other energetic particle populations in the inner heliosphere from both theoretical and forecasting perspectives. Typically, these frameworks combine heliospheric solar wind models with a particle transport code in a modular setup. One example is the Solar Energetic Particle MODel (*SEPMOD*; Luhmann et al. 2017) that simulates the scatter-free SEP transport by utilising background solar wind configurations obtained by the 3D heliospheric MHD model *Enlil* (Odstrcil et al., 2004, 2005; Pizzo et al., 2011). Another noteworthy approach is the Energetic Particle Radiation Environment Module (*EPREM*; Kozarev et al. 2010), which incorporates diffusion and drift effects during particle transport. Initially coupled to *Enlil* (Kozarev et al., 2010), *EPREM* was later upgraded (Kozarev et al., 2013) to accept input from the Block-Adaptive-Tree Solar Wind Roe-type Upwind Scheme (*BATS-R-US*) model (Manchester et al., 2012).

With some exceptions, such as *BATS-R-US*, many heliospheric solar wind models employ uniform equidistant grids. While this simplifies computational tasks such as computing gradients and tracing particle trajectories, it also introduces challenges. Increasing the resolution in one region requires refining the entire computational domain, which creates high computational costs and thereby limits the maximum resolution. This constraint directly affects the *EUHFORIA-PARADISE* model, motivating an update of the model to support more flexible grids that allow for localised resolution enhancements without impractical technological demands.

For this reason, we present the *Icarus-PARADISE* model as an advancement of the previous *EUHFORIA-PARADISE* framework and demonstrate its capabilities in an initial theoretical application. *Icarus* surpasses *EUHFORIA* by incorporating techniques such as AMR and grid stretching, which allow for targeted resolution increases in specific regions of the simulation domain. Section 4.2 describes the numerical setup, the background solar wind configuration, and the energetic particle composition. In this study, we generated a synthetic solar wind containing two CIRs, extending from 0.1 au to 2 au. Using *PARADISE*, we injected monoenergetic 1 MeV protons in the forward and reverse CIR shock regions, and tracked their intensities as the particles propagated through interplanetary space. Section 4.3 presents the simulation results, beginning with a validation of *Icarus-PARADISE* through comparison with the established *EUHFORIA-PARADISE* model in Section 4.3.1. To illustrate the effects of AMR, we present in Section 4.3.2 simulation results with varying levels of refinement applied to the *Icarus* solar wind, assessing the impact of increased resolution on particle intensity profiles at the shocks. The chapter concludes with a summary and discussion in Section 4.4.

4.2 Numerical setup

To simulate particle acceleration and transport with *PARADISE*, we generated a background solar wind configuration with *Icarus* and, for validation purposes only, with *EUHFORIA*. We used identical inner boundary conditions in both models, derived from a synthetic solar wind map, whose radial solar wind velocity component is shown as a contour plot in Fig. 4.2. The map is based on the work of Pizzo (1991) and features a band of slow solar wind embedded within a faster stream of solar wind. This configuration mimics a slow stream originating from a helmet streamer near the magnetic equator. The magnetic axis of the Sun is assumed to be tilted by 30° with respect to its rotation axis. The resulting solar wind map produces a global configuration containing two symmetrically arranged CIRs in the inner heliosphere. The left panel of Fig. 4.3 displays the radial solar wind velocity component in the ecliptic plane from 0.1 au to 2 au as simulated with *Icarus*. The corresponding *EUHFORIA* solution looks visually identical and omitted here for brevity.

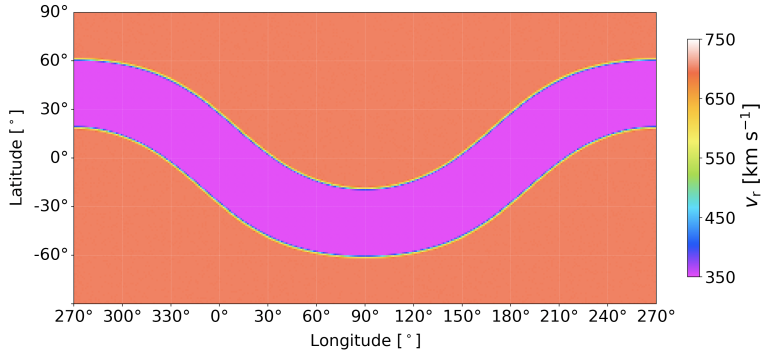

Figure 4.2. Contour plot (latitude versus longitude) of the radial solar wind velocity component at the inner boundary (0.1 au or 21.5 $R_\odot$) both for *Icarus* and *EUHFORIA*.

The injection region for the test particles was determined by computing the divergence of the solar wind velocity in both the *Icarus* and *EUHFORIA* wind. The right panel of Fig. 4.3, taken from the *Icarus* run, shows a contour plot of the velocity divergence in the ecliptic plane (colatitude $\theta = 90°$) from 0.1 au to 2 au. The two pairs of forward and reverse shock waves appear as blue spiral arms, indicating regions of negative velocity divergence. Given the idealised symmetry of the synthetic solar wind setup, we arbitrarily selected the CIR in the lower half-plane for particle injection. Within this region, we identified the areas of negative velocity divergence and injected monoenergetic 1 MeV protons

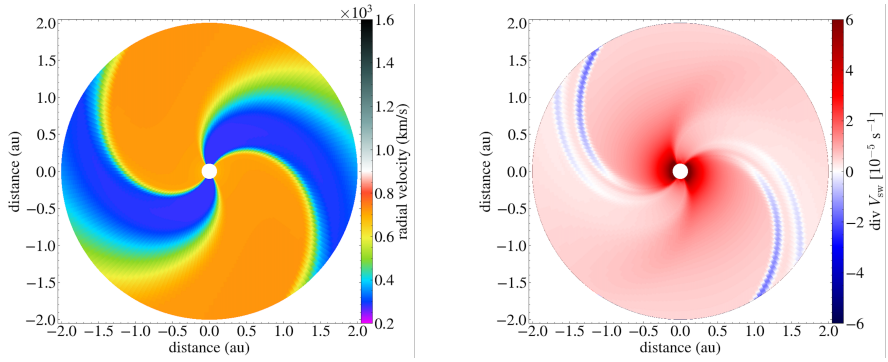

(a) Radial velocity component. **(b)** Velocity divergence.

Figure 4.3. Contour plots of key solar wind parameters in the ecliptic plane from 0.1 au to 2 au obtained from the *Icarus* simulation. Panel a) shows the radial component of the solar wind velocity, while panel b) displays the solar wind velocity divergence.

between 0.12 au and 2 au in the radial direction, and over a colatitudinal range of $\theta = 90° \pm 2°$. We note that an injection energy on the order of 1 MeV is significantly higher than the anticipated energies of seed particle populations at CIR shocks. This divergence stems from the primary objective of our current study, which is to validate our model and demonstrate the impact of AMR on acceleration efficiency within the model, rather than replicating a real CIR event. In this context, the 1 MeV protons may be interpreted as a pre-accelerated population originating from earlier shock encounters or impulsive SEP events.

The protons were injected according to the differential intensity distribution

$$j(r, E) = C\,\delta(E - 1\ \text{MeV})\,r^{-2}\,, \tag{4.1}$$

where j is the differential intensity, r the radial distance, E the particle energy, C a constant of proportionality ensuring correct physical units, and δ the Dirac delta distribution. Equation (4.1) was applied in regions where div $U_{\text{sw}} < 0$ (i.e. negative solar wind velocity divergence), and the intensity was related to the particle distribution function f and the particle momentum magnitude p via the relation $j = p^2 f$. In practice, this is accomplished within *PARADISE* by uniformly distributing 1 MeV protons across all regions satisfying div $\mathbf{U}_{\text{sw}} < 0$, thereby mapping the CIR shocks, and assigning each particle a statistical weight proportional to $1/r^2$. To trace the shock, we used a modified version of the shock tracer code from Wijsen et al. (2022) and Niemela et al. (2024). Furthermore, we assumed that j is independent of time. To achieve this, we first calculated the Green's function solution for the FTE, which emerges when all particles are

injected at time $t = 0$. Subsequently, we derived the steady-state solution for particle injection with no time dependence by convolving the Green's function solution with a time-independent function. This procedure was applied in all simulations presented in Section 4.3.

In *PARADISE*, we model both pitch angle diffusion and CFD. Spatial CFD has been proposed to explain various observational features, including SEP events detected at locations that are seemingly not magnetically connected to the particle source (e.g. Klassen et al. 2015), and is therefore commonly included in interplanetary particle transport simulations. In this study, we adopted a simplified approach by prescribing a constant perpendicular MFP length $\lambda_\perp = 3 \times 10^{-4}$ au (see Section 2.2). Combined with a constant parallel MFP length $\lambda_\parallel = 0.3$ au, this yields a ratio $\lambda_\perp/\lambda_\parallel = 10^{-3}$, indicating that particle propagation remained primarily aligned with the interplanetary magnetic field. Figure 4.4 shows the effect of CFD on the simulated particle intensity distributions in the radial-longitudinal plane at colatitude $\theta = 90°$, 48 hours after injection, for a selected energy channel. Panel a) displays the case without CFD, where particles remain confined near the forward and reverse shock regions, with precise spatial separation and peak intensities at the injection zones. In panel b), where CFD is included, the particle distributions are visibly more diffuse. While particle propagation remains largely field-aligned, particles can now move across the magnetic field lines, leading to a partial merging of the two intensity regions and reduced peak intensities near the shocks. For simplicity, guiding centre drift velocities were excluded from the *PARADISE* simulations by setting Eq. (2.25) in the FTE to **0**.

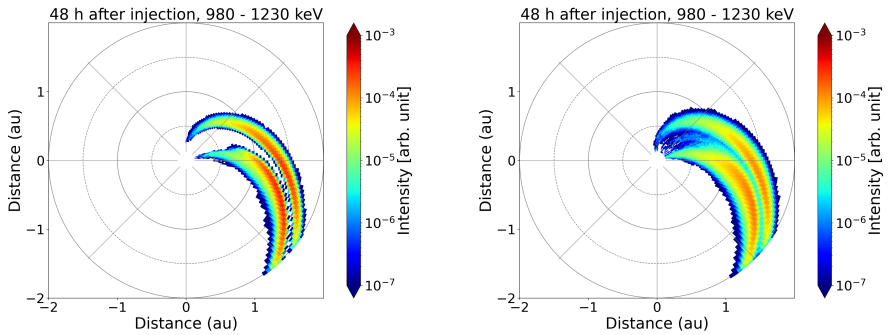

(a) Without CFD. **(b)** With CFD

Figure 4.4. Illustration of CFD effects on particle intensity distributions obtained with *PARADISE* from 0.12 au to 2 au in the ecliptic plane. Panel a) shows the particle intensities 48 h after particle injection in the energy channel 980–1230 keV without CFD. Panel b) displays the corresponding results with CFD included.

For the *Icarus* simulations using AMR, we mostly restricted the refinement to the CIR in the third quadrant in Fig. 4.3. Following the approach outlined in Wijsen et al. (2021) and Verbeke et al. (2022), we estimated the longitudinal position $\hat{\phi}$ of the CIR to be refined by

$$\hat{\phi} = \phi + \frac{r - r_{\text{in}}}{U} \Omega_{\text{r}} \,. \tag{4.2}$$

In Eq. (4.2), r and ϕ are the radial and longitudinal coordinates in the domain, respectively, U is a characteristic speed of the solar wind stream (here set to $U = 500$ km s^{-1}), and Ω_{r} is the solar synodic rotation rate ($\Omega_{\text{r}} \approx 2.67 \times 10^{-6}$ s^{-1}). To approximate the CIR spiral, Eq. (4.2) must satisfy the condition

$$\phi_{\text{lo}} < \hat{\phi} < \phi_{\text{up}} \,, \tag{4.3}$$

where ϕ_{lo} and ϕ_{up} specify the lower and upper longitudinal bounds of the refined region, respectively. While the default *Icarus* setup uses the solar sidereal rotation rate ($\approx 2.97 \times 10^{-6}$ s^{-1}), we replaced it by the solar synodic rotation rate used in *EUHFORIA* to minimise the discrepancies between the two models during validation.

MPI-AMRVAC offers a variety of numerical schemes suited for shock-related problems. For the present study, we used the second-order (in both time and space) Total Variation Diminishing Lax-Friedrichs (TVDLF) scheme for shock capturing (Tóth & Odstrčil, 1996), combined with the Woodward limiter (Woodward & Colella, 1984). While TVDLF is known for its robustness, it is also more diffusive than other solvers, such as the Harten-Lax-van-Leer (HLL) Riemann solver (Harten et al., 1983). A key difference between the numerical setups in *EUHFORIA* and *Icarus* lies in the treatment of the solenoidal condition $\nabla \cdot \mathbf{B} = 0$, where in *EUHFORIA*, the magnetic field is strictly divergence-free by construction. In contrast, *Icarus* allows for minor local deviations from this constraint. These are mitigated using the elliptic divergence cleaning method described in Section 2.1, following Teunissen & Keppens (2019).

In Section 4.3, we validated the *Icarus*-*PARADISE* model by reproducing results from the *EUHFORIA*-*PARADISE* model. To achieve this, we applied similar resolution settings and identical inner boundary conditions (Fig. 4.2) in *EUHFORIA* to generate a solar wind configuration matching that shown in Fig. 4.3a. For a quantitative comparison, Fig. 4.5 presents longitudinal profiles of the magnetic field (top panel), solar wind speed (middle panel), and solar wind particle number density (bottom panel) at 1 au and $\theta = 90°$, obtained from *Icarus* (solid blue) and *EUHFORIA* (dashed red). The profiles show overall good agreement, with only minor differences attributed to the entirely different numerical schemes used in both models. For both simulations, the domain spanned a radial range of 0.1 au to 2 au, a colatitudinal range of 30°–150°,

and a full 0°–360° coverage in longitude. The extension to 2 au accounted for the common assumption that CIR-related particle acceleration processes occur primarily beyond 1 au (Richardson, 2004, 2018). The grid consisted of 600 cells in radial direction (corresponding to a radial resolution of $\Delta r \approx 1.2\,R_\odot$), with 60 cells in colatitude and 180 cells in longitude, yielding an angular resolution of $\Delta\theta = \Delta\phi = 2°$.

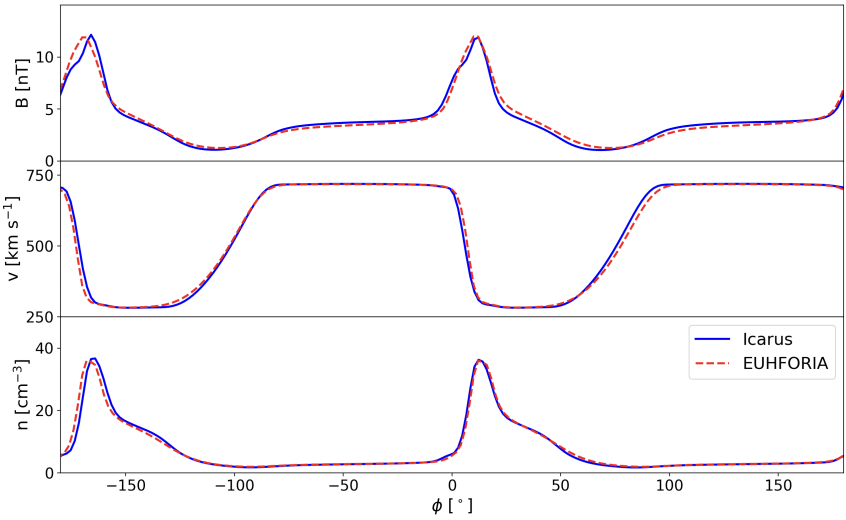

Figure 4.5. Comparison of solar wind parameters between *Icarus* and *EUHFORIA*. The plots show the magnetic field magnitude (top panel), the solar wind speed (middle panel), and the solar wind particle number density (bottom panel) as functions of longitude ϕ at a radial distance $r = 1$ au and colatitude $\theta = 90°$. *Icarus* results are shown as blue solid lines, and *EUHFORIA* results as red dashed lines.

For the study of the impact of using different AMR levels in *Icarus* in Section 4.3, we used the same *Icarus* wind configuration as in the validation case, but started with a lower base resolution to account for the subsequent refinements. At AMR level 1, corresponding to a uniform grid, the simulation domain was resolved with 300 cells in radial direction, 40 cells in colatitude, and 96 cells in longitude (excluding ghost cells). With each additional level of AMR, the number of cells in a block doubles locally within the refinement region, that is, where the AMR criterion is satisfied. At the highest refinement level applied (AMR level 5), we thus obtained an effective resolution of 4800 cells radially, 640 cells in colatitude, and 1536 cells in longitude. These numbers correspond to grid spacings of approximately 3.96×10^{-4} au $\approx 8.5 \times 10^{-2}\,R_\odot$ radially, about 0.19° in colatitude, and around 0.23° in longitude.

Finally, we address two modifications to the inner boundary conditions in the *Icarus* version used here, compared to the default implementation in *MPI-AMRVAC*. First, in initial simulations, we observed notable differences in the v_ϕ and B_ϕ components between *Icarus* and *EUHFORIA* near the inner boundary, primarily due to the use of different coordinate systems in the two wind models. As discussed in Sections 3.1.1 and 3.1.2, *Icarus* solves the ideal MHD equations in a corotating frame, while *EUHFORIA* operates in HEEQ coordinates. These differences led to larger discrepancies in the particle intensities computed with *PARADISE*. To mitigate this, we modified the boundary condition for v_ϕ in *Icarus* to match that of *EUHFORIA* by imposing

$$v_\phi = -r_{\mathrm{in}}\,\Omega_{\mathrm{r}}\,\sin(\theta)\,, \tag{4.4}$$

which yields $v_\phi \approx 0$ at the inner boundary r_{in} in the inertial frame.

The second modification concerned the adjustment of the longitudinal magnetic field component B_ϕ. Following Pomoell & Poedts (2018), we set

$$B_\phi = B_{\mathrm{r}}\frac{v_\phi}{v_{\mathrm{r}}}, \tag{4.5}$$

with the radial velocity and magnetic field components v_{r} and B_{r}, respectively. Equation (4.5) ensures that the electric field vanishes in the corotating frame, which is necessary to obtain a steady-state solution of the solar wind in the corotating frame, consistent with the implementation in *EUHFORIA*.

4.3 Simulation results

This section presents the simulation results obtained using the *Icarus-PARADISE* model with the numerical setup described in Section 4.2. We begin in Section 4.3.1 by validating *Icarus-PARADISE* through a comparison with results from *EUHFORIA-PARADISE*. Subsequently, in Section 4.3.2, we explore the impact of increasing levels of AMR in *Icarus* on particle acceleration and the resulting intensity distributions.

4.3.1 Validating the Icarus-PARADISE model

Figures 4.6 and 4.7 show the validation of the *Icarus-PARADISE* model by comparing longitudinal profiles of particle intensities at radial distances $r = 1$ au and $r = 1.5$ au, respectively. These intensities were computed by *PARADISE* using background solar wind conditions generated by both *EUHFORIA* and

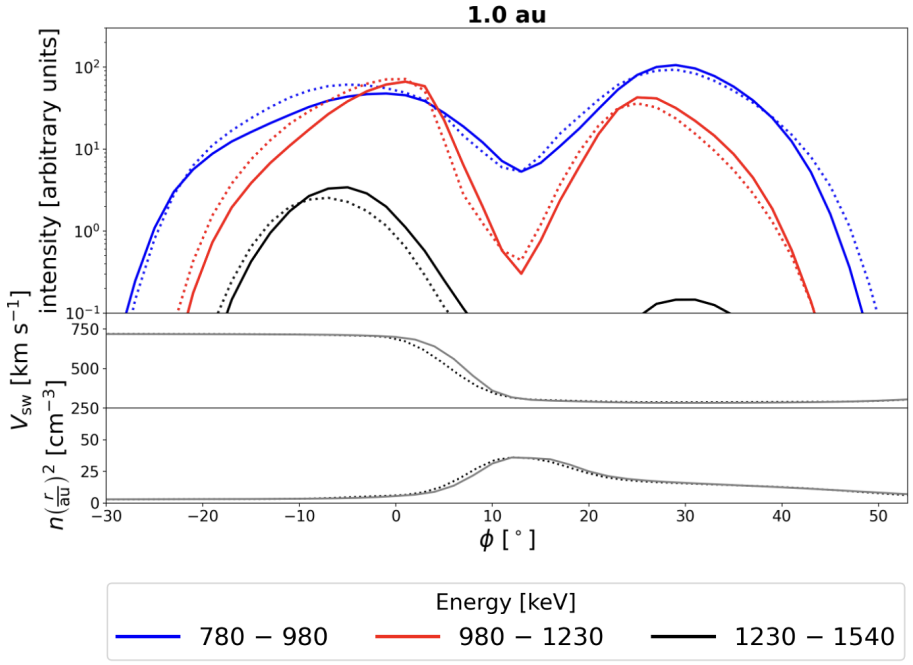

Figure 4.6. Longitudinal profiles of particle intensities and solar wind parameters at $r = 1$ au and $\theta = 90°$. The top panel shows particle intensities, with different colours corresponding to the energy channels listed in the legend below. The middle and bottom panels display the solar wind speed and solar wind particle number density, respectively. In all panels, solid lines indicate *EUHFORIA*-based results, while dotted lines refer to those obtained with the *Icarus* wind.

Icarus. Each figure follows the same layout, with the top panel displaying the particle intensity profiles in three selected channels (as indicated in the figure legend), and the middle and bottom panels presenting the corresponding solar wind speed and particle number density. In all panels, solid lines represent results based on *EUHFORIA*, and dashed lines indicate those derived from *Icarus*.

Starting with Fig. 4.6, which shows the results at 1 au, we observe that the protons undergo both adiabatic deceleration (visible in the channels below 1 MeV) and shock acceleration (visible in the channels above 1 MeV). The deceleration is predicted from theory (Parker, 1965; Ruffolo, 1995) and arises from the expansion of the solar wind, leading to energy loss due to the diverging flow field. At the shock waves, protons are likely accelerated via DSA. The figure also clearly reveals the characteristic double-peaked structure commonly

associated with CIRs and consistent with observations (Wijsen et al., 2021). The right-hand peak in Figure 4.6 results from acceleration at the forward shock of the CIR, while the left-hand peak is caused by acceleration at the reverse shock. The valley between the two peaks coincides with the stream interface of the CIR, where the transition between the compressed slow wind and the fast wind occurs.

Additionally, the results indicate that particle acceleration is more efficient at the reverse shock than at the forward shock. This is partly due to the fact that the reverse shock tends to adopt a quasi-parallel configuration, which is more favourable for DSA. Moreover, the reverse shock propagates sunward into the fast solar wind, resulting in a higher relative speed between the shock and the upstream plasma, and thus a stronger shock. In contrast, the forward shock propagates into the slower wind in the anti-sunward direction, resulting in a weaker shock. These findings are consistent with previous theoretical investigations (Giacalone & Jokipii, 1997; Wijsen et al., 2019a) as well as observational studies (Classen et al., 1998; Gómez-Herrero et al., 2009).

Figure 4.7, showing results at a radial distance of 1.5 au, reveals qualitatively similar features to those observed at 1 au in Fig. 4.6, including adiabatic deceleration, shock acceleration, and the characteristic two-peaked structure in the intensity profiles. Quantitatively, however, the intensity peaks are noticeably higher across both energy channels below and above 1 MeV at 1.5 au. This outcome is expected, as CIR-associated shocks typically intensify with increasing heliocentric distance, particularly beyond 1 au, due to stronger compression of the solar wind. Furthermore, the converging magnetic field lines and plasma within the CIR structure may create magnetic mirror-like configurations, temporarily trapping particles. This trapping increases particle residence times in the vicinity of the shocks, thereby enhancing DSA efficiency and resulting in higher particle intensities at higher energies. Simultaneously, adiabatic deceleration continues to act as particles propagate outward into the increasingly expanding solar wind and decreasing magnetic field, resulting in enhanced intensities in lower energy channels as well.

Comparing the *PARADISE* results across the two solar wind models, we find that the outputs are overall in reasonable agreement. In the two lowest energy channels, the two models exhibit the greatest similarity in both shape and trend. Depending on longitude, the *Icarus*-based intensities sometimes exceed those from the *EUHFORIA*-based simulation, and vice versa. These slight discrepancies can be attributed to the small differences in the solar wind configurations generated by the two wind models. Since the solar wind solutions are not identical due to the different numerical schemes underlying each code, variations in the resulting particle distributions are expected. As the particles propagate over substantial distances before reaching the observer, even minor

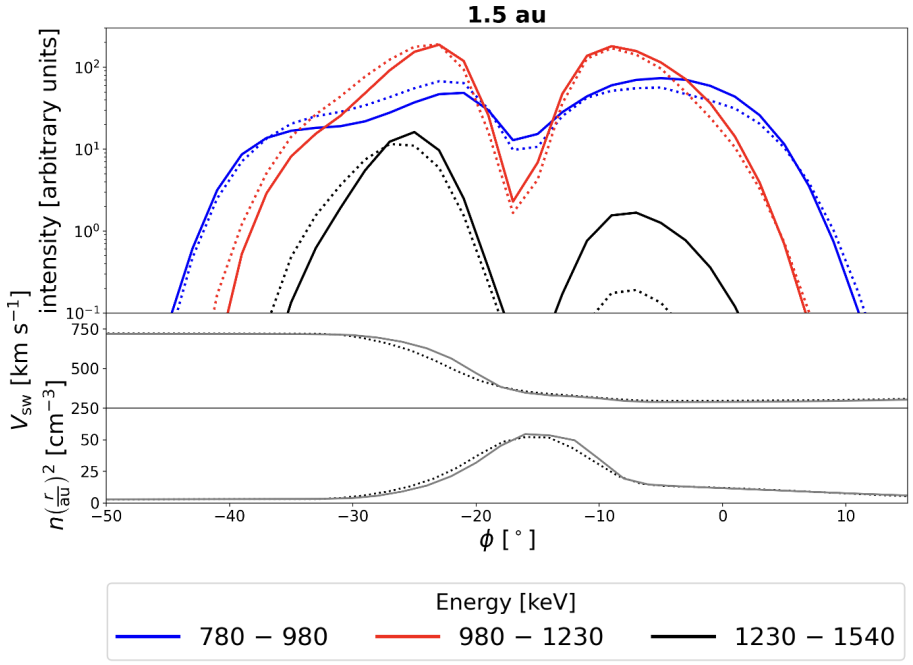

Figure 4.7. Longitudinal profiles of particle intensities and solar wind parameters at $r = 1.5$ au and $\theta = 90°$. The top panel shows particle intensities, with different colours corresponding to the energy channels listed in the legend below. The middle and bottom panels display the solar wind speed and solar wind particle number density, respectively. In all panels, solid lines indicate *EUHFORIA*-based results, while dotted lines refer to those obtained with the *Icarus* wind.

differences can accumulate and cumulatively impact a particle's properties. The largest discrepancy appears in the highest energy channel at the forward shock, where more particles are accelerated in the *EUHFORIA*-based wind. This can be attributed to the slightly greater amount of numerical diffusion in the *Icarus* simulation compared to *EUHFORIA*, resulting from the TVDLF scheme, which leads to smoother shocks and reduced particle acceleration efficiency. This effect is evident in the solar wind speed and particle number density profiles in the middle and bottom panels of Figs. 4.6 and 4.7, where *EUHFORIA* produces steeper gradients than *Icarus*.

In the following section, however, we demonstrate that applying AMR in *Icarus* significantly increases the resolution at the CIR shocks, allowing us to surpass the performance observed in Figs. 4.6 and 4.7 by *EUHFORIA*-*PARADISE*.

4.3.2 Application of AMR

While *EUHFORIA* and similar inner heliospheric solar wind models, such as *Enlil*, employ uniform equidistant grids, *MPI-AMRVAC* provides advanced techniques, including AMR and grid stretching. In this section, we focus on demonstrating the effects of AMR. To illustrate the impact of AMR application, we repeated the simulations from Section 4.3.1 using *Icarus-PARADISE*, now starting from the lower-resolution setup described in Section 4.2, and applying up to five levels of AMR. The results are presented in Fig. 4.8, where the panels show the intensities at a heliocentric distance of $r = 1.8$ au. The figure follows the same structure as Figs. 4.6 and 4.7, with the top panel displaying particle intensities, and the middle and bottom panels showing solar wind speed and particle number density, respectively. We note again that AMR level 1 corresponds to a uniform equidistant grid, and that each additional level of AMR halves a cell size in each direction locally within the refined region.

Similar to Figs. 4.6 and 4.7, we observe two intensity peaks corresponding to the forward and reverse shocks. From AMR levels 1 to 3 (panels a–c), the left intensity peak dominates, illustrating that near 2 au, particle acceleration is most efficient at the reverse shock. At higher AMR levels 4 and 5 (panels d and e), the right peak also becomes pronounced, with increasingly populated higher-energy channels.

A crucial aspect of simulations, including shock waves in 3D MHD models, is that shocks are represented much wider than in reality. Indeed, in ideal MHD, shocks are not resolved physically, but appear merely as discontinuities smoothed by numerical diffusion. However, since the ratio of the MFP length to the shock width plays a pivotal role in determining how efficiently particles can cross the shock for DSA to occur, simulations with higher shock resolution (as achieved here through finer AMR) enhance particle acceleration for the same MFP length (e.g. Wijsen et al. 2022).

To further highlight the impact of higher AMR levels on particle acceleration, Fig. 4.9 presents intensity-energy profiles at different radial distances, exemplarily sampled at the reverse shock. These intensity profiles represent the peak intensities within each energy channel. The four panels display the results at $r = 0.5$ au (panel a), $r = 1$ au (panel b), $r = 1.5$ au (panel c), and $r = 1.8$ au (panel d). We refrain from extracting values at the domain's outer edge (2 au) to avoid potential distortions from outer boundary effects. Across all panels, we consistently observe that particle intensities at higher energies increase with increasing AMR levels, further confirming that enhanced shock resolution improves particle acceleration efficiency.

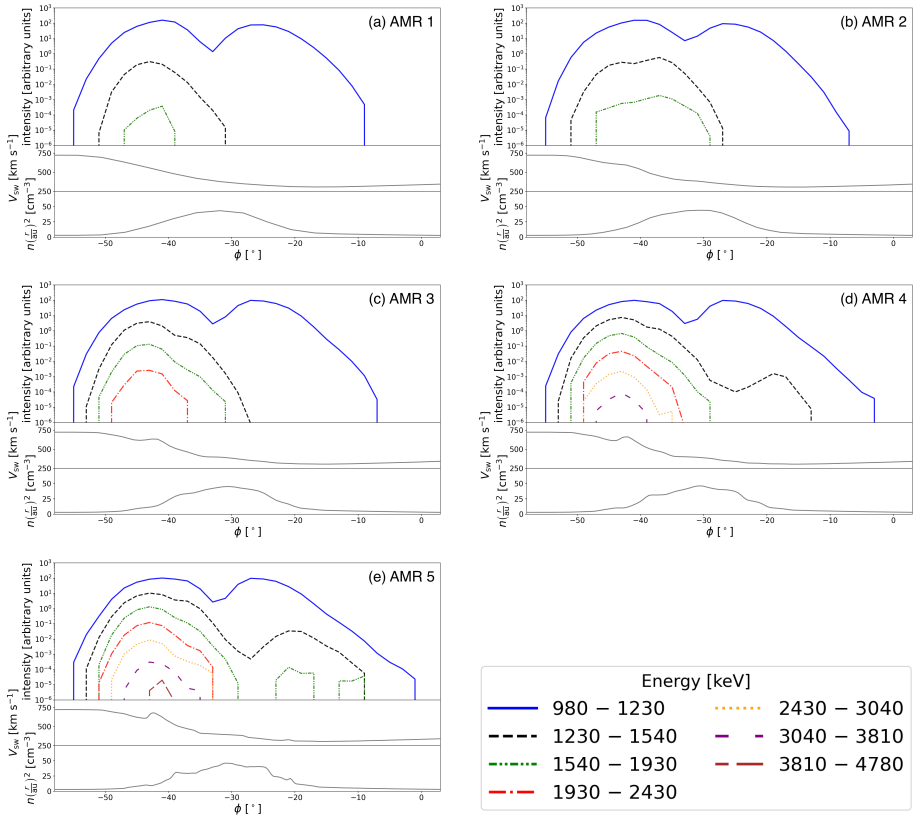

Figure 4.8. Longitudinal profiles of particle intensities and solar wind parameters observed at $r = 1.8$ au and $\theta = 90°$, illustrating the effects of AMR. Panels a) through e) correspond to AMR levels 1 through 5, respectively. In each panel, the top subpanel shows the particle intensities, while the middle and bottom subpanels display the solar wind speed and particle number density, respectively.

We note that with increasing resolution, the particle intensities and their energy spectra should converge to a stable solution, provided that the underlying solar wind configuration also converges to a stable solution. However, higher resolution in the MHD simulations additionally resolves smaller-scale solar wind structures. Because particle acceleration and transport are highly sensitive to such details, these fine-scale features can significantly influence the energetic particle population, especially at larger distances where effects accumulate over longer propagation paths. Figure 4.10 illustrates this point by showing two cutouts of the radial solar wind velocity component contour plots, similar to panel a) of Fig. 4.3, using the same colour bar (not shown here). Here, panel

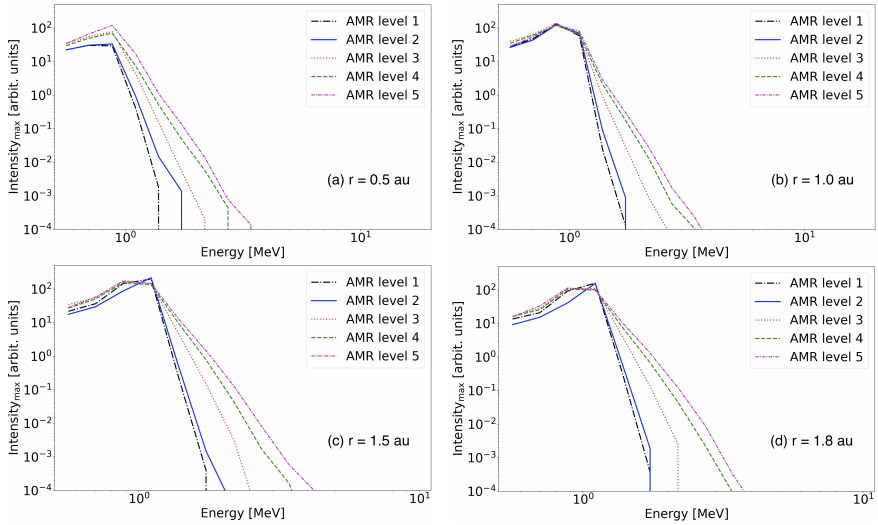

Figure 4.9. Intensity-energy plots illustrating the effects of AMR. The four panels show the peak particle intensities across energy channels at the reverse shock, sampled at $r = 0.5$ au (panel a), $r = 1$ au (panel b), $r = 1.5$ au (panel c), and $r = 1.8$ au (panel d).

a) of Fig. 4.10 corresponds to the simulation with AMR level 1, and panel b) to the simulation with AMR level 5. In the former panel, the high-speed stream lacks substructure due to the coarse resolution, showing only large-scale features. In contrast, the higher-resolution case in panel b) reveals small-scale features at the outer edge of the high-speed stream, which may be indicative of Kelvin-Helmholtz (KH) instability-like patterns. Such features have been previously observed in the solar wind and linked to KH instability processes at shear interfaces between the slow and fast solar wind in the corona and inner heliosphere (Kieokaew et al., 2021; Mostafavi et al., 2022; Telloni et al., 2022). These structural differences may account for the lack of full convergence in the intensity-energy profiles in Fig. 4.9. However, the differences between consecutive levels of AMR appear to decrease progressively.

4.4 Summary and discussion

Energetic particles in the heliosphere pose increasing risks to spacecraft and astronauts, necessitating reliable and efficient modelling tools. To overcome the limitations of the *EUHFORIA-PARADISE* model, particularly concerning

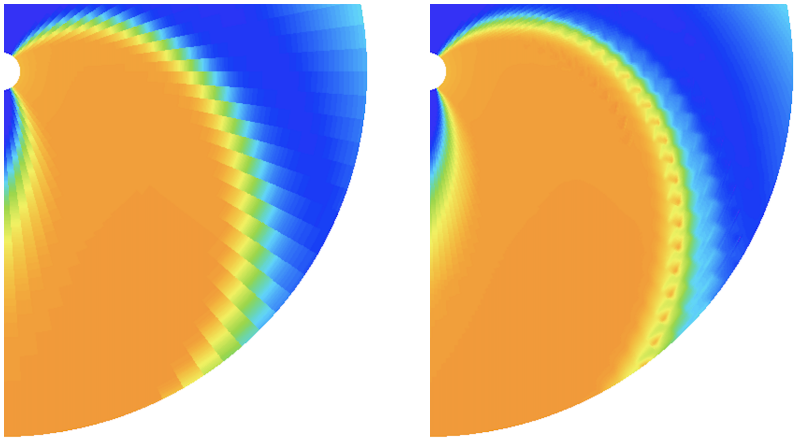

(a) AMR level 1. **(b)** AMR level 5.

Figure 4.10. Cutouts of contour plots showing the radial component of the solar wind velocity. Panel a) displays the high-speed stream refined at AMR level 1, panel b) at AMR level 5.

shock resolution on the equidistant *EUHFORIA*-grid, we introduced the *Icarus*-*PARADISE* model. It combines the *MPI-AMRVAC*-based *Icarus* solar wind model, including AMR, with the transport code *PARADISE*.

In this first application of *Icarus*-*PARADISE*, we conducted a theoretical study of particle acceleration and transport at CIR shocks. For this, we generated a synthetic solar wind configuration up to 2 au, containing two high-speed streams in which CIRs formed. Model validation was performed by reproducing results from the earlier *EUHFORIA*-*PARADISE* setup. Longitudinal intensity profiles at two radial distances showed overall good agreement, especially in the lower-energy channels. Discrepancies at higher energies were attributed to the different shock-capturing schemes. *Icarus* used the more diffusive TVDLF scheme, while *EUHFORIA* employed an approximate Riemann solver with a sharper shock capturing capability (see Section 3.1.1 for details). Less diffusive alternatives in the *MPI-AMRVAC* framework, such as the HLL or some Roe-type approximate Riemann solvers (Keppens et al., 2023), may improve shock resolution and will be explored in future work.

A significant advantage of *Icarus* over *EUHFORIA* is its support for advanced techniques such as AMR and grid stretching. In this work, we focused on AMR, demonstrating its impact by repeating the validation runs starting from a coarse grid (AMR level 1) and refining only the regions around the shock up to level 5. We presented longitudinal intensity profiles near 2 au and constructed

intensity-energy plots at the reverse shock across four radial distances. Both visualisations consistently showed that higher AMR levels led to more efficient particle acceleration. This result holds significant implications for models that simulate particle acceleration at shock waves generated by MHD models, see, for instance, Wijsen et al. (2022) using *EUHFORIA*-*PARADISE* to study proton acceleration in the inner heliosphere, or Young et al. (2021) using *EPREM* and the CORona-HELiosphere (*CORHEL*) model to investigate proton acceleration in the corona.

With the introduction of *Icarus*-*PARADISE*, numerous future applications become feasible. These include studies of real SEP events involving CIRs or CMEs, building on prior work with *EUHFORIA*-*PARADISE* (Wijsen et al., 2021, 2023). Future investigations may explore the impact of grid stretching (isolated or combined with AMR) on particle acceleration and transport. Notably, Baratashvili et al. (2022) demonstrated that combining grid stretching with AMR can significantly speed up the MHD component of the simulation chain. Furthermore, *Icarus* has been recently updated to include time-dependent inner boundary conditions (Baratashvili et al., 2025). Since the Sun is a dynamic star, whose variability on the surface and in the corona translates into continuously changing conditions in interplanetary space, future work can assess how temporal variations in the solar wind and CIRs influence the distribution, acceleration, and transport of SEPs. Additionally, substantial updates to *PARADISE* are planned, particularly in data handling. Currently, *PARADISE* loads full solar wind snapshots, potentially importing unused data, which a more selective domain-loading approach could replace. This and other enhancements are designed to accelerate simulations inside *PARADISE*, enable the use of higher levels of AMR, and augment the already significant acceleration of simulation time achieved by *Icarus*.

5

Modelling energetic particle dynamics in the solar corona

Most of this chapter was published in "Cross-field Diffusion Effects on Particle Transport in a Solar Coronal Flux Rope", 2024a, Astrophys. J. Lett., 976, L31 (Husidic et al., 2024b), and parts of the text and figures have been reproduced here directly. E. Husidic implemented the necessary modifications in the particle transport code PARADISE to work with COCONUT, including the development of a particle tracer and algorithms for numerically calculating derivatives on an unstructured grid, and a code to interpolate the unstructured COCONUT grid onto a EUHFORIA-like grid, as detailed in Section. 3.3. The COCONUT MHD simulation data were provided by Luis Linan. E. Husidic performed all remaining simulations, generated and processed the data, created the figures, and drafted the complete original manuscript.

Abstract. This chapter[1] presents the *COCONUT-PARADISE* model and its initial application to simulate particle transport in the solar corona in the presence of a CME flux rope. While the original *EUHFORIA-PARADISE* model and its upgrade, *Icarus-PARADISE*, simulate particle acceleration and transport in the inner heliosphere starting at a heliocentric distance $r = 0.1$ au, important physical processes occurring below this height are ignored, including CME evolution, shock formation, or SEP acceleration. To address this limitation and extend the simulation domain to $r < 0.1$ au, we introduce the *COCONUT-PARADISE* framework. In this study we generated a coronal background configuration using *COCONUT* containing a CME, modelled as an analytical TD flux rope. Energetic protons were injected into the flux rope, and their transport was simulated by solving the FTE with and without the CFD coefficient. In the absence of CFD, particles remained fully confined to the flux rope, as the CME

[1]This chapter is based on SI units.

expanded outwards. For simulations including CFD, we tested two commonly used phenomenological approaches regarding the perpendicular MFP length $\lambda_\perp$: a constant $\lambda_\perp$ and a Larmor radius-dependent $\lambda_\perp$. The results illustrated under which conditions particles remain confined to the CME flux rope and those under which they are able to escape. Moreover, they showed that even relatively small perpendicular MFPs, as typically used in heliospheric transport simulations, can lead to significant perpendicular diffusion. Finally, we discuss the relevance of this new modelling approach for future investigations on particle acceleration and transport in a unified domain encompassing both the corona and inner heliosphere.

5.1 Background and motivation

SEPs, accelerated at solar flare sites or at the fronts of shock waves driven by fast CMEs (Desai & Giacalone, 2016; Reames, 2021), are a key focus of space weather research due to their threats to spacecraft and astronauts (Vainio et al., 2009; Gopalswamy, 2018). While gradual SEP events are typically associated with continuous acceleration at CME-driven shock fronts as they propagate through interplanetary space, important processes such as CME evolution (Wang et al., 2014), shock formation (Mann et al., 2003), and particle acceleration (Reames, 1999; Desai & Giacalone, 2016) often begin already deep in the corona. Consequently, it is essential to consider particle acceleration and transport within the coronal domain when modelling SEP events.

In-situ measurements by PSP (Fox et al., 2016) within the solar corona have opened new opportunities to examine the interaction between MFRs and SEPs. In this context, the massive SEP event of 5 September 2022, when PSP was at a radial distance of about 15 $R_\odot$, has attracted considerable interest (e.g. Paouris et al. 2023; Trotta et al. 2024). By examining energetic proton populations, Cohen et al. (2024) found that PSP recorded a significant intensity drop at the shock, followed by a rapid increase in intensity by multiple orders of magnitude, as PSP crossed the CME flank and entered a region of closed magnetic field lines, identified as a magnetic cloud. The authors also highlighted the confinement of protons within the cloud and occasional anisotropies observed in the proton distribution inside the cloud.

In another study, using data from PSP orbit 5 in 2020 at radial distances from 0.45 au down to 0.2 au, Pecora et al. (2021) showed that flux ropes can act as boundaries, separating trapped particle populations within the flux rope from those moving outside of it. Schwadron et al. (2024b) reached similar conclusions when they investigated PSP observations from March 2022 at a radial distance

of 0.2 au, when PSP passed through the flank of a CME. They found energetic particle populations trapped within flux tubes, with the edges of the flux tubes acting as barriers to other particles.

So-called Forbush Decreases (FD; Cane 2000; Belov 2009) further support the view that MFRs can act as barriers for energetic particles. Observations of galactic CR fluxes often show sudden two-step decreases that are attributed, among other causes, to passing CMEs. The first step in the decay of galactic CR fluxes is associated with the CME-driven shock and the turbulent sheath between the shock and the driver. The second, faster step is then caused by isolated MFRs blocking the particles. Recently, Benella et al. (2020) and Laitinen & Dalla (2021) performed full-orbit particle simulations and showed that isolated flux ropes significantly hinder galactic CRs from penetrating the CME, while the CRs could enter the CME via the x-point.

Besides the recent PSP observations, type IV radio bursts are another indicator for energetic particles trapped within flux ropes (Morosan et al., 2019). Among the proposed explanations for these phenomena is cyclotron emission by electrons trapped inside CME loops (Bastian, 2007), which is discussed in detail in Chapter 6.

Over the last two decades, considerable efforts have been made to develop and improve different simulation tools for modelling SEP transport in the corona. As with heliospheric models, these tools typically combine MHD models of the coronal plasma with energetic particle transport codes. A prominent example is *EPREM* (Kozarev et al., 2010) that utilises input from *CORHEL* (Young et al., 2021), both integrated into the Solar particle event Threat Assessment Tool (*STAT*) software suite. More recently, *EPREM* has also been used in combination with the Magnetohydrodynamic Algorithm outside a Sphere (*MAS*) model to study particle acceleration in quasi-separatrix layers, which are regions in the corona where magnetic field lines rapidly diverge, enabling the formation of current sheets and MR (Schwadron et al., 2024a). Another recent model is the Multiple-Field-Line-Advection Model for Particle Acceleration (*M-FLAMPA*; Borovikov et al. 2018) that takes input from the Alfvén Wave-driven Solar atmosphere Model (*AWSoM*; Sokolov et al. 2021) to simulate particle acceleration and transport in the corona. Lastly, the improved Particle Acceleration and Transport in the Heliosphere (*iPATH*) framework (Hu et al., 2017; Ding et al., 2024) uses MHD simulations of CME-driven shocks, for instance computed with the MHD code *ZEUS* (Hayes et al., 2006), to model SEP events upstream of these shock waves.

Building on the motivation to extend SEP modelling into the corona, we introduce the *COCONUT-PARADISE* model as an extension of the heliosphere-focused frameworks *EUHFORIA-PARADISE* and *Icarus-PARADISE*. As a first

application, we present a theoretical study of particle transport in the corona in the presence of a CME. Using *COCONUT*, we first generated a coronal background configuration spanning from 1 $R_\odot$ to 21.5 $R_\odot$ (≈ 0.1 au), which included a CME modelled as an unstable modified TD flux rope (Titov & Démoulin, 1999; Titov et al., 2014). We then utilised *PARADISE* to inject monoenergetic 100 keV protons near one of the footpoints of the MFR, close to its central axis, and simulated their propagation through the evolving *COCONUT* snapshots. To examine the impact of CFD on particle transport in the corona, we performed three types of simulations. First, we simulated particle transport by solving the FTE without the CFD coefficient. We then conducted simulations using two different approaches to modelling CFD, and explored various parameter settings. In one case, the perpendicular MFP for CFD was set to a constant value, while in the other, it was defined as a function of the proton's Larmor radius (see Section 2.2 for details).

The remaining part of the chapter is structured as follows. Section 5.2 describes the numerical setup. The simulation results are presented and discussed in Section 5.3, starting with the case without CFD in Section 5.3.1, followed by simulations using a constant perpendicular MFP in Section 5.3.2, and a Larmor radius-dependent perpendicular MFP in Section 5.3.3. Supplementary modelling details are provided in Section 5.4, including a discussion on the two CFD approaches in Section 5.4.1, the interpolation from the unstructured *COCONUT* grid onto a structured grid in Section 5.4.2, and a note on numerical diffusion in the *COCONUT*-*PARADISE* model in Section 5.4.3. The chapter concludes with a summary in Section 5.5.

5.2 Numerical setup

This section outlines the configuration of *COCONUT* and *PARADISE* to simulate particle transport in the corona in the presence of a CME. The *COCONUT* setup closely follows the approach of Linan et al. (2023) to generate the required background corona configurations. The corona is reconstructed from an HMI magnetogram from 2nd July 2019 (during solar minimum), which provides the inner boundary conditions for the MHD simulation (see Section 3.1.3).

A CME was introduced at $t = 0$ using the modified analytical circular TD flux rope model (Titov & Démoulin, 1999; Titov et al., 2014). We adopted the $\zeta = 12$ case from Linan et al. (2023) in this study (see Section 3.1.3 and Eq. 3.1). The MFR had an initial magnetic field strength of $B_{\mathrm{TD},0} = 10.5\,\mathrm{G}$ (or $10.5 \times 10^5\,\mathrm{nT}$), resulting in an initial eruption speed of $v_{\mathrm{TD},0} = 827\,\mathrm{km/s}$. It

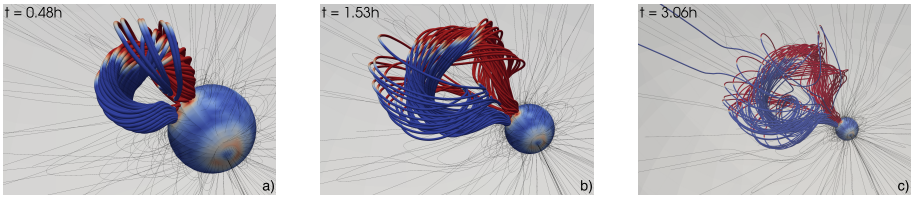

Figure 5.1. Visualisation of the flux rope CME modelled with *COCONUT*. The three panels show the evolved flux rope at different times: $t = 0.48\,\mathrm{h}$ (panel a), $t = 1.53\,\mathrm{h}$ (panel b), and $t = 3.06\,\mathrm{h}$ (panel c). The sphere of radius $1\,R_\odot$ represents the Sun, with the mapped radial magnetic field component on its surface. The sphere and MFR are colour-coded by magnetic polarity: red indicates positive polarity, blue indicates negative polarity, and white corresponds to zero values. Black lines illustrate a sample of the global magnetic field.

was placed at colatitude $\theta = 90°$ and Carrington longitude $\phi = 180°$, while the centre of the toroidal axis was located at a height of $0.15\,R_\odot$ above the solar surface. The major and minor radii were $0.3\,R_\odot$ and $0.1\,R_\odot$, respectively.

The *COCONUT* domain comprised approximately 2 million prism-shaped cells arranged in concentric shells that increased in size with radial distance (see Section 5.4.2 and Brchnelova et al. 2022 for details). Simulation outputs were produced every 289 s ($\approx 5\,\mathrm{min}$). For the transport simulations in Section 5.3, we used the first $\sim 7\,\mathrm{h}$ of the COCONUT run, which covered the propagation of the MFR up to the outer boundary at $21.5\,R_\odot$. To minimise possible outer boundary effects, the coronal simulation extended to $25\,R_\odot$, as recommended by Brchnelova et al. (2022).

Figure 5.1 shows the evolution of the MFR at three time steps: $t = 0.48\,\mathrm{h}$ (panel a), 1.53 h (panel b), and 3.06 h (panel c). The sphere of radius $1\,R_\odot$ represents the Sun. Instead of showing numerical values, we visualise the magnetic polarity of the radial magnetic field component B_r via shading: red indicates positive polarity ($B_\mathrm{r} > 0$), blue indicates negative polarity ($B_\mathrm{r} < 0$), and white corresponds to regions where $B_\mathrm{r} = 0$. The black field lines trace a sample of the global magnetic field. The panels illustrate the dynamic evolution of the MFR as the CME propagates through the solar corona. Panel a) highlights the highly twisted magnetic field configuration at an early stage of the CME evolution, with field lines spiralling tightly around the central axis of the MFR. This twist creates a complex magnetic topology, characterised by variations in both magnetic field strength and curvature. Panels b) and c) show the continued expansion of the flux rope as it propagates radially outward, introducing time-dependent variations in the magnetic field's magnitude and geometry. Moreover, as the MFR expands, MR occurs both at the footpoints

and the apex of the CME, altering the magnetic topology.

For all subsequent transport simulations with *PARADISE* in Section 5.3, we used a constant parallel MFP $\lambda_{\parallel} = 21.5\,R_{\odot}$ (0.1 au), corresponding to the radius of the simulation domain[2]. For the simulations that accounted for CFD, we employed two approaches to describe the CFD tensor (see Section 2.2 for details). In Section 5.3.2, we first assumed a constant perpendicular MFP $\lambda_{\perp}$ in Eq. (2.29), following a similar approach as Wijsen et al. (2021) and Husidic et al. (2024a). Then in Section 5.3.3, we applied a model by Dröge et al. (2010), which also had been employed in other studies (e.g. Wijsen et al. 2019b; Niemela et al. 2024). In this model, $\lambda_{\perp}$ is a function of the particle's Larmor radius r_{L} (Eq. 2.31) and is given by the expression in Eq. (2.32). The form of $\lambda_{\perp}$ contains also a reference Larmor radius r_{L0} and a dimensionless scaling parameter χ. In this study, we assumed r_{L0} for a 1 MeV proton in a magnetic field of strength $B_0 = 30\,\mathrm{nT}$, corresponding to a typical field strength value at the outer boundary. For comparison, B at the inner boundary point was approximately $5 \times 10^4\,\mathrm{nT}$. This way, only the parameter χ was varied to determine the effect of different levels of CFD on the particle distributions.

In all simulations, particles were uniformly injected within the radial range of $1.49\,R_{\odot}$ to $1.50\,R_{\odot}$, specifically in regions where the magnetic field strength exceeded 9×10^4 nT, and the magnetic polarity was inward. This effectively placed the initial particle distribution near the central axis of the flank of the flux rope with negative polarity, close to the inner boundary of the simulation. We injected an isotropic (in pitch angle) monoenergetic distribution of 100 keV protons, with all particles introduced at $t = 0.46$ h into the simulation (where $t = 0$ corresponds to the flux rope insertion). By this time, the apex of the erupting flux rope had reached a heliocentric distance of approximately $3\,R_{\odot}$. Since the FTE is solved in a stochastic manner, we injected a total of 3.6 million pseudo-particles to guarantee adequate statistics. Absorbing boundary conditions were used at both the inner and outer boundaries of the *PARADISE* simulation domain.

5.3 Simulation results

In this section, we present and analyse the simulation results, starting with the case that excludes CFD.

[2]When the CME apex reached $21.5\,R_{\odot}$, some twisted field lines of the flux rope could reach lengths up to $10 \times \lambda_{\parallel}$.

5.3.1 Simulations without CFD

Figure 5.2 shows a time-lapse of the results of a particle transport simulation without CFD (i.e. $\lambda_\perp = 0$). The four panels display 3D plots of the evolving MFR together with contours of the particle intensity at four different times: 0.48 h, 1.53 h, 3.06 h, and 4.5 h, shown in panels a) through d), respectively. Panel a) shows that after their injection at the base of the MFR flank, the particles have propagated upwards along the interior field lines of the MFR, which follow the arc-shaped axis of the MFR, and remain confined to these field lines. In panel b), the particles reach the opposite footpoint of the MFR. Some are magnetically reflected and return towards the original flank, while others fall back to the Sun and are removed from the simulation. In panel c), roughly 2.5 h after their injection, some particles at the base of the MFR gain access to its exterior magnetic field lines, which wrap around the interior ones, and begin propagating along them. In panel d), particles continue to propagate both along the interior and exterior MFR field lines.

This behaviour likely results from MR between interior and exterior MFR field lines near its footpoints and is influenced by numerical diffusion. Any ideal MHD simulation will include numerical diffusion and thus induce artificial MR. However, the reconnection in this case occurs in regions where real MR is physically expected. The highest particle intensities remain concentrated along the central axis of the flux rope throughout the simulation. Furthermore, open magnetic field lines are visible in panels c) and d); however, without the CFD mechanism, the protons with an initial energy of 100 keV do not gain access to those or the global magnetic field lines in our simulation and stay confined to the MFR. Nonetheless, MR between the MFR field lines and the global magnetic field is also present, suggesting that particle escape into the global field may eventually occur.

5.3.2 CFD with a constant perpendicular MFP length

Figure 5.3 shows particle transport simulations that include CFD using a constant perpendicular MFP length $\lambda_\perp$. The layout of the figure is organised such that the three columns represent increasing simulation times, from left to right: 1.53 h, 3.06 h, and 4.5 h. The three rows correspond to decreasing values of $\lambda_\perp$, from top to bottom: $2.15 \times 10^{-2}\,R_\odot$, $1.075 \times 10^{-2}\,R_\odot$, and $2.15 \times 10^{-3}\,R_\odot$.

In the top row, where $\lambda_\perp = 2.15 \times 10^{-2}\,R_\odot$ (or 10^{-4} au), we used a value commonly employed in heliospheric simulations (e.g. Wijsen et al. 2019b; Husidic

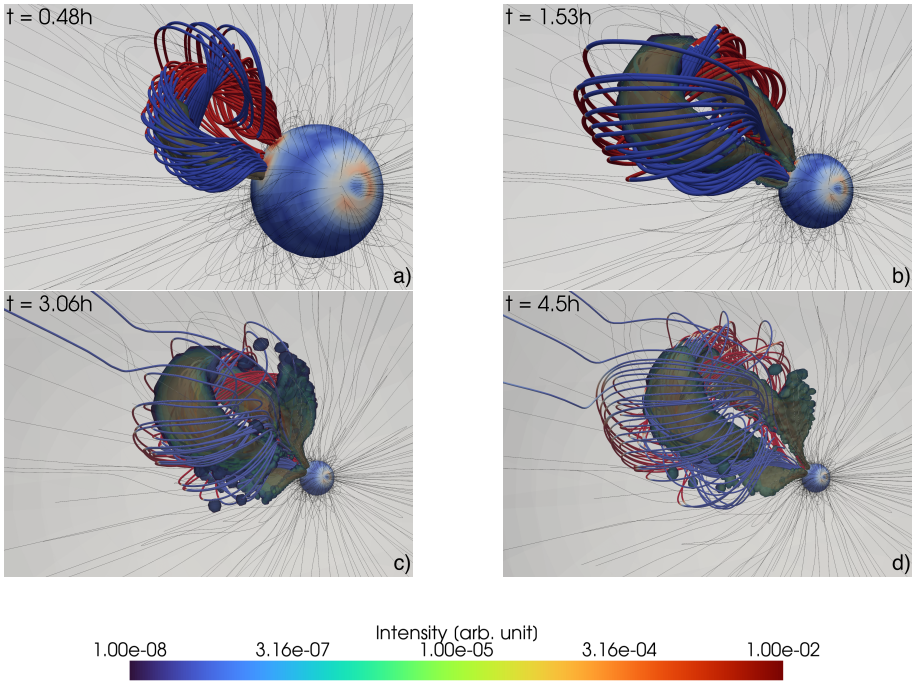

Figure 5.2. Time-lapse of particle propagation in the flux rope without CFD. Panels a) through d) show particle intensity contours at $t = 0.48$ h, 1.53 h, 3.06 h, and 4.5 h, respectively, plotted together with the MFR. The sphere of 1 $R_\odot$ with the mapped radial magnetic field component symbolises the Sun.

et al. 2024a). Despite the small ratio $\lambda_\perp/\lambda_\parallel = 10^{-3}$, we see that CFD has a significant effect on particle transport. Comparing panel a) of Fig. 5.3 to panel a) of Fig. 5.2 (no CFD), we see that particles not only diffuse along the exterior field lines of the MFR, but also escape the CME region, primarily in the propagation direction of the CME. Panels b) and c) show that this effect is more pronounced at later steps, indicating that particles also diffuse longitudinally. Once particles access open field lines ahead of the CME, they can easily escape the computational domain through parallel transport aided by magnetic focusing.

In the middle row, with $\lambda_\perp = 1.075 \times 10^{-2}\, R_\odot$ and $\lambda_\perp/\lambda_\parallel = 5 \times 10^{-4}$, we observe considerably less CFD. In panel d), particles already access the exterior field lines of the MFR but remain largely confined to it, with some particles escaping the CME site along its propagation direction. This behaviour aligns

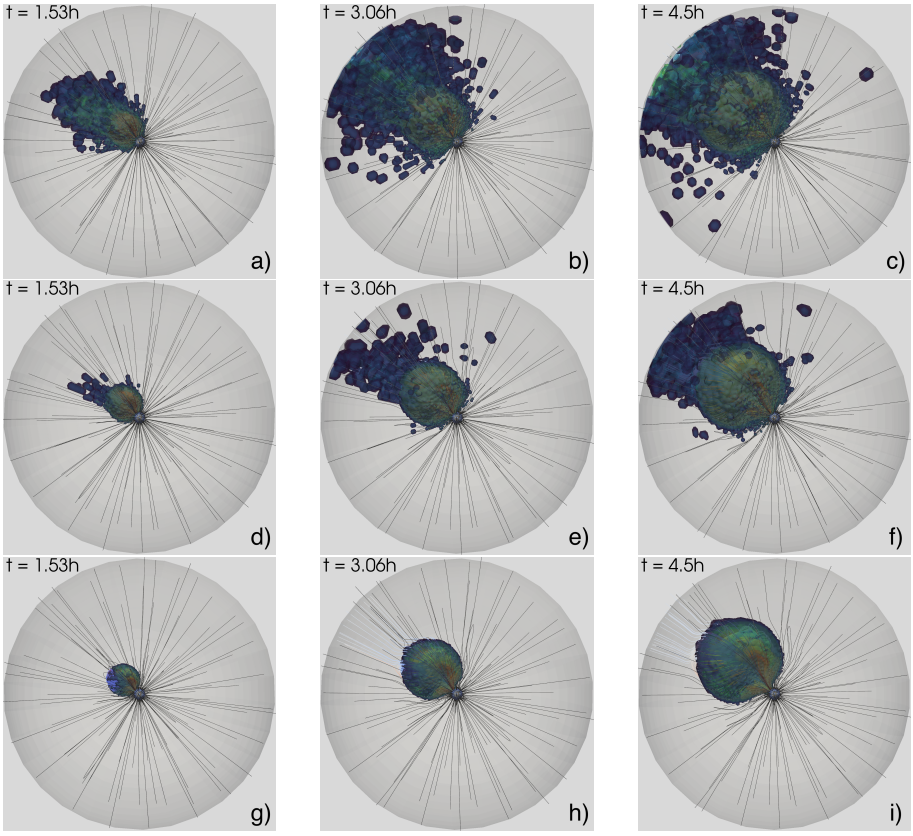

Figure 5.3. Time-lapse of particle propagation in a MFR using the CFD approach with a constant $\lambda_\perp$. Panels a) through c) in the top row show the results for $\lambda_\perp = 2.15 \times 10^{-2}\, R_\odot$; panels d) through f) in the middle row correspond to $\lambda_\perp = 1.075 \times 10^{-2}\, R_\odot$; and panels g) through i) in the bottom row show results for $\lambda_\perp = 2.15 \times 10^{-3}\, R_\odot$. The three columns represent simulation times of 1.53 h, 3.06 h, and 4.5 h, respectively. The colour bar for the particle intensities from Fig. 5.2 also applies here.

with our expectations, as the propagation direction is where significant MR and, thus, the opening of flux rope field lines is anticipated. In panels e) and f), more particles escape the MFR, and compared to the case in the top row, the longitudinal spread of the particles is significantly reduced.

Finally, in the last row of Fig. 5.3, where $\lambda_\perp = 2.15 \times 10^{-3}\, R_\odot \approx 1500$ km and $\lambda_\perp / \lambda_\parallel = 10^{-5}$, as expected, the least amount of CFD is observed. Across all three panels, particles wrap around the CME but remain primarily confined to it. However, in Fig. 5.5 in Sec. 5.3.3 it is shown that even in this case,

some particles manage to escape the flux rope along the opening magnetic field lines at the apex of the flux rope. In general, the results indicate that varying $\lambda_\perp$ within one order already drastically changes the effect of CFD on particle transport.

5.3.3 CFD with a Larmor radius-dependent perpendicular MFP length

Finally, we present simulation results in which CFD was implemented in the FTE using $\lambda_\perp = \lambda_\perp(\chi, \lambda_\parallel, r_\mathrm{L})$ which in particular depends on the r_L of the particle, since $\lambda_\parallel$ is kept constant. Different χ-values were prescribed (see Sec. 2.2 and Eq. 2.32). The columns in Fig. 5.4 are arranged similarly to those in Fig. 5.3, but here, the top, middle, and bottom rows display results using $\chi = 10$, $\chi = 5$, and $\chi = 1$, respectively. Because $\lambda_\perp$ is inversely proportional to the magnetic field strength, $\lambda_\perp$ became very large in our simulations (about one order of magnitude larger than $\lambda_\parallel$) in regions containing a current sheet, where the magnetic field strength was very small. For this reason, we limited $\lambda_\perp$ to a maximum value of $\lambda_\parallel$. That is, within the central regions of the current sheets, we prescribed an isotropic spatial diffusion coefficient.

In the top row, where $\chi = 10$, we observe the strongest CFD effects, even stronger than in the case of a constant $\lambda_\perp = 2.15 \times 10^{-2}\, R_\odot$ in the top row of Fig. 5.3. Already in panel a) of Fig. 5.4, particles stream away from the CME in all directions, while in panels b) and c), the half-plane containing the flux rope is nearly filled with the test particles. Furthermore, panels b) and c) show that particles move increasingly into the opposite half-circle.

Decreasing χ to a value of 5, as shown in the panels of the middle row, results in a significant reduction of CFD compared to the prior case, but still exhibits widespread test particles. In panel d), particles already tend to move away from the MFR in all directions, while in panels e) and f), the test particles further fill out the half-circle into which the CME is propagating.

Reducing χ further to 1, as illustrated in the bottom row, the least amount of CFD is observed among the three presented cases. In panels g) and h), particles are still mainly confined to the CME along the interior and exterior magnetic field lines. Panel i) is comparable to the case of constant $\lambda_\perp = 2.15 \times 10^{-3}\, R_\odot$ in Fig. 5.3, showing that particles still do not spread as widely as in the previous cases but receive access to the open field lines at the flux rope apex.

To quantify the number of particles that escaped the CME in the simulations with CFD, we integrated the intensities at the outer boundary of the simulation

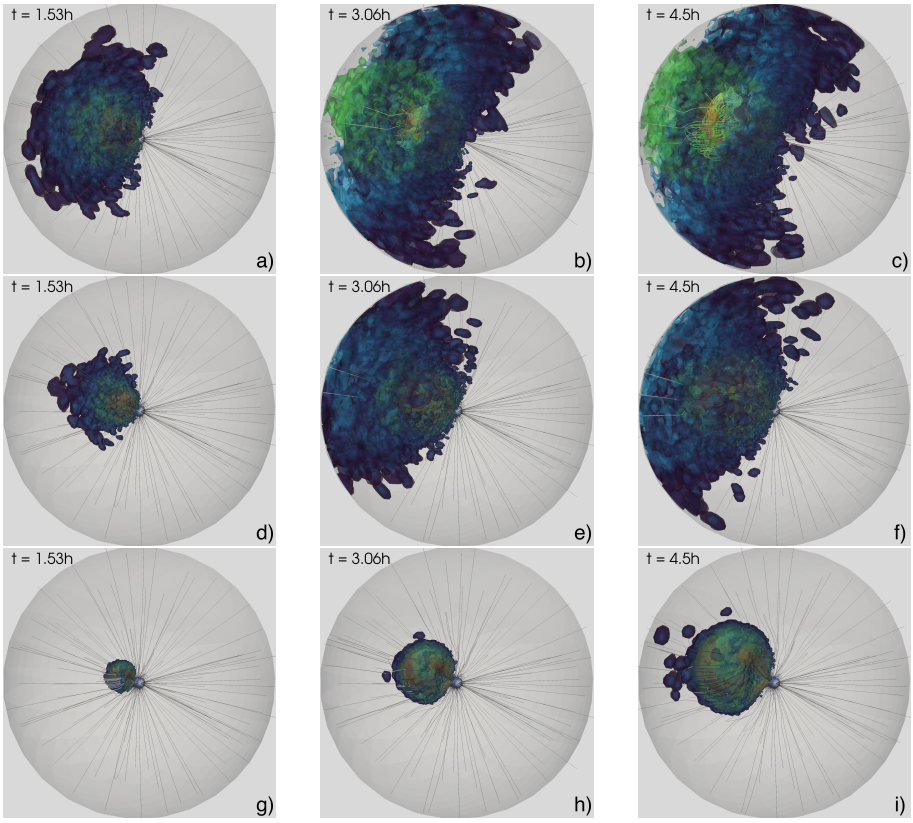

Figure 5.4. Time-lapse of particle propagation in a MFR using the CFD approach with a $\lambda_\perp$ that is a function of the Larmor radius. Panels a) through c) in the top row show the results for $\chi = 10$; panels d) through f) in the middle row correspond to $\chi = 5$, and panels g) through i) in the bottom row show the results for $\chi = 1$. The three columns represent simulation times 1.53 h, 3.06 h, and 4.5 h, respectively. The colour bar for the particle intensities from Fig. 5.2 also applies here.

domain from $t = 0$ to $t = 6.5\,\mathrm{h}$ (shortly before the apex of the MFR reaches $21.5\,R_\odot$). The 2D intensity contour plots in the $\theta - \phi$ plane are shown in Fig. 5.5. The top row contains the plots for the Larmor radius-dependent model ($\chi = 10; 5; 1$ in panels a through c, respectively), while the bottom row displays the plots for a constant $\lambda_\perp$ ($\lambda_\perp = 2.15 \times 10^{-2}; 1.075 \times 10^{-2}; 2.15 \times 10^{-3}\,R_\odot$ in panels d through f, respectively). The largest spread of particles and the highest number of escaped particles was observed in the Larmor radius-dependent model with $\chi = 10$, where most of the particles escaped in the direction parallel to the flanks of the TD flux rope. Even the case with $\chi = 5$ results in a

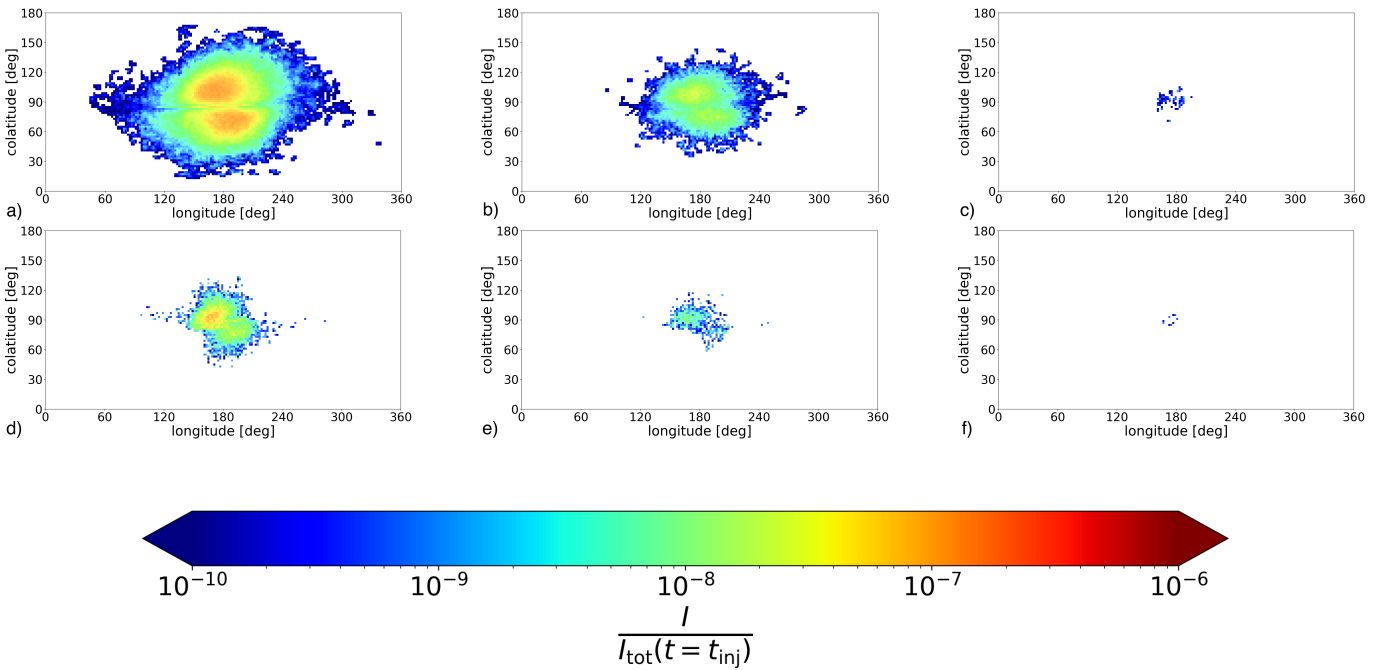

Figure 5.5. Particle intensities integrated over the first ~ 6.5 hours at the outer boundary ($21.5\ R_\odot$), shown in the θ-ϕ plane, illustrating particle escape from the flux rope. The top row shows results for the Larmor radius-dependent $\lambda_\perp$: $\chi = 10$ (panel a), $\chi = 5$ (panel b), and $\chi = 1$ (panel c). The bottom row shows results using a constant $\lambda_\perp$: $\lambda_\perp = 2.15 \times 10^{-2}\ R_\odot$ (panel d), $\lambda_\perp = 1.075 \times 10^{-2}\ R_\odot$ au (panel e), and $2.15 \times 10^{-3}\ R_\odot$ (panel f).

broader spread of particles compared to all cases with constant $\lambda_\perp$. In general, Fig. 5.5 illustrates that in all CFD simulations, the most substantial effect of CFD is noticeable in the propagation direction of the CME (evident in the most significant intensities being around 90° colatitude and 180° longitude.) As suggested by the plots in Figs. 5.3 and 5.4, the cases with the smallest parameter values in both models show the least amount of escaped particles and the narrowest spread of particles.

5.4 Supplementary modelling notes

We present here additional analyses of the simulations conducted in Section 5.3.

5.4.1 A note on the CFD models

To provide the reader with an understanding of the Larmor radius-dependent $\lambda_\perp$ and the χ-values in the case of constant $\lambda_\perp$, Fig. 5.6 presents contour plots of these parameters in the two planes perpendicular to the CME. The left panel shows the Larmor radius-dependent $\lambda_\perp$ in the case of $\chi = 5$ (corresponding to the middle row of Fig. 5.4), while the right panel displays the χ-values based on the case of constant $\lambda_\perp = 1.075 \times 10^{-2}\, R_\odot$ (see middle row of Fig. 5.3). In both cases, r_L (Eq. 2.30) was calculated based on the speed of a proton of 100 keV energy. The left panel shows distinct regions where $\lambda_\perp$ has comparatively large values, which would exceed those of $\lambda_\parallel$ by an order of magnitude if the limit were not set to $\lambda_\parallel$. These large $\lambda_\perp$-values result from very small local magnetic field strengths due to current sheets. In the simulations discussed in Sec. 5.3, the level of CFD was largely influenced by the $\lambda_\perp$-values in and near the CME, rather than by the large $\lambda_\perp$-values along the CME propagation direction.

5.4.2 Interpolating unstructured COCONUT to a structured grid

As described in Section 3.3, the unstructured grid in *COCONUT* required the implementation of alternative algorithms in *PARADISE*, such as those for tracing the particles or calculating the gradients of the magnetic field and velocity components on an unstructured grid. Because these new algorithms take significantly longer than the original methods in *PARADISE*, we developed a code to interpolate the unstructured grid onto a *EUHFORIA*-like structured grid,

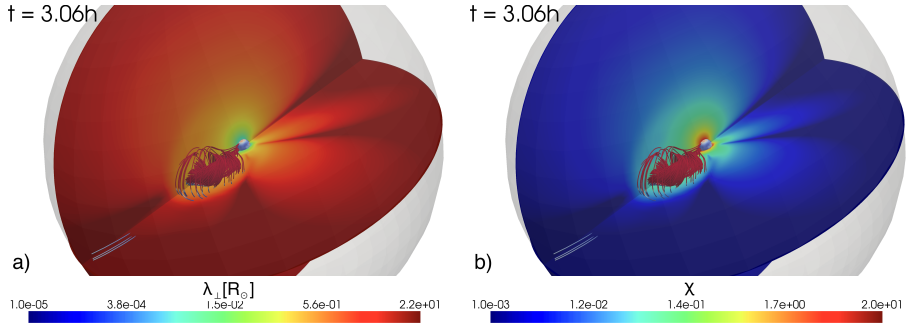

Figure 5.6. Contour plots comparing the parameters of the two CFD approaches. Panel a) shows the Larmor radius-dependent $\lambda_\perp$ in the case of $\chi = 5$ (corresponding to the results in the middle row of Fig. 5.4), while panel b) illustrates values of χ based on a constant $\lambda_\perp = 1.075 \times 10^{-2}\, R_\odot$ (corresponding to the results in the middle row of Fig. 5.3). Both panels show the contours in the two planes perpendicular to the MFR at $t = 3.06$ h.

enabling us to utilise the faster existing architecture of *EUHFORIA-PARADISE*. Figure 5.7 compares particle intensities at two different times (1.04 h and 2.01 h), where panels a) and c) show results based on the unstructured grid, and panels b) and d) are based on the interpolated grid. Since the MFR erupts in the direction of $\phi = 180°$, we limited the domain in the interpolated snapshots in colatitude to $\theta \in \{40°, 140°\}$ and $\phi \in \{90°, 270°\}$, which allowed us to increase the resolution of the interpolated snapshots. On the structured grid, the cells increased in length in the radial direction from about $8.5 \times 10^{-4}\, R_\odot$ to about $1\, R_\odot$, approximately matching the radial spacing of the original *COCONUT* grid towards the outer boundary, while having a coarser grid at the inner boundary compared to the unstructured grid.

In comparison, the unstructured grid has the smallest cell lengths at the inner boundary, with approximately $2.5 \times 10^{-4}\, R_\odot$, which increase to $1\, R_\odot$ at the outer boundary. The cell spacing in both colatitudinal and longitudinal directions was set to a constant value, with an angular resolution of approximately 0.8°. The solar wind plasma variables were interpolated from the *COCONUT* grid to the structured grid using all locally connected cells (i.e. a group of cells that share at least one node with the local cell) in *COCONUT*, weighted linearly with distance. The plots at 1.04 h (upper row) show the particle intensities about 30 min after injection. The intensities at this time are highly similar, whereas at the later time of 2.01 h (lower row), the particles in the simulation with the interpolated grid experience slightly more diffusion, possibly due to a smoothing of the solar wind values by the interpolation onto the structured

grid. While *COCONUT* itself has been benchmarked against other models and observations (Perri et al., 2022a, 2023; Kuźma et al., 2023), the interpolation of *COCONUT* to a *EUHFORIA*-like grid also serves as a test for the correct implementation of the unstructured grid in *PARADISE*.

We continue to improve *PARADISE* working with the unstructured grid, but also intend to enhance the interpolated model by implementing more elaborate interpolation schemes to reduce the additional diffusive effects. The wall time component plays a crucial role, as the aim is to eventually use *COCONUT*-*PARADISE* as a forecasting tool. A further advantage of using the original *EUHFORIA*-*PARADISE* architecture also with *COCONUT*, is the coupling of *COCONUT* to *EUHFORIA* (Linan et al., 2025), allowing particle transport simulations from the Sun's surface up to 1 au and beyond in *PARADISE* in a consistent manner.

5.4.3 A note on numerical diffusion

Solving Partial Differential Equations (PDEs) numerically, such as the ideal MHD equations (2.4)–(2.7) with models such as *EUHFORIA*, *Icarus*, or *COCONUT*, requires a discrete numerical representation of the functions involved. Typically, one performs a Taylor expansion of the original functions to derive a finite difference scheme for the PDEs. In general, such a procedure leads to additional terms appearing in the new representation of the PDEs. A commonly used example to illustrate this is the (1D version of the) continuity equation (Eq. 2.4). In its discrete numerical representation, an additional factor has units of a diffusion (or viscosity) coefficient and is interpreted as numerical diffusion or dissipation (e.g. Bodenheimer et al. 2007). While numerical diffusion is sometimes desired to stabilise solutions and remove spurious oscillations (Teyssier & Commerçon, 2019), at other times, the cumulative effects of numerical diffusion lead to inaccuracies and significant deviations from the true solution. The significance of numerical diffusive artefacts caused by field discretisation has been recently addressed by Guzmán et al. (2024).

To examine effects of numerical diffusion concerning the particle transport simulations, we compared simulation outcomes using different timesteps within *PARADISE* and different output intervals in *COCONUT*, illustrated in Fig. 5.8. The four panels show 3D plots of the particle intensities, similar to Sections 5.3.1–5.3.3. Panel a) shows the results for the default setup for all simulations in the main part, employing a minimal time step of $\Delta t_{\min} = 10^{-4}$ s and a *COCONUT* output interval of about 5 min. Here, $\Delta t_{\min}$ represents a user-specified lower bound for the adaptive time step used in *PARADISE*. During a *PARADISE* simulation, the actual timestep Δt is dynamically determined at each substep

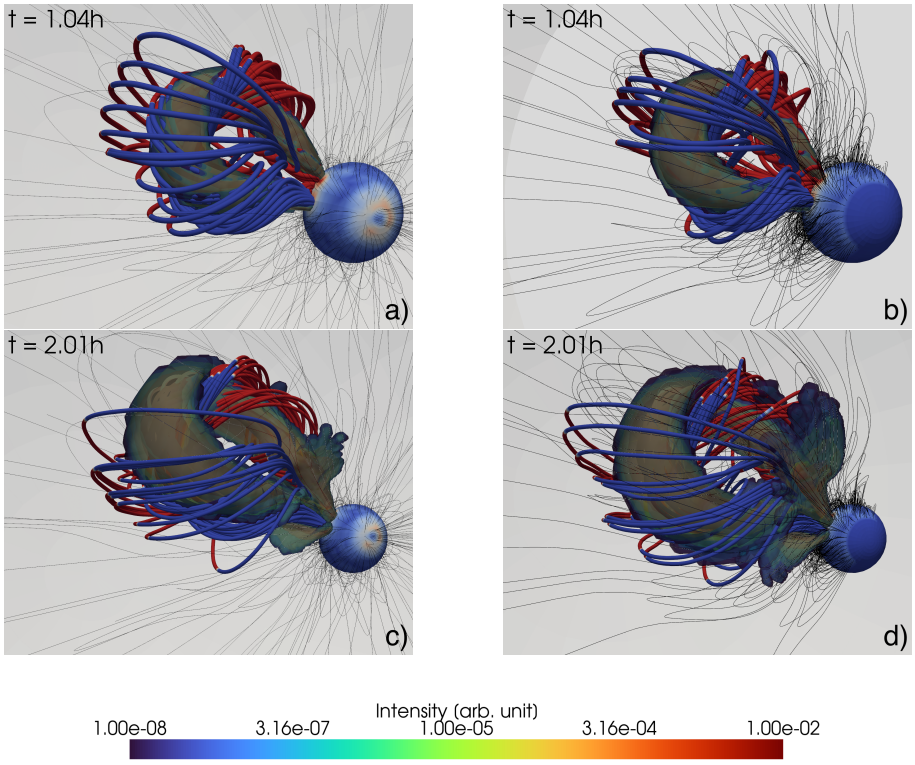

Figure 5.7. Comparison of unstructured *COCONUT* to *COCONUT* interpolated onto a structured grid. Panels a) and c) show 3D plots of particle intensity contours and the MFR on the (original) unstructured *COCONUT* grid, while panels b) and d) show the results on the interpolated structured grid. The top two panels correspond to $t = 1.04$ h, and the bottom two panels to $t = 2.01$ h.

based on several physical constraints, including particle speed, local spatial resolution, magnetic field focusing, and the parallel and perpendicular diffusion coefficients, but cannot fall below Δt_{min}. This approach ensures numerical stability and prevents excessively small timesteps that would increase the computational time. For panels b) and c), Δt_{min} is the same as in panel a), but the *COCONUT* output cadences are 15 min and 20 min, respectively. While panel b) shows only a slight increase in numerical diffusion, in panel c), the particles exhibit significant additional diffusion within the CME, allowing particles to escape the CME.

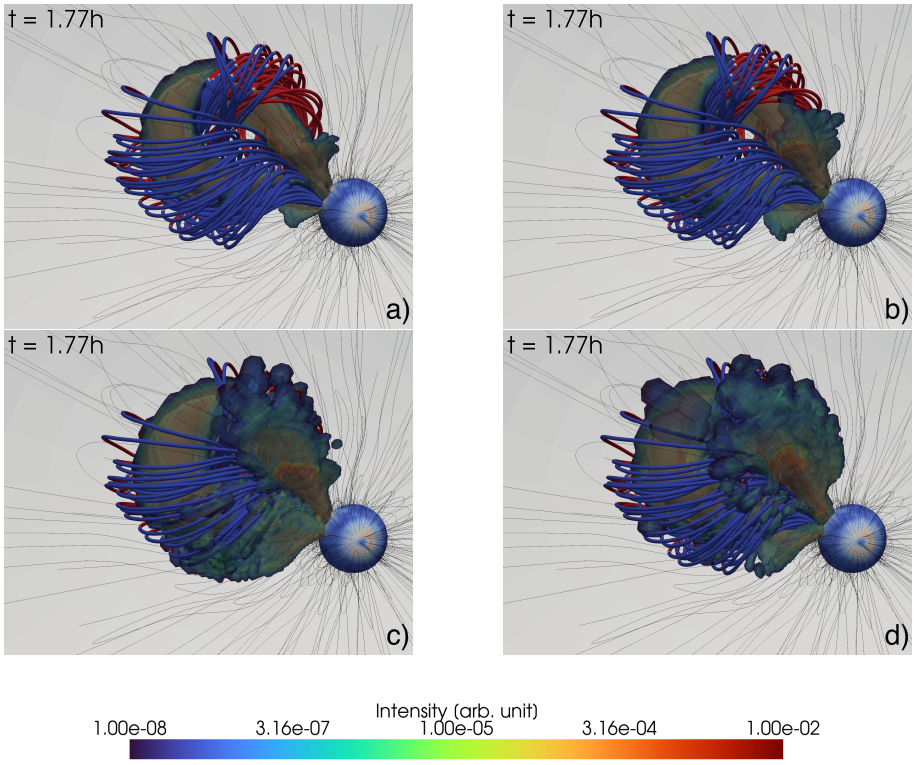

Figure 5.8. Illustration of numerical diffusion effects using *COCONUT*-*PARADISE*. Panels a) through c) show a *COCONUT* snapshot at $t = 1.77$ h from simulations with an output interval of approximately 5, 15, and 20 minutes, respectively, and a minimal timestep of $\Delta t_{\mathrm{min}} = 10^{-4}$ s within *PARADISE*. Panel d) uses a simulation with an output interval of 5 min but $\Delta t_{\mathrm{min}} = 5$ s.

In panel d), the MHD output cadence is the same as in panel a), but Δt_{min} is increased to 5 s. The additional numerical diffusion in panel d) is comparable to the case in panel c). Decreasing $\Delta t_{\mathrm{min}} = 10^{-4}$ s by a factor of 100 led to significantly longer wall times without a sufficiently notable reduction in numerical diffusion. We conclude that the minimal timestep in panel a) already causes a sufficiently small amount of numerical diffusion for the given particle energy and MHD output interval of 289 s, and thus $\Delta t_{\mathrm{min}} = 10^{-4}$ s has been selected as the default setup for all simulations in the main part of this chapter. Reducing the output interval in *COCONUT* to a value such as 1 min would minimise numerical diffusion further. However, it would significantly increase

the data volume, which needs to be considered in relation to the potential use of *COCONUT-PARADISE* as a forecasting tool.

5.5 Summary and discussion

In this chapter, we introduced the novel *COCONUT-PARADISE* model aimed at simulating the transport of energetic particles in the solar corona in the presence of an MFR. Using *COCONUT*, we generated coronal background configurations containing a CME modelled as a modified TD flux rope. Subsequently, we employed *PARADISE* to evolve energetic particles through these backgrounds in order to investigate the general propagation of particles within the MFR and, in particular, the effects of CFD on particle transport in the corona by using two different approaches for the CFD coefficient in the FTE. In all simulations, we injected monoenergetic 100 keV protons in one of the flanks of the MFR close to its footpoint. The simulation without any CFD mechanism showed that particles initially spread along the interior field lines of the MFR, later gaining access to the exterior field lines of the MFR. However, the particles remained confined to the CME and did not gain access to the field lines ahead of the CME that had opened due to MR.

The first approach for the CFD coefficient assumed a constant perpendicular MFP. Even a relatively small value typically used in heliospheric simulations that employs this type of CFD model, such as $\lambda_\perp/\lambda_\parallel = 10^{-3}$ with $\lambda_\parallel = 21.5\,R_\odot$, yields a large spread of particles along the longitudinal range in our coronal simulations. In the second approach to modelling CFD, we used a $\lambda_\perp$ dependent on the particle's Larmor radius and obtained qualitatively similar results to those of the first approach. In both models, by reducing the constant $\lambda_\perp$ or the χ-parameter by one order of magnitude, we observed considerably less CFD. However, in all three presented cases, particles gained access to the reconnected open magnetic field lines at the apex of the MFR and, as a result, escaped the flux rope primarily in the propagation direction of the CME.

As discussed in Section 5.1, observations by PSP, along with phenomena such as type IV radio bursts and FDs, indicate that CMEs trap particles within their flux ropes and prevent external particles from entering the MFR. The rapid increases in SEP intensity recorded by PSP in the solar corona during the massive September 2022 SEP event inside an MFR suggest limited perpendicular diffusion across the CME boundaries. Consequently, the simulations without CFD or with weak CFD would be more physically realistic, demonstrating that particles can remain trapped in a flux rope for an extended period. However, our simulations reveal that the effect of CFD is most pronounced at the apex

of the CME. Since PSP passed through the flank and backside of the CME during the September 2022 SEP event, it may thus have missed any strong CFD signatures.

Several projects using the *COCONUT-PARADISE* model are anticipated. *COCONUT* has been integrated with *EUHFORIA* (Linan et al., 2025) to simulate CME propagation from the lower corona to 1 au and beyond. This will help extend our current study on particle confinement within MFRs and investigate widespread SEP events. Such studies could extend this chapter's solar minimum-based coronal simulations by modelling solar maximum conditions, where increased interaction between energetic particles, CMEs, and the ambient solar wind is expected. Furthermore, in the present work, we neglected the minor acceleration of particles escaping the CME and crossing the shock driven by the CME. We plan to conduct a more detailed analysis of particle acceleration with the fully coupled *EUHFORIA-COCONUT* model. We also aim to explore particle guiding centre drifts, which are essential for understanding perpendicular transport (e.g. van den Berg et al. 2021). Additionally, the *COCONUT-PARADISE* model combined with *EUHFORIA* (or *Icarus*) may be used to investigate the back-propagation of energetic particles during long-duration gamma-ray flares (e.g. Hutchinson et al. 2022). Future work will benefit from observations by various spacecraft, especially PSP, which will provide valuable in-situ data to validate and refine our simulations, thereby enhancing our understanding of particle dynamics in the solar environment. Finally, we plan to compare particle transport in complex flux ropes (such as the TD flux rope) with that in static, twisted and untwisted coronal loops, to explore the differences in particle confinement and CFD between these magnetic structures, offering deeper insights into the effects of magnetic twist and evolving magnetic fields.

6

Modelling gyrosynchrotron emission in the solar corona

Most of this chapter was published in "Modelling gyrosynchrotron emission from coronal energetic electrons in a CME flux rope", 2025, Astron. Astrophys., 701, A53 (Husidic et al., 2025), and parts of the text and figures have been reproduced here directly. E. Husidic developed the coupling between COCONUT-PARADISE and the UFGSCs, implemented the code for generating virtual observer configurations, and designed tools to trace particles and solar wind parameters along lines of sight. Furthermore, E. Husidic performed all the simulations, generated the data and figures, and drafted the complete original manuscript.

Abstract. This chapter[1] presents a modelling framework to simulate GS emission from electrons trapped in a coronal CME flux rope. SRBs are closely linked to space weather phenomena such as flares, CMEs, and SEP events, offering valuable diagnostic tools for local particle populations and plasma conditions. Among them, type IV radio bursts stand out for their complexity and not fully understood origin and mechanisms. In this study, we explored how various parameters shape type IV-like GS spectra and demonstrated the diagnostic potential of the model for future applications. Using *COCONUT*, we generated coronal configurations containing an analytical TD MFR. Energetic electrons following a power-law spectrum were injected into the MFR and propagated as the CME evolved outwards. The resulting MHD snapshots and electron distributions were used as inputs to the *UFGSC*s to compute GS emission. We found that the injected electrons remained largely confined and produced GS spectra resembling observed type IV features. Varying observer vantage points, CME properties, and electron spectral indices affected burst intensities and durations. The strongest GS emission was observed to

[1]This chapter is based on CGS units.

originate from the CME flanks. Our results suggest that GS emission is a major contributor to type IV bursts, though additional mechanisms cannot be ruled out.

6.1 Background and motivation

The solar corona is a highly dynamic environment, characterised by spatio-temporal variations that manifest across its broadband electromagnetic spectrum, extending from radio wavelengths to gamma rays. Fundamental plasma processes in the corona give rise to diverse radiative phenomena and are broadly categorised by how individual electrons contribute to the observed radiation (Kundu, 1965). A standard classification distinguishes between coherent and incoherent emissions (Kaplan & Tsytovich, 1969). In coherent emission, many thermal or non-thermal electrons act collectively, producing phase-correlated waves. This collective behaviour can lead to highly amplified and organised bursts of radiation (Zheleznyakov, 1970; Melrose, 1980, 2017). In contrast, incoherent emission occurs when electrons radiate independently with random phases, resulting in more gradual and less intense radiation (Schwinger, 1949; Ginzburg & Syrovatskii, 1964; Born & Wolf, 1999). These classifications relate to the underlying emission mechanisms. Spontaneous emission, for instance, occurs when electrons radiate independently, typically resulting in incoherent radiation. Induced (or stimulated) emission, on the other hand, occurs when incident radiation triggers electrons to emit additional phase-aligned radiation, often resulting in coherent bursts (Galeev et al., 1965; Litvak & Trakhtengerts, 1971; Papadopoulos & Freund, 1979).

Under typical coronal conditions, and more broadly in space plasmas, characteristic plasma frequencies, such as the electron plasma frequency and the electron gyrofrequency, fall within the radio regime, making radio observations a powerful diagnostic tool (Nindos, 2020). Spontaneous, incoherent processes generally dominate in thermal plasmas. In contrast, spontaneous and induced processes may occur in non-thermal environments, such as during solar flares, giving rise to a rich variety of radio emission features (Pick & Vilmer, 2008). During extreme releases of the Sun's magnetic energy, whether through solar flares or CMEs, all types of radio emissions may be observed, providing a unique window into high-energy physics that remains inaccessible at other wavelengths (Knock & Cairns, 2005; Jebaraj et al., 2021; Alissandrakis et al., 2021; Klein et al., 2022; Jebaraj et al., 2023, 2024; Wilson et al., 2025). This makes radio emission a valuable probe of the acceleration, release, and transport of SEPs. However, only energetic electrons directly produce radio emissions that are

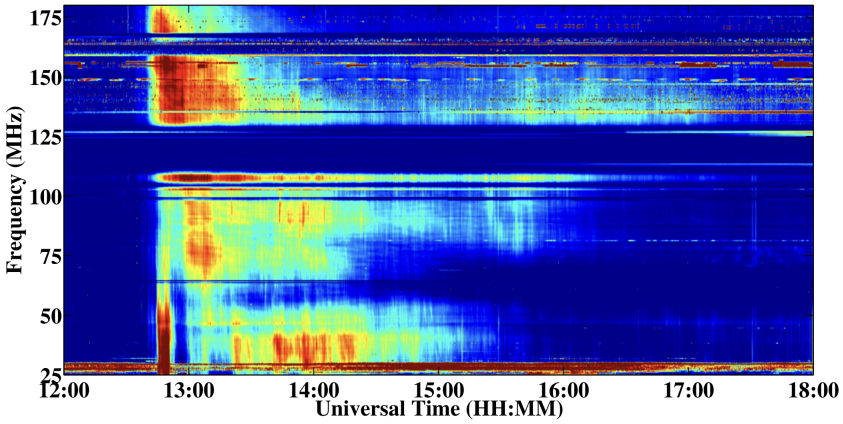

Figure 6.1. Dynamic radio spectrum of a type IV radio burst detected by the Sagamore Hill Solar Radio Observatory on 24 September 2011. Adapted from Kumari (2022).

detectable from the solar atmosphere (Kouloumvakos et al., 2015).

Solar radio emissions have been studied extensively (e.g. Melrose 1980; Gary & Keller 2004), but several fundamental questions remain. An enduring conundrum involves the origin of type IV bursts, which are associated with energetic eruptions. The name type IV refers to both a broadband continuum and the bursty emission that may occur within it. It is important to distinguish between the two because their emission mechanisms are believed to be fundamentally different and occur under distinct conditions. Typically, the background continuum is attributed to incoherent GS emission (Tun & Vourlidas, 2013; Bastian et al., 2001), whereas the bursty fine structures are linked to coherent emission sources (Aurass et al., 2003; Morosan et al., 2019). Figure 6.1 shows a dynamic radio spectrum of a type IV burst recorded by the Sagamore Hill Radio Observatory on 24 September 2011 (Kumari, 2022). The spectrum displays several features commonly observed in type IV bursts, including a gradual drift of the peak intensity toward lower frequencies over time (above 125 MHz), stationary (in frequency) structures (between 25 and 50 MHz), and a bursty, high-intensity core surrounded by regions of weaker emission. While the depicted type IV burst lasted around 5 hours, typical durations of type IVs range from minutes to about an hour (Robinson, 1978; Gergely, 1986).

Type IV emissions are subdivided into moving and stationary spectral types, referred to as type IVm and type IVs, respectively (e.g. Vourlidas 2004 and references therein). Type IVm can be synchrotron, GS, or plasma emission of electrons entrained within CMEs (e.g. Dulk 1973). Type IVs radio bursts are

usually attributed to plasma emission (Melrose, 1980). Historically, spectral drift has often been interpreted as a proxy for radio source motion, with spectral drift implying spatial motion of the emission region (Weiss, 1963; Robinson, 1978; Zlotnik et al., 2003; Chernov, 2006; Nishimura et al., 2013; Bain et al., 2014; Kumari et al., 2021), and the absence of spectral drift suggesting a stationary source (Weiss, 1963; Robinson & Smerd, 1975; Dulk, 1985; Lv et al., 2021). However, it should be noted that imaging observations have indicated that both (spectrally defined) IVm and IVs continua can exhibit spatial drift (Koval et al., 2016; Salas-Matamoros & Klein, 2020; Morosan et al., 2021). In addition, Lv et al. (2021) have reported frequency-dependent spatial structuring for IVs events, possibly reflecting embedded CMEs. Furthermore, Kumari et al. (2021) found in their study that while most CMEs were accompanied by type IV bursts, only a minority of these were actually of the moving type. If such a spectral and spatial decorrelation exists in type IV behaviour, it must be an intrinsic property of the source itself.

Non-thermal electrons accelerated during CME eruptions can emit GS radiation if they remain trapped within an erupting flux rope or plasmoid. This type of emission, sometimes referred to as a 'radio CME', differs from the radiation originating at shock fronts or from remote flare loops. Relativistic electrons (with Lorentz factors $\gamma \gtrsim 1$) spiralling along solar magnetic field lines produce GS radiation, whereas ultra-relativistic electrons ($\gamma \gg 1$) generate synchrotron emission. According to the standard theory, GS emission occurs in magnetoactive plasma environments where dispersive effects significantly modify the radiation and must be considered (Melrose, 1968a; Zheleznyakov, 1969). In contrast, pure synchrotron emission is typically treated as a vacuum process, and it is appropriate when plasma densities are low or emission frequencies are high enough to minimise medium-related effects (Schwinger, 1949; Ginzburg, 1979).

For these reasons, type IVm bursts have an important space weather aspect, as they carry information of the magnetic content of the CME (Vourlidas et al., 2020). However, they have been challenging to detect and study. Coherent emissions tend to dominate the radio spectra during eruptions, hindering the detection of faint emission from the CME interior. Joint white-light and radio observations of transients were rare until the launch of the SOlar and Heliospheric Observatory (SOHO) in the mid-1990s. Soon after, Bastian et al. (2001) reported the first direct radio imaging of a white-light CME, revealing a moving radio source within the CME with a spectrum consistent with GS emission. The study determined the spatial distribution of energetic electrons within the CME and estimated both the internal magnetic field strength of the CME and the properties of the electron population. Since then, several additional events have been detected (Maia et al., 2007; Tun & Vourlidas, 2013; Mondal et al., 2020; Kansabanik et al., 2024).

A key research focus in type IV bursts is using their emission to estimate CME magnetic fields, which are nearly impossible to assess by other means (Morosan et al., 2019; Kumari et al., 2021). Various studies have interpreted GS emission as the primary mechanism in type IV radio bursts to infer magnetic field strengths within CMEs at specific solar radial distances (Gopalswamy & Kundu, 1987; Bastian et al., 2001; Maia et al., 2007; Tun & Vourlidas, 2013; Bain et al., 2014; Hariharan et al., 2016; Carley et al., 2017). However, significant uncertainties remain regarding the inferred magnetic field strengths and the detailed relationship between CMEs and type IV radio bursts, particularly when relying solely on remote observational methods (Morosan et al., 2019; Kumari et al., 2021).

Numerical models capable of realistically reproducing complex solar wind structures and simulating the acceleration and transport of energetic particles, combined with radio emission models, can help address open questions regarding the mechanisms underlying particle acceleration and radio emission. We demonstrate this approach in this chapter by coupling three numerical models to simulate GS emission from energetic electrons, including mildly relativistic and ultra-relativistic populations trapped within an erupting flux rope. We deployed *COCONUT* (Perri et al., 2022b), constrained by observational magnetogram data at the inner boundary, to generate the background coronal configurations, where CMEs are modelled as analytical TD flux ropes (Titov & Démoulin, 1999; Titov et al., 2014). The transport of energetic electrons was modelled with the *PARADISE* code (Wijsen et al., 2019a; Wijsen, 2020). The MHD parameters derived from *COCONUT* and electron distributions obtained from *PARADISE* were then passed into the *UFGSC*s (Fleishman & Kuznetsov, 2010; Kuznetsov & Fleishman, 2021) to derive synthetic type IV radio spectra by computing the full GS emission and absorption coefficients using fast and accurate numerical approximations. By varying electron injection spectra and MFR configurations, and observing the evolving CME from different vantage points in the solar corona, we investigated how electron and CME properties influence the characteristics of radio spectra, including intensity, spectral shape, duration, and frequency range.

The remainder of this chapter is structured as follows. In Section 6.2, we describe the numerical setup used to generate synthetic radio spectra. Simulation results are presented and discussed in Section 6.3, and we conclude with a summary and outlook in Section 6.4.

6.2 Numerical setup

In this work, we used the recently updated version of *COCONUT* (Baratashvili et al., 2024), which incorporates additional source terms for coronal heating, radiation losses, and thermal conduction into the energy conservation equation (see Section 2.1). The generation of the coronal background proceeded in two stages. First, we computed the relaxed background solar wind using a magnetogram obtained from HMI on board the SDO, dated July 2, 2019. We then restarted the *COCONUT* simulation, modifying only the magnetic field by superimposing an MFR at the solar surface. The magnetogram was taken from a period of solar minimum, providing a less complex coronal environment that minimises additional influences on the evolution of the CME and the energetic particle distribution.

As outlined in Section 3.1.3, the CME can be characterised by the dimensionless parameter ζ. In this work, we used two setups: one with $\zeta = 30$ and one with $\zeta = 70$. The case $\zeta = 30$ produced a CME with an initial magnetic field strength of about 5.8 G and an initial speed of about 940 km/s, whereas the case $\zeta = 70$ resulted in a CME with a stronger field of about 10.6 G and a faster speed of roughly 1300 km/s. The remaining parameters for the two CMEs used in the TD model were identical.

The initial placement of the CME footpoints (i.e. the locations where the MFR is magnetically anchored in the lower corona or photosphere) was around colatitude $\theta = 90°$ and Carrington longitude $\phi = 180°$, with the centre of the toroidal axis located at a height $\tilde{d} = 0.15\,R_\odot$ above the solar surface. The minor radius was set to $\tilde{a} = 0.1\ R_\odot$, while the major radius was set to $\tilde{R} = 0.3\ R_\odot$. The unstructured COCONUT grid comprised about 1.5 million prism-shaped cells in concentric, radially expanding shells (see Brchnelova et al. 2022 for details). The output cadence of the MHD snapshots was about 87 seconds, and we used the first 2.5 hours of the *COCONUT* simulations for the subsequent particle transport simulations. We further note that the actual computational domain of *COCONUT* in our simulations extended to 25 $R_\odot$, but we set the outer boundary in the subsequent particle transport simulations to 21.5 $R_\odot$ to avoid any numerical outer boundary effects, following the recommendations by Brchnelova et al. (2022).

Next, the particle transport code *PARADISE* was used to inject and propagate energetic electron distributions within the erupting MFR. We selected two different spectral indices for the electron injection spectra. Assuming a power-law energy distribution $\mathrm{d}N/\mathrm{d}E \propto E^{-\delta}$, we chose $\delta = 2$ and $\delta = 3$ with an initial energy range from 10 keV to 10 MeV and an isotropic pitch angle distribution.

The electrons were injected as a delta distribution in time, approximately 30 minutes after the eruption of the CME, within one of the CME flanks (i.e. the side regions of the MFR, curving downward from the apex) near its central axis and about 0.5 $R_\odot$ above the solar surface. We adopted an injection method similar to that used by Husidic et al. (2024b), in which a specified high magnetic field value is used to identify the injection site. This approach has previously proven effective to ensure particle confinement within the CME (see Chapter 5). The selected energy range is motivated by previous studies identifying 10 keV to 10 MeV as relevant for GS emission (Dulk & Marsh, 1982; Fleishman & Kuznetsov, 2010; Kuznetsov & Fleishman, 2021), while spectral indices $\delta \geq 2$ are commonly observed (e.g. Maksimovic et al., 1997) and frequently adopted in GS calculations and modelling (e.g. Dulk 1973; Dulk & Marsh 1982; Kuznetsov & Fleishman 2021). At injection time, the CME reached a height of about 2.7 $R_\odot$ for $\zeta = 30$, and for $\zeta = 70$, approximately 3.9 $R_\odot$. By the end of the simulation, the corresponding CME heights were about 8.1 $R_\odot$ and 13.1 $R_\odot$, respectively.

The simulation results from *PARADISE* are expressed as differential intensities j, from which the particle distribution function f can be derived according to

$$j(\mathbf{r}, p, \mu, t) = p^2 \, f(\mathbf{r}, p, \mu, t) \, . \tag{6.1}$$

Because the FTE is linear, its solutions can be scaled by an arbitrary constant. Below, we describe the required units for the GS code and how they are obtained.

In this study, we used the *UFGSC*s in hybrid mode and set $\tilde{\eta} = 12$ (see Section 3.1.5) as a threshold for switching both to the continuous code and to the use of approximated Bessel functions, so that the code operated primarily in continuous mode, which smoothed out harmonic structures and ensured a clean approximation of incoherent GS emission. While the *UFGSC*s also allow for the inclusion of bremsstrahlung from electron-ion (free-free) and electron-neutral (neutral bremsstrahlung) collisions, we disabled those processes to isolate GS emission.

To compute the GS emission from the *COCONUT-PARADISE* simulation, we defined structured sets of LOS and prepared the corresponding plasma input parameters at each discretised node, including the magnetic field magnitude B, the background solar wind number density n, the solar wind temperature T, and the viewing angle θ (i.e. the angle between a line of sight and the local magnetic field vector), along with the *PARADISE* electron distribution values. The *UFGSC*s independently calculate the emission and absorption coefficients along each line of sight. In many GS calculations, the emission is computed along a single line of sight and scaled by the assumed source area, which is sufficient for unresolved or compact sources. In our setup, the virtual spacecraft is located outside the MFR but still in the corona, so the emission had to be

Table 6.1. Observer geometry and parameter combinations in the simulation setup.

Perspective	Coordinates $[R_\odot, R_\odot, R_\odot]$		ζ	δ
	Base point	Spacecraft		
halo view	$(-1.1, 0, 0)$	$(-18, 0, 0)$	30, 70	2, 3
edge-on view	$(-8, -10, 0)$	$(-3, 14, 0)$	30, 70	2, 3
face-on view	$(-10, 0, -12)$	$(-1.5, 0, 14)$	30, 70	2, 3

computed over an extended field of view that captures the complete spatial structure of the source.

For this study, we explored three distinct observational geometries by placing a virtual spacecraft at different locations relative to the erupting CME. Each spacecraft position was associated with a central line of sight perpendicular to a viewing field of $16\,R_\odot \times 16\,R_\odot$. The three viewing geometries are defined as follows: 1) the 'halo view', where the CME propagates directly towards the observer—a configuration typical of Earth-directed events and commonly observed as halo CMEs in coronagraph data (e.g. Howard et al. 1982; Schwenn et al. 2005); 2) the 'edge-on view', where the observer is positioned to the side of the CME, with the central line of sight across the central axes of both flanks—a geometry less commonly observed, as it would require the CME to be observed at the solar limb and tilted by approximately 90°; and 3) the 'face-on view', where the observer is positioned above the CME, viewing the full curvature of the flux rope—a configuration commonly encountered when CMEs are observed near the solar limb (e.g. Bastian et al. 2001; Kansabanik et al. 2024). The coordinates of the spacecraft and base points of the central line of sight, along with the vantage points, CME and electron injection distribution parameters, are summarised in Table 6.1. Figure 6.2 illustrates these configurations, showing the virtual spacecraft (black cube), the CME, and the viewing field (violet-shaded area), along with some representative LOS. In all three cases, we used a resolution of 20×20 LOS, with each line of sight assigned an area of $A_{\rm total}/N_{\rm LOS}$, that is, the total viewing field area $A_{\rm total}$ is divided by the total number of LOS $N_{\rm LOS} = 400$.

To ensure robust statistics in the particle transport simulations, a total of 10.8 million electrons were injected in each simulation. While the pitch angle diffusion coefficient is included in the FTE, for simplicity, we excluded CFD (perpendicular) diffusion, and the guiding-centre drift velocity was set to zero, since it is expected to be negligible for electrons. The parallel MFP length was fixed to $\lambda_\parallel = 0.1$ au.

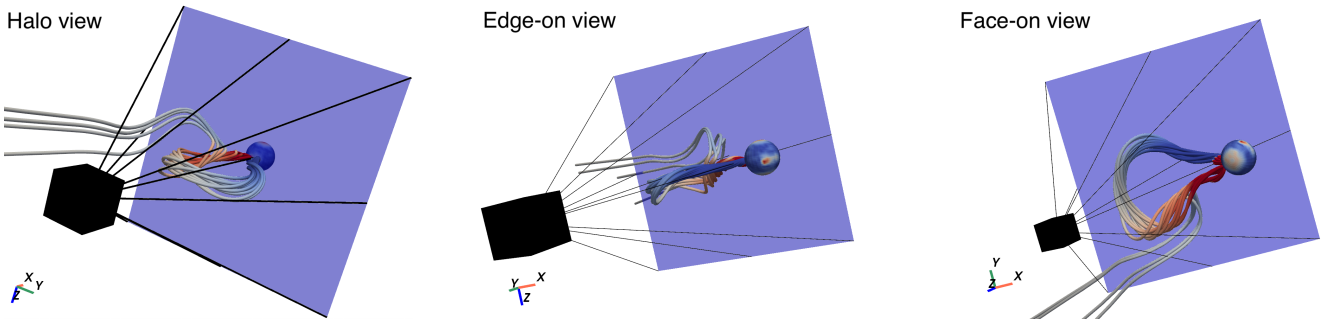

Figure 6.2. Positions of the virtual spacecraft and their respective viewing fields. The black cube represents the spacecraft, while the violet area illustrates the field of view. Some representative lines of sight are included.

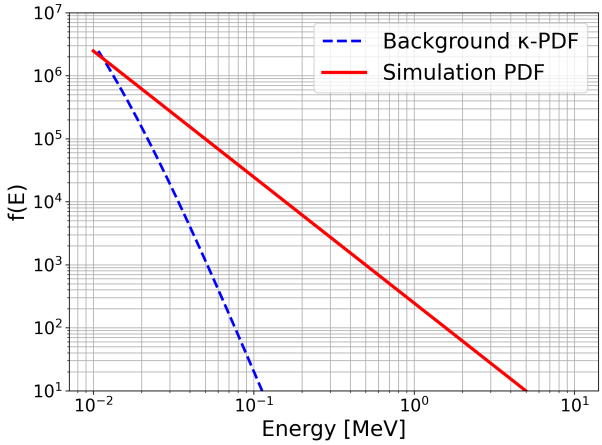

Figure 6.3. Comparing the distribution function tails of the background and the injected electron distribution. The particle distribution function (PDF) is plotted as a red solid graph, while the background rRKD with $\kappa = 8$ and $\xi = 0.001$ is plotted as a blue dashed graph.

At each node along a line of sight and for each time step, the particle distribution function f, obtained from *PARADISE*, was passed to the *UFGSC*s as a 2D array $f_{i,j} = f(E_i, \mu_j)$ in energy-pitch angle space. Here, E denotes the kinetic energy, and f has the units $\mathrm{cm}^{-3}\,\mathrm{MeV}^{-1}$. We added a background electron component to the *PARADISE* output to avoid exact zeros resulting from the logarithmic energy grid. This background was based on the relativistic Regularised Kappa Distribution (rRKD; Han Thanh et al. 2022), reformulated in terms of relativistic kinetic energy $E = \sqrt{(p\,c)^2 + (m_0\,c^2)^2} - m_0\,c^2$ with electron rest mass m_0. The local number density and temperature at a given time and position in the rRKD were extracted from the MHD simulation.

To ensure that the *PARADISE* electron distribution had physically meaningful units, we computed the scaling factor by matching the injected particle distribution at 10 keV to the rRKD, parametrised by the local solar wind conditions obtained from the MHD simulation at the injection region and time. The influence of the background was minimised in all simulations by choosing $\kappa = 8$ and a cut-off parameter $\xi = 0.001$ for the rRKD (for details, see Scherer et al. 2017; Han Thanh et al. 2022). Figure 6.3 shows the injected electron distribution (red solid curve) for $\delta = 2$ and the background rRKD (blue dashed curve), demonstrating the scaling. As illustrated, the background distribution aligns with the *PARADISE* simulation at the lowest energy of the injection spectrum and remains below it across the whole energy range. Since

the *PARADISE* distribution steepens during the transport simulation, selecting a κ-value of 8 ensures the background stays below. This also helped to avoid excessively steep gradients in the total distribution, which could otherwise lead to numerical artefacts in the GS calculation and provide conditions resulting in occasional oversaturated pixels in the computed spectra, with intensities sometimes exceeding those of neighbouring pixels by several tens of orders of magnitude.

Including the background inevitably introduced a small GS contribution from it. However, due to the non-linearity of the emission and absorption coefficients, the background contribution could not be directly subtracted. Nevertheless, simulations ran with the background distribution alone showed that subtracting its GS emission from that of the combined (*PARADISE* + background) distribution resulted in a change of less than 0.01% at the peak intensities.

6.3 Simulation results

We investigate the impact of different CME configurations and energy injection spectra on the resulting GS emission. Two CME setups were considered, classified by the ζ-parameter with values 30 and 70, and each was paired with injected electron energy distributions of spectral index $\delta = 2$ and $\delta = 3$. This section refers to individual cases by their respective ζ- and initial δ-values. However, the actual spectral indices of the electron populations vary over time and location due to transport effects, such as adiabatic cooling, particle losses, and scattering.

We begin by outlining the general features shared across all computed radio spectra and comparing them to real observations of type IV bursts. All obtained radio spectra (Figs. 6.4 and 6.5) exhibit a similar structure, containing a high-intensity centre surrounded by weaker emission. This feature is more pronounced in the $\delta = 2$ cases compared to those with $\delta = 3$. Similar intensity structures are regularly observed in dynamic spectra of type IV bursts, as illustrated in Fig. 6.1 and documented by studies such as Melnik et al. (2018), Vasanth et al. (2019), Morosan et al. (2020), and Kumari (2022). The high-intensity cores in our simulations emerge from the local electron distribution, the CME magnetic field strength, and the viewing geometry (see paragraphs below). Broadband features with locally spiky or burst-like enhancements are often associated with emission originating in the MFR flanks near the footpoints (Bastian et al., 2001; Carley et al., 2017; Mondal et al., 2020; Chhabra et al., 2021), where magnetic field strengths are high and pitch angle anisotropies are pronounced. These conditions are entirely consistent with the GS framework.

Furthermore, all twelve spectra exhibit a drift of the intensity peak from higher to lower frequencies over time, resulting in broad, upward-drifting emission lanes in the time-frequency domain (with the frequency axis being inverted in the plots). This behaviour is typical for synchrotron emission from electrons in the energy range of 1 – 10 MeV in expanding, twisted MFRs, such as the TD model used in our simulations, where the internal magnetic field weakens with time. Since the synchrotron peak frequency scales approximately with the square of the magnetic field strength ($f_{\omega,\mathrm{peak}} \propto B^2$), this leads to a downward shift in frequency as the CME evolves. This effect is reinforced by the adiabatic cooling of electrons, which reduces their energy as they propagate through the medium. To quantify this behaviour, Table 6.2 lists the estimated drift rates (in MHz/s) for all twelve spectra shown in Figs. 6.4 and 6.5. Drift rates were obtained by applying a linear fit to the time evolution of the intensity peaks over the first $\sim$ 30 min (to compare across all cases). While no consistent trend emerges across all cases, we find that the halo-view configuration consistently exhibits the strongest negative drift rates.

Table 6.2. Frequency drift rates, R_{drift}, estimated over the first $\sim$ 30 minutes after electron injection, and peak intensities for the different simulation configurations.

δ	ζ	View	R_{drift} [MHz/s]	I_{max} [sfu]
2	30	Halo	-0.0875	$\sim$ 2
2	30	Edge-on	-0.0199	$\sim$ 28
2	30	Face-on	-0.0251	$\sim$ 48
3	30	Halo	-0.0614	$\sim$ 0.002
3	30	Edge-on	-0.0064	$\sim$ 0.05
3	30	Face-on	-0.0025	$\sim$ 0.09
2	70	Halo	-0.0372	$\sim$ 35
2	70	Edge-on	-0.0271	$\sim$ 248
2	70	Face-on	-0.0075	$\sim$ 442
3	70	Halo	-0.0192	$\sim$ 0.06
3	70	Edge-on	-0.0051	$\sim$ 0.8
3	70	Face-on	-0.0010	$\sim$ 2

Frequency drifts in type IV spectra, especially those associated with CMEs, have been frequently reported across a broad range of values. For instance, Kumari

et al. (2021) identified downward frequency drifts in the majority of CMEs in their sample, using drift rates (in absolute value) $|R_{\rm drift}| \geq 0.03$ MHz/s as an indicator for IVm bursts. The authors found that most type IV bursts exhibited drift rates $|R_{\rm drift}| \leq 0.5$ MHz/s. Other studies reported higher drift rates for fine structures embedded within type IV continua, ranging from several MHz/s up to tens of MHz/s (Nishimura et al., 2013; Melnik et al., 2018), while the background continuum typically drifts more slowly, with $|R_{\rm drift}| \approx 10$ kHz/s (Melnik et al., 2018). In this context, the drift rates obtained from our simulations fall towards the lower end of the reported literature values. A plausible explanation may lie in our modelling framework, including only synchrotron/GS emission, where frequency drifts primarily arise from the gradual weakening of the magnetic field within the expanding MFR. It should be further noted that the reported drift rates were mainly derived from lower frequencies compared to our results, which may also explain the discrepancies.

The GS emission is detected at all spacecraft positions from the time of electron injection (approximately 30 min into the simulation, with $t = 0$ min being the time of CME eruption), as the CME is initially entirely within the field of view. In general, the radio bursts are obtained in frequency ranges between 20 MHz and 8 GHz, with core intensities $> 10^{-4}$ solar flux units (sfu) and $< 10^3$ sfu (see peak intensities in Table 6.2), and durations between ~ 30 min and ~ 2 h. While type IV bursts are commonly detected in the 10^1–10^2 MHz range (Melnik et al., 2018; Vasanth et al., 2019; Morosan et al., 2020; Kumari et al., 2021; Kumari, 2022; Mohan et al., 2024), observations also show extensions to higher frequencies from 10^2–10^3 MHz (Liu et al., 2018; Morosan et al., 2019) to several 10^3 MHz (Xie et al., 2002; Nishimura et al., 2013; Karlický & Rybák, 2020). Similarly, reported spectral flux densities span a wide range, from 10^1–10^2 sfu (Dulk, 1973; Carley et al., 2017; Melnik et al., 2018) to multiple 10^2 sfu (Bouratzis et al., 2015), to around 10^3 sfu (Melnik et al., 2018), and even approaching 10^4 sfu in cases involving fine structures (Alissandrakis et al., 2019). It is important to note that the peak intensities also depend on the number of injected electrons. Finally, recorded type IV durations are also highly variable, ranging from a few minutes (Karlický & Rybák, 2020; Morosan et al., 2021; Kumari et al., 2021; Mohan et al., 2024) to several hours (Liu et al., 2018; Melnik et al., 2018; Vasanth et al., 2019). Historically, type IVm were associated with durations < 1 h, while durations > 1 h were attributed to type IVs. However, more recent studies reported IVm events lasting > 1.5 h (Ramesh et al., 2013) and even > 2.5 h (Vasanth et al. 2019; see also the discussion in Kumari et al. 2021). These comparisons suggest that our synthetic GS spectra are physically realistic in terms of frequency range, spectral flux density, and duration. The simulated spectra represent a broadband GS continuum consistent with the full range theoretically permitted by the electron energy distribution. In the optically thin regime, the high-frequency cut-off is determined by the electron

distribution, while the low-frequency turnover arises from self-absorption and Razin suppression. Observations usually show narrower bandwidths, possibly due to limited sensitivity of the instruments.

When comparing the intensities for different spectral indices of the injected electrons at each spacecraft location, we consistently find higher intensities and longer radio burst durations for $\delta = 2$ compared to $\delta = 3$. This outcome is expected, as the spectrum with $\delta = 2$ is flatter than that with $\delta = 3$, meaning a larger fraction of the electron population is in the high-energy range. Consequently, the GS spectrum is dominated by higher-energy electrons, which produce stronger emission due to their greater radiative power (see Liénard formula or Eq. 6.2). We further note that, due to the energy dependence of particle transport, the intensity ratios between these two cases are not constant over time. The case with initial $\delta = 2$ not only contains more electrons of higher energy, but also a greater fraction of faster particles, yielding different transport behaviour over time and leading to a distinct evolution of the injection spectra.

Next, we analyse the individual CME cases. Figure 6.4 presents the radio spectra obtained for the case $\zeta = 30$, with $\delta = 2$ in the left column and $\delta = 3$ in the right column. The spectra are shown from the point of particle injection up to about 2.5 hours into the simulation. Considering the left column ($\delta = 2$), at the first spacecraft position, where the observer is directly ahead of the CME, we find a peak intensity ratio of approximately $I_{\mathrm{max},\delta=2}/I_{\mathrm{max},\delta=3} \approx 1100$. At the second spacecraft location (observer viewing the MFR edge-on), the ratio is about 564. A similar ratio of roughly 560 is observed when the observer is directly above the CME (face-on view). The results are qualitatively similar for the $\delta = 3$ cases in the right column (see Table 6.3).

The synthetic GS emission across different spacecraft positions also reveals noteworthy differences. Comparison of peak intensities between the edge-on and halo view for $\zeta = 30$ and $\delta = 2$ (panels a and c in Fig. 6.4) indicates a ratio of $I_{\mathrm{max,edge-on}}/I_{\mathrm{max,halo}} \approx 13$. In contrast, a comparison between the face-on and halo view (panels a and e) yields $I_{\mathrm{max,face-on}}/I_{\mathrm{max,halo}} \approx 23$, highlighting the substantial variation in GS intensity with observer vantage point.

The variation in the radio emission spectra across the three observer positions can be understood in terms of the local magnetic field strength and the viewing angle. The GS emission is sensitive to the observer's viewpoint relative to the MFR geometry. The GS brightness is proportional to the component of the magnetic field perpendicular to the electron motion, given by the electron pitch angle, as $B_\perp = B \sin\alpha$. Thus, the viewing angle has a strong influence on both the emission intensity and the visibility of frequency drift.

The halo view aligns the observer's LOS with the magnetic field lines that are

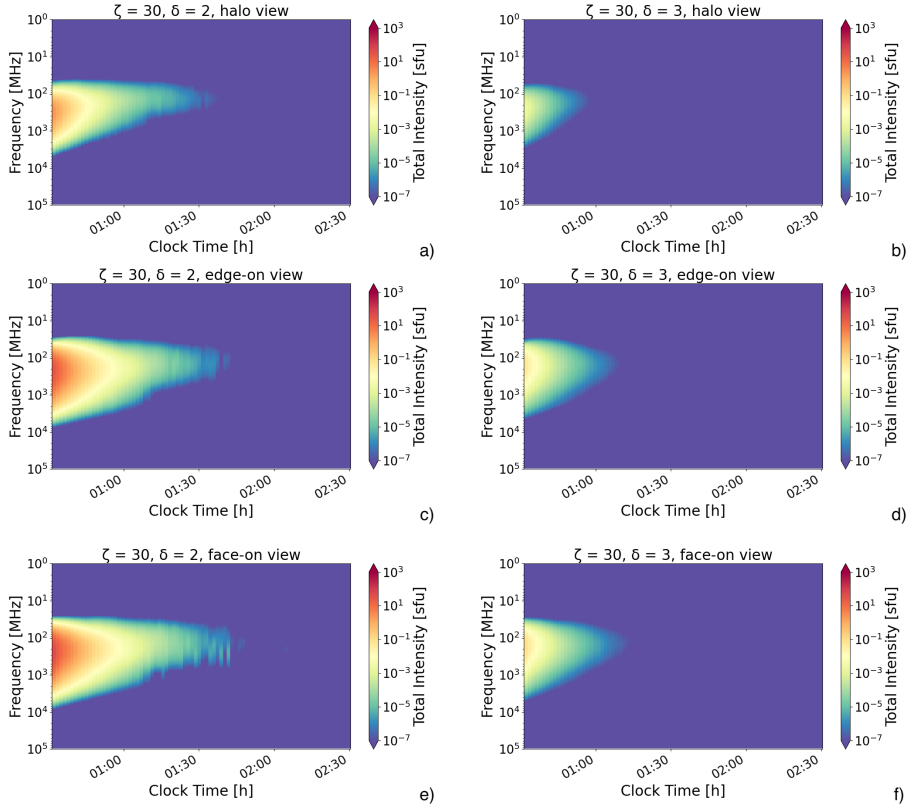

Figure 6.4. Synthetic radio spectra for the CME case with $\zeta = 30$. The panels in the left column show the observed radio emission from the injection spectrum with $\delta = 2$ seen from the three spacecraft locations, while the panels in the right column contain the radio emission from the injection spectrum with $\delta = 3$.

Table 6.3. Peak intensity ratios across observer positions, spectral indices, and CME cases.

(1) Intensity ratios across views			
ζ	δ	$I_{\mathrm{edge-on}}/I_{\mathrm{halo}}$	$I_{\mathrm{face-on}}/I_{\mathrm{halo}}$
30	2	13.1	22.5
30	3	25.5	44.1
70	2	7.2	12.8
70	3	14.3	38.1
(2) Intensity ratios across spectral indices			
ζ	View	$I_{\delta=2}/I_{\delta=3}$	
30	halo	1100	
	edge-on	564	
	face-on	560	
70	halo	620	
	edge-on	310	
	face-on	208	
(3) Intensity ratios across CME cases			
δ	View	$I_{\zeta=70}/I_{\zeta=30}$	
2	halo	16.2	
	edge-on	8.9	
	face-on	9.2	
3	halo	28.6	
	edge-on	16.1	
	face-on	24.7	

essentially approximately parallel to the viewing direction, particularly along the MFR flanks. The field lines become more perpendicular only closer to the CME apex. Because GS emission is strongest when the magnetic field is perpendicular to the LOS, this geometry results in weaker overall emission, although the frequency drift remains visible.

From the edge-on view, the observer's LOS traverse both CME flanks, encountering a thicker cross-section of the MFR where magnetic fields are both stronger and more perpendicular to the LOS. This configuration enhances the GS brightness. It supports magnetic mirroring, as the magnetic field converges near the anchored MFR footpoints, which remain part of the closed field structure and exhibit the highest magnetic field strengths in the simulation. These conditions enable effective particle trapping and sustained GS emission.

Finally, the face-on view provides visibility of both CME flanks and part of the apex, with many LOS quasi-perpendicular to the flux rope axis. This geometry yields the strongest GS emission of the three configurations, owing to both favourable pitch angle orientation and a large effective emitting region. Again, qualitatively similar results were obtained for the simulations with spectral index $\delta = 3$ (see Table 6.3). It is worth noting that these results are specific to the generated MFR configuration. Increasing the twist of the MFR would modify the magnetic field geometry, change local viewing angles, and thus modify the observed GS emission.

Figure 6.5 shows the radio spectra obtained from the COCONUT simulation with the CME of $\zeta = 70$. The plots are arranged similarly to those in Fig. 6.4, that is, the left column presents results based on spectral index $\delta = 2$, while the right column shows the plots for $\delta = 3$. Comparing the results for different spectral indices and spacecraft positions, we find qualitatively the same trends as in the CME case $\zeta = 30$. Again considering the $\delta = 2$ spectrum, we find that, for the halo view, the ratio between the peak intensities for the two spectral indices is approximately $I_{\mathrm{max},\delta=2}/I_{\mathrm{max},\delta=3} \approx 620$. At the edge-on-view location, we find a ratio of approximately 310, while at the face-on-view position, a ratio of about 208 is observed. The $\delta = 3$ electron spectrum results are qualitatively similar (see Table 6.3). The differences across observer positions again indicate that from the face-on-view vantage point, the highest intensity is detected, followed by the edge-on-view and halo-view positions. The ratios between the peak intensities are $I_{\mathrm{max,edge-on}}/I_{\mathrm{max,halo}} \approx 7.2$ and $I_{\mathrm{max,face-on}}/I_{\mathrm{max,halo}} \approx 12.8$.

In the $\zeta = 70$ case, our simulations additionally reveal a secondary emission lane at higher frequencies, distinct in drift rate and typically weaker than the main lane. These secondary lanes appear only in the edge-on and face-on view configurations, where some of the LOS from the observer's viewing field intersect regions in the lower MFR flanks close to the MFR footpoints. Although the actual footpoints are not directly visible in these views, the detected GS emission originates from nearby locations where the magnetic field is strong, and the LOS orientation is largely perpendicular to the local field direction. These regions also exhibit enhanced pitch angle anisotropies and may contain distinct populations of high-energy electrons. The footpoints themselves remain anchored and largely static; however, the close MFR flank regions continue to

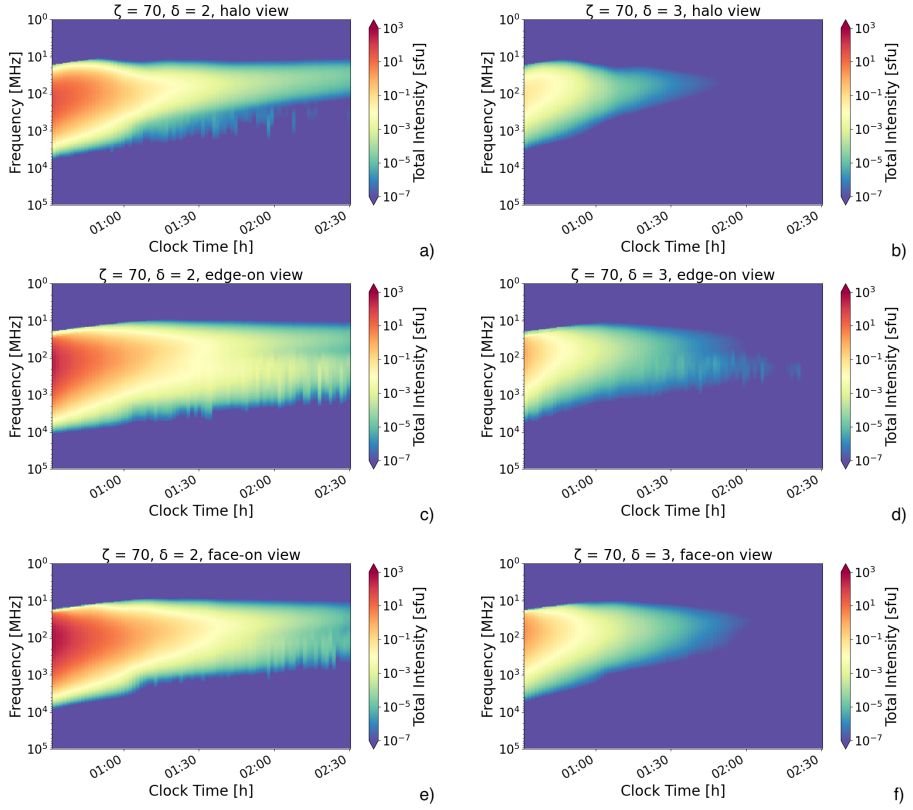

Figure 6.5. Synthetic radio spectra for the CME case with $\zeta = 70$. The panels in the left column show the observed radio emission from the injection spectrum with $\delta = 2$ seen from the three spacecraft locations, while the panels in the right column contain the radio emission from the injection spectrum with $\delta = 3$.

expand over time, leading to moderate field weakening and a slight frequency drift. As electrons move into stronger magnetic fields near the footpoint regions, they conserve their magnetic moment (Eq. 2.19), requiring an increase in pitch angle and leading to magnetic mirroring. This process results in localised, time-varying enhancements in GS brightness that manifest as the observed secondary emission lanes, visible in the plots at frequencies above 100 MHz and extending into the GHz range.

The total synchrotron power from a single relativistic electron can be derived from the Liénard formula (Rybicki & Lightman, 1986), and is approximately given by

$$P_{\rm syn} \approx \frac{4}{3}\,\sigma_{\rm T}\,c\,\gamma^2\,\beta^2\,U_B\,\sin^2\alpha\,, \tag{6.2}$$

where the emission strength depends on the electron speed, the magnetic energy density $U_B = B^2/(8\,\pi)$, and the pitch angle term $\sin^2\alpha$. Here, $\sigma_{\rm T}$ denotes the Thomson scattering cross-section. Near the MFR footpoints, both B and α tend to be large, substantially enhancing $P_{\rm syn}$. As electrons are trapped within the MFR, they mirror at the stronger magnetic fields near the footpoints and travel back towards the weaker field near the MFR apex. Each time they pass through the footpoint regions, they produce bursts of local synchrotron emission, leading to a periodic emission pattern. Since the lower MFR regions near the magnetic footpoints are compact and maintain strong magnetic fields and large pitch angles, they produce locally strong GS emission despite their limited spatial extent. In our simulation setup, electrons are magnetically confined and mirror in these lower regions of the MFR, which remain anchored to the surface. This trapping mechanism contributes to the intermittent GS enhancements observed along the LOS intersecting these regions.

In contrast, the primary GS lane originating from the main body of the expanding MFR appears smoother and more continuous. The gradual expansion of the MFR causes the magnetic field magnitude to decrease, leading to a steady, upward frequency drift. Although magnetic fields near the footpoints are stronger, the total emission is dominated by the larger electron population distributed throughout the main body of the flux rope. The secondary emission lane, by comparison, appears more intermittent and consists of faint, locally enhanced features of GS emission. These features arise from a smaller electron population and are linked to confined mirroring in lower regions of the MFR flanks near the footpoints.

In more complex scenarios, flux ropes can expand rapidly and non-ideally in the solar corona, developing kinks, deflections, and asymmetries. These deformations may produce multiple distinct drifting GS lanes, each dependent on observer perspective and characterised by unique emission signatures. While

our model assumes a simplified scenario with constant footpoints and no new flux emergence or footpoint diffusion, more intricate flux rope dynamics, such as increased twist or enhanced poloidal magnetic fields, could introduce localised gradients that might alter electron mirroring. In such cases, bursty broadband emissions can arise near footpoints and throughout other regions of the flux rope structure.

We note that the employed MFR model is already significantly more realistic than many idealised models historically used in GS studies (e.g. Dulk 1973; Fleishman & Melnikov 2003; Kuznetsov et al. 2015). Our erupting MFR introduces a dynamically evolving magnetic topology with strong twist, leading to varying field curvatures and strengths, all of which directly affect particle transport and confinement. Furthermore, the continued expansion and radial outward propagation of the MFR also involves time-dependent variations in both field strength and geometry, capturing important physical aspects relevant to GS emission in a type IV burst. In contrast, flux emergence and footpoint diffusion processes occur on much longer timescales (e.g. Giacalone & Jokipii 2004) than those associated with the particle acceleration and GS emission modelled here in the low corona, and are therefore expected to have a negligible influence on the simulation results.

Finally, we may compare the differences in the intensities of the GS emission for the different CME cases. Considering the spectral index $\delta = 2$, we note from the halo view observer that the peak intensity in the $\zeta = 70$ case is about 16 times higher compared to $\zeta = 30$, at the edge-on view about 9 times higher, and at the face-on view also about 9 times higher. Qualitatively similar results are found for the $\delta = 3$ spectra, and all ratios are summarised in Table 6.3. The stronger GS intensities in the $\zeta = 70$ simulation can be attributed to the stronger magnetic field strengths present within the CME, consistent with Eq. (6.2). Additionally, a higher degree in twist associated with larger ζ-values may enhance the variation in the magnetic field along the MFR, promoting more effective magnetic mirroring and particle confinement, thus yielding longer-lasting and more intense GS emission.

To further illustrate the differences in the observed GS emission intensities and their relationship to the magnetic field configuration, Fig. 6.6 shows the weighted mean magnetic field strength evolution for different observer vantage points and CME setups. The mean field was computed by weighting the magnetic field along each line of sight using the electron distribution from the $\delta = 2$ case, followed by averaging across all LOS for each observer position. These values are not direct measurements of the local field at emission sites, but rather effective field strengths that contribute to the observed GS signal from each vantage point. As a result, they tend to be lower than typical observational estimates (e.g. Maia et al. 2007; Tun & Vourlidas 2013), which often reflect localised peak

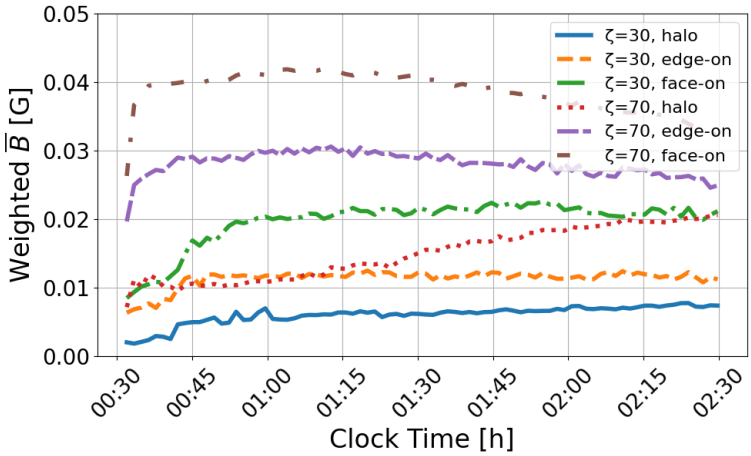

Figure 6.6. Comparing the weighted mean magnetic field strength over time for different observer positions and CME cases. For calculating the weighted average $\overline{B}$, we used the electron distribution of the $\delta = 2$ case. Each curve corresponds to a specific vantage point (halo, edge-on, face-on) and CME case ($\zeta = 30$, $\zeta = 70$).

values near the emission core. In our model, localised fields in parts of the CME (e.g. in the MFR flanks) are indeed higher, but their contribution is diluted in the averaged LOS-weighted magnetic field.

A clear positive correlation is observed between stronger magnetic fields and higher GS emission intensities. The highest emission levels occur in the $\zeta = 70$ CME simulation for the face-on and edge-on views, which coincide with the strongest weighted magnetic fields in Fig. 6.6. Additionally, the halo view observer in the $\zeta = 70$ case registers stronger magnetic fields than the halo and edge-on view observers in the $\zeta = 30$ simulation, consistent with the observed peak GS intensities (see also Fig. 6.8).

The magnetic fields observed in the $\zeta = 70$ halo view are initially weaker than those in the $\zeta = 30$ face-on view, which is consistent with the detection of slightly lower GS intensities; however, this trend reverses at later times. Notably, the rising trend of the $\zeta = 70$ halo view curve does not necessarily indicate an increase in the CME's field strength but may result from CME expansion. When comparing field strengths along individual halo view LOS, we observe that increasing values occur along LOS farther from 90° colatitude and 180° longitude (i.e. the central launch coordinates of the CME) and into which the CME expands. In contrast, LOS already intersecting the CME and closer to these coordinates show a declining field strength over time. As a result, the final curve in Fig. 6.6 reflects the growing contribution of oblique LOS contributing

to the overall averaging.

As described earlier, the simulations both in Figs. 6.4 and 6.5 indicate a shift of the peak intensities from higher to lower frequencies with time. To illustrate this frequency drift, we present two examples in Fig. 6.7, where the left panel shows the case $\zeta = 30$ (same as the top left panel in Fig. 6.4), and the right panel shows the case $\zeta = 70$ (same as the top left panel in Fig. 6.5). Both panels correspond to the halo view and are based on $\delta = 2$. The black dotted curve indicates the peak intensities in the observed radio spectrum at each time step. To compare the results with theoretical expectations and to serve as a form of model validation, we additionally calculated the characteristic synchrotron peak frequencies following Ginzburg (1979) and Longair (1992) as

$$f_{\omega,\mathrm{peak}}(t) = \frac{3}{4\,\pi}\,\frac{e\,B(t)}{m_\mathrm{e}\,c}\,\gamma^2 = \frac{3}{4\,\pi}\,\Omega(t)\,\gamma^2\,, \tag{6.3}$$

which are included as dark-red dashed curves in Fig 6.7. Here, Ω is the gyrofrequency as defined in Eq. (A.83). For the magnetic field in Eq. (6.3), we calculated a linearly weighted mean of B along each line of sight, using normalised particle intensities as weights. The simulation and theoretical peak frequencies are in reasonable agreement, showing a similar trend. We note that Eq. (6.3) is formulated for a single (constant) Lorentz factor. Since the highest-energy electrons contribute most to the GS emission in type IV radio bursts, we computed the Lorentz factor based on an electron kinetic energy of 9 MeV. However, choosing lower energies can significantly alter the theoretical curve, as the Lorentz factor in Eq. (6.3) is a constant scaling factor. For instance, using a kinetic energy of 6 MeV instead of 9 MeV would reduce the theoretical frequencies to approximately 47% of their original values.

Finally, we illustrate in Fig. 6.8 single-line profiles of the observed intensities as a function of frequency, approximately 32 minutes into the simulation and about 3 minutes after the electron injection. The left column shows $\zeta = 30$ results, while the right column corresponds to $\zeta = 70$, with rows ordered according to the three spacecraft positions. Each panel contains results based on the two spectral indices $\delta = 2$ (black solid curve) and $\delta = 3$ (red dashed curve). As noted in the discussion of the histograms above, the smaller spectral index (i.e. a flatter slope) consistently produced higher intensities.

Furthermore, in all cases, the roll-over (i.e. the transition from the optically thick, self-absorbed regime to the optically thin, emission-dominated regime), indicated by the vertical lines, occurs at higher frequencies for the $\delta = 2$ electron spectrum compared to the $\delta = 3$ spectrum. The roll-overs are found between 165 MHz and 300 MHz in the $\zeta = 30$ simulation, and between 65 MHz and 145 MHz in the $\zeta = 70$ simulation, with those for the smaller spectral index being shifted to higher frequencies by approximately 40 MHz to 70 MHz.

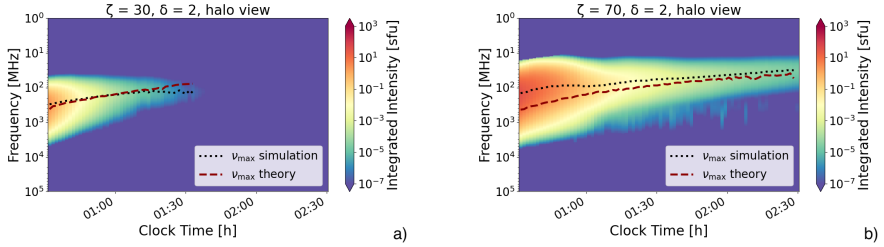

Figure 6.7. Radio spectra with the peak intensity drifts from the simulation results and those calculated from theory. Exemplary, the drift of the peak intensity from higher to lower frequencies with time is shown for the case $\zeta = 30$, $\delta = 2$ (left panel), and $\zeta = 70$, $\delta = 2$ (right panel), both seen from the halo view. The black dotted curve shows the peak intensities from the simulation results, while the dark-red dashed curve shows the theoretical peak intensities calculated with Eq. (6.3).

Comparing the spectra across the spacecraft positions for each CME case also reveals a shift of the roll-over frequency to lower values for vantage points where stronger GS emission was observed. When comparing the results across the two CME cases, we find that for $\zeta = 70$ (a stronger magnetic field), the roll-over occurs at lower frequencies (approximately 65 MHz to 145 MHz) compared to the corresponding $\zeta = 30$ case (approximately 165 MHz to 300 MHz).

At first glance, this contradicts Eq. (6.3), since the frequency at the intensity peak scales with the electron gyrofrequency and thus with the magnetic field strength. However, the spectra in Fig. 6.8 show that the slopes of the intensity curves in the $\zeta = 70$ case are steeper than in the $\zeta = 30$ case, suggesting stronger self-absorption, which shifts the roll-over to lower frequencies, reducing the transition to the optically thin regime.

Although the intensity curves displayed in Fig. 6.8 do not have a clear power-law form, they nonetheless suggest spectral indices χ that are steeper than those predicted by conventional analytical models of synchrotron and GS emission. In the optically thin regime, the typical relation for synchrotron emission is $\chi = (\delta - 1)/2$ (Ginzburg & Syrovatskii, 1964), while a commonly used approximation for GS emission is $\chi = 0.9\,\delta - 1.22$ (Dulk & Marsh, 1982). As expected, the GS slope is steeper than that of pure synchrotron emission, likely due to propagation effects and the influence of the ambient medium. At the same time, these idealised expressions do not fully capture the complexities of real systems. Observational data frequently reveal significantly steeper indices in electron distributions, and our particle transport simulations are consistent with this pattern, showing early deviations from the initial spectral index of the injected electron distributions towards steeper slopes (Milligan

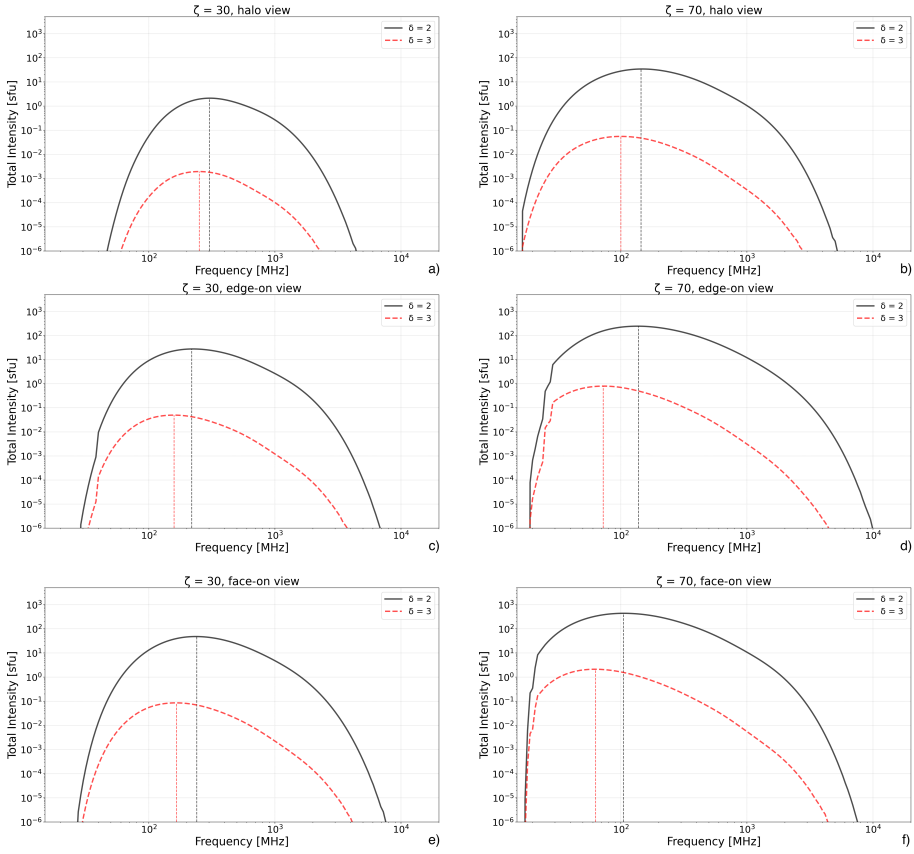

Figure 6.8. Intensity curves as a function of frequency for a single time. The panels in the left column show the emission spectra in the case $\zeta = 30$ of the electrons injected with spectral indices $\delta = 2$ (black solid line) and $\delta = 3$ (red dashed line). In contrast, the right column depicts the equivalent results in the case $\zeta = 70$. Vertical lines mark the roll-over (or peak) frequencies. All spectra were recorded approximately 32 minutes into the simulation, which is about 3 minutes after the injection of the electrons.

et al., 2006; Glesener et al., 2020; Wang et al., 2021). This steepening may, in part, be explained by energy-dependent transport effects. Lower-energy electrons (e.g. $\sim$ 100 keV) have longer effective residence times in the flux rope due to their smaller velocities and reduced mirroring rates. In contrast, higher-energy electrons undergo more frequent magnetic mirroring between footpoints, increasing their probability of entering the loss cone and precipitating. Thus, their reduced contribution to the observed emission can lead to a steeper spectral slope. Additional discrepancies between analytical predictions and our numerical results may arise from uncertainties in the ambient plasma properties and simplifications inherent in analytical models.

While we considered only (incoherent) GS emission in the present study, the presence of coherent emission mechanisms, often proposed for type IV bursts, cannot be ruled out. Plasma emission, in particular, has been suggested for both type IVs (Weiss, 1963; Benz & Tarnstrom, 1976) and type IVm bursts (Gary et al., 1985; Morosan et al., 2019). In addition, maser emission driven by a maser instability in non-thermal electron populations with strong perpendicular anisotropy, typically characterised by a loss-cone distribution, has frequently been proposed as a contributing mechanism (Winglee & Dulk, 1986; Aschwanden & Benz, 1988; Treumann et al., 2011; Morosan et al., 2016). Under suitable conditions, such instabilities can amplify electromagnetic waves near the electron gyrofrequency (e.g. Tsytovich 1970; Papadopoulos & Freund 1979; Galeev & Krasnoselskikh 1979). Whether such plasma instabilities actually develop in coronal conditions similar to those modelled here, and whether the resulting coherent emission is present in observed type IV radio spectra, remains an open and debated question (e.g. Morosan et al. 2016; Carley et al. 2017).

6.4 Summary and discussion

With this study, we presented a novel coupling of three models to generate synthetic radio spectra and investigate the influence of different injection spectra and initial CME parameters on the observed emission spectra. Using the 3D MHD coronal model *COCONUT*, we constructed a coronal configuration based on an HMI magnetogram. We then performed two simulations, each modelling a CME as an MFR with different initial properties in terms of magnetic field strength and speed, encapsulated in the dimensionless parameter ζ, here with values of 30 and 70. Next, we used the SEP model *PARADISE* to simulate energetic electrons trapped within the erupting MFR. Finally, using *COCONUT*'s plasma parameters and the electron energy distributions obtained from *PARADISE*, we applied the *UFGSC*s to compute GS emission from the

trapped electron populations as observed from three different vantage points (halo view, edge-on view, face-on view) in the solar corona.

Comparing the radio spectra for each CME across different spectral indices, we found that the flatter spectrum with $\delta = 2$ consistently produced stronger GS radiation and longer-lasting radio bursts than the steeper spectrum with $\delta = 3$. A comparison between the two CMEs revealed that the electrons in the $\zeta = 70$ CME, characterised by a stronger initial magnetic field strength (nearly twice that of the $\zeta = 30$ CME) and a higher initial speed, generated much more intense GS emission. Finally, benchmarking the three observer positions against each other demonstrated that the strongest GS emission was detected when the spacecraft was above the CME, followed by the perspective viewing both CME flanks from an edge-on view. In contrast, the weakest GS emission was detected when the observer faced the front of the approaching CME (halo view).

It should be noted that modifying the employed energy range or further steepening the injection spectrum would significantly affect the resulting GS emission, including frequency range, intensity, and duration. Since an electron's pitch angle directly influences its radiated power, the initial pitch angle distribution of the injected population can also impact the morphology and quantitative properties of the resulting type IV spectra. While we adopted an isotropic distribution in this study, test simulations with highly beamed electron populations revealed a range of pitch angle distributions at early times in the type IV event, depending on the energy channel and location. For instance, we found single electron beams (both field-aligned and anti-field-aligned), counter-beam populations, and populations transitioning towards isotropy. The computed spectra were morphologically similar, but showed slightly reduced peak intensities (by ~ 20 %). This is consistent with theoretical expectations for smaller pitch angles. Furthermore, the reduced GS emission may also stem from a significant fraction of particles entering the magnetic bottle's loss cone, leading to precipitation into the inner simulation boundary and their removal from the simulation.

A detailed exploration of these dependencies goes beyond the scope of the present study. In future work, we aim to conduct MHD and transport simulations with significantly higher temporal resolution (e.g. 10 s sampling times), focusing on the early evolution (first 30–60 min) of type IV events to investigate the role of pitch angle and other energy distributions (e.g. initially monoenergetic or kappa-distributed, or using different energy ranges) more systematically.

The radio spectra obtained from our simulations suggest that type IV radio bursts contain GS radiation from electrons trapped within the strong magnetic field lines of CMEs. Furthermore, our results indicate that the GS emission primarily originates from the CME flanks, consistent with imaging observations

and previous studies (see, e.g. Gopalswamy & Kundu 1990; Bastian et al. 2001; Bain et al. 2014; Carley et al. 2020). Additionally, our simulations demonstrate that the orientation of the flux rope relative to the observer's LOS significantly influences the detected emission (e.g. Nindos 2020). This finding highlights the importance of multi-messenger observations, as the evolution of the radio source cannot be fully understood without complementary observational constraints.

All computed emission spectra exhibit a similar structure, consisting of a high-intensity core surrounded by regions of weaker emission, with the peak intensity gradually drifting to lower frequencies over time. These spectral features are physical within the GS framework implemented in the *UFGSC*s and arise entirely from incoherent GS emission. The spatial and spectral variations, such as LOS-dependent intensity patterns and secondary emission lanes, can be consistently understood using the Liénard formula (Schwinger, 1949). GS emission is particularly enhanced in MFR flank regions near the footpoints, where the local pitch angle distribution and magnetic field geometry favour spiky, burst-like signatures. These regions naturally support GS radiation, as similar behaviour is expected whenever electrons are injected into an MFR. However, the absolute brightness depends on the flux rope structure itself.

While the present work did not attempt a case study, several aspects support the physical realism of our simulation results. All three coupled models are physics based, providing physical credibility beyond empirical parameter fitting. Moreover, the morphological features of the obtained spectra match type IV observations. Finally, our results quantitatively fall within the observationally established ranges in terms of frequency intervals, spectral flux densities, frequency drift rates (supported by both literature values and theoretical expectations), and event durations.

In conclusion, our simulation results yield several key insights regarding GS emission in type IV radio bursts:

1. A synchrotron or GS background is likely present in most type IV radio bursts. The brightness of this background is determined by the high-energy electron distribution, the magnetic field strength, the topology, and other properties of the MFR confining the electrons, as well as its orientation relative to the observer.

2. GS emission is strongest in the CME flanks near the footpoints rather than the CME apex, due to stronger magnetic field strengths and more favourable pitch angle distributions, supporting earlier observations of enhanced GS emission from CME flanks.

3. Both spectral and spatial drift are natural consequences of CME expansion and evolving field conditions. In our simulations, the GS emission source

(i.e. energetic electrons) moves outwards with the expanding MFR, while the associated spectral drift depends on the magnetic field evolution and energetic electron distribution. This may help explain why some type IV bursts are observed as moving, while others appear stationary in radio imaging.

These findings emphasise the importance of considering GS emission as a fundamental mechanism in type IV radio bursts, and illustrate how CME properties and observer geometry shape the observed radio spectra. Additionally, our results suggest that type IVm spectra can exhibit drift rates below thresholds proposed in previous studies (e.g. Kumari et al. 2021), implying that some bursts classified as IVs might still be associated with erupting MFRs. While our analysis is based solely on the incoherent background continuum GS radiation, which nonetheless produces burst-like features consistent with the GS framework and the applied model, it does not necessarily exclude the presence of other emission mechanisms that may contribute to, or modify the observed spectral features. In particular, the observed spectral flux densities may result from a superposition of multiple mechanisms, including coherent processes, which may yield stronger emission than the GS component alone in our simulations. Ultimately, this study helps clarify the role of GS emission in shaping radio spectra and provides a framework for identifying regions where additional coherent emission from the maser instability might occur, which is beyond the scope of this work.

Finally, we would like to contrast our study with the recent work by Kozarev & Nedal (2025). The authors investigated whether GS emission contributes substantially to the quiet Sun's low-frequency radio spectrum (20–90 MHz). To achieve this, they employed a synoptic MHD model providing steady-state plasma parameters of the corona, and combined it with the *UFGSC*s using idealised electron distributions to generate GS emission maps under quiet-Sun conditions. The synthetic emission, comprising thermal bremsstrahlung and gyroresonance radiation, was then compared with LOw-Frequency ARray (LOFAR) observations. Subtracting the thermal images from the LOFAR data revealed an on-desk excess. The authors then compared separately computed synthetic GS maps to this excess and found broad spatial agreement, suggesting that quiet-Sun GS emission contributes to the observed excess. Both studies highlight that GS emission likely plays a crucial role in shaping solar radio spectra, whether during quiescent periods or eruptive events.

The present study with *COCONUT-PARADISE* and the *UFGSC*s provides a foundation for future research on CME kinematics and GS emission to infer electron properties and magnetic field characteristics within CMEs, with the potential for direct validation using radio and particle measurements from PSP.

Future work will also explore magnetoionic properties of GS radiation, focusing on polarisation to refine estimates of magnetic field strength and topology.

7

Conclusions

In this concluding chapter, we summarise and discuss the key findings of the thesis in Section 7.1, and outline potential directions for future research in Section 7.2, building on the modelling framework established in this work.

7.1 Summary and discussion

This thesis introduced a novel modelling framework to simulate the acceleration and transport of energetic particles in the solar corona and inner heliosphere, including the generation of associated radio signatures in the corona. Each development stage was accompanied by a dedicated application, designed to both demonstrate the model's capabilities and yield initial physical insights.

In Chapter 1, we discussed key aspects of solar physics and highlighted the complexity of the processes in coronal and heliospheric plasmas. To motivate the work presented in this thesis, we emphasised the increasing impact of space weather events on spacecraft and astronauts. Given the limited number of operating spacecraft providing in-situ and remote measurements in the heliosphere, and the interpretation difficulties of ML-based forecasting tools, sophisticated physics-based models are essential for advancing our understanding of the underlying physical mechanisms. For this reason, we extended the *EUHFORIA*-*PARADISE* framework for energetic particle modelling in the heliosphere in three stages: incorporating the advanced heliospheric model *Icarus*, the coronal model *COCONUT*, and the *UFGSC*s to compute GS emission.

In Chapter 2, we outlined the theoretical and mathematical foundations underlying the numerical models used throughout the thesis. For simulating

the heliospheric and coronal plasma environments, *EUHFORIA*, *Icarus*, and *COCONUT* solve the set of 3D ideal MHD equations, closed by an ideal equation of state. In-situ measurements frequently reveal the ubiquitous existence of non-thermal particle populations in (nearly) collisionless space plasmas. Nevertheless, the single-fluid MHD approach, implicitly assuming particle distributions close to Maxwellian, often works well at large scales because of the collective bulk behaviour and the high conductivity of the coronal plasma and solar wind.

Nonetheless, the MHD approach neglects important processes on the kinetic scale, such as MR and turbulence, which are crucial in dynamic plasma environments. To describe the propagation of energetic particle populations, including pitch angle scattering from turbulent magnetic fluctuations and CFD, the FTE is solved in *PARADISE*, bridging the gap between microscopic and macroscopic scales. The test particle approach employed in *PARADISE* is justified when energetic particle density and pressure are small compared to the background plasma. However, this framework does not account for wave-particle interactions amplifying Alfvénic turbulence that are believed to be significant near strong shocks, thereby neglecting the particle feedback on turbulence. Further limitations arise from our incomplete understanding of turbulence in the corona and heliosphere.

We also derived the full GS emission and absorption coefficients from first principles, motivated by the fragmented and sometimes inconsistent original literature, which dates back to the 1950s and 1960s. By presenting a consistent and complete derivation, we illustrated how particle motion, background plasma parameters, and the shape of the electron distribution influence the GS emission. However, the current treatment only explicitly includes spontaneous emission but not stimulated emission, and neglects scattering, which may become relevant in dense or turbulent coronal conditions. Stimulated emission is implicitly included in the GS framework in Section 2.3 by defining the net absorption coefficient as the difference between stimulated absorption and stimulated emission. When the emission frequency approaches the low harmonics of the gyrofrequency and the electron distribution exhibits strong anisotropy, the Electron Cyclotron Maser Instability (ECMI) can occur, manifested as a negative absorption coefficient corresponding to wave amplification. However, using the *UFGSC*s primarily in the continuous mode smooths out the discrete resonance structure that enables the ECMI (Fleishman & Kuznetsov, 2010).

Furthermore, the macroscopic description of radiative transfer relies on assumptions from geometrical optics and overlooks constraints imposed by quantum uncertainty. This approach may break down when spatial or directional variations occur on scales comparable to the wavelength (i.e. $\mathrm{d}A\,\mathrm{d}\Omega_\mathrm{s} \gg \lambda_\mathrm{w}^2$). The frequency range considered in this work ($\sim 10^7$–10^{10} Hz) corresponds to wavelengths of approximately 10^{-2}–10^{1} m. Consequently, spatial structures and

angular variations in the simulation are expected to be large compared to the radio wavelengths, and the initial assumption should remain valid. Additionally, the straight-line transport approximation used for the ray paths is largely justified in the considered frequency range, but may become inaccurate at lower frequencies or in regions with strong gradients in plasma density and refractive index, where refraction can no longer be neglected. Thus, once lower frequencies in the kilohertz range or below are considered, where wavelengths approach $\sim 10^5$ m and small-scale structures such as thin current sheets become relevant, alternative methods beyond the standard RTE application may have to be considered (e.g. Rybicki & Lightman 1986). Moreover, at such low frequencies the Razin effect becomes increasingly relevant, suppressing GS emission.

In Chapter 3, we described the numerical models used in this work and detailed the main modifications implemented in *PARADISE* to support outputs of the MHD models. To enable coupling with *Icarus*, we included the necessary algorithms to trace particles, locate grid points, and compute the various gradients of the solar wind parameters on block-based grids. Special care was required to handle cases near block edges, which requires communication between several blocks, particularly when multiple levels of AMR are applied. To enable coupling with *COCONUT*, we further modified *PARADISE* by including algorithms for unstructured grids. A major difference involved the gradient computation, where the finite difference schemes used for structured *EUHFORIA* and *Icarus* grids had to be replaced by a least-squares approach with Taylor expansions. These upgrades significantly extend the range of applications for *PARADISE*, allowing energetic particle studies across the heliosphere and low corona. However, these developments also led to increased computational costs due to larger data volumes, finer time resolution requirements in coronal simulations, and a greater number of individual steps in the modelling chain.

In Chapter 4, we introduced *Icarus-PARADISE* as the first enhancement of the original *EUHFORIA-PARADISE* framework, primarily to overcome resolution limitations and reduce computational costs associated with *EUHFORIA*. We applied this model to study particle acceleration and transport at a CIR using a synthetic solar wind configuration. After validating the new model against results from the original setup, we systematically increased the levels of AMR at the CIR shocks to explore their effect on particle acceleration. The obtained particle intensity profiles and intensity-energy spectra clearly showed that higher refinement led to more efficient particle acceleration, highlighting the importance of shock resolution for correctly capturing DSA processes. Additionally, we observed the emergence of small-scale solar wind structures at higher AMR levels, which may further modulate particle transport. While AMR improves shock modelling in *Icarus*, the relatively diffusive TVDLF scheme may still limit the sharpness of shocks. Future work can benefit from exploring sharper

numerical schemes available in the *MPI-AMRVAC* framework.

In Chapter 5, we introduced the *COCONUT-PARADISE* model to study particle transport in the corona, potentially including CMEs. This step was motivated by recognising that critical space weather processes, including CME evolution, shock formation, and SEP acceleration, originate in the lower corona. As a first application, we generated realistic coronal configurations with a CME modelled as an MFR, and injected energetic protons inside one of the MFR flanks. To investigate particle confinement and escape, we first performed simulations without CFD, in which particles remained entirely confined within the CME. We then considered two different CFD approaches, one assuming a constant perpendicular MFP, and another using a Larmor radius-dependent MFP. In both cases, we found that reducing the relevant parameter by just one order of magnitude produced substantial differences in the degree of particle escape via CFD, illustrating that even values commonly used in heliospheric models—while yielding moderate CFD there—can lead to significantly enhanced CFD in the corona. These results highlight the sensitivity of particle access to open magnetic field lines to the underlying CFD model and parameter choice.

Qualitative comparisons to PSP observations indicate consistency in the simulations with only weak CFD effects. However, the observations come from CME flanks, whereas in the simulations CFD was strongest at the CME apex. Limitations of our study involve the neglect of any acceleration processes that may occur for particles leaving the CME and becoming trapped at the shock front. Additionally, guiding centre drifts were omitted, though they may become more important for heavier or higher-energy ions and should be addressed in future work. Importantly, this coupling between *COCONUT* and *PARADISE* serves as a crucial intermediate step towards a comprehensive modelling chain from the solar surface to Earth's orbit and beyond, by additionally including *EUHFORIA* or *Icarus* to the simulation setup.

In Chapter 6, we presented the third stage of the development of the new modelling framework by incorporating GS emission into the coronal simulations. We motivated this step by the relevance of radio signatures in space weather, particularly their potential to serve as precursors of CME and SEP events, and their use in inferring magnetic field strengths in CMEs near the Sun. Building on the setup from Chapter 5, we simulated confined electron transport within an MFR. We investigated how GS emission spectra depend on CME properties, injection spectra, and the observer's vantage point. We considered two CME setups, differing in initial magnetic field strength and eruption speed, two power-law indices for electron injection, and three idealised observer positions.

Using the MHD and transport simulation results as inputs for the *UFGSC*s, we computed GS emission. The resulting spectra resembled observed type IV

spectra, displaying realistic frequencies, durations, solar flux densities, and morphological features, including a bursty core surrounded by weaker emission, and a gradual frequency drift over time. We showed that GS emission alone can produce features typically seen in type IV spectra, without requiring additional coherent mechanisms. The variations in duration and intensity across different spectral indices, CME cases, and viewing geometries were physically consistent with differences in particle energies, magnetic field topology and strength, and LOS effects. However, it is commonly believed that GS emission forms the background continuum, while the bursty spikes are attributed to coherent plasma or maser emission.

Our main findings included that GS emission is a key contributor to type IV spectra, and that GS emission is strongest near the CME flanks close to their footpoints, where stronger magnetic fields and favourable pitch angle distributions enhance GS emission. While spatial drifts were naturally explained by the CME expansion, spectral drifts were associated with changing field strengths and electron energies. The sensitivity of our results to observer geometry highlights the importance of multi-messenger radio measurements during space weather events.

The ability of the model to reproduce characteristic type IV features from first principles, without empirical fitting, offers a powerful diagnostic tool for interpreting type IV bursts. However, the current implementation overlooks coherent emission mechanisms, which may predominate in certain real events and thus lead to underestimations of the spectral flux. Ideally, future frameworks would allow for multiple emission mechanisms that can be switched on and off to isolate contributions. Additionally, we adopted an isotropic pitch angle distribution, while test cases with electron beam populations showed notable differences in the spectra, motivating a more systematic exploration in future GS studies.

7.2 Outlook

We conclude this thesis by discussing some of the possible future research directions that can be built upon using the developed modelling framework and established results. While Chapters 4–6 already introduced some of the anticipated applications, we summarise here the main ideas along with additional opportunities.

Possible studies involving the *Icarus*-*PARADISE* framework include the following projects:

- Less diffusive shock-capturing schemes, such as HLL or Roe-type solvers, can be explored to improve shock resolution and enhance particle acceleration modelling.
- In the initial study in Chapter 4, we only applied AMR, but future studies will also consider grid stretching. Although currently implemented only in the radial direction, a generalised version allowing stretching along any coordinate axis (limited to one axis at a time) could be implemented in *PARADISE* with little effort.
- With the ability to locally achieve high resolution in the solar wind, the model can be applied to study particle dynamics in the HCS, where the role of classical drifts, and enhanced trapping or scattering remain debated (e.g. Burger et al. 1985; Khabarova et al. 2015).
- As discussed in Section 1.2.3, non-thermal particle populations are ubiquitously present in the heliosphere. Previous theoretical studies have shown that superthermal particles, well-described by standard Kappa or regularised Kappa distributions, can significantly enhance transport coefficients (Husidic et al., 2021, 2022). Future studies may explore the use of these more realistic Kappa distributions as seed populations in particle acceleration and transport models, implement and test transport coefficients derived from non-Maxwellian theory, and compare model predictions with data from PSP, SolO, and others.
- Another promising direction involves exploiting recent upgrades in the Icarus code, which now supports dynamic inner boundary conditions (Baratashvili et al., 2025). In contrast to the steady-state inner boundary used in this thesis or in earlier studies, time-updated magnetograms allow for a more realistic modelling of the evolving solar wind, which may affect the results of particle acceleration and transport studies at CIR and CME-driven shocks.

Potential future work with *COCONUT-PARADISE*, including the extension for modelling GS emission and potential combinations with *EUHFORIA* or *Icarus*, may involve the following points:

- The next logical step is to extend the energetic particle modelling domain to cover both the corona and the inner heliosphere. This can be done by using *COCONUT-PARADISE* either with *EUHFORIA* or *Icarus*. Such a setup would allow to study particle acceleration at a CME-driven shock already from the low corona through interplanetary space, both in theoretical and real-event simulations, and across different solar cycle phases.

- With a global model, CFD effects can be examined in more detail. This includes testing alternative CFD approaches, exploring parameter ranges different for coronal and heliospheric transport, and possibly including guiding centre drifts.
- The combined model encompassing the corona and heliosphere may allow to study conditions under which particles accelerated at CME-driven shock waves could return to the solar surface and produce long-duration gamma-ray flares.
- For space weather forecasting, fast simulations are essential. Since particle tracing and gradient computations on unstructured grids are computationally demanding, improving the interpolated structured-grid version of *COCONUT-PARADISE* with more sophisticated interpolation methods, such as those beyond simple linear interpolation, could provide a valuable alternative to the unstructured version.
- The combined framework of *COCONUT-PARADISE* and the *UFGSC*s allows detailed studies of the early phase of type IV events with higher spatial and temporal resolution, particularly how varying pitch angle and energy distributions affect the shape and intensity of GS spectra.
- Since GS emission is modelled in isolation, we can explore how the intrinsic magnetic field of CMEs influences GS emission and may derive magnetic field strengths from GS spectra.
- While our current work focused on incoherent GS emission, future projects may incorporate coherent emission mechanisms, such as maser emission, to evaluate their contribution to real type IV spectra.
- Finally, the polarisation states of the radio emission can be investigated to determine under which conditions polarisation-altering effects, such as Faraday rotation or mode coupling, can be neglected, and when they must be explicitly taken into account.

Common to all the modelling efforts presented in this thesis is the growing potential for model validation, parameter constraints, and case studies, utilising data from modern spacecraft, most notably PSP and SolO. Due to their unprecedented proximity to the Sun, these missions have already delivered valuable insights into solar eruptive events and the properties of energetic particles in the corona and inner heliosphere (see references in Chapter 5). Several upcoming missions are expected to expand our observational capabilities. For instance, the Japanese mission SOLAR-C, scheduled for launch in 2028, is designed to address the coronal heating problem, solar wind generation, and MR

processes through high-resolution spectroscopic imaging (Suematsu et al., 2021). In addition, NASA's Interstellar Mapping and Acceleration Probe (IMAP), planned for launch in September 2025, will investigate the interaction between the solar wind and the interstellar medium via Energetic Neutral hydrogen Atom (ENA) imaging, and will provide in-situ measurements of accelerated SEPs (McComas et al., 2018). In this context, IMAP's ENA observations may also serve to probe SEP acceleration and transport processes (Mewaldt et al., 2009). As PSP and SolO continue to explore different regions of the solar atmosphere and interplanetary space, and as upcoming missions become operational, their findings can be incorporated into the modelling framework presented here to further improve realism and predictive capabilities.

In conclusion, the thesis presented a versatile, physics-based modelling framework capable of generating complex and realistic coronal and heliospheric 3D configurations, simulating the acceleration and transport of energetic particles, including diffusive processes due to turbulence, and modelling radio signatures generated by energetic particles propagating through the MHD backgrounds. While each model has its limitations, including simplifying assumptions about the background plasmas and shocks, uncertainties in turbulence and diffusion models, and the neglect of scattering effects together with the use of straight-line approximations in the radiative transfer, the combined framework nonetheless offers a significant step towards self-consistent multi-scale modelling of SEP events and associated radio signatures derived from fundamental physical principles.

A

Appendix

In this appendix[1], we provide supplementary derivations that expand on the formalism presented in Section 2.3.

A.1 Validity of the straight-line transport approximation of radio waves

In Section 2.3.1, we assume that electromagnetic radiation emitted by a radio source propagates as straight rays towards the observer. This is a reasonable and commonly used approximation in a (nearly) perfect vacuum. However, in a magnetoionic medium such as the coronal plasma, spatial gradients in density and the presence of magnetic fields can significantly modify the propagation and characteristics of electromagnetic waves. These effects may include ray bending due to spatial variations in the refractive index (e.g. Moschou et al. 2018), suppression of propagation if the wave frequency falls below the local plasma cut-off (e.g. Melnikov et al. 2008), a change in polarisation due to Faraday rotation (e.g. Mancuso & Spangler 2000), energy exchange between different wave modes via mode coupling (e.g. Sirenko et al. 2002), and scattering of photons into or out of the ray path (e.g. Murphy et al. 2021).

The total intensity and the polarisation state of electromagnetic radiation can be described by the four Stokes parameters I, Q, U, and V (Chandrasekhar, 1960; Schaefer et al., 2007). In Chapter 6, we consider only the total intensity (i.e. sum over all polarisation components, represented by Stokes parameter I), which is generally not affected by Faraday rotation or mode coupling under

[1]This appendix is based on CGS units.

typical coronal conditions. However, scattering can significantly impact the observed intensity, for instance, when the radio emission is near the local plasma frequency or propagates through regions of strong density turbulence (Krupar et al., 2018; Kontar et al., 2019). A detailed treatment of polarisation and scattering effects is deferred to future work. Therefore, in this section[2], we outline the limitations of the straight-line transport approximation, describe the conditions under which it remains valid, and address the effects of emission suppression and ray-bending that may influence radio wave propagation in a magnetised plasma, within the scope of the present thesis.

Propagation limits and transmissibility in a plasma

For electromagnetic waves to propagate through a plasma, their frequency must exceed the local plasma frequency. Otherwise, due to the collective behaviour of the plasma, waves become evanescent, with a decay length given by the (electron) inertial length or skin depth, defined as $l_e = c/\omega_{pe}$ (e.g. Goedbloed et al. 2019). In the case considered in Chapter 6 (cold plasma limit), wave frequencies must exceed the local cut-offs: the O-mode requires $\omega > \omega_{pe}$, while the X-mode has an angle-dependent cut-off. In the high-frequency limit, the refractive index for both modes tends to unity ($n_\pm \to 1$), and the medium becomes effectively transparent (Stix, 1962; Budden, 1985). At low frequencies, GS emission can be suppressed by the Razin effect, which becomes important below a characteristic scale $\omega_{Ra} \sim \omega_{pe}^2/\Omega_e \propto n_e/B$. The Razin effect refers to the suppression of synchrotron or GS radiation at low frequencies in a dense plasma, where $n < 1$ (Ginzburg & Syrovatskii, 1965). Since the frequencies used in this work satisfy $\omega \gg \{\omega_{pe}, \Omega_e, \omega_{Ra}\}$, dispersion effects are weak and GS emission is not suppressed (Dulk, 1985), and the radiation can propagate through the coronal plasma to reach the observer in our simulations.

Refraction of electromagnetic waves

Electromagnetic waves can undergo refraction (i.e. a change in propagation direction), when the ambient medium exhibits spatial variations in refractive index (Eq. 2.52), typically caused by gradients in the dielectric response. Moschou et al. (2018) demonstrate ray-bending in ray-tracing simulations of (magnetoionic) coronal models (see their Eqs. 8–10), particularly at low radio frequencies (tens to hundreds of MHz) and in regions with strong density gradients. In addition, small-scale density fluctuations can cause scattering and angular broadening of the rays (e.g. Ingale et al. 2015).

[2]I would like to thank Dr Immanuel Christopher Jebaraj for valuable discussions and assistance with this section.

In the present work, we restrict our model to the high-frequency, weak-gradient magnetoionic limit. We denote the angular wave frequency as ω, and the (electron) plasma frequency as $\omega_{\rm pe} = \sqrt{4\,\pi\,n_{\rm e}\,e^2/m_{\rm e}}$, where $n_{\rm e}$ is the electron number density, e the elementary charge, and $m_{\rm e}$ the electron mass. The electron gyrofrequency is given by $|\Omega_{\rm e}| = e\,B/(m_{\rm e}\,c)$, with B the magnetic field strength and c the speed of light in vacuum. The Appleton-Hartree formula (Stix, 1962; Budden, 1985) shows that in the limit $\omega \gg \omega_{\rm pe}$ and $\omega \gg |\Omega_{\rm e}|$, the two magnetoionic modes, X-mode (corresponding to the plus sign) and O-mode (corresponding to the minus sign), satisfy

$$n_{\pm}^2 = 1 - \frac{\omega_{\rm pe}^2}{\omega^2} \pm \frac{\omega_{\rm pe}^2\,\Omega_{\rm e}\,\cos(\theta)}{\omega^3} + \mathcal{O}\left(\frac{\omega_{\rm pe}^4}{\omega^4}\right), \tag{A.1}$$

$$\Delta n \coloneqq n_+ - n_- \simeq \frac{\omega_{\rm pe}^2\,\Omega_{\rm e}\,\cos(\theta)}{\omega^3}, \tag{A.2}$$

$$n_{\pm} = n \simeq 1 - \frac{1}{2}\,(\omega_{\rm pe}/\omega)^2, \tag{A.3}$$

where θ is the emission angle (see also Section 2.3.8 and Appendix A.11). Equation (A.2) shows that birefringence decreases even more rapidly with increasing frequency, while Eq. (A.3) gives the first-order Taylor expansion of the refractive index for both modes (neglecting the birefringence term).

The bending of rays can be described using geometrical optics, assuming that spatial scales are much larger than the wavelength of the radiation, via the equations

$$\frac{{\rm d}\mathbf{r}}{{\rm d}s} = \hat{\mathbf{s}}, \tag{A.4}$$

$$\frac{\rm d}{{\rm d}s}(n\,\hat{\mathbf{s}}) = \nabla n, \tag{A.5}$$

along a ray path parametrised by arc length s, with unit tangent vector $\hat{\mathbf{s}}$ (see Chandrasekhar 1960; Born & Wolf 1999, and compare with Moschou et al. 2018). The local curvature of the rays is approximately given by $\kappa_{\rm c} \approx |\nabla_\perp \ln(n)|$, where $\nabla_\perp$ denotes the gradient component perpendicular to the local ray direction. Over a path of length L, the total bend angle satisfies

$$\theta_{\rm bend} \lesssim \int_0^L {\rm d}s\,\frac{|\nabla_\perp n|}{n}. \tag{A.6}$$

Using Eq. (A.3) for the refractive index, and defining a transverse density scale of $L_{\rm n} \coloneqq |\nabla_\perp \ln(n_{\rm e})|^{-1}$ (where $n_{\rm e}$ is assumed normalised to a reference value

before taking the logarithm), Eq. (A.6) becomes

$$\theta_{\rm bend} \lesssim \frac{1}{2} \left(\frac{\omega_{\rm pe}}{\omega}\right)^2 \frac{L}{L_{\rm n}} \,. \tag{A.7}$$

It follows from Eq. (A.7) that the straight-line approximation holds when $(\omega_{\rm pe}/\omega)^2 \, (L/L_{\rm n}) \ll 1$ (see the numerical estimate below, which shows that this condition is well satisfied in the high-frequency range). This is consistent with coronal ray-tracing studies showing that curved rays and straight lines converge at high frequencies above a few GHz (Moschou et al., 2018). While this condition is satisfied at the upper end of the frequency range obtained in the radio spectra in Chapter 6, for frequencies in the range of a few hundred MHz to a few GHz, the straight-line approximation could be regarded as a first-order treatment.

In Chapter 6, we solve the scalar RTE (Eq. 2.38) along fixed LOS, which approximate true ray paths. This is justified when the bend angle is small, as illustrated by the numerical example below at the upper frequency end of our computed spectra. The *UFGSC*s compute the GS emission and absorption coefficients (Eqs. 2.180 and 2.181, respectively) at each node along the LOS using the local plasma and magnetic parameters, and incorporating Razin suppression and self-absorption that are intrinsic to the plasma GS formulas.

To estimate the amount of ray bending, we use some of the values typical for our model in Chapter 6. Taking $n_{\rm e} \sim 10^8 \, {\rm cm}^{-3}$, we find $\omega_{\rm pe}/(2\,\pi) \approx 90 \, {\rm MHz}$. Assuming $B \sim 50 \, {\rm G}$, we obtain $|\Omega_{\rm e}|/(2\,\pi) \approx 140 \, {\rm MHz}$. Furthermore, we assume an observed frequency of $\omega/(2\,\pi) = 8 \, {\rm GHz}$, a ray path length of $L \sim 10^{10} \, {\rm cm}$, and a transverse density scale of $L_{\rm n} \sim 5 \times 10^9 \, {\rm cm}$, which are typical length scales associated with coronal loops (Reale, 2010; Peter et al., 2013). With these values, we find from Eq. (A.7) that $\theta_{\rm bend} \lesssim 1.3 \times 10^{-4} \, {\rm rad}$ ($\approx 0.007°$), which is negligible for our purposes.

Even at larger distances such as $L = 20 \, R_\odot \approx 1.39 \times 10^{12}$ cm, corresponding to the farthest virtual spacecraft positions in our simulations, the ray-bending amounts to only $\theta_{\rm bend} \approx 1.009°$. These values are representative of large-scale coronal conditions without strong discontinuities. However, we note that radio emission passing through regions such as CME shock sheaths may enhance refractive and scattering effects due to sharper density gradients and increased turbulence.

In conclusion, the straight-line approach using the scalar RTE (Eq. 2.38) is intended for cases with weak refraction, transparent and weakly dispersive propagation (i.e. $\omega \gg \{\omega_{\rm pe}, \Omega_{\rm e}, \omega_{\rm Ra}\}$, such that $n_\pm \approx 1$, and cut-offs are irrelevant), and an intensity-only scope. Under these conditions, straight-line transport accurately captures the Stokes parameter I for the GS problem

addressed in this thesis. A fully polarised, ray-traced treatment is beyond the scope of this work.

A.2 Derivation of Einstein-like relations

To derive relations between the coefficients for spontaneous emission (Eq. 2.39), stimulated emission (Eq. 2.41), and stimulated absorption (Eq. 2.43), we assume that electrons in a dilute plasma radiate independently. This implies that the differential rates η_ω, $\eta_{\omega\mathrm{S}}$, and $\eta_{\omega\mathrm{A}}$ (see Section 2.3.2) depend only on the position and momentum of individual electrons, and not directly on the distribution function. These rates are therefore microscopic, single-particle properties that characterise quantum mechanical transition probabilities between electron states induced by interaction with the electromagnetic mode density. The distribution function enters only when computing macroscopic quantities, such as j_ω and α_ω, via integration over phase space.

To calibrate the relative strength of spontaneous and stimulated processes, we consider a plasma volume element enclosed within an adiabatic shield at constant temperature, and assume Local Thermodynamics Equilibrium (LTE). In this regime, the radiation field must correspond to the black body spectrum, which, when accounting for dispersion, is described by the Planck formula (Bekefi, 1966)

$$B_\omega(\omega, \Theta) = \frac{n^2\,\hbar\,\omega^3}{8\,\pi^3\,c^2}\left[\exp\left(\frac{\hbar\,\omega}{k_\mathrm{B}\,\Theta}\right) - 1\right]^{-1}, \tag{A.8}$$

where k_B is Boltzmann's constant, and Θ is the temperature.

We then apply the principle of detailed balance, or equivalently microreversibility, which asserts that the probability of a process and its time-reversed counterpart are governed by the same quantum mechanical matrix elements (see Fermi's golden rule). For this, we require that the rate of emission from state $p \to p'$ equals the rate of absorption from state $p' \to p$. Using Eqs. (2.39), (2.41) and (2.43), this condition leads to

$$\begin{aligned}&\eta_\omega(\mathbf{r}, \mathbf{p})\, f(\mathbf{r}, \mathbf{p})\, \mathrm{d}^3p = \\ &I_\omega\left[\eta_{\omega\mathrm{A}}(\mathbf{r}, \mathbf{p}')\, f(\mathbf{r}, \mathbf{p}')\, \mathrm{d}^3p' - \eta_{\omega\mathrm{S}}(\mathbf{r}, \mathbf{p})\, f(\mathbf{r}, \mathbf{p})\, \mathrm{d}^3p\right],\end{aligned} \tag{A.9}$$

where I_ω is the spectral intensity of the radiation field.

Since the system is assumed in LTE, the electron momenta follow the relativistic Maxwell-Jüttner distribution. For our derivation, it is sufficient to note its

exponential dependence, given by

$$f(\mathbf{r},\mathbf{p}) \propto \exp\left(-\frac{E}{k_\mathrm{B}\,\Theta}\right), \tag{A.10a}$$

$$f(\mathbf{r},\mathbf{p}') \propto \exp\left(-\frac{E'}{k_\mathrm{B}\,\Theta}\right), \tag{A.10b}$$

where E and E' are the relativistic energies of the electron in states $\mathbf{p}$ and $\mathbf{p}'$, respectively.

Using the Maxwellian nature of the electron distributions from Eqs. (A.10a) and (A.10b), inserting them into Eq. (A.9), and noting that the radiation field satisfies $I_\omega = B_\omega$, we obtain

$$\eta_\omega(\mathbf{r},\mathbf{p})\,\exp\left(-\frac{E}{k_\mathrm{B}\,\Theta}\right)\mathrm{d}^3p = B_\omega(\omega,\Theta)$$
$$\times\left[\eta_{\omega\mathrm{A}}(\mathbf{r},\mathbf{p}')\,\exp\left(-\frac{E'}{k_\mathrm{B}\,\Theta}\right)\mathrm{d}^3p' - \eta_{\omega\mathrm{S}}(\mathbf{r},\mathbf{p})\,\exp\left(-\frac{E}{k_\mathrm{B}\,\Theta}\right)\mathrm{d}^3p\right]. \tag{A.11}$$

We now rearrange Eq. (A.11) to isolate $B_\omega(\omega,\Theta)$, divide both numerator and denominator by $\eta_{\omega\mathrm{S}}(\mathbf{r},\mathbf{p})\,\mathrm{d}^3p$, and apply energy conservation $E = E' + \hbar\,\omega$. Substituting the Planck function from Eq. (A.8), we find

$$\frac{n^2\,\hbar\,\omega^3}{8\,\pi^3\,c^2}\left[\exp\left(\frac{\hbar\,\omega}{k_\mathrm{B}\,\Theta}\right)-1\right]^{-1} =$$
$$\frac{\eta_\omega(\mathbf{r},\mathbf{p})/\eta_{\omega\mathrm{S}}(\mathbf{r},\mathbf{p})}{\{\eta_{\omega\mathrm{A}}(\mathbf{r},\mathbf{p}')\,\mathrm{d}^3p'/\left[\eta_{\omega\mathrm{S}}(\mathbf{r},\mathbf{p})\,\mathrm{d}^3p\right]\}\,\exp\left[\hbar\,\omega/\left(k_\mathrm{B}\,\Theta\right)\right]-1}. \tag{A.12}$$

Since this relation must hold for every frequency ω, the only way this equality can be satisfied consistently is if both the numerators and denominators on either side match separately. Equating these terms yields the Einstein-like relations

$$\eta_\omega(\mathbf{r},\mathbf{p}) = \frac{n^2\,\hbar\,\omega^3}{8\,\pi^3\,c^2}\eta_{\omega\mathrm{S}}(\mathbf{r},\mathbf{p}), \tag{A.13a}$$

$$\eta_{\omega\mathrm{A}}(\mathbf{r},\mathbf{p}')\mathrm{d}^3p' = \eta_{\omega\mathrm{S}}(\mathbf{r},\mathbf{p})\,\mathrm{d}^3p, \tag{A.13b}$$

which match Eqs. (2.46a) and (2.46b).

A.3 Momentum-space expansion of the distribution function

In the general expression for the absorption coefficient in Eq. (2.48), the difference between the electron distribution functions in momentum states $\mathbf{p}$ and $\mathbf{p}'$ appears. Since we work in the classical limit, assuming that the photon energy is much smaller than the electron energy, the momentum state transitions involve only small changes. Consequently, the difference $f(\mathbf{r}, \mathbf{p}') - f(\mathbf{r}, \mathbf{p})$ in Eq. (2.48) is small and can be approximated using a first-order Taylor expansion (Ramaty, 1969). In this expansion, derivatives are taken with respect to the Lorentz factor γ (representing energy) and pitch angle α, reading

$$f(\mathbf{r}, \mathbf{p}') - f(\mathbf{r}, \mathbf{p}) \approx \frac{\partial f}{\partial \gamma}(\gamma' - \gamma) + \frac{\partial f}{\partial \alpha}(\alpha' - \alpha)\,. \tag{A.14}$$

However, since particle transport equations are commonly expressed using momentum magnitude p and pitch angle cosine μ as independent variables, we transform the derivatives $\partial/\partial\gamma \to \partial/\partial p$ and $\partial/\partial\alpha \to \partial/\partial\mu$. To achieve this, we use the expressions for total electron energy and the Lorentz factor in terms of momentum magnitude, given by

$$E = \gamma\, m\, c^2\,, \tag{A.15}$$

$$\gamma = \sqrt{1 + \left(\frac{p}{m\, c}\right)^2}\,, \tag{A.16}$$

$$p = m\, c\, \sqrt{\gamma^2 - 1}\,, \tag{A.17}$$

where the third line is obtained from the second line. Then, from Eq. (A.17), we get the coordinate transformation using the chain rule for derivatives,

$$\frac{\partial p}{\partial \gamma} = \frac{m\, c\, \gamma}{\sqrt{\gamma^2 - 1}} = \frac{m^2\, c^2\, \gamma}{p}\,, \tag{A.18}$$

$$\frac{\partial f}{\partial \gamma} = \frac{\partial f}{\partial p}\frac{\partial p}{\partial \gamma} = \frac{m^2\, c^2\, \gamma}{p}\frac{\partial f}{\partial p}\,, \tag{A.19}$$

where $f = f(\mathbf{r}, \mathbf{p})$

When an electron emits a photon with energy $\hbar\,\omega$, its energy reduces to $E' = E - \hbar\,\omega$. Substituting the energies using Eq. (A.15), we obtain for the change in Lorentz factor, $\Delta\gamma \coloneqq \gamma' - \gamma$,

$$\Delta\gamma = -\frac{\hbar\,\omega}{m\, c^2}$$

$$= -\frac{\hbar\,\omega\,\beta\,\gamma}{p\,c}\,, \tag{A.20}$$

where we incorporate $p = \beta\,\gamma\,m\,c$ in the second line.

For the pitch angle component in Eq. (A.14), we obtain for the coordinate transformation

$$\mu = \cos(\alpha)\,, \tag{A.21}$$

$$\frac{\partial\mu}{\partial\alpha} = -\sin(\alpha) = -\sqrt{1-\mu^2}\,, \tag{A.22}$$

$$\frac{\partial f}{\partial\alpha} = \frac{\partial f}{\partial\mu}\frac{\partial\mu}{\partial\alpha} = -\sqrt{1-\mu^2}\,\frac{\partial f}{\partial\mu}\,, \tag{A.23}$$

where we use the Pythagorean trigonometric identity in Eq. (A.22).

We now evaluate $\Delta\alpha \coloneqq \alpha' - \alpha$ in Eq. (A.14). Let $\mathbf{p}$ be the electron momentum vector and $\mathbf{p}_{\rm ph} = \hbar\,\mathbf{k}$ the photon momentum vector, with magnitude $p = \hbar\,\omega\,n/c$. When considering the spontaneous emission of a single photon by a free electron, conservation of energy and momentum generally requires accounting for the exchange with the external electromagnetic field (e.g. Sokolov et al. 2009). However, under the assumption of a uniform, steady magnetic field, the symmetry between emission and absorption processes is preserved, and it becomes consistent to evaluate energy-momentum conservation using only the electron and photon momenta. The influence of the external field is implicitly accounted through this symmetry. While the numerical simulations in Chapter 6 involve globally time-dependent and spatially varying magnetic fields, the GS emission and absorption coefficients are computed locally at individual grid nodes using a single snapshot in time. Moreover, the electron gyroradii and gyroperiods are much smaller than the modelled variation of the magnetic field, justifying the assumption of a locally uniform and steady field during the gyromotion.

Using these assumptions, the parallel and perpendicular momentum changes can be formulated as

$$\Delta p_{\parallel} = p'_{\parallel} - p_{\parallel} = -p_{\rm ph\parallel} = -\frac{\hbar\,\omega\,n}{c}\cos(\theta)\,, \tag{A.24}$$

$$\Delta p_{\perp} = p'_{\perp} - p_{\perp} = -p_{\rm ph\perp} = -\frac{\hbar\,\omega\,n}{c}\sin(\theta)\,. \tag{A.25}$$

Using $\alpha = \arctan(p_{\perp}/p_{\parallel})$ and the derivative of the arc tangent, $\mathrm{d}/\mathrm{d}x[\arctan(x)] = (x^2+1)^{-1}$, the total differential is

$$\mathrm{d}\alpha = \frac{\partial\alpha}{\partial p_{\parallel}}\mathrm{d}p_{\parallel} + \frac{\partial\alpha}{\partial p_{\perp}}\mathrm{d}p_{\perp}\,, \tag{A.26}$$

$$\mathrm{d}\alpha = \frac{p_\parallel \,\mathrm{d}p_\perp - p_\perp \,\mathrm{d}p_\parallel}{p^2}\,, \tag{A.27}$$

where $p^2 = p_\parallel^2 + p_\perp^2$. Approximating $\mathrm{d}\alpha \approx \Delta\alpha$ and inserting the expressions from Eqs. (A.24) and (A.25) into Eq. (A.27), we find

$$\begin{aligned}\Delta\alpha &= \frac{p_\parallel \,\Delta p_\perp - p_\perp \,\Delta p_\parallel}{p^2} \\ &= \frac{\hbar\,\omega}{p\,c} n[\cos(\theta)\,\sin(\alpha) - \cos(\alpha)\,\sin(\theta)]\,.\end{aligned} \tag{A.28}$$

Using the trigonometric identity $\cos(\theta-\alpha) = \cos(\theta)\,\cos(\alpha) + \sin(\theta)\,\sin(\alpha)$, it can be shown that[3]

$$n\,\beta\,\cos(\theta-\alpha) = n\,\beta\,[\cos(\theta)\,\cos(\alpha) + \sin(\theta)\,\sin(\alpha)] \approx 1 \tag{A.29}$$

$$\Leftrightarrow \sin(\theta) = \frac{1 - n\,\beta\,\cos(\theta)\,\cos(\alpha)}{n\,\beta\,\sin(\alpha)}\,. \tag{A.30}$$

We prove the approximation used in Eq. (A.29) in the paragraph below. Substituting Eq. (A.30) into (A.28), we obtain the simplified form

$$\Delta\alpha = \frac{\hbar\,\omega}{p\,c}\frac{n\,\beta\,\cos(\theta) - \cos(\alpha)}{\beta\,\sin(\alpha)}\,. \tag{A.31}$$

Finally, inserting Eqs. (A.19), (A.20), (A.23), and (A.31) into Eq. (A.14) yields

$$\begin{aligned}f(\mathbf{p}') - f(\mathbf{p}) \approx &-\frac{\hbar\,\omega}{p\,c} \\ &\times \left[\frac{\beta\,m^2\,c^2\,\gamma^2}{p}\frac{\partial f}{\partial p} + \frac{n\,\beta\,\cos(\theta) - \cos(\alpha)}{\beta\,\sin(\alpha)}\sqrt{1-\mu^2}\frac{\partial f}{\partial \mu}\right]\,,\end{aligned} \tag{A.32}$$

which matches Eq. (2.49).

We now verify the validity of the approximation in Eq. (A.29). For this purpose, we define the four-momentum p^μ of an electron and four-momentum p^μ_{ph} of a photon as

$$p^\mu = (\gamma\,m\,c, \gamma\,m\,c\,\boldsymbol{\beta})^{\mathrm{T}}\,, \tag{A.33}$$

$$p^\mu_{\mathrm{ph}} = \left(\frac{\hbar\,\omega}{c}, \frac{\hbar\,\omega\,n}{c}\hat{\mathbf{k}}\right)^{\mathrm{T}}\,, \tag{A.34}$$

[3] I would like to thank Prof Nicolas Wijsen for pointing this out to me.

where $\boldsymbol{\beta} \coloneqq \mathbf{v}/c$ is the dimensionless electron velocity, and $\hat{\mathbf{k}}$ is the unit vector in the photon propagation. The conservation of electron rest mass then implies

$$g_{\mu\nu}\, p^{\mu}\, p^{\nu} = p^2 = m^2\, c^2\,, \tag{A.35}$$

with $g_{\mu\nu}$ denoting the Minkowski metric. Using momentum conservation $p' = p - p_{\mathrm{ph}}$, we obtain

$$\begin{aligned}(p - p_{\mathrm{ph}})^2 - p'^2 &= 0\\ -2\, p\, p_{\mathrm{ph}} + p_{\mathrm{ph}}^2 &= 0\,,\end{aligned} \tag{A.36}$$

where we use $p^2 = p'^2$ due to Eq. (A.35). From Eq. (A.34), we obtain for p_{ph}^2

$$g_{\mu\nu}\, p_{\mathrm{ph}}^{\mu}\, p_{\mathrm{ph}}^{\nu} = p_{\mathrm{ph}}^2 = \left(\frac{\hbar\,\omega}{c}\right)^2 (1 - n^2)\,. \tag{A.37}$$

Furthermore, the mixed inner product in Eq. (A.36) becomes

$$g_{\mu\nu}\, p^{\mu}\, p_{\mathrm{ph}}^{\nu} = \gamma\, m\, \hbar\,\omega\, [1 - \beta\, n\, \cos(\psi)]\,, \tag{A.38}$$

where $\psi = \theta - \alpha$ is the angle between the electron and photon directions. Substituting Eqs. (A.37) and (A.38) into Eq. (A.36), we find

$$\begin{aligned}-2\,\gamma\, m\, \hbar\,\omega\, [1 - \beta\, n\, \cos(\psi)] + \left(\frac{\hbar\,\omega}{c}\right)^2 (1 - n^2) &= 0\\ \Leftrightarrow 1 - \beta\, n\, \cos(\psi) &= -\frac{1}{2}\underbrace{\frac{\hbar\,\omega}{\gamma\, m\, c^2}}_{\ll 1}(1 - n^2)\\ \Rightarrow n\,\beta\, \cos(\psi) &\approx 1\,.\end{aligned} \tag{A.39}$$

In the second line of Eq. (A.39), we use the assumption $\hbar\,\omega \ll \gamma\, m\, c^2$ (i.e. photon energy is much smaller than the electron energy), from which the third line follows, implying the approximation $\psi = \theta - \alpha \approx 0$.

A.4 On the spontaneous emission probability in quantum mechanical terms

To describe the spontaneous emission and absorption of GS radiation, we adopt a semi-classical approach that neglects an explicit[4] calculation of stimulated

[4]Stimulated emission is implicitly included via the absorption coefficient $\alpha_{\omega}^{\pm}$ in Eq. (2.181), which represents the difference between stimulated absorption and stimulated emission. Hence, if $\alpha_{\omega}^{\pm}$ becomes negative, stimulated emission is present.

emission (for which a more rigorous quantum mechanical treatment is required, see Melrose 1968a). In Section 2.3.3, the total power radiated in a particular mode is expressed in terms of the quantum mechanical probability $w_{\mathcal{S}}^{\mathcal{S}'}(\mathbf{k})$ for an electron to transition from an initial state $\mathcal{S}$ to a final state $\mathcal{S}'$, emitting a photon with wave vector $\mathbf{k}$. The total emissivity is obtained by summing over all possible final states $\mathcal{S}'$ (see Eq. 2.50, first line). This sum is commonly replaced by a sum over all harmonics. The equivalence of these two descriptions can be understood through the structure of quantum states in a magnetic field.

In quantum mechanics, the state of a charged particle in a uniform magnetic field is characterised by a set of quantum numbers. The transverse (perpendicular) motion of a charged particle is quantised into discrete Landau levels, indexed by the quantum number[5] n_{L}. These levels are related to the (canonical) perpendicular momentum, $q_\perp$, by (Melrose, 1968a; Tsytovich, 1970)

$$\begin{aligned} q_\perp^2 &= \frac{|q|\,B\,\hbar}{c}(2\,n_{\mathrm{L}}+1) \\ &= m\,\Omega\,\hbar\,(2\,n_{\mathrm{L}}+1) \\ &= \frac{\tilde{\Omega}\,E}{c^2}\hbar\,(2\,n_{\mathrm{L}}+1)\,, \end{aligned} \tag{A.40}$$

with $n_{\mathrm{L}} \in \mathbb{Z}_{\geq 0}$. In the second line, we use the classical gyrofrequency from Eq. (A.83). In the third line of Eq. (A.40), we include the energy formula from Eq. (A.15) to incorporate the relativistic gyrofrequency from Eq. (A.84).

The longitudinal motion along the magnetic field (taken to point in z-direction) remains unquantised, so parallel (canonical) momentum q_z is treated as a continuous quantum variable. This asymmetry reflects the fact that the Lorentz force restricts motion in the plane perpendicular to the field, but allows free propagation along it. The energy spectrum of the Landau levels is given by $E^2 = m^2\,c^4 + q_\perp^2\,c^2 + q_z^2\,c^2$ (Tsytovich, 1970).

We denote the particle's quantum state as

$$\begin{aligned} \mathcal{S} &= \{q_z, n_{\mathrm{L}}\}\,, \\ \mathcal{S}' &= \{q_z - \hbar\,k_z, n_{\mathrm{L}} - \nu\}\,, \end{aligned} \tag{A.41a}$$

where the final state $\mathcal{S}' = \{q_z', n_{\mathrm{L}}'\}$ is determined by conservation laws. The longitudinal momentum is reduced by $\hbar\,k_z$, representing the momentum carried away by the emitted photon. Simultaneously, the particle transitions between Landau levels in the transverse plane, from n_{L} to $n_{\mathrm{L}} - \nu$, corresponding to the

[5] The subscript 'L' is used in this thesis to distinguish it from the refractive index n.

emission of a photon with frequency ω. Since the energy levels in the transverse plane are quantised, the radiated energy corresponds to an integer multiple of the fundamental cyclotron energy, resulting in harmonic emission.

The integer ν therefore represents the number of Landau levels traversed during the transition and determines the harmonic number of the emitted radiation. A positive ν corresponds to normal Doppler emission, where the particle loses transverse energy by transitioning to lower Landau levels, while a negative ν represents anomalous Doppler emission, in which the particle gains transverse energy by transitioning to higher Landau levels (Melrose, 1968a). Consequently, the sum over final quantum states $\mathcal{S}'$ can be reformulated as a sum over harmonics $\nu \in \mathbb{Z}$. Although the Landau quantum number n_{L} must remain non-negative, the sum over all ν is justified, since transition probabilities for forbidden values of ν vanish.

A.5 Energy density in electromagnetic fields

In the following, we derive the electromagnetic energy density used in Section 2.3.4. Maxwell's equations form the foundation of electrodynamics and plasma physics. They are used to derive the ideal MHD equations discussed in Section 2.1, the (in)homogeneous wave equation in Appendix A.7, and the cold plasma dispersion relation in Appendix A.10. In differential form and Gaussian units, Maxwell's equations are expressed as

$$\nabla \cdot \mathbf{D} = 4\,\pi\,\rho_{\mathrm{c}}\,, \tag{A.42}$$

$$\nabla \cdot \mathbf{B} = 0\,, \tag{A.43}$$

$$\nabla \times \mathbf{E} = -\frac{1}{c}\frac{\partial \mathbf{B}}{\partial t}\,, \tag{A.44}$$

$$\nabla \times \mathbf{B} = \frac{4\,\pi}{c}\mathbf{j} + \frac{1}{c}\frac{\partial \mathbf{D}}{\partial t}\,. \tag{A.45}$$

Equation (A.42), known as Gauss's law, relates the electric displacement field $\mathbf{D} = \epsilon\,\mathbf{E}$ (with the permittivity ϵ potentially being a tensor) to the charge density ρ_{c}. Equation (A.43) is the solenoidal constraint, enforcing the absence of magnetic monopoles. Equations (A.44) and (A.45) correspond to Faraday's and Ampére's laws, respectively. Throughout the following derivation, we assume $\mathbf{B} = \mathbf{H}$ with $\mathbf{H}$ being the magnetic field strength, but keep $\mathbf{D} \neq \mathbf{E}$ to allow for dielectric effects.

To derive the electromagnetic energy density, we begin with the vector identity for the divergence of a cross product,

$$\nabla \cdot (\mathbf{E} \times \mathbf{B}) = \mathbf{B} \cdot (\nabla \times \mathbf{E}) - \mathbf{E} \cdot (\nabla \times \mathbf{B}) \,. \tag{A.46}$$

Next, we take the dot products of $\mathbf{E}$ with Eq. (A.45), and the dot product of $\mathbf{B}$ with Eq. (A.44), to obtain

$$\mathbf{E} \cdot (\nabla \times \mathbf{B}) = \frac{1}{c}\mathbf{E} \cdot \frac{\partial \mathbf{D}}{\partial t} + \frac{4\,\pi}{c}\mathbf{E} \cdot \mathbf{j} \,, \tag{A.47}$$

$$\mathbf{B} \cdot (\nabla \times \mathbf{E}) = -\frac{1}{c}\mathbf{B} \cdot \frac{\partial \mathbf{B}}{\partial t} \,. \tag{A.48}$$

Inserting Eqs. (A.47) and (A.48) into Eq. (A.46) yields

$$\begin{aligned} \nabla \cdot (\mathbf{E} \times \mathbf{B}) &= -\frac{1}{c}\mathbf{B} \cdot \frac{\partial \mathbf{B}}{\partial t} - \frac{1}{c}\mathbf{E} \cdot \frac{\partial \mathbf{D}}{\partial t} - \frac{4\,\pi}{c}\mathbf{E} \cdot \mathbf{j} \,, \\ \frac{c}{4\,\pi}\nabla \cdot (\mathbf{E} \times \mathbf{B}) &= -\frac{1}{4\,\pi}\left(\mathbf{B} \cdot \frac{\partial \mathbf{B}}{\partial t} + \mathbf{E} \cdot \frac{\partial \mathbf{D}}{\partial t}\right) - \mathbf{E} \cdot \mathbf{j} \,, \end{aligned} \tag{A.49}$$

where the second line follows by multiplying both sides by $c/(4\,\pi)$ and factoring out $1/(4\,\pi)$.

The bracket expression in Eq. (A.49) motivates the definition of the electromagnetic energy density W as

$$W = \frac{1}{8\,\pi}\left(\mathbf{B} \cdot \mathbf{B} + \mathbf{E} \cdot \mathbf{D}\right) \,, \tag{A.50}$$

which represents the combined energy stored in the electric and magnetic fields. Taking the time derivative of W, we obtain

$$\frac{\partial W}{\partial t} = \frac{1}{4\,\pi}\left(\mathbf{B} \cdot \frac{\partial \mathbf{B}}{\partial t} + \mathbf{E} \cdot \frac{\partial \mathbf{D}}{\partial t}\right) \,. \tag{A.51}$$

Substituting Eq. (A.51) into the right-hand side of (A.49), we arrive at the energy conservation equation for the electromagnetic field, given by

$$\begin{aligned} \frac{\partial W}{\partial t} &= -\frac{c}{4\,\pi}\nabla \cdot (\mathbf{E} \times \mathbf{B}) - \mathbf{E} \cdot \mathbf{j} \\ &= -\nabla \cdot \mathbf{S} - \mathbf{E} \cdot \mathbf{j} \,, \end{aligned} \tag{A.52}$$

where $\mathbf{S} \coloneqq c/(4\,\pi)\,\mathbf{E} \times \mathbf{B}$ is the Poynting vector, representing the energy flux of the electromagnetic field.

A.6 Mathematical identities involving the adjugate tensor λ_{ij}

We derive two key identities involving the adjugate tensor λ_{ij} that are used in computing the total radiated power in Sections 2.3.4 and 2.3.7.

First, we derive the identity from Eq. (2.83) in Section 2.3.4. We begin by considering the wave equation

$$\Lambda_{ij}\, E_j = 0\,, \tag{A.53}$$

which is the homogeneous form of Eq. (A.75) derived in Appendix A.7. In the resonant case where the determinant of the dispersion tensor Λ, $\mathcal{L} = 0$, the matrix Λ has rank two and admits a single non-trivial null vector, denoted E_j and corresponding to the polarisation vector of the wave. From the general identity for the adjugate matrix in Eq. (2.74), we see that for $\mathcal{L} = 0$, it reduces to

$$\Lambda_{ij}\, \lambda_{jl} = 0\,. \tag{A.54}$$

Thus, each column of λ_{ij} lies in the null space of Λ_{ij}, which is 1D. It follows that λ_{ij} must be of rank one.

Moreover, since the dielectric tensor ϵ_{ij} (in Eq. A.74) and hence Λ_{ij} are Hermitian, the same holds for λ_{ij}. A Hermitian, rank-one matrix can always be written as the outer product of a vector with its Hermitian conjugate,

$$\lambda_{ij} = \iota\, \upsilon_i\, \upsilon_j^*\,, \tag{A.55}$$

for some complex vector υ and scalar ι. Given that E_i spans the kernel of Λ_{ij}, it is natural to identify υ_i with the normalised polarisation vector e_i from Eq. (A.76). Therefore, Eq. (A.55) becomes

$$\lambda_{ij} = \iota\, e_i\, e_j^*\,. \tag{A.56}$$

Taking the trace of both sides of Eq. (A.56), and using the normalisation condition from Eq. (A.77), we find

$$\mathrm{tr}(\lambda) = \iota \sum_i e_i\, e_i^* = \iota\,. \tag{A.57}$$

Thus, the scalar coefficient ι equals $\mathrm{tr}(\lambda)$. This gives the final form as

$$\lambda_{ij} = \mathrm{tr}(\lambda)\, e_i\, e_j^*\,, \tag{A.58}$$

which is the identity in Eq. (2.83).

We now derive the formula to compute the components of the polarisation vector $\mathbf{e}$ based on an auxiliary vector $\mathbf{a}$, as given in Eq. (2.151). This derivation applies in the $\mathcal{L} = 0$ case and relies on the fact that λ_{ij} is a Hermitian matrix of rank one. Since $\Lambda_{ij}\,\lambda_{jk} = 0$ for $\mathcal{L} = 0$, the adjugate λ_{ij} is constructed from the kernel eigenvector $\mathbf{E}$, and takes the form of an outer product involving the polarisation vector, as in Eq. (A.58). Consequently, any vector of the form $\lambda_{ij}\,a_j$ is parallel to $\mathbf{e}$, provided that $\mathbf{a}$ satisfies the condition Eq. (2.150) in Section 2.3.7. We therefore write

$$e_i = C\,\lambda_{ij}\,a_j\,, \tag{A.59}$$

for some complex normalisation constant C to be determined. Imposing the condition in Eq. (A.77) on Eq. (A.59), we obtain

$$\begin{aligned} e_i\,e_i^* &= 1 \\ &= |C|^2\,\lambda_{ij}\,a_j\,\lambda_{ik}^*\,a_k^* \\ &= |C|^2\,\lambda_{ij}\,a_j\,\lambda_{ki}\,a_k^*\,, \end{aligned} \tag{A.60}$$

where we exploit in the third line the Hermitian property $\lambda_{ik}^* = \lambda_{ki}$. Since the result of Eq. (A.60) is a scalar, we can reorder it to

$$\begin{aligned} e_i\,e_i^* &= |C|^2\,a_k^*\,\lambda_{ki}\lambda_{ij}\,a_j \\ &= |C|^2\,a_k^*\,\lambda_{kj}\lambda_{ii}\,a_j\,, \end{aligned} \tag{A.61}$$

applying in the second line the identity from Eq. (2.148). We identify λ_{ii} in Eq. (A.61) as the trace of λ, and thus obtain

$$\begin{aligned} e_i\,e_i^* &= |C|^2\,\mathrm{tr}(\lambda)\,a_k^*\,\lambda_{kj}\,a_j \\ &= |C|^2\,\mathrm{tr}(\lambda)\,a_i^*\,\lambda_{ij}\,a_j\,, \end{aligned} \tag{A.62}$$

where we rename the dummy index $k \to i$ in the final step. Solving Eq. (A.62) for C, we obtain the normalisation constant as

$$C = \frac{1}{\sqrt{\mathrm{tr}(\lambda)\,a_i^*\,\lambda_{ij}\,a_j}}\,. \tag{A.63}$$

Substituting Eq. (A.63) into (A.59) yields the final expression for the normalised polarisation vector,

$$e_i = \frac{\lambda_{ij}\,a_j}{\sqrt{\mathrm{tr}(\lambda)\,a_i^*\,\lambda_{ij}\,a_j}}\,, \tag{A.64}$$

which matches the expression in Eq. (2.151).

A.7 Inhomogeneous wave equation

In the following, we derive the inhomogeneous wave equation in Fourier space from Maxwell's equations in a linear dielectric medium. We assume all fields vary as $\exp[i(\mathbf{k}\cdot\mathbf{r}) - \omega\, t]$, which allows us to use the known transformations

$$\frac{\partial}{\partial t} \to -i\,\omega\,, \tag{A.65}$$

$$\nabla \to i\,\mathbf{k}\,. \tag{A.66}$$

Applying Fourier transforms to Eqs. (A.44) and (A.45) yields

$$\mathbf{k}\times\mathbf{E} = \frac{\omega}{c}\mathbf{B}\,, \tag{A.67}$$

$$\mathbf{k}\times\mathbf{B} = -\frac{\omega}{c}\mathbf{D} - \frac{i\,4\,\pi}{c}\mathbf{j}\,. \tag{A.68}$$

To eliminate $\mathbf{B}$ in Eq. (A.68), we solve Eq. (A.67) for $\mathbf{B}$ and substitute into Eq. (A.68), resulting in

$$\begin{aligned}\mathbf{k}\times(\mathbf{k}\times\mathbf{E}) &= -\frac{\omega^2}{c^2}\mathbf{D} - \frac{i\,4\,\pi\,\omega}{c^2}\mathbf{j}\\ &= -\frac{\omega^2}{c^2}\epsilon\,\mathbf{E} - \frac{i\,4\,\pi\,\omega}{c^2}\mathbf{j}\,,\end{aligned} \tag{A.69}$$

where we use $\mathbf{D} = \epsilon\,\mathbf{E}$. Using the Graßmann identity $\mathbf{k}\times(\mathbf{k}\times\mathbf{E}) = \mathbf{k}(\mathbf{k}\cdot\mathbf{E}) - k^2\,\mathbf{E}$, we rewrite Eq. (A.69) as

$$\begin{aligned}&(\mathbf{k}\mathbf{k} - k^2\,\mathcal{I})\mathbf{E} + \frac{\omega^2}{c^2}\epsilon\,\mathbf{E} = -\frac{i\,4\,\pi\,\omega}{c^2}\mathbf{j}\\ \Leftrightarrow\ &\frac{\omega^2\,k^2}{c^2}\left(\frac{\mathbf{k}\mathbf{k}}{k^2} - \mathcal{I}\right)\mathbf{E} + \epsilon\,\mathbf{E} = -\frac{i\,4\,\pi}{\omega}\mathbf{j}\,,\end{aligned} \tag{A.70}$$

where the second line is obtained by multiplying the first line by c^2/ω^2 and factoring out k^2 on the left-hand side.

We now define the refractive index n and unit directional wave vector $\hat{\mathbf{k}}$ as

$$n^2 = \frac{k^2\,c^2}{\omega^2}\,, \tag{A.71}$$

$$\hat{\mathbf{k}} = \frac{\mathbf{k}}{k}\,. \tag{A.72}$$

Substituting these into Eq. (A.70) and using index notation, we obtain

$$[n^2(\hat{k}_i\hat{k}_j - \delta_{ij}) + \epsilon_{ij}]E_j = -\frac{i\,4\,\pi}{\omega} j_i \,. \tag{A.73}$$

Equation (A.73) motivates the definition of the dispersion tensor

$$\Lambda_{ij} = n^2(\hat{k}_i\hat{k}_j - \delta_{ij}) + \epsilon_{ij} \,, \tag{A.74}$$

with which Eq. (A.73) takes the compact form

$$\Lambda_{ij}(\mathbf{k},\omega)E_j(\mathbf{k},\omega) = -\frac{i\,4\,\pi}{\omega} j_i(\mathbf{k},\omega) \,. \tag{A.75}$$

This equation is also known as the inhomogeneous wave equation (or dispersion relation) for a cold plasma (see Appendix A.10), while the corresponding homogeneous wave equation in Eq. (A.53) determines the natural modes of the plasma in the absence of sources.

Finally, we define the normalised polarisation vector[6] $\mathbf{e}$, which describes the direction of the electric field oscillations, given by

$$\mathbf{e}(\mathbf{k},\omega) = \frac{\mathbf{E}(\mathbf{k},\omega)}{|\mathbf{E}(\mathbf{k},\omega)|} \,, \tag{A.76}$$

$$\mathbf{e}\cdot\mathbf{e}^* = 1 \,, \tag{A.77}$$

where the second line ensures unit norm.

A.8 Particle motion

To derive the equations of motion for a charged particle in a plasma, we assume a uniform magnetic field pointing along the z-axis,

$$\mathbf{B} = (0,0,B)^{\mathrm{T}} \,. \tag{A.78}$$

We begin with the relativistic Newton-Lorentz equation

$$\frac{\mathrm{d}\mathbf{p}}{\mathrm{d}t} = \frac{q}{c}\left(\mathbf{E} + \mathbf{v}\times\mathbf{B}\right) \,, \tag{A.79}$$

$$\mathbf{p}(t) = \gamma\, m\, \mathbf{v}(t) \,, \tag{A.80}$$

[6] We sometimes refer to both $\mathbf{E}$ and $\mathbf{e}$ as the polarisation vector, where $\mathbf{e}$ encodes only the orientation of the field, while $\mathbf{E}$ is the full electric field vector.

where Eq. (A.80) gives the relativistic momentum vector. For simplicity, we neglect the electric field $\mathbf{E}$, and define the initial condition for the velocity at $t = 0$ as

$$\mathbf{v}(0) = (\varepsilon\, v_\perp, 0, v_z)^{\mathrm{T}}\,, \tag{A.81}$$

where $v_\perp$ is the perpendicular velocity component, v_z is the parallel velocity component, and the sign variable ε is defined as

$$\varepsilon = \frac{q}{|q|} = \pm 1\,. \tag{A.82}$$

For the following derivation, it is useful to define the gyrofrequency Ω and the relativistic gyrofrequency $\tilde{\Omega}$, given by

$$\Omega = \frac{|q|\,B}{m\,c}\,, \tag{A.83}$$

$$\tilde{\Omega} = \Omega \frac{m\,c^2}{E} = \frac{\Omega}{\gamma}, \tag{A.84}$$

Using $\mathbf{v} = (v_x, v_y, v_z)^{\mathrm{T}}$, evaluating the cross product in Eq. (A.79) with $\mathbf{B}$ from Eq. (A.78), incorporating Eq. (A.80) and the definitions from Eqs. (A.82)–(A.84), while treating γ as a constant, we obtain

$$\frac{\mathrm{d}v_x}{\mathrm{d}t} = \varepsilon\,\tilde{\Omega}\,v_y\,, \tag{A.85}$$

$$\frac{\mathrm{d}v_y}{\mathrm{d}t} = -\varepsilon\,\tilde{\Omega}\,v_x\,, \tag{A.86}$$

$$\frac{\mathrm{d}v_z}{\mathrm{d}t} = 0\,. \tag{A.87}$$

Differentiating Eqs. (A.85) and (A.86) with respect to time once more and substituting into them, we find

$$\frac{\mathrm{d}^2 v_x}{\mathrm{d}t^2} = \varepsilon\,\tilde{\Omega}\,\frac{\mathrm{d}v_y}{\mathrm{d}t} = -(\varepsilon\,\tilde{\Omega})^2\,v_x\,, \tag{A.88}$$

$$\frac{\mathrm{d}^2 v_y}{\mathrm{d}t^2} = -\varepsilon\,\tilde{\Omega}\,\frac{\mathrm{d}v_x}{\mathrm{d}t} = -(\varepsilon\,\tilde{\Omega})^2\,v_y\,. \tag{A.89}$$

Hence, $v_x(t)$ and $v_y(t)$ are harmonic oscillators of angular frequency $\tilde{\Omega}$, describing a circular motion in the x-y plane. The general solutions for such differential equations are (e.g. Martin & Shaw 2015)

$$v_x(t) = C_1\,\cos(\varepsilon\,\tilde{\Omega}\,t) + C_2\,\sin(\varepsilon\,\tilde{\Omega}\,t)\,, \tag{A.90}$$

$$v_y(t) = C_3 \cos(\varepsilon\,\tilde{\Omega}\,t) + C_4 \sin(\varepsilon\,\tilde{\Omega}\,t)\,. \tag{A.91}$$

Using the initial condition from Eq. (A.81), we determine the constants to be $C_1 = \varepsilon\,v_\perp$, $C_2 = C_3 = 0$, and $C_4 = -\varepsilon\,v_\perp$. This yields the velocity vector as

$$\mathbf{v}(t) = [\varepsilon\,v_\perp \cos(\varepsilon\,\tilde{\Omega}\,t), -\varepsilon\,v_\perp \sin(\varepsilon\,\tilde{\Omega}\,t), v_z]^{\mathrm{T}}\,. \tag{A.92}$$

With $\mathbf{r}(t) = \int \mathrm{d}t\,\mathbf{v}(t)$ and the initial condition

$$\mathbf{r}(0) = (0, R_{\mathrm{g}}, 0)^{\mathrm{T}}\,, \tag{A.93}$$

where the gyroradius R_{g} is defined as

$$R_{\mathrm{g}} \coloneqq \frac{v_\perp}{\tilde{\Omega}} = \frac{p_\perp}{m\,\Omega}\,, \tag{A.94}$$

we find for the position vector

$$\mathbf{r}(t) = [R_{\mathrm{g}} \sin(\varepsilon\,\tilde{\Omega}\,t), R_{\mathrm{g}} \cos(\varepsilon\,\tilde{\Omega}\,t), v_z\,t]^{\mathrm{T}}\,. \tag{A.95}$$

The above assumptions of a uniform, constant magnetic field are consistent with the numerical computations of the GS emission and absorption coefficients in Chapter 6, where the coefficients are computed locally, instantaneously, and individually at each node. In this limit, the electron motion describes a helical trajectory, where the field can be treated as uniform and constant across a single gyration.

A.9 Regularisation of products of Dirac delta distributions

Equation (2.121) in Section 2.3.6 contains a product of two Dirac delta distributions that becomes a delta-squared expression, which is mathematically ill-defined and requires regularisation to proceed with the derivation of the spontaneous emission probability expression. In this section, we illustrate how the identity in Eq. (2.122) emerges as a valid regularisation of the delta product.

Let $x = \omega - k_z\,v_z$, $a = \nu\,\varepsilon\,\tilde{\Omega}$, and $b = \nu'\,\varepsilon\,\tilde{\Omega}$. Then the product of delta distributions in Eq. (2.121) becomes

$$\delta(\omega - \nu\,\varepsilon\,\tilde{\Omega} - k_z\,v_z)\,\delta(\omega - \nu'\,\varepsilon\,\tilde{\Omega} - k_z\,v_z) = \delta(x-a)\,\delta(x-b)\,. \tag{A.96}$$

As distributions in the variable x (with parameters a, b), we have that for any test function $\mathcal{Y}(x)$[7],

$$\int \mathcal{Y}(x)\,\delta(x-a)\,\delta(x-b)\,\mathrm{d}x = \mathcal{Y}(a)\,\delta(a-b)$$

$$= \int \mathcal{Y}(x)\,\delta(x-a)\,\delta(a-b)\,\mathrm{d}x\,. \tag{A.97}$$

The identity shows, in the distributional sense, that

$$\delta(x-a)\,\delta(x-b) = \delta(x-a)\,\delta(a-b)\,. \tag{A.98}$$

We now regularise the otherwise ill-defined expression in Eq. (A.98) using the Fourier representation of the Dirac delta. The singularity arises when $a = b$, in which case the product $\delta(x-a)\,\delta(x-b)$ becomes $[\delta(x-a)]^2$, which is not defined in standard distribution theory. The standard identity in Eq. (2.63) can be reformulated in terms of the period T to

$$\delta(\omega) = \frac{1}{2\,\pi}\int_{-\infty}^{\infty}\mathrm{d}t\,\exp(i\,\omega\,t)$$

$$= \lim_{T\to\infty}\frac{1}{2\,\pi}\int_{-T/2}^{T/2}\mathrm{d}t\,\exp(i\,\omega\,t)\,, \tag{A.99}$$

and regularised over a finite interval T as

$$\delta_T(\omega) \coloneqq \frac{1}{2\,\pi}\int_{-T/2}^{T/2}\mathrm{d}t\,\exp(i\,\omega\,t)$$

$$= \frac{1}{\pi}\left[\frac{\exp(i\,\omega\,T/2)-\exp(-i\,\omega\,T/2)}{2\,i\,\omega}\right]$$

$$= \frac{\sin(\omega\,T/2)}{\pi\,\omega}$$

$$= \frac{T}{2\,\pi}\,\mathrm{sinc}\left(\frac{\omega\,T}{2}\right)\,, \tag{A.100}$$

where $\mathrm{sinc}(x) \coloneqq \sin(x)/x$.

Furthermore, we consider the behaviour of $\delta_T(a-b)$ as $b \to a$. Using Eq. (A.100) and applying L'Hôpital's rule to evaluate the sinc expression, we find

$$\lim_{b\to a}\delta_T(a-b) = \frac{T}{2\,\pi}\,. \tag{A.101}$$

[7]The result is symmetric in a and b, so picking b would just result in relabelling later ν and ν'.

This suggests that

$$\lim_{b\to a}\delta(a-b) \simeq \lim_{T\to\infty}\lim_{b\to a}\delta_T(a-b) = \infty\,, \tag{A.102}$$

in agreement with the interpretation of the Dirac delta as a distribution. Consequently, the regularised product $\delta(a-b)\,\delta(x-a)$ in the case of $a=b$ can be interpreted as

$$\delta(a-b)\,\delta(x-a) \simeq \frac{T}{2\,\pi}\,\delta(x-a)\,. \tag{A.103}$$

Applying this to the double delta sum in Eq. (2.121), we now write

$$\begin{aligned}&\sum_{\nu,\nu'}\delta(\omega-\nu\,\varepsilon\,\tilde{\Omega}-k_z\,v_z)\,\delta(\omega-\nu'\,\varepsilon\,\tilde{\Omega}-k_z\,v_z)\\ \longrightarrow\quad &\frac{T}{2\,\pi}\sum_{\nu}\delta(\omega-\nu\,\varepsilon\,\tilde{\Omega}-k_z\,v_z)\,,\end{aligned} \tag{A.104}$$

which matches Eq. (2.122).

A.10 Cold plasma dispersion relation

In the following, we derive the expressions for the cold plasma conductivity and dielectric tensors. The cold plasma dispersion relation is a classical result in plasma physics (e.g. Stix 1962; Boyd & Sanderson 2003), which we derive here in more detail. In the cold plasma approximation, thermal motions and pressure are neglected. Starting from the Newton-Lorentz equation in Eq. (A.79), we assume small-amplitude wave perturbations and linearise Eq. (A.79). We denote the background magnetic field as $\mathbf{B}_0$, and assume small perturbations in velocity $\mathbf{v}_1$, electric field $\mathbf{E}_1$ and magnetic field $\mathbf{B}_1$, superimposed on static background fields. The velocity, electric field, and magnetic field are then written as

$$\mathbf{v} = \mathbf{v}_0 + \mathbf{v}_1\,, \tag{A.105}$$

$$\mathbf{E} = \mathbf{E}_0 + \mathbf{E}_1\,, \tag{A.106}$$

$$\mathbf{B} = \mathbf{B}_0 + \mathbf{B}_1\,. \tag{A.107}$$

We assume the plasma is initially at rest, implying $\mathbf{v}_0 = \mathbf{0}$, and that $\mathbf{E}_0 = \mathbf{0}$, while $\mathbf{B}_0$ is uniform and constant. Since $\mathbf{v}_1, \mathbf{E}_1, \mathbf{B}_1 \ll 1$, we ignore second-order

terms during linearisation. The resulting linearised Newton-Lorentz equation then reads

$$\frac{\mathrm{d}\mathbf{v}_1}{\mathrm{d}t} = \frac{q_\varsigma}{m_\varsigma}(\mathbf{E}_1 + \mathbf{v}_1 \times \mathbf{B}_0)\,, \tag{A.108}$$

where the subscript ς denotes the particle species.

Considering plane-wave solutions of the form $\mathbf{v}_1(\mathbf{r},t), \mathbf{E}_1(\mathbf{r},t), \mathbf{B}_1(\mathbf{r},t) \propto \exp[i(\mathbf{k}\cdot\mathbf{r} - \omega\, t)]$, we perform the transformations from Eqs. (A.65) and (A.66) to write Eq. (A.108) as

$$-i\,\omega\,\mathbf{v}_1 = \frac{q_\varsigma}{m_\varsigma}\,(\mathbf{E}_1 + \mathbf{v}_1 \times \mathbf{B}_0)\,. \tag{A.109}$$

To simplify the vector equations, we introduce the complex variables

$$v_{1\pm} = v_{1x} \pm i\, v_{1y}\,, \tag{A.110}$$

$$E_{1\pm} = E_{1x} \pm i\, E_{1y}\,, \tag{A.111}$$

going from Cartesian coordinates to a polarisation basis. The velocity components then become

$$v_{1\pm} = \frac{i\, q_\varsigma}{m_\varsigma\,(\omega \mp \varepsilon_\varsigma\,\Omega_\varsigma)}\,E_{1\pm}\,,$$

$$v_{1z} = \frac{i\, q_\varsigma}{m_\varsigma\,\omega}\,E_{1z}\,, \tag{A.112}$$

where Ω_ς and ε_ς are defined in Eqs. (2.131) and (2.132), respectively. The total current density vector is defined as the sum over all particle species ς,

$$\mathbf{j}_1 = \sum_\varsigma q_\varsigma\, n_\varsigma\, \mathbf{v}_1\,. \tag{A.113}$$

Ohm's law, accounting for all particle species, is expressed as

$$\mathbf{j} = \sum_\varsigma \sigma_\varsigma\, \mathbf{E}\,, \tag{A.114}$$

where $\sigma = \sum_\varsigma \sigma_\varsigma$ is the total conductivity tensor. We can obtain the components of the current density vector by substituting the velocity components from Eq. (A.112) into (A.113) to find

$$j_{1\pm} = \sum_\varsigma \frac{i\,\omega_{\mathrm{p}\varsigma}^2}{4\,\pi\,(\omega \mp \varepsilon_\varsigma\,\Omega_\varsigma)}\,E_{1\pm}\,,$$

$$j_{1z} = \sum_{\varsigma} \frac{i\,\omega_{\mathrm{p}\varsigma}^2}{4\,\pi\,\omega}\,E_{1z}\,, \tag{A.115}$$

where we rewrite the components using the plasma frequency

$$\omega_{\mathrm{p}\varsigma}^2 = \frac{4\,\pi\,n_\varsigma\,q_\varsigma^2}{m_\varsigma} \tag{A.116}$$

of particle species ς. Comparing Eqs. (A.114) and (A.115) allows us to identify the expression for the conductivity tensor (in circular basis) as

$$\sigma_{\mathrm{circular}} = \frac{i}{4\,\pi}\begin{pmatrix} \sum_\varsigma \frac{\omega_{\mathrm{p}\varsigma}^2}{\omega-\varepsilon_\varsigma\,\Omega_\varsigma} & 0 & 0 \\ 0 & \sum_\varsigma \frac{\omega_{\mathrm{p}\varsigma}^2}{\omega+\varepsilon_\varsigma\,\Omega_\varsigma} & 0 \\ 0 & 0 & \sum_\varsigma \frac{\omega_{\mathrm{p}\varsigma}^2}{\omega} \end{pmatrix}. \tag{A.117}$$

To compute the conductivity tensor in Cartesian basis, we can obtain the x- and y-components of the current density and electric field vectors (dropping the index 1) via

$$\begin{aligned} E_+ + E_- &\Rightarrow E_x = \frac{1}{2}(E_+ + E_-)\,, \\ E_+ - E_- &\Rightarrow E_y = \frac{1}{2\,i}(E_+ - E_-)\,, \\ j_+ + j_- &\Rightarrow j_x = \frac{1}{2}(j_+ + j_-) = \frac{1}{2}(\sigma_+\,E_+ + \sigma_-\,E_-)\,, \\ j_+ - j_- &\Rightarrow j_y = \frac{1}{2\,i}(j_+ - j_-) = \frac{1}{2\,i}(\sigma_+\,E_+ - \sigma_-\,E_-)\,, \end{aligned} \tag{A.118}$$

where σ_+ and σ_- are the elements 11 and 22 of the tensor in Eq. (A.117), respectively. Combining the relations in Eq. (A.118) allows us to obtain

$$\begin{aligned} j_x &= \frac{1}{2}[(\sigma_+ + \sigma_-)\,E_x + i\,(\sigma_+ - \sigma_-)\,E_y]\,, \\ j_y &= \frac{1}{2}[-i\,(\sigma_+ - \sigma_-)\,E_x + (\sigma_+ + \sigma_-)\,E_y]\,. \end{aligned} \tag{A.119}$$

Then, using Eq. (A.119) and the expression for j_z from Eq. (A.115), we can identify the conductivity tensor elements in

$$\begin{pmatrix} j_x \\ j_y \\ j_z \end{pmatrix} = \begin{pmatrix} \sigma_{\mathrm{xx}} & \sigma_{\mathrm{xy}} & 0 \\ \sigma_{\mathrm{yx}} & \sigma_{\mathrm{yy}} & 0 \\ 0 & 0 & \sigma_{\mathrm{zz}} \end{pmatrix} \cdot \begin{pmatrix} E_x \\ E_y \\ E_z \end{pmatrix}. \tag{A.120}$$

To derive an expression for the dielectric tensor, we combine Eqs. (A.69) and (A.114) to find

$$\mathbf{k} \times (\mathbf{k} \times \mathbf{E}) = -\frac{\omega^2}{c^2} \left[\epsilon + \frac{i\,4\,\pi}{\omega} \sigma \right] \mathbf{E}\,, \tag{A.121}$$

where the term in brackets is the total dielectric tensor. In a cold plasma, $\epsilon = \mathcal{I}$. For general cases, we write

$$\begin{aligned} \epsilon^{\mathrm{tot}} &= \epsilon + \sum_{\varsigma} \frac{i\,4\,\pi}{\omega} \sigma_{\varsigma}\,, \\ \epsilon_{ij}^{\mathrm{tot}} &= \delta_{ij} + \frac{i\,4\,\pi}{\omega} \sigma_{ij}\,, \end{aligned} \tag{A.122}$$

using index notation in the second line.

From this, we derive the tensor elements $\epsilon_{ij}^{\mathrm{tot}}$ by inserting the computed conductivity tensor elements. It is possible to identify specific recurring terms, known as Stix parameters, which enable a more compact notation. The dielectric tensor can then be expressed as Eq. (2.125) with the dimensionless Stix parameters in Eqs. (2.126)–(2.130).

A.11 Altar-Appleton-Hartree approximations

The AAH approximations are derived from the Stix parameters by considering only the contribution of the electrons to the dielectric properties of the plasma (Stix, 1962), appropriate in high-frequency regimes where electron dynamics dominate. We define the dimensionless parameter

$$\omega^{\dagger} := \frac{\omega_{\mathrm{pe}}^2}{\omega^2}\,, \tag{A.123}$$

where ω_{pe} is the electron plasma frequency from Eq. (A.116). Additionally, since we consider the electron limit, we explicitly define the (signed) electron gyrofrequency

$$\Omega_{\mathrm{e}} = -\frac{e\,B}{m_{\mathrm{e}}\,c}\,. \tag{A.124}$$

Using this, the Stix parameters in Eqs. (2.126), (2.127), and (2.130) reduce to

$$R = 1 - \frac{\omega^{\dagger}\,\omega}{\omega - \Omega_e}\,, \tag{A.125}$$

$$L = 1 - \frac{\omega^\dagger\,\omega}{\omega + \Omega_e}\,, \tag{A.126}$$

$$P = 1 - \omega^\dagger\,. \tag{A.127}$$

Hence, ion contributions are negligible when $\omega \gg |\Omega_\mathrm{i}|$ and $\omega \gg \omega_\mathrm{pi}$.

From these approximations, we can derive expressions for various combinations of the Stix parameters that appear frequently in the dispersion relation calculations, including

$$R\,L = \left(1 - \frac{\omega^\dagger\,\omega}{\omega - \Omega_e}\right)\left(1 - \frac{\omega^\dagger\,\omega}{\omega + \Omega_e}\right) = \frac{\omega^2\,(1-\omega^\dagger)^2 - \Omega_\mathrm{e}^2}{\omega^2 - \Omega_\mathrm{e}^2}\,, \tag{A.128}$$

$$D = \frac{1}{2}\,(R - L) = -\frac{\omega^\dagger\,\omega\,\Omega_\mathrm{e}}{\omega^2 - \Omega_\mathrm{e}^2}\,, \tag{A.129}$$

$$S = \frac{1}{2}\,(R + L) = \frac{\omega^2\,(1-\omega^\dagger) - \Omega_\mathrm{e}^2}{\omega^2 - \Omega_\mathrm{e}^2}\,, \tag{A.130}$$

$$P\,S = (1-\omega^\dagger)\frac{\omega^2\,(1-\omega^\dagger) - \Omega_\mathrm{e}^2}{\omega^2 - \Omega_\mathrm{e}^2} = \frac{\omega^2\,(1-\omega^\dagger)^2 - \Omega_\mathrm{e}^2\,(1-\omega^\dagger)}{\omega^2 - \Omega_\mathrm{e}^2}\,. \tag{A.131}$$

A helpful identity in this context is $S^2 - D^2 = R\,L$.

To obtain an approximate expression for the quantity $\mathcal{F}$ appearing in Eq. (2.141), we start from the general form of $\mathcal{F}^2$ in Eq. (2.142). Inserting the AAH expressions for $R\,L$, $P\,S$, and D from above, after regrouping and simplifying, we eventually identify the common factor

$$\Delta^2 = \Omega_\mathrm{e}^2\,\sin^4(\theta) + 4\,\omega^2\,(1-\omega^\dagger)^2\,\cos^2(\theta)\,. \tag{A.132}$$

Using this, we can write $\mathcal{F}$ as

$$\begin{aligned}\mathcal{F}^2 &= (R\,L - P\,S)^2\sin^4(\theta) + 4\,D^2\,P^2\,\cos^2(\theta) \\ &= \frac{(\omega^\dagger)^2\,\Omega_\mathrm{e}^2\,\Delta^2}{\left(\omega^2 - \Omega_\mathrm{e}^2\right)^2}\end{aligned} \tag{A.133}$$

$$\Rightarrow \mathcal{F} = \frac{\omega^\dagger\,\Omega_\mathrm{e}\,\Delta}{\omega^2 - \Omega_\mathrm{e}^2}\,, \tag{A.134}$$

where in the last line, we keep only the positive root, consistent with physical wave modes.

To derive an expression for $n_\pm^2$, which emerges in Eq. (2.167), we start from the general solution of the homogeneous dispersion relation $\mathcal{A}\,n^4 - \mathcal{B}\,n^2 + \mathcal{C} = 0$,

whose solutions are

$$\begin{aligned} n_{\pm}^2 &= \frac{\mathcal{B} \pm \sqrt{\mathcal{B}^2 - 4\,\mathcal{A}\,\mathcal{C}}}{2\,\mathcal{A}} \\ &= \underbrace{1-1}_{\text{adding a zero}} + \frac{\mathcal{B} \pm \sqrt{\mathcal{B}^2 - 4\,\mathcal{A}\,\mathcal{C}}}{2\,\mathcal{A}} \\ &= 1 - \frac{2\,\mathcal{A} - \mathcal{B} \mp \sqrt{\mathcal{B}^2 - 4\,\mathcal{A}\,\mathcal{C}}}{2\,\mathcal{A}}\,. \end{aligned} \tag{A.135}$$

In the second line, we add a strategic zero. In the third line we then expand the -1 with the denominator of the fraction, and combine the terms. Next, we multiply both numerator and denominator of the fraction in Eq. (A.135) by $2\,\mathcal{A} - \mathcal{B} \pm \sqrt{\mathcal{B}^2 - 4\,\mathcal{A}\,\mathcal{C}}$ to obtain

$$n_{\pm}^2 = 1 - \frac{2\,(\mathcal{A} - \mathcal{B} + \mathcal{C})}{2\,\mathcal{A} - \mathcal{B} \pm \sqrt{\mathcal{B}^2 - 4\,\mathcal{A}\,\mathcal{C}}}\,. \tag{A.136}$$

Now, applying the AAH approximations to the coefficients $\mathcal{A}$, $\mathcal{B}$, and $\mathcal{C}$ from Eqs. (2.138)–(2.140) and inserting them into Eq. (A.136) yields the final form for the refractive index squared as

$$n_{\pm}^2 = 1 - \frac{2\,\omega^{\dagger}\,\omega^2\,(1-\omega^{\dagger})}{2\,\omega^2\,(1-\omega^{\dagger}) - \Omega_{\mathrm{e}}^2\,\sin^2(\theta) \pm \Omega_{\mathrm{e}}\,\Delta}\,. \tag{A.137}$$

To evaluate the longitudinal and transverse components of the polarisation vector (with respect to the wave vector), given in Eqs. (2.159) and (2.160), respectively, it is necessary to find an expression for the tensor element λ_{22}. From the λ tensor in Eq. (2.135), we have (accounting for the two modes)

$$\begin{aligned} \lambda_{22\pm} &= P\,S - n_{\pm}^2\,\left[P\,\cos^2(\theta) + S\,\sin^2(\theta)\right] \\ &= P\,S - n_{\pm}^2\,\mathcal{A}\,, \end{aligned} \tag{A.138}$$

where we identify $\mathcal{A}$ from Eq. (2.138) in the second line. Using $\mathcal{A} = (\mathcal{B} \pm \mathcal{F})/(2\,n_{\pm}^2)$, this becomes

$$\lambda_{22\pm} = P\,S - \frac{\mathcal{B} \pm \mathcal{F}}{2}\,. \tag{A.139}$$

Inserting the expression for $\mathcal{B}$ from Eq. (2.139) into Eq. (A.139), we arrive at the simplified form

$$\lambda_{22\pm} = \frac{1}{2}\,\left[(P\,S - R\,L)\sin^2(\theta) \mp \mathcal{F}\right]\,. \tag{A.140}$$

With Eq. (A.140) in hand, we can find expressions for $\mathcal{K}_\pm$ and $\mathcal{T}_\pm$ by substituting $\lambda_{22\pm}$ into Eqs. (2.159) and (2.160), yielding

$$\mathcal{K}_\pm = \frac{D\,\sin(\theta)\,\left(n_\pm^2 - P\right)}{\lambda_{22\pm}} = -\frac{2\,D\,\sin(\theta)\,(P - n_\pm^2)}{(P\,S - R\,L)\,\sin^2(\theta) \mp \mathcal{F}}\,, \tag{A.141}$$

$$\mathcal{T}_\pm = -\frac{D\,P\,\cos(\theta)}{\lambda_{22\pm}} = -\frac{2\,D\,P\,\cos(\theta)}{(P\,S - R\,L)\,\sin^2(\theta) \mp \mathcal{F}}\,. \tag{A.142}$$

Equation (2.161) can be further evaluated by using Eqs. (2.149) and (A.140) to find

$$\frac{1}{\mathcal{T}_\pm^2 + 1} = \frac{\mathcal{F} \mp (P\,S - R\,L)\,\sin^2(\theta)}{2\,\mathcal{F}}\,. \tag{A.143}$$

Applying the AAH approximations to Eq. (A.143) by using Eq. (A.134) and $P\,S - R\,L = \Omega_\mathrm{e}^2\,\omega^\dagger/(\omega^2 - \Omega_\mathrm{e}^2)$, we obtain

$$\frac{1}{\mathcal{T}_\pm^2 + 1} = \frac{\Delta \mp \Omega_\mathrm{e}\,\sin^2(\theta)}{2\,\Delta}\,. \tag{A.144}$$

We use the AAH relations also in Eqs. (A.141) and (A.142) to derive approximations for $\mathcal{K}_\pm$ and $\mathcal{T}_\pm$. Using Eq. (A.134) for $\mathcal{F}$, we find for $\mathcal{K}_\pm$,

$$\mathcal{K}_\pm = \frac{2\,\omega\,(1 - \omega^\dagger - n_\pm^2)\,\sin(\theta)}{\Omega_\mathrm{e}\,\sin^2(\theta) \mp \Delta}\,, \tag{A.145}$$

and similarly for $\mathcal{T}_\pm$ we obtain

$$\mathcal{T}_\pm = \frac{2\,(1 - \omega^\dagger)\,\omega\,\cos(\theta)}{\Omega_\mathrm{e}\,\sin^2(\theta) \mp \Delta}\,. \tag{A.146}$$

To derive an expression for $\mathfrak{A}_\pm$ in Eq. (2.176), we first find expressions for $\mathfrak{a}_\pm$ and $\mathfrak{b}_\pm$ in Eqs. (2.163) and (2.164), respectively. Using Eqs. (A.145) and (A.146), we find for $\mathfrak{a}_\pm$,

$$\begin{aligned}\mathfrak{a}_\pm &= \mathcal{K}_\pm\,\sin(\theta) + \mathcal{T}_\pm\,\cos(\theta) \\ &= \frac{2\,\omega[(1 - \omega^\dagger) - n_\pm^2\,\sin^2(\theta)]}{\Omega_\mathrm{e}\,\sin^2(\theta) \mp \Delta}\,.\end{aligned} \tag{A.147}$$

Similarly, we obtain for $\mathfrak{b}_\pm$ the expression

$$\mathfrak{b}_\pm = \mathcal{K}_\pm\,\cos(\theta) - \mathcal{T}_\pm\,\sin(\theta)$$

$$= -\frac{2\,\omega\,n_{\pm}^{2}\,\cos(\theta)\,\sin(\theta)}{\Omega_{\mathrm{e}}\,\sin^{2}(\theta) \mp \Delta}\,. \tag{A.148}$$

Finally, we can compute $\mathfrak{A}_{\pm}$ by inserting $\mathfrak{a}_{\pm}$ and $\mathfrak{b}_{\pm}$ from Eqs. (A.147) and (A.148) into Eq. (2.176), resulting in

$$\begin{aligned}
\mathfrak{A}_{\pm} &= \mathfrak{a}_{\pm}\frac{\nu}{\tilde{z}_{\pm}} + \mathfrak{b}_{\pm}\frac{\beta_{\parallel}}{\beta_{\perp}} \\
&= \mathcal{T}_{\pm}\left[\cos(\theta)\frac{\nu}{\tilde{z}_{\pm}} - \sin(\theta)\frac{\beta_{\parallel}}{\beta_{\perp}}\right] + \mathcal{K}_{\pm}\left[\sin(\theta)\frac{\nu}{\tilde{z}_{\pm}} + \cos(\theta)\frac{\beta_{\parallel}}{\beta_{\perp}}\right] \\
&= \mathcal{T}_{\pm}\left[\frac{\cos(\theta) - n_{\pm}\,\beta_{\parallel}}{n_{\pm}\,\beta_{\perp}\,\sin(\theta)}\right] + \frac{\mathcal{K}_{\pm}}{n_{\pm}\,\beta_{\perp}}\,.
\end{aligned} \tag{A.149}$$

Bibliography

Abramowitz, M., & Stegun, I. A. 1972, Handbook of Mathematical Functions (United States of America: United States Department of Commerce, National Bureau of Standards)

Agueda, N., & Vainio, R. 2013, J. Space Weather Space Clim., 3, A10, doi: 10.1051/swsc/2013034

Agueda, N., Vainio, R., Lario, D., & Sanahuja, B. 2008, Astrophys. J., 675, 1601, doi: 10.1086/527527

Alfvén, H. 1943, Ark. Mat. Astr. Fys., 29B, 1

—. 1950, Cosmical electrodynamics (Oxford: Clareondon Press)

Alissandrakis, C. E., Bouratzis, C., & Hillaris, A. 2019, Astron. Astrophys., 627, A133, doi: 10.1051/0004-6361/201935627

Alissandrakis, C. E., Nindos, A., Patsourakos, S., & Hillaris, A. 2021, Astron. Astrophys., 654, A112, doi: 10.1051/0004-6361/202141672

Allen, R. C., Ho, G. C., Jian, L. K., et al. 2020, Space Weather, 18, e02437, doi: 10.1029/2019SW002437

Allen, R. C., Ho, G. C., Mason, G. M., et al. 2021, Geophys. Res. Lett., 48, e91376, doi: 10.1029/2020GL091376

Antiochos, S. K., Mikić, Z., Titov, V. S., Lionello, R., & Linker, J. A. 2011, Astrophys. J., 731, 112, doi: 10.1088/0004-637X/731/2/112

Aran, A., Agueda, N., Afanasiev, A., & Sanahuja, B. 2018, in Astrophys. Space Sci. Libr., Vol. 444, Solar Particle Radiation Storms Forecasting and Analysis, ed. O. E. Malandraki & N. B. Crosby, 63–78, doi: 10.1007/978-3-319-60051-2_4

Arge, C. N., Odstrcil, D., Pizzo, V. J., & Mayer, L. R. 2003, in AIP Conf. Proc., Vol. 679, Solar Wind Ten, ed. M. Velli, R. Bruno, F. Malara, & B. Bucci (AIP), 190–193, doi: 10.1063/1.1618574

Aschwanden, M. J. 2005, Physics of the Solar Corona. An Introduction with Problems and Solutions (2nd edition) (Berlin Heidelberg: Springer-Verlag), doi: 10.1007/3-540-30766-4

Aschwanden, M. J., & Benz, A. O. 1988, Astrophys. J., 332, 466, doi: 10.1086/166670

Aurass, H., Klein, K. L., Zlotnik, E. Y., & Zaitsev, V. V. 2003, Astron. Astrophys., 410, 1001, doi: 10.1051/0004-6361:20031249

Axford, W. I., Leer, E., & Skadron, G. 1977, in Int. Cosmic Ray Conf., Vol. 11, International Cosmic Ray Conference, 132

Bai, T., & Ramaty, R. 1978, Astrophys. J., 219, 705, doi: 10.1086/155830

Bain, H. M., Krucker, S., Saint-Hilaire, P., & Raftery, C. L. 2014, Astrophys. J., 782, 43, doi: 10.1088/0004-637X/782/1/43

Bajnoková, N., Hannah, I. G., Collier, H., et al. 2025, Astrophys. J. Lett., 992, L1, doi: 10.3847/2041-8213/ae0b58

Ball, L., & Melrose, D. B. 2001, Publ. Astron. Soc. Aust., 18, 361, doi: 10.1071/AS01047

Ballai, I., & Forgács-Dajka, E. 2010, in J. Phys. Conf. Ser., Vol. 218, Journal of Physics Conference Series (IOP), 012002, doi: 10.1088/1742-6596/218/1/012002

Balogh, A., & Erdõs, G. 2013, Space Sci. Rev., 176, 177, doi: 10.1007/s11214-011-9835-3

Bame, S. J., McComas, D. J., Barraclough, B. L., et al. 1992, Astron. Astrophys. Suppl. Ser., 92, 237

Bandyopadhyay, R., Matthaeus, W. H., McComas, D. J., et al. 2022, Astrophys. J. Lett., 926, L1, doi: 10.3847/2041-8213/ac4a5c

Baratashvili, T., Brchnelova, M., Linan, L., Lani, A., & Poedts, S. 2024, Astron. Astrophys., 690, A184, doi: 10.1051/0004-6361/202449389

Baratashvili, T., & Poedts, S. 2024, Astron. Astrophys., 683, A81, doi: 10.1051/0004-6361/202347864

Baratashvili, T., Popescu Braileanu, B., Bacchini, F., Keppens, R., & Poedts, S. 2025, Astron. Astrophys., 694, A306, doi: 10.1051/0004-6361/202452705

Baratashvili, T., Verbeke, C., Wijsen, N., & Poedts, S. 2022, Astron. Astrophys., 667, A133, doi: 10.1051/0004-6361/202244111

Bastian, T. S. 2007, Astrophys. J., 665, 805, doi: 10.1086/519246

Bastian, T. S., Pick, M., Kerdraon, A., Maia, D., & Vourlidas, A. 2001, Astrophys. J. Lett., 558, L65, doi: 10.1086/323421

Baumjohann, W., & Treumann, R. A. 1996, Basic space plasma physics (London: Imperial College Press), doi: 10.1142/p015

Bekefi, G. 1966, Radiation processes in plasmas (New York: Wiley)

Bell, A. R. 1978a, Mon. Not. R. Astron. Soc., 182, 147, doi: 10.1093/mnras/182.2.147

—. 1978b, Mon. Not. R. Astron. Soc., 182, 443, doi: 10.1093/mnras/182.3.443

Belov, A. V. 2009, in IAU Symposium, Vol. 257, Universal Heliophysical Processes, ed. N. Gopalswamy & D. F. Webb, 439–450, doi: 10.1017/S1743921309029676

Benella, S., Laurenza, M., Vainio, R., et al. 2020, Astrophys. J., 901, 21, doi: 10.3847/1538-4357/abac59

Benz, A. O. 2017, Living Rev. Sol. Phys., 14, 2, doi: 10.1007/s41116-016-0004-3

Benz, A. O., & Tarnstrom, G. L. 1976, Astrophys. J., 204, 597, doi: 10.1086/154208

Blandford, R. D., & Ostriker, J. P. 1978, Astrophys. J. Lett., 221, L29, doi: 10.1086/182658

Boas, M. L. 2006, Mathematical methods in the physical sciences (Hoboken, NJ: Wiley)

Bobra, M. G., & Couvidat, S. 2015, Astrophys. J., 798, 135, doi: 10.1088/0004-637X/798/2/135

Bobra, M. G., & Ilonidis, S. 2016, Astrophys. J., 821, 127, doi: 10.3847/0004-637X/821/2/127

Bodenheimer, P., Laughlin, G. P., Rózyczka, M., & Yorke, H. W., eds. 2007, Numerical Methods in Astrophysics: An Introduction (Boca Raton: Taylor & Francis Group)

Bolduc, L. 2002, J. Atmos. Sol.-Terr. Phys., 64, 1793, doi: 10.1016/S1364-6826(02)00128-1

Boldyrev, S., Forest, C., & Egedal, J. 2020, Proc. Natl. Acad. Sci. U.S. A., 117, 9232, doi: 10.1073/pnas.1917905117

Born, M., & Wolf, E. 1999, Principles of Optics (Cambridge: Cambridge University Press)

Borovikov, D., Sokolov, I. V., Roussev, I. I., Taktakishvili, A., & Gombosi, T. I. 2018, Astrophys. J., 864, 88, doi: 10.3847/1538-4357/aad68d

Borovsky, J. E. 2008, J. Geophys. Res. Space Phys., 113, A08110, doi: 10.1029/2007JA012684

Bothmer, V., & Mrotzek, N. 2017, Sol. Phys., 292, 157, doi: 10.1007/s11207-017-1171-7

Bouratzis, C., Hillaris, A., Alissandrakis, C. E., et al. 2015, Sol. Phys., 290, 219, doi: 10.1007/s11207-014-0562-2

Boyd, T. J. M., & Sanderson, J. J. 2003, The Physics of Plasmas (Cambridge: Cambridge University Press), doi: 10.1017/CBO9780511755750

Brackbill, J. U., & Barnes, D. C. 1980, J. Comput. Phys., 35, 426, doi: 10.1016/0021-9991(80)90079-0

Braginskii, S. I. 1965, Rev. Plasma Phys., 1, 205

Brchnelova, M., Zhang, F., Leitner, P., et al. 2022, J. Plasma Phys., 88, 905880205, doi: 10.1017/S0022377822000241

Budden, K. G. 1985, The propagation of radio waves. (Cambridge: Cambridge University Press)

Burger, R. A., Moraal, H., & Webb, G. M. 1985, Astrophys. Space Sci., 116, 107, doi: 10.1007/BF00649278

Cairns, I. H., Knock, S. A., Robinson, P. A., & Kuncic, Z. 2003, Space Sci. Rev., 107, 27, doi: 10.1023/A:1025503201687

Cane, H. V. 2000, Space Sci. Rev., 93, 55, doi: 10.1023/A:1026532125747

Cane, H. V., & Erickson, W. C. 2005, Astrophys. J., 623, 1180, doi: 10.1086/428820

Cane, H. V., Erickson, W. C., & Prestage, N. P. 2002, J. Geophys. Res. Space Phys., 107, 1315, doi: 10.1029/2001JA000320

Cane, H. V., Richardson, I. G., & von Rosenvinge, T. T. 2010, J. Geophys. Res. Space Phys., 115, A08101, doi: 10.1029/2009JA014848

Cannon, P., Angling, M., Barclay, L., et al. 2013, Extreme space weather: impacts on engineered systems and infrastructure (London: Royal Academy of Engineering)

Carley, E. P., Vilmer, N., Simões, P. J. A., & Ó Fearraigh, B. 2017, Astron. Astrophys., 608, A137, doi: 10.1051/0004-6361/201731368

Carley, E. P., Vilmer, N., & Vourlidas, A. 2020, Frontiers in Astronomy and Space Sciences, 7, 79, doi: 10.3389/fspas.2020.551558

Carrington, R. C. 1859, Mon. Not. R. Astron. Soc., 20, 13, doi: 10.1093/mnras/20.1.13

Chancellor, J., Scott, G., & Sutton, J. 2014, Life, 4, 491, doi: 10.3390/life4030491

Chandrasekhar, S. 1960, Radiative transfer (New York: Dover Publications)

Charbonneau, P. 2014, Ann. Rev. Astron. Astrophys., 52, 251, doi: 10.1146/annurev-astro-081913-040012

—. 2020, Living Rev. Sol. Phys., 17, 4, doi: 10.1007/s41116-020-00025-6

Chen, F. F. 2016, Introduction to Plasma Physics and Controlled Fusion (Cham: Springer), doi: 10.1007/978-3-319-22309-4

Chen, P. F. 2011, Living Rev. Sol. Phys., 8, 1, doi: 10.12942/lrsp-2011-1

Chernov, G., & Fomichev, V. 2021, Astrophys. J., 922, 82, doi: 10.3847/1538-4357/ac1f32

Chernov, G. P. 2006, Space Sci. Rev., 127, 195, doi: 10.1007/s11214-006-9141-7

Chernov, G. P., Markeev, A. K., Poquerusse, M., et al. 1998, Astron. Astrophys., 334, 314

Chhabra, S., Gary, D. E., Hallinan, G., et al. 2021, Astrophys. J., 906, 132, doi: 10.3847/1538-4357/abc94b

Chi, Y., Shen, C., Luo, B., Wang, Y., & Xu, M. 2018, Space Weather, 16, 1960, doi: 10.1029/2018SW001894

Classen, H. T., Mann, G., & Keppler, E. 1998, Astron. Astrophys., 335, 1101

Cliver, E. W. 2000, in AIP Conf. Proc., Vol. 528, Acceleration and Transport of Energetic Particles Observed in the Heliosphere, ed. R. A. Mewaldt, J. R. Jokipii, M. A. Lee, E. Möbius, & T. H. Zurbuchen (AIP), 21–31, doi: 10.1063/1.1324277

Cohen, C. M. S., Leske, R. A., Christian, E. R., et al. 2024, Astrophys. J., 966, 148, doi: 10.3847/1538-4357/ad37f8

Cranmer, S. R., Asgari-Targhi, M., Miralles, M. P., et al. 2015, Philos. Transact. A Math. Phys. Eng. Sci., 373, 20140148, doi: 10.1098/rsta.2014.0148

Cranmer, S. R., Gibson, S. E., & Riley, P. 2017, Space Sci. Rev., 212, 1345, doi: 10.1007/s11214-017-0416-y

Cranmer, S. R., & Winebarger, A. R. 2019, Ann. Rev. Astron. Astrophys., 57, 157, doi: 10.1146/annurev-astro-091918-104416

Decker, R. B., & Vlahos, L. 1985, J. Geophys. Res., 90, 47, doi: 10.1029/JA090iA01p00047

Dedner, A., Kemm, F., Kröner, D., et al. 2002, J. Comput. Phys., 175, 645, doi: 10.1006/jcph.2001.6961

Demtröder, W. 2019, Electrodynamics and Optics (Cham: Springer), doi: 10.1007/978-3-030-02291-4

Desai, M., & Giacalone, J. 2016, Living Rev. Sol. Phys., 13, 3, doi: 10.1007/s41116-016-0002-5

Ding, Z., Li, G., Mason, G., et al. 2024, Astron. Astrophys., 681, A92, doi: 10.1051/0004-6361/202347506

Downs, C., Roussev, I. I., van der Holst, B., et al. 2010, Astrophys. J., 712, 1219, doi: 10.1088/0004-637X/712/2/1219

Drake, J. F., Cassak, P. A., Shay, M. A., Swisdak, M., & Quataert, E. 2009, Astrophys. J. Lett., 700, L16, doi: 10.1088/0004-637X/700/1/L16

Drake, J. F., Swisdak, M., & Fermo, R. 2013, Astrophys. J. Lett., 763, L5, doi: 10.1088/2041-8205/763/1/L5

Dröge, W., Kartavykh, Y. Y., Klecker, B., & Kovaltsov, G. A. 2010, Astrophys. J., 709, 912, doi: 10.1088/0004-637X/709/2/912

Dulk, G. A. 1973, Sol. Phys., 32, 491, doi: 10.1007/BF00154962

—. 1985, Ann. Rev. Astron. Astrophys., 23, 169, doi: 10.1146/annurev.aa.23.090185.001125

Dulk, G. A., Gary, D. E., & Suzuki, S. 1980, Astron. Astrophys., 88, 218

Dulk, G. A., & Marsh, K. A. 1982, Astrophys. J., 259, 350, doi: 10.1086/160171

Eastwood, J. P., Biffis, E., Hapgood, M. A., et al. 2017, Risk Anal., 37, 206, doi: 10.1111/risa.12765

Eidman, V. Y. 1958, Sov. Phys. JETP, 7, 91

—. 1959, Sov. Phys. JETP, 9, 947

Fan, Y. 2021, Living Rev. Sol. Phys., 18, 5, doi: 10.1007/s41116-021-00031-2

Feldman, U., Landi, E., & Schwadron, N. A. 2005, J. Geophys. Res. Space Phys., 110, A07109, doi: 10.1029/2004JA010918

Fermi, E. 1949, Phys. Rev., 75, 1169, doi: 10.1103/PhysRev.75.1169

Fisk, L. A., & Lee, M. A. 1980, Astrophys. J., 237, 620, doi: 10.1086/157907

Fleishman, G. D., & Kuznetsov, A. A. 2010, Astrophys. J., 721, 1127, doi: 10.1088/0004-637X/721/2/1127

Fleishman, G. D., & Melnikov, V. F. 2003, Astrophys. J., 587, 823, doi: 10.1086/368252

Fletcher, L., Dennis, B. R., Hudson, H. S., et al. 2011, Space Sci. Rev., 159, 19, doi: 10.1007/s11214-010-9701-8

Fokker, A. D. 1963, Space Sci. Rev., 2, 70, doi: 10.1007/BF00174028

Forbush, S. E. 1946, Phys. Rev., 70, 771, doi: 10.1103/PhysRev.70.771

Fox, N. J., Velli, M. C., Bale, S. D., et al. 2016, Space Sci. Rev., 204, 7, doi: 10.1007/s11214-015-0211-6

Galeev, A. A., Karpman, V. I., & Sagdeev, R. Z. 1965, Sov. Phys. Dokl., 9, 681

Galeev, A. A., & Krasnoselskikh, V. V. 1979, Sov. Astron. Lett., 5, 257

Gary, D. E., Dulk, G. A., House, L. L., et al. 1985, Astron. Astrophys., 152, 42

Gary, D. E., & Keller, C. U., eds. 2004, Astrophys. Space Sci. Libr., Vol. 314, Solar and Space Weather Radiophysics - Current Status and Future Developments

Gary, G. A. 2001, Sol. Phys., 203, 71, doi: 10.1023/A:1012722021820

Geiss, J., Gloeckler, G., & von Steiger, R. 1995, Space Sci. Rev., 72, 49, doi: 10.1007/BF00768753

Gergely, T. E. 1986, Sol. Phys., 104, 175, doi: 10.1007/BF00159959

Giacalone, J. 1999, Adv. Space Res., 23, 581, doi: 10.1016/S0273-1177(99)80014-3

Giacalone, J., & Jokipii, J. R. 1997, Geophys. Res. Lett., 24, 1723, doi: 10.1029/97GL01631

—. 2004, Astrophys. J., 616, 573, doi: 10.1086/424870

Ginzburg, V. L. 1979, Theoretical physics and astrophysics (Pergamon Press, Oxford)

Ginzburg, V. L., & Syrovatskii, S. I. 1964, The Origin of Cosmic Rays (Amsterdam: Elsevier)

—. 1965, Ann. Rev. Astron. Astrophys., 3, 297, doi: 10.1146/annurev.aa.03.090165.001501

Glesener, L., Krucker, S., Duncan, J., et al. 2020, Astrophys. J. Lett., 891, L34, doi: 10.3847/2041-8213/ab7341

Goedbloed, H., Keppens, R., & Poedts, S. 2019, Magnetohydrodynamics of Laboratory and Astrophysical Plasmas (Cambridge: Cambridge University Press), doi: 10.1017/9781316403679

Gómez-Herrero, R., Klassen, A., Müller-Mellin, R., et al. 2009, J. Geophys. Res. Space Phys., 114, A05101, doi: 10.1029/2008JA013755

Gopalswamy, N. 2016, Geosci. Lett., 3, 8, doi: 10.1186/s40562-016-0039-2

—. 2018, in Extreme Events in Geospace, ed. N. Buzulukova (Amsterdam: Elsevier), 37, doi: 10.1016/B978-0-12-812700-1.00002-9

Gopalswamy, N., & Kundu, M. R. 1987, Sol. Phys., 114, 347, doi: 10.1007/BF00167350

—. 1990, Sol. Phys., 128, 377, doi: 10.1007/BF00838474

Gopalswamy, N., Xie, H., Yashiro, S., et al. 2012, Space Sci. Rev., 171, 23, doi: 10.1007/s11214-012-9890-4

Gosling, J. T. 1993, J. Geophys. Res., 98, 18937, doi: 10.1029/93JA01896

Grodji, O. D. F., Doumbia, V., Amaechi, P. O., et al. 2021, Atmos., 13, 69, doi: 10.3390/atmos13010069

Guo, J. H., Linan, L., Poedts, S., et al. 2024, Astron. Astrophys., 683, A54, doi: 10.1051/0004-6361/202347634

Guzmán, J. G. A., Florinski, V., Tóth, G., et al. 2024, Astrophys. J. Suppl., 272, 46, doi: 10.3847/1538-4365/ad4637

Han Thanh, L., Scherer, K., & Fichtner, H. 2022, Phys. Plasmas, 29, 022901, doi: 10.1063/5.0080293

Hapgood, M. A. 2011, Adv. Space Res., 47, 2059, doi: 10.1016/j.asr.2010.02.007

Hariharan, K., Ramesh, R., Kathiravan, C., & Wang, T. J. 2016, Sol. Phys., 291, 1405, doi: 10.1007/s11207-016-0918-x

Harten, A., Lax, P. D., & van Leer, B. 1983, Soc. Ind. Appl. Math., 25, 35, doi: 10.1137/1025002

Hasselmann, K., & Wibberenz, G. 1970, Astrophys. J., 162, 1049, doi: 10.1086/150736

Hathaway, D. H. 2015, Living Rev. Sol. Phys., 12, 4, doi: 10.1007/lrsp-2015-4

Hayes, J. C., Norman, M. L., Fiedler, R. A., et al. 2006, Astrophys. J. Suppl., 165, 188, doi: 10.1086/504594

He, J. S., Tu, C. Y., & Marsch, E. 2007, Astron. Astrophys., 468, 307, doi: 10.1051/0004-6361:20066423

He, J. S., Tu, C. Y., Tian, H., & Marsch, E. 2010, Adv. Space Res., 45, 303, doi: 10.1016/j.asr.2009.07.020

Hodgson, R. 1859, Mon. Not. R. Astron. Soc., 20, 15, doi: 10.1093/mnras/20.1.15a

Hoeksema, J. T., Wilcox, J. M., & Scherrer, P. H. 1983, J. Geophys. Res., 88, 9910, doi: 10.1029/JA088iA12p09910

Hollweg, J. V. 1976, J. Geophys. Res., 81, 1649, doi: 10.1029/JA081i010p01649

—. 1978, Rev. Geophys. Space Phys., 16, 689, doi: 10.1029/RG016i004p00689

Howard, R. A. 2006, Geophys. Monogr. Ser., 165, 7

Howard, R. A., Michels, D. J., Sheeley, Jr., N. R., & Koomen, M. J. 1982, Astrophys. J. Lett., 263, L101, doi: 10.1086/183932

Hu, J., Li, G., Ao, X., Zank, G. P., & Verkhoglyadova, O. 2017, J. Geophys. Res. Space Phys., 122, 10,938, doi: 10.1002/2017JA024077

Hudson, H. S. 2011, Space Sci. Rev., 158, 5, doi: 10.1007/s11214-010-9721-4

—. 2021, Ann. Rev. Astron. Astrophys., 59, 445, doi: 10.1146/annurev-astro-112420-023324

Husidic, E., Lazar, M., Fichtner, H., Scherer, K., & Poedts, S. 2021, Astron. Astrophys., 654, A99, doi: 10.1051/0004-6361/202141760

Husidic, E., Scherer, K., Lazar, M., Fichtner, H., & Poedts, S. 2022, Astrophys. J., 927, 159, doi: 10.3847/1538-4357/ac4af4

Husidic, E., Wijsen, N., Baratashvili, T., Poedts, S., & Vainio, R. 2024a, J. Space Weather Space Clim., 14, 11, doi: 10.1051/swsc/2024009

Husidic, E., Wijsen, N., Jebaraj, I. C., et al. 2025, Astron. Astrophys., 701, A53, doi: 10.1051/0004-6361/202555534

Husidic, E., Wijsen, N., Linan, L., et al. 2024b, Astrophys. J. Lett., 976, L31, doi: 10.3847/2041-8213/ad8d56

Hutchinson, A., Dalla, S., Laitinen, T., et al. 2022, Astron. Astrophys., 658, A23, doi: 10.1051/0004-6361/202142002

Ingale, M., Subramanian, P., & Cairns, I. 2015, Mon. Not. R. Astron. Soc., 447, 3486, doi: 10.1093/mnras/stu2703

Isavnin, A. 2016, Astrophys. J., 833, 267, doi: 10.3847/1538-4357/833/2/267

Isenberg, P. A. 1997, J. Geophys. Res., 102, 4719, doi: 10.1029/96JA03671

Jaekel, U., & Schlickeiser, R. 1992, Ann. Geophys., 10, 541

Jebaraj, I. C., Kouloumvakos, A., Magdalenic, J., et al. 2021, Astron. Astrophys., 654, A64, doi: 10.1051/0004-6361/202141695

Jebaraj, I. C., Kouloumvakos, A., Dresing, N., et al. 2023, Astron. Astrophys., 675, A27, doi: 10.1051/0004-6361/202245716

Jebaraj, I. C., Agapitov, O. V., Gedalin, M., et al. 2024, Astrophys. J. Lett., 976, L7, doi: 10.3847/2041-8213/ad8eb8

Jian, L., Russell, C. T., Luhmann, J. G., & Skoug, R. M. 2006, Sol. Phys., 239, 337, doi: 10.1007/s11207-006-0132-3

Jiao, Y., Liu, Y. D., Ran, H., & Cheng, W. 2024, Astrophys. J., 960, 42, doi: 10.3847/1538-4357/ad0dfe

Jokipii, J. R. 1966, Astrophys. J., 146, 480, doi: 10.1086/148912

—. 1982, Astrophys. J., 255, 716, doi: 10.1086/159870

—. 1987, Astrophys. J., 313, 842, doi: 10.1086/165022

Kahler, S. W., Hildner, E., & Van Hollebeke, M. A. I. 1978, Sol. Phys., 57, 429, doi: 10.1007/BF00160116

Kallenrode, M.-B. 2001, Space physics : an introduction to plasmas and particles in the heliosphere and magnetospheres (Berlin, Heidelberg: Springer-Verlag), doi: 10.1007/978-3-662-04443-8

Kallenrode, M. B. 2003, J. Phys. G: Nucl. Part. Phys., 29, 965, doi: 10.1088/0954-3899/29/5/316

Kansabanik, D., Mondal, S., & Oberoi, D. 2024, Astrophys. J., 968, 55, doi: 10.3847/1538-4357/ad43e9

Kaplan, S. A., & Tsytovich, V. N. 1969, Sov. Phys. Uspekhi, 12, 42, doi: 10.1070/PU1969v012n01ABEH003916

Karlický, M., & Rybák, J. 2020, Astrophys. J. Suppl., 250, 31, doi: 10.3847/1538-4365/abb19f

Keppens, R., Meliani, Z., van Marle, A. J., et al. 2012, J. Comput. Phys., 231, 718, doi: 10.1016/j.jcp.2011.01.020

Keppens, R., Popescu Braileanu, B., Zhou, Y., et al. 2023, Astron. Astrophys., 673, A66, doi: 10.1051/0004-6361/202245359

Khabarova, O., Zank, G. P., Li, G., et al. 2015, Astrophys. J., 808, 181, doi: 10.1088/0004-637X/808/2/181

Khabarova, O., Malandraki, O., Malova, H., et al. 2021, Space Sci. Rev., 217, 38, doi: 10.1007/s11214-021-00814-x

Kieokaew, R., Lavraud, B., Yang, Y., et al. 2021, Astron. Astrophys., 656, A12, doi: 10.1051/0004-6361/202140915

Kissmann, R., & Pomoell, J. 2012, SIAM J. Sci. Comput., 34, A763, doi: 10.1137/110834329

Klassen, A., Dresing, N., Gómez-Herrero, R., & Heber, B. 2015, Astron. Astrophys., 580, A115, doi: 10.1051/0004-6361/201525700

Klein, K. L. 1987, Astron. Astrophys., 183, 341

Klein, K.-L. 2018, in Astrophys. Space Sci. Libr., Vol. 444, Solar Particle Radiation Storms Forecasting and Analysis, ed. O. E. Malandraki & N. B. Crosby, 27–43, doi: 10.1007/978-3-319-60051-2_2

Klein, K.-L., Matamoros, C. S., & Zucca, P. 2018, C. R. Phys., 19, 36, doi: 10.1016/j.crhy.2018.01.005

Klein, K.-L., Musset, S., Vilmer, N., et al. 2022, Astron. Astrophys., 663, A173, doi: 10.1051/0004-6361/202243903

Klimas, A. J., & Sandri, G. 1971, Astrophys. J., 169, 41, doi: 10.1086/151116

Knipp, D. J. 2017, Space Weather, 15, 549, doi: 10.1002/2017SW001639

Knock, S. A., & Cairns, I. H. 2005, J. Geophys. Res., 110, A01101, doi: 10.1029/2004JA010452

Kong, Q., Siauw, T., & Bayen, A. M. 2020, Python Programming and Numerical Methods (London: Academic Press, an imprint of Elsevier), doi: 10.1016/C2018-0-04165-1

Kontar, E. P., Chen, X., Chrysaphi, N., et al. 2019, Astrophys. J., 884, 122, doi: 10.3847/1538-4357/ab40bb

Kouloumvakos, A., Nindos, A., Valtonen, E., et al. 2015, Astron. Astrophys., 580, A80, doi: 10.1051/0004-6361/201424397

Koval, A., Stanislavsky, A., Chen, Y., et al. 2016, Astrophys. J., 826, 125, doi: 10.3847/0004-637X/826/2/125

Kozarev, K., & Nedal, M. 2025, arXiv e-prints, arXiv:2505.00435, doi: 10.48550/arXiv.2505.00435

Kozarev, K., Schwadron, N. A., Dayeh, M. A., et al. 2010, Space Weather, 8, S00E08, doi: 10.1029/2009SW000550

Kozarev, K. A., Evans, R. M., Schwadron, N. A., et al. 2013, Astrophys. J., 778, 43, doi: 10.1088/0004-637X/778/1/43

Krupar, V., Maksimovic, M., Kontar, E. P., et al. 2018, Astrophys. J., 857, 82, doi: 10.3847/1538-4357/aab60f

Krymskii, G. F. 1977, Dokl. Akad. Nauk SSSR, 234, 1306

Kumari, A. 2022, Sol. Phys., 297, 98, doi: 10.1007/s11207-022-02032-2

Kumari, A., Morosan, D. E., & Kilpua, E. K. J. 2021, Astrophys. J., 906, 79, doi: 10.3847/1538-4357/abc878

Kumari, A., Morosan, D. E., Kilpua, E. K. J., & Daei, F. 2023, Astron. Astrophys., 675, A102, doi: 10.1051/0004-6361/202244015

Kundu, M. R. 1965, Solar radio astronomy (New York: Interscience Publishers)

Kuwabara, T., Bieber, J. W., Clem, J., et al. 2006, Space Weather, 4, S08001, doi: 10.1029/2005SW000204

Kuźma, B., Brchnelova, M., Perri, B., et al. 2023, Astrophys. J., 942, 31, doi: 10.3847/1538-4357/aca483

Kuznetsov, A. A., & Fleishman, G. D. 2021, Astrophys. J., 922, 103, doi: 10.3847/1538-4357/ac29c0

Kuznetsov, A. A., Van Doorsselaere, T., & Reznikova, V. E. 2015, Sol. Phys., 290, 1173, doi: 10.1007/s11207-015-0662-7

Laitinen, T., & Dalla, S. 2021, Astrophys. J., 906, 9, doi: 10.3847/1538-4357/abc622

Lamy, P. L., Floyd, O., Boclet, B., et al. 2019, Space Sci. Rev., 215, 39, doi: 10.1007/s11214-019-0605-y

Landau, L. D., & Lifshitz, E. M. 1975, The classical theory of fields (Oxford: Pergamon Press)

Lani, A. 2009, PhD thesis, Université Libre de Bruxelles, von Karman Institute for Fluid Dynamics, Aeronautics and Aerospace Department

Lazar, M., & Fichtner, H., eds. 2021, Astrophys. Space Sci. Libr., Vol. 464, Kappa Distributions; From Observational Evidences via Controversial Predictions to a Consistent Theory of Nonequilibrium Plasmas, doi: 10.1007/978-3-030-82623-9

Lazar, M., Pierrard, V., Shaaban, S. M., Fichtner, H., & Poedts, S. 2017, Astron. Astrophys., 602, A44, doi: 10.1051/0004-6361/201630194

le Roux, J. A., & Webb, G. M. 2009, Astrophys. J., 693, 534, doi: 10.1088/0004-637X/693/1/534

Lee, J.-O., Cho, K.-S., An, J., et al. 2021, Astrophys. J. Lett., 920, L6, doi: 10.3847/2041-8213/ac2422

Lee, M. A., Mewaldt, R. A., & Giacalone, J. 2012, Space Sci. Rev., 173, 247, doi: 10.1007/s11214-012-9932-y

Lee, S.-Y., Yoon, P. H., Lee, E., & Tu, W. 2022, Astrophys. J., 924, 36, doi: 10.3847/1538-4357/ac32bb

Lemen, J. R., Title, A. M., Akin, D. J., et al. 2012, Sol. Phys., 275, 17, doi: 10.1007/s11207-011-9776-8

Liemohn, H. B. 1965, Radio Sci., 69D, 5

Linan, L., Baratashvili, T., Lani, A., et al. 2025, Astron. Astrophys., 693, A229, doi: 10.1051/0004-6361/202451854

Linan, L., Regnault, F., Perri, B., et al. 2023, Astron. Astrophys., 675, A101, doi: 10.1051/0004-6361/202346235

Litvak, A. G., & Trakhtengerts, V. Y. 1971, Sov. Phys. JETP, 33, 921

Liu, H., Chen, Y., Cho, K., et al. 2018, Sol. Phys., 293, 58, doi: 10.1007/s11207-018-1280-y

Longair, M. S. 1992, High energy astrophysics. Vol.1: Particles, photons and their detection (Cambridge: Cambridge University Press)

Love, J. J., Hayakawa, H., & Cliver, E. W. 2019, Space Weather, 17, 1281, doi: 10.1029/2019SW002250

Luhmann, J. G., Mays, M. L., Odstrcil, D., et al. 2017, Space Weather, 15, 934, doi: 10.1002/2017SW001617

Lv, M., Chen, Y., Vasanth, V., et al. 2021, Sol. Phys., 296, 38, doi: 10.1007/s11207-021-01769-6

Lysenko, A. L., Frederiks, D. D., Fleishman, G. D., et al. 2020, Phys.-Uspekhi, 63, 818, doi: 10.3367/UFNe.2019.06.038757

Magnus, J. R., & Neudecker, H. 2019, Matrix Differential Calculus with Applications in Statistics and Econometrics (Hoboken, NJ: Wiley), doi: 10.1002/9781119541219

Maharana, A., Isavnin, A., Scolini, C., et al. 2022, Adv. Space Res., 70, 1641, doi: 10.1016/j.asr.2022.05.056

Maharana, A., Scolini, C., Schmieder, B., & Poedts, S. 2023, Astron. Astrophys., 675, A136, doi: 10.1051/0004-6361/202345902

Maia, D. J. F., Gama, R., Mercier, C., et al. 2007, Astrophys. J., 660, 874, doi: 10.1086/508011

Maksimovic, M., Pierrard, V., & Riley, P. 1997, Geophys. Res. Lett., 24, 1151, doi: 10.1029/97GL00992

Maksimovic, M., Zouganelis, I., Chaufray, J. Y., et al. 2005, J. Geophys. Res. Space Phys., 110, A09104, doi: 10.1029/2005JA011119

Manchester, IV, W. B., van der Holst, B., Tóth, G., & Gombosi, T. I. 2012, Astrophys. J., 756, 81, doi: 10.1088/0004-637X/756/1/81

Mancuso, S., & Spangler, S. R. 2000, Astrophys. J., 539, 480, doi: 10.1086/309205

Mann, G., Klassen, A., Aurass, H., & Classen, H. T. 2003, Astron. Astrophys., 400, 329, doi: 10.1051/0004-6361:20021593

Mansfield, V. N. 1967, Astrophys. J., 147, 672, doi: 10.1086/149043

Marsch, E. 2006, Living Rev. Sol. Phys., 3, 1, doi: 10.12942/lrsp-2006-1

Martin, B. R., & Shaw, G. 2015, Mathematics for Physicists (Chichester: Wiley)

Matthaeus, W. H., & Velli, M. 2011, Space Sci. Rev., 160, 145, doi: 10.1007/s11214-011-9793-9

McComas, D. J., Bame, S. J., Barker, P., et al. 1998, Space Sci. Rev., 86, 563, doi: 10.1023/A:1005040232597

McComas, D. J., Christian, E. R., Schwadron, N. A., et al. 2018, Space Sci. Rev., 214, 116, doi: 10.1007/s11214-018-0550-1

Melnik, V. N., Rucker, H. O., Konovalenko, A. A., et al. 2018, arXiv, arXiv:1802.06249, doi: 10.48550/arXiv.1802.06249

Melnikov, V. F., Gary, D. E., & Nita, G. M. 2008, Sol. Phys., 253, 43, doi: 10.1007/s11207-008-9275-8

Melrose, D. B. 1968a, Astrophys. Space Sci., 2, 171, doi: 10.1007/BF00651567

—. 1968b, Astrophys. J., 154, 803, doi: 10.1086/149802

—. 1980, Sol. Phys., 67, 357, doi: 10.1007/BF00149813

—. 2017, Rev. Mod. Plasma Phys., 1, 5, doi: 10.1007/s41614-017-0007-0

Mewaldt, R. A., Mason, G. M., Gloeckler, G., et al. 2001, in AIP Conf. Proc., Vol. 598, Joint SOHO/ACE workshop "Solar and Galactic Composition", ed. R. F. Wimmer-Schweingruber (AIP), 165–170, doi: 10.1063/1.1433995

Mewaldt, R. A., Leske, R. A., Stone, E. C., et al. 2009, Astrophys. J. Lett., 693, L11, doi: 10.1088/0004-637X/693/1/L11

Meyer, P., Parker, E. N., & Simpson, J. A. 1956, Phys. Rev., 104, 768, doi: 10.1103/PhysRev.104.768

Mikić, Z., Linker, J. A., Schnack, D. D., Lionello, R., & Tarditi, A. 1999, Phys. Plasmas, 6, 2217, doi: 10.1063/1.873474

Milligan, R. O., Gallagher, P. T., Mathioudakis, M., et al. 2006, Astrophys. J. Lett., 638, L117, doi: 10.1086/500555

Mohan, A., Mondal, S., Wedemeyer, S., & Gopalswamy, N. 2024, Astron. Astrophys., 686, A51, doi: 10.1051/0004-6361/202347924

Mondal, S., Oberoi, D., & Vourlidas, A. 2020, Astrophys. J., 893, 28, doi: 10.3847/1538-4357/ab7fab

Morosan, D. E., Kilpua, E. K. J., Carley, E. P., & Monstein, C. 2019, Astron. Astrophys., 623, A63, doi: 10.1051/0004-6361/201834510

Morosan, D. E., Kumari, A., Kilpua, E. K. J., & Hamini, A. 2021, Astron. Astrophys., 647, L12, doi: 10.1051/0004-6361/202140392

Morosan, D. E., Palmerio, E., Pomoell, J., et al. 2020, Astron. Astrophys., 635, A62, doi: 10.1051/0004-6361/201937133

Morosan, D. E., Zucca, P., Bloomfield, D. S., & Gallagher, P. T. 2016, Astron. Astrophys., 589, L8, doi: 10.1051/0004-6361/201628392

Morton, R. J., Tomczyk, S., & Pinto, R. 2015, Nat. Commun., 6, 7813, doi: 10.1038/ncomms8813

Moschou, S.-P., Sokolov, I., Cohen, O., et al. 2018, Astrophys. J., 867, 51, doi: 10.3847/1538-4357/aae58c

Mostafavi, P., Merkin, V. G., Provornikova, E., et al. 2022, Astrophys. J., 925, 181, doi: 10.3847/1538-4357/ac3fb4

Müller, D., St. Cyr, O. C., Zouganelis, I., et al. 2020, Astron. Astrophys., 642, A1, doi: 10.1051/0004-6361/202038467

Murphy, P. C., Carley, E. P., Ryan, A. M., Zucca, P., & Gallagher, P. T. 2021, Astron. Astrophys., 645, A11, doi: 10.1051/0004-6361/202038518

National Research Council. 2008, Severe Space Weather Events: Understanding Societal and Economic Impacts: A Workshop Report (Washington, DC: The National Academies Press), doi: 10.17226/12507

Ndacyayisenga, T., Uwamahoro, J., Uwamahoro, J. C., et al. 2024, Ann. Geophys., 42, 313, doi: 10.5194/angeo-42-313-2024

Niemela, A., Wijsen, N., Aran, A., et al. 2024, Astrophys. J. Lett., 967, L35, doi: 10.3847/2041-8213/ad4c70

Nindos, A. 2020, Front. Astron. Space Sci., 7, 57, doi: 10.3389/fspas.2020.00057

Nindos, A., Aurass, H., Klein, K. L., & Trottet, G. 2008, Sol. Phys., 253, 3, doi: 10.1007/s11207-008-9258-9

Nishimura, Y., Ono, T., Tsuchiya, F., et al. 2013, Earth Planets Space, 65, 1555, doi: 10.5047/eps.2013.09.009

Nool, M., & Keppens, R. 2002, Comput. Methods Appl. Math., 2, 92, doi: 10.2478/cmam-2002-0005

Noyes, R. W. 1982, The Sun, our star (Cambridge: Harvard University Press), doi: 10.4159/harvard.9780674429291

Odstrcil, D., Pizzo, V. J., & Arge, C. N. 2005, J. Geophys. Res. Space Phys., 110, A02106, doi: 10.1029/2004JA010745

Odstrcil, D., Riley, P., & Zhao, X. P. 2004, J. Geophys. Res. Space Phys., 109, A02116, doi: 10.1029/2003JA010135

Øksendal, B. 1995, Stochastic Differential Equations – An Introduction with Applications (Berlin Heidelberg: Springer), doi: 10.1007/978-3-662-03185-8

Owens, M. J., & Forsyth, R. J. 2013, Living Rev. Sol. Phys., 10, 5, doi: 10.12942/lrsp-2013-5

Paouris, E., Vourlidas, A., Kouloumvakos, A., et al. 2023, Astrophys. J., 956, 58, doi: 10.3847/1538-4357/acf30f

Papadopoulos, K., & Freund, H. P. 1979, Space Sci. Rev., 24, 511, doi: 10.1007/BF00172213

Parker, E. N. 1958, Astrophys. J., 128, 664, doi: 10.1086/146579

—. 1965, Planet. Space Sci., 13, 9, doi: 10.1016/0032-0633(65)90131-5

—. 2009, Space Sci. Rev., 144, 15, doi: 10.1007/s11214-008-9445-x

Pecora, F., Servidio, S., Greco, A., et al. 2021, Mon. Not. R. Astron. Soc., 508, 2114, doi: 10.1093/mnras/stab2659

Perri, B., Kuźma, B., Brchnelova, M., et al. 2023, Astrophys. J., 943, 124, doi: 10.3847/1538-4357/ac9799

Perri, B., Leitner, P., Brchnelova, M., et al. 2022a, Astrophys. J., 936, 19, doi: 10.3847/1538-4357/ac7237

Perri, S., Bykov, A., Fahr, H., Fichtner, H., & Giacalone, J. 2022b, Space Sci. Rev., 218, 26, doi: 10.1007/s11214-022-00892-5

Peter, H., Bingert, S., Klimchuk, J. A., et al. 2013, Astron. Astrophys., 556, A104, doi: 10.1051/0004-6361/201321826

Petrosian, V. 1981, Astrophys. J., 251, 727, doi: 10.1086/159517

—. 2012, Space Sci. Rev., 173, 535, doi: 10.1007/s11214-012-9900-6

—. 2016, Astrophys. J., 830, 28, doi: 10.3847/0004-637X/830/1/28

Petrosian, V., & Liu, S. 2004, Astrophys. J., 610, 550, doi: 10.1086/421486

Pevtsov, A. A., Fisher, G. H., Acton, L. W., et al. 2003, Astrophys. J., 598, 1387, doi: 10.1086/378944

Pezzi, O., Pecora, F., Le Roux, J., et al. 2021, Space Sci. Rev., 217, 39, doi: 10.1007/s11214-021-00799-7

Pick, M. 1986, Sol. Phys., 104, 19, doi: 10.1007/BF00159942

Pick, M. 2004, in Astrophys. Space Sci. Libr., Vol. 314, Astrophys. Space Sci. Libr., ed. D. E. Gary & C. U. Keller, 17, doi: 10.1007/1-4020-2814-8_2

Pick, M., & Vilmer, N. 2008, Astron. Astrophys. Rev., 16, 1, doi: 10.1007/s00159-008-0013-x

Pierrard, V., & Lazar, M. 2010, Sol. Phys., 267, 153, doi: 10.1007/s11207-010-9640-2

Pierre Auger Collaboration, Aab, A., Abreu, P., et al. 2017, Sci., 357, 1266, doi: 10.1126/science.aan4338

Pizzo, V. 1978, J. Geophys. Res., 83, 5563, doi: 10.1029/JA083iA12p05563

Pizzo, V., Millward, G., Parsons, A., et al. 2011, Space Weather, 9, 03004, doi: 10.1029/2011SW000663

Pizzo, V. J. 1991, J. Geophys. Res., 96, 5405, doi: 10.1029/91JA00155

Pomoell, J., & Poedts, S. 2018, J. Space Weather Space Clim., 8, A35, doi: 10.1051/swsc/2018020

Porth, O., Xia, C., Hendrix, T., Moschou, S. P., & Keppens, R. 2014, Astrophys. J. Suppl., 214, 4, doi: 10.1088/0067-0049/214/1/4

Priest, E. 2014, Magnetohydrodynamics of the Sun (Cambridge: Cambridge University Press), doi: 10.1017/CBO9781139020732

Ramaty, R. 1969, Astrophys. J., 158, 753, doi: 10.1086/150235

Ramaty, R., & Lingenfelter, R. E. 1968, Sol. Phys., 5, 531, doi: 10.1007/BF00147018

Ramesh, R., Kishore, P., Mulay, S. M., et al. 2013, Astrophys. J., 778, 30, doi: 10.1088/0004-637X/778/1/30

Reale, F. 2010, Living Reviews in Solar Physics, 7, 5, doi: 10.12942/lrsp-2010-5

Reames, D. V. 1999, Space Sci. Rev., 90, 413, doi: 10.1023/A:1005105831781

—. 2013, Space Sci. Rev., 175, 53, doi: 10.1007/s11214-013-9958-9

—. 2021, Solar Energetic Particles. A Modern Primer on Understanding Sources, Acceleration and Propagation, Vol. 978 (Cham: Springer International Publishing), doi: 10.1007/978-3-030-66402-2

Rees, C., Ryden, K., Hands, A., & Clewer, B. 2023, J. Space Saf. Eng., 10, 197, doi: https://doi.org/10.1016/j.jsse.2023.03.002

Reid, H. A. S., & Kontar, E. P. 2018, Astron. Astrophys., 614, A69, doi: 10.1051/0004-6361/201732298

Reid, H. A. S., & Ratcliffe, H. 2014, Res. Astron. Astrophys., 14, 773, doi: 10.1088/1674-4527/14/7/003

Richardson, I. G. 2004, Space Sci. Rev., 111, 267, doi: 10.1023/B:SPAC.0000032689.52830.3e

—. 2018, Living Rev. Sol. Phys., 15, 1, doi: 10.1007/s41116-017-0011-z

Richardson, J. D., Burlaga, L. F., Elliott, H., et al. 2022, Space Sci. Rev., 218, 35, doi: 10.1007/s11214-022-00899-y

Riley, P. 2012, Space Weather, 10, 02012, doi: 10.1029/2011SW000734

Riley, P., Lionello, R., Mikić, Z., & Linker, J. 2008, Astrophys. J., 672, 1221, doi: 10.1086/523893

Robinson, R. D. 1978, Sol. Phys., 60, 383, doi: 10.1007/BF00156538

Robinson, R. D., & Smerd, S. F. 1975, Publ. Astron. Soc. Aust., 2, 374, doi: 10.1017/S1323358000014375

Roelof, E. C. 1969, in Lectures in High-Energy Astrophysics, ed. H. Ögelman & J. R. Wayland, 111

Rosner, R., Tucker, W. H., & Vaiana, G. S. 1978, Astrophys. J., 220, 643, doi: 10.1086/155949

Roth, I., & Temerin, M. 1997, Astrophys. J., 477, 940, doi: 10.1086/303731

Ruffolo, D. 1995, Astrophys. J., 442, 861, doi: 10.1086/175489

Rybicki, G. B., & Lightman, A. P. 1986, Radiative Processes in Astrophysics (Weinheim: Wiley-VCH)

Sakurai, T. 2017, Proc. Jpn. Acad., Ser. B., 93, 87, doi: 10.2183/pjab.93.006

Salas-Matamoros, C., & Klein, K.-L. 2020, Astron. Astrophys., 639, A102, doi: 10.1051/0004-6361/202037989

Schaefer, B., Collett, E., Smyth, R., Barrett, D., & Fraher, B. 2007, American Journal of Physics, 75, 163, doi: 10.1119/1.2386162

Scherer, K., Fichtner, H., & Lazar, M. 2017, Europhys. Lett., 120, 50002, doi: 10.1209/0295-5075/120/50002

Scherer, K., Husidic, E., Lazar, M., & Fichtner, H. 2022, Astron. Astrophys., 663, A67, doi: 10.1051/0004-6361/202243477

Scherer, K., Lazar, M., Husidic, E., & Fichtner, H. 2019, Astrophys. J., 880, 118, doi: 10.3847/1538-4357/ab1ea1

Scherrer, P. H., Schou, J., Bush, R. I., et al. 2012, Sol. Phys., 275, 207, doi: 10.1007/s11207-011-9834-2

Schrijver, C. J., Dobbins, R., Murtagh, W., & Petrinec, S. M. 2014, Space Weather, 12, 487, doi: 10.1002/2014SW001066

Schrijver, C. J., Kauristie, K., Aylward, A. D., et al. 2015, Adv. Space Res., 55, 2745, doi: 10.1016/j.asr.2015.03.023

Schwadron, N. A., Caplan, R. M., Linker, J. A., Palmerio, E., & Young, M. A. 2024a, arXiv, arXiv:2410.07420, doi: 10.48550/arXiv.2410.07420

Schwadron, N. A., Bale, S. D., Bonnell, J., et al. 2024b, Astrophys. J., 970, 98, doi: 10.3847/1538-4357/ad527f

Schwenn, R. 2006, Living Rev. Sol. Phys., 3, 2, doi: 10.12942/lrsp-2006-2

Schwenn, R., dal Lago, A., Huttunen, E., & Gonzalez, W. D. 2005, Ann. Geophys., 23, 1033, doi: 10.5194/angeo-23-1033-2005

Schwinger, J. 1949, Phys. Rev., 75, 1912, doi: 10.1103/PhysRev.75.1912

Scolini, C., Rodriguez, L., Mierla, M., Pomoell, J., & Poedts, S. 2019, Astron. Astrophys., 626, A122, doi: 10.1051/0004-6361/201935053

Scolini, C., Chané, E., Temmer, M., et al. 2020, Astrophys. J. Suppl., 247, 21, doi: 10.3847/1538-4365/ab6216

Shamsuddin, S., Ansor, N., Hamidi, Z., & Shariff, N. 2023, in J. Phys. Conf. Ser., Vol. 2543, J. Phys. Conf. Ser.(IOP), 012013, doi: 10.1088/1742-6596/2543/1/012013

Sheeley, Jr., N. R. 2005, Living Rev. Sol. Phys., 2, 5, doi: 10.12942/lrsp-2005-5

Shibata, K., & Magara, T. 2011, Living Rev. Sol. Phys., 8, 6, doi: 10.12942/lrsp-2011-6

Shibata, K., Masuda, S., Shimojo, M., et al. 1995, Astrophys. J. Lett., 451, L83, doi: 10.1086/309688

Sirenko, O., Voitenko, Y., & Goossens, M. 2002, Astron. Astrophys., 390, 725, doi: 10.1051/0004-6361:20020770

Sitenko, A. G., & Kirochkin, Y. A. 1966, Sov. Phys. Uspekhi, 9, 430, doi: 10.1070/PU1966v009n03ABEH002893

Skilling, J. 1971, Astrophys. J., 170, 265, doi: 10.1086/151210

—. 1975, Mon. Not. R. Astron. Soc., 172, 557, doi: 10.1093/mnras/172.3.557

Smith, E. J., & Wolfe, J. H. 1976, Geophys. Res. Lett., 3, 137, doi: 10.1029/GL003i003p00137

Sokolov, I. V., Naumova, N. M., Nees, J. A., Mourou, G. A., & Yanovsky, V. P. 2009, Phys. Plasmas, 16, 093115, doi: 10.1063/1.3236748

Sokolov, I. V., Holst, B. v. d., Manchester, W. B., et al. 2021, Astrophys. J., 908, 172, doi: 10.3847/1538-4357/abc000

Sonnerup, B. U. Ö. 1969, J. Geophys. Res., 74, 1301, doi: 10.1029/JA074i005p01301

Stansby, D., Green, L. M., van Driel-Gesztelyi, L., & Horbury, T. S. 2021, Sol. Phys., 296, 116, doi: 10.1007/s11207-021-01861-x

Stix, M. 2002, The Sun: An Introduction (Berlin, Heidelberg: Springer), doi: 10.1007/978-3-642-56042-2

Stix, T. H. 1962, The Theory of Plasma Waves (New York: McGraw-Hill Book Co.)

Stone, E. C., Frandsen, A. M., Mewaldt, R. A., et al. 1998, Space Sci. Rev., 86, 1, doi: 10.1023/A:1005082526237

Strauss, R. D. T., & Effenberger, F. 2017, Space Sci. Rev., 212, 151, doi: 10.1007/s11214-017-0351-y

Suematsu, Y., Shimizu, T., Hara, H., et al. 2021, in Proc. SPIE, Vol. 11852, International Conference on Space Optics — ICSO 2020, ed. B. Cugny, Z. Sodnik, & N. Karafolas, 118523K, doi: 10.1117/12.2599610

Szudzik, M. P. 2017, arXiv, arXiv:1706.04129, doi: 10.48550/arXiv.1706.04129

Tan, Y., Hu, Q., Wang, Z., & Zhong, Q. 2018, Space Weather, 16, 406, doi: 10.1002/2017SW001764

Tang, J. F., Wu, D. J., & Tan, C. M. 2013, Astrophys. J., 779, 83, doi: 10.1088/0004-637X/779/1/83

Telloni, D., Adhikari, L., Zank, G. P., et al. 2022, Astrophys. J., 929, 98, doi: 10.3847/1538-4357/ac5cc3

Temerin, M., & Roth, I. 1992, Astrophys. J. Lett., 391, L105, doi: 10.1086/186408

Temmer, M. 2021, Living Rev. Sol. Phys., 18, 4, doi: 10.1007/s41116-021-00030-3

Teunissen, J., & Keppens, R. 2019, Comput. Phys. Commun., 245, 106866, doi: 10.1016/j.cpc.2019.106866

Teyssier, R., & Commerçon, B. 2019, Front. Astron. Space Sci., 6, 51, doi: 10.3389/fspas.2019.00051

Titov, V. S., & Démoulin, P. 1999, Astron. Astrophys., 351, 707

Titov, V. S., Downs, C., Mikić, Z., et al. 2018, Astrophys. J. Lett., 852, L21, doi: 10.3847/2041-8213/aaa3da

Titov, V. S., Török, T., Mikic, Z., & Linker, J. A. 2014, Astrophys. J., 790, 163, doi: 10.1088/0004-637X/790/2/163

Tobias, S. M. 2002, Philos. Transact. A Math. Phys. Eng. Sci., 360, 2741, doi: 10.1098/rsta.2002.1090

Tóth, G., & Odstrčil, D. 1996, J. Comput. Phys., 128, 82, doi: 10.1006/jcph.1996.0197

Treumann, R. A., Nakamura, R., & Baumjohann, W. 2011, Ann. Geophys., 29, 1673, doi: 10.5194/angeo-29-1673-2011

Trotta, D., Larosa, A., Nicolaou, G., et al. 2024, Astrophys. J., 962, 147, doi: 10.3847/1538-4357/ad187d

Trulsen, J., & Fejer, J. A. 1970, J. Plasma Phys., 4, 825, doi: 10.1017/S0022377800005468

Tsubouchi, K. 2017, J. Geophys. Res. Space Phys., 122, 3935, doi: 10.1002/2016JA023817

Tsurutani, B. T., Gonzalez, W. D., & Kamide, Y. 1997, Surv. Geophys., 18, 363, doi: 10.1023/A:1006555215463

Tsurutani, B. T., Gonzalez, W. D., Lakhina, G. S., & Alex, S. 2003, J. Geophys. Res. Space Phys., 108, 1268, doi: 10.1029/2002JA009504

Tsurutani, B. T., Smith, E. J., Pyle, K. R., & Simpson, J. A. 1982, J. Geophys. Res., 87, 7389, doi: 10.1029/JA087iA09p07389

Tsytovich, V. N. 1970, Nonlinear Effects in Plasma (New York: Springer)

Tun, S. D., & Vourlidas, A. 2013, Astrophys. J., 766, 130, doi: 10.1088/0004-637X/766/2/130

Vainio, R., & Afanasiev, A. 2018, in Astrophys. Space Sci. Libr., Vol. 444, Solar Particle Radiation Storms Forecasting and Analysis, ed. O. E. Malandraki & N. B. Crosby, 45–61, doi: 10.1007/978-3-319-60051-2_3

Vainio, R., Pönni, A., Battarbee, M., et al. 2014, J. Space Weather Space Clim., 4, A08, doi: 10.1051/swsc/2014005

Vainio, R., Desorgher, L., Heynderickx, D., et al. 2009, Space Sci. Rev., 147, 187, doi: 10.1007/s11214-009-9496-7

van den Berg, J., Strauss, D. T., & Effenberger, F. 2020, Space Sci. Rev., 216, 146, doi: 10.1007/s11214-020-00771-x

van den Berg, J. P., Engelbrecht, N. E., Wijsen, N., & Strauss, R. D. 2021, Astrophys. J., 922, 200, doi: 10.3847/1538-4357/ac2736

Vasanth, V., Chen, Y., Feng, S., et al. 2016, Astrophys. J. Lett., 830, L2, doi: 10.3847/2041-8205/830/1/L2

Vasanth, V., Chen, Y., Lv, M., et al. 2019, Astrophys. J., 870, 30, doi: 10.3847/1538-4357/aaeffd

Vasyliunas, V. M. 1968, J. Geophys. Res., 73, 2839, doi: 10.1029/JA073i009p02839

Vennerstrom, S., Lefevre, L., Dumbović, M., et al. 2016, Sol. Phys., 291, 1447, doi: 10.1007/s11207-016-0897-y

Verbeke, C., Baratashvili, T., & Poedts, S. 2022, Astron. Astrophys., 662, A50, doi: 10.1051/0004-6361/202141981

Verbeke, C., Pomoell, J., & Poedts, S. 2019, Astron. Astrophys., 627, A111, doi: 10.1051/0004-6361/201834702

Verkhoglyadova, O. P., Zank, G. P., & Li, G. 2015, Phys. Rep., 557, 1, doi: 10.1016/j.physrep.2014.10.004

Verscharen, D., Klein, K. G., & Maruca, B. A. 2019, Living Rev. Sol. Phys., 16, 5, doi: 10.1007/s41116-019-0021-0

Vourlidas, A. 2004, in Astrophys. Space Sci. Libr., Vol. 314, Astrophys. Space Sci. Libr., ed. D. E. Gary & C. U. Keller, 223, doi: 10.1007/1-4020-2814-8_11

Vourlidas, A., Carley, E. P., & Vilmer, N. 2020, Front. Astron. Space Sci., 7, 43, doi: 10.3389/fspas.2020.00043

Vourlidas, A., Howard, R. A., Esfandiari, E., et al. 2010, Astrophys. J., 722, 1522, doi: 10.1088/0004-637X/722/2/1522

Wang, W., Wang, L., Krucker, S., et al. 2021, Astrophys. J., 913, 89, doi: 10.3847/1538-4357/abefce

Wang, Y., Qin, G., & Zhang, M. 2012, Astrophys. J., 752, 37, doi: 10.1088/0004-637X/752/1/37

Wang, Y., Wang, B., Shen, C., Shen, F., & Lugaz, N. 2014, J. Geophys. Res. Space Phys., 119, 5117, doi: 10.1002/2013JA019537

Wang, Y. M., & Sheeley, Jr., N. R. 1990, Astrophys. J., 355, 726, doi: 10.1086/168805

Wang, Y. M., Sheeley, Jr., N. R., & Rich, N. B. 2007, Astrophys. J., 658, 1340, doi: 10.1086/511416

Warwick, J. W. 1967, Astrophys. J., 150, 1081, doi: 10.1086/149405

Webb, G. M. 1985, Astrophys. J., 296, 319, doi: 10.1086/163451

Weinberg, S. 2005, The Quantum Theory of Fields (Cambridge: Cambridge University Press)

Weiss, A. A. 1963, Aust. J. Phys., 16, 526, doi: 10.1071/PH630526

White, S. M. 2024, arXiv, arXiv:2405.00959, doi: 10.48550/arXiv.2405.00959

Wijsen, N. 2020, PhD thesis, Katholieke University of Leuven, Belgium

Wijsen, N., Aran, A., Pomoell, J., & Poedts, S. 2019a, Astron. Astrophys., 622, A28, doi: 10.1051/0004-6361/201833958

Wijsen, N., Aran, A., Pomoell, J., & Poedts, S. 2019b, in J. Phys. Conf. Ser., Vol. 1332, J. Phys. Conf. Ser.(IOP), 012018, doi: 10.1088/1742-6596/1332/1/012018

Wijsen, N., Samara, E., Aran, À., et al. 2021, Astrophys. J. Lett., 908, L26, doi: 10.3847/2041-8213/abe1cb

Wijsen, N., Aran, A., Scolini, C., et al. 2022, Astron. Astrophys., 659, A187, doi: 10.1051/0004-6361/202142698

Wijsen, N., Lario, D., Sánchez-Cano, B., et al. 2023, Astrophys. J., 950, 172, doi: 10.3847/1538-4357/acd1ed

Wilcox, J. M., Hoeksema, J. T., & Scherrer, P. H. 1980, Sci., 209, 603, doi: 10.1126/science.209.4456.603

Wild, J. P. 1950a, Aust. J. Sci. Res. A Phys. Sci., 3, 399, doi: 10.1071/CH9500399

—. 1950b, Aust. J. Sci. Res. A Phys. Sci., 3, 541, doi: 10.1071/CH9500541

Wild, J. P., & McCready, L. L. 1950, Aust. J. Sci. Res. A Phys. Sci., 3, 387, doi: 10.1071/CH9500387

Wild, J. P., Sheridan, K. V., & Trent, G. H. 1959, in IAU Symposium, Vol. 9, URSI Symp. 1: Paris Symposium on Radio Astronomy, ed. R. N. Bracewell, 176

Wild, J. P., Smerd, S. F., & Weiss, A. A. 1963, Ann. Rev. Astron. Astrophys., 1, 291, doi: 10.1146/annurev.aa.01.090163.001451

Willmott, P. 2019, An Introduction to Synchrotron Radiation (New Jersey: Wiley), doi: 10.1002/9781119280453

Wilson, L. B., Mitchell, J. G., Szabo, A., et al. 2025, Astrophys. J., 987, 31, doi: 10.3847/1538-4357/add6a8

Winglee, R. M., & Dulk, G. A. 1986, Astrophys. J., 307, 808, doi: 10.1086/164467

Woo, R., & Habbal, S. R. 2000, J. Geophys. Res., 105, 12667, doi: 10.1029/1999JA000255

Woodward, P., & Colella, P. 1984, J. Comput. Phys., 54, 115, doi: 10.1016/0021-9991(84)90142-6

Xia, C., Teunissen, J., El Mellah, I., Chané, E., & Keppens, R. 2018, Astrophys. J. Suppl., 234, 30, doi: 10.3847/1538-4365/aaa6c8

Xie, H., Ofman, L., & Lawrence, G. 2004, J. Geophys. Res. Space Phys., 109, A03109, doi: 10.1029/2003JA010226

Xie, R., Wang, M., Duan, C., et al. 2002, Sci. China Math., 45, 97, doi: 10.1007/BF02889690

Yadav, R., Díaz Baso, C. J., de la Cruz Rodríguez, J., Calvo, F., & Morosin, R. 2021, Astron. Astrophys., 649, A106, doi: 10.1051/0004-6361/202039857

Yalim, M. S. 2008, PhD thesis, Université Libre de Bruxelles, von Karman Institute for Fluid Dynamics, Aeronautics and Aerospace Department

Yang, Z., Bethge, C., Tian, H., et al. 2020, Sci., 369, 694, doi: 10.1126/science.abb4462

Young, M. A., Schwadron, N. A., Gorby, M., et al. 2021, Astrophys. J., 909, 160, doi: 10.3847/1538-4357/abdf5f

Zank, G. P. 2014, Transport Processes in Space Physics and Astrophysics, Vol. 877 (New York: Springer Science+Business Media), doi: 10.1007/978-1-4614-8480-6

Zhang, M., Qin, G., & Rassoul, H. 2009, Astrophys. J., 692, 109, doi: 10.1088/0004-637X/692/1/109

Zhang, P. J., Wang, C. B., & Ye, L. 2018, Astron. Astrophys., 618, A165, doi: 10.1051/0004-6361/201833260

Zhao, J., Wang, S., Sun, W., et al. 2025, Astrophys. J., 980, 89, doi: 10.3847/1538-4357/ad9b28

Zhao, X. P., Plunkett, S. P., & Liu, W. 2002, J. Geophys. Res. Space Phys., 107, 1223, doi: 10.1029/2001JA009143

Zheleznyakov, V. V. 1969, Astrophys. J., 155, 1129, doi: 10.1086/149941

—. 1970, Radio emission of the sun and planets (Oxford: Pergamon Press)

Zheleznyakov, V. V., & Zaitsev, V. V. 1968, Sov. Astron., 12, 14

Zlotnik, E. Y., Zaitsev, V. V., Aurass, H., Mann, G., & Hofmann, A. 2003, Astron. Astrophys., 410, 1011, doi: 10.1051/0004-6361:20031250

Zouganelis, I., Meyer-Vernet, N., Landi, S., Maksimovic, M., & Pantellini, F. 2005, Astrophys. J. Lett., 626, L117, doi: 10.1086/431904

Curriculum Vitae

Personal Details

Name:	Edin Husidic
Place of birth:	Duisburg, Germany
Citizenship:	German
Email:	mc115zr@gmail.com

Education

- **Double-degree PhD in Mathematics and Physics**:
  Doctorate in Mathematics at Centre for Mathematical Plasma-Astrophysics, Department of Mathematics, KU Leuven, Leuven, Belgium, 2021–2025
  Doctorate in Physics at Department of Physics and Astronomy, University of Turku, Turku, Finland, 2021–2025
  PhD thesis: *Multi-scale modelling of energetic particle dynamics and radio signatures in coronal and heliospheric plasmas*
  Supervisors: Prof Stefaan Poedts, Prof Rami Vainio, Prof Nicolas Wijsen

- **Master of Science in Physics**:
  Ruhr-University Bochum, Bochum, Germany, 2016–2019
  Master's thesis at Chair for Theoretical Physics IV: *Linear Dispersion Theory for Regularized Kappa-Distributions*
  Supervisor: PD Dr Horst Fichtner

- **Bachelor of Science in Physics**:
  Ruhr-University Bochum, Bochum, Germany, 2012–2016
  Bachelor's thesis at Chair for Astrophysics: *Kinematics of the H-Alpha Emission Line in Seyfert-1 Nuclei*
  Supervisor: Prof Rolf Chini

Research Experience / Internships

- **Research stay at University of Turku**:
  9-month (12/2023–08/2024) research stay in the context of the double-degree PhD at the University of Turku, Turku, Finland, under supervision of Prof Rami Vainio. Funded by the travel grant V477923N from the Fonds voor Wetenschappelijk OnderzoekVlaanderen (FWO).

- **Industrial internship**:
  3-month (09/2023–11/2023) full-time position at *Space Applications Services* in Sint-Stevens-Woluwe, Belgium, under supervision of Matthieu Melcot and Dr Carla Jacobs.

  – Contributed to the *AIDefSpace* project (KU Leuven–Belgian Defence collaboration) on AI-based space weather forecasting.
  – Worked on developing and evaluating ML models for predicting solar flare activity and related events.

- **Solar observational training**:
  1-month (07/2023) full-time stay at the Gyula Bay Zoltán Solar Observatory in Gyula, Hungary, under supervision of Prof Robertus von Fay-Siebenburgen Erdélyi and Dr Marianna B. Korsós.

  – Conducted solar observations.
  – Performed maintenance and debugging work on observational equipment.

- **Research Assistant**:
  2019–2021, Heliophysics Group led by PD Dr Horst Fichtner at Chair for Theoretical Physics IV, Ruhr-University Bochum, Bochum, Germany

  – Conducted scientific research.
  – First- and co-authored publications.

  - Assisted in teaching, tutored students, and contributed to lecture notes.

- **Erasmus traineeship**:
  5-month (02/2020–06/2020) full-time stay at the Centre for Mathematical Plasma-Astrophysics, Department of Mathematics, KU Leuven, Leuven, Belgium, under supervision of Prof Stefaan Poedts and Prof Marian Lazar. Funded by the Ruhr-University Bochum, Bochum, Germany within the Erasmus exchange programme.
  - Observational documentation of nonequilibrium plasma conditions in heliosphere.
  - Advanced kinetic modelling of particle velocity distributions using κ-power-laws.
  - Stability properties of κ-distributed plasmas: analytical/numerical methods.
  - Applications: kinetic instabilities responsible for electromagnetic fluctuations.

First-authored Publications

- **Husidic, E.**, Wijsen, N., Jeberaj, I. C., Vourlidas, A., Linan, L., Vainio, R., Poedts, S.: *Modelling gyrosynchrotron emission from coronal energetic electrons in a CME flux rope.* Astronomy & Astrophysics, 701, A53, 2025. DOI: https://doi.org/10.1051/0004-6361/202555534
- **Husidic, E.**, Wijsen, N., Linan, L., Brchnelova, M., Vainio, R., Poedts, S.: *Cross-field Diffusion Effects on Particle Transport in a Solar Coronal Flux Rope.* The Astrophysical Journal Letters, 976, L31, 2024. DOI: https://doi.org/10.3847/2041-8213/ad8d56
- **Husidic, E.**, Wijsen, N., Baratashvili, T., Poedts, S., Vainio, R.: *Energetic particle acceleration and transport with the novel Icarus + PARADISE model.* Journal of Space Weather and Space Climate, 14, 11, 2024. DOI: https://doi.org/10.1051/swsc/2024009
- **Husidic, E.**, Scherer, K., Lazar, M., Fichtner, H., Poedts, S.: *Towards a realistic evaluation of transport coefficients in non-equilibrium space plasmas.* The Astrophysical Journal, 927 (2), 159, 2022. DOI: https://doi.org/10.3847/1538-4357/ac4af4

- **Husidic, E.**, Lazar, M., Fichtner, H., Scherer, K., Poedts, S.: *Transport coefficients enhanced by suprathermal particles in nonequilibrium heliospheric plasmas.* Astronomy & Astrophysics, 654, A99, 2021. DOI: https://doi.org/10.1051/0004-6361/202141760

- **Husidic, E.**, Lazar, M., Scherer, K., Fichtner, H., Gaelzer, R.: *Regularized Kappa Distributions: Linear Dispersion and Stability Theory.* In: Kappa Distributions - From Observational Evidences via Controversial Predictions to a Consistent Theory of Nonequilibrium Plasmas, Chapt. 13, (279-297), 2021. Cham: Springer Nature Switzerland AG. ISBN: 978-3-030-82622-2. DOI: https://doi.org/10.1007/978-3-030-82623-9_13

- **Husidic, E.**, Lazar M., Fichtner H., Scherer K., Astfalk P.: *Linear dispersion theory of parallel electromagnetic modes for regularized Kappa-distributions.* Physics of Plasmas, 27, 042110, 2020. DOI: https://doi.org/10.1063/1.5145181

Co-authored Publications

- Wang, H., Yang, L., Poedts, S., Lani, A., Zhou, Y., Gao, Y., Linan, L., Lv, J., Baratashvili, T., Guo, J., Lin, R., Su, Z., Li, C., Zhang, M., Wei, W., Yang, Y., Li, Y., Ma, X., **Husidic, E.**, Jeong, H.-j., Mahdi, N.-Z., Wang, J., Schmieder, B.: *SIP-IFVM: A time-evolving coronal model with an extended magnetic field decomposition strategy.* The Astrophysical Journal Supplement Series, 278, 59, 2025. DOI: https://doi.org/10.3847/1538-4365/add0b1

- Scherer, K., **Husidic, E.**, Lazar, M., Fichtner, H.: *Revisiting Ulysses electron data with a triple fit of velocity distributions.* Astronomy & Astrophysics, 663, A67, 2022. DOI: https://doi.org/10.1051/0004-6361/202243477

- Scherer, K., **Husidic, E.**, Fichtner, H., Lazar, M.: *From Standard Kappa to a Regularized Kappa, or Even More Generalized Kappa "Cookbook".* In: Kappa Distributions - From Observational Evidences via Controversial Predictions to a Consistent Theory of Nonequilibrium Plasmas, Chapt. 15, (307-318), 2021. Cham: Springer Nature Switzerland AG. ISBN: 978-3-030-82622-2. DOI: https://doi.org/10.1007/978-3-030-82623-9_15

- Scherer K., **Husidic, E.**, Lazar M., Fichtner H.: *Generalized anisotropic κ-cookbook: 2D fitting of Ulysses electron data.* Monthly Notices of the Royal Astronomical Society, 501, 606, 2020. DOI: https://doi.org/10.1093/mnras/staa3641
- Scherer K., **Husidic, E.**, Lazar M., Fichtner H.: *The κ-cookbook: a novel generalizing approach to unify κ-like distributions for plasma particle modeling.* Monthly Notices of the Royal Astronomical Society, 497, 1738, 2020. DOI: https://doi.org/10.1093/mnras/staa1969
- Scherer, K., Lazar, M., **Husidic, E.**, Fichtner, H.: *Moments of the Anisotropic Regularized κ-distributions, The Astrophysical Journal.* 880, 118, 2019. DOI: https://doi.org/10.3847/1538-4357/ab1ea1

Invited Talks

- **Husidic, E.**, Wijsen, N., Vainio, R., Poedts, S.: *Modelling Energetic Particle Transport in the Inner Heliosphere and Solar Corona*, GGCW Gulberg A.S.H. Conference, 30 October–1 November 2024, in Lahore, Pakistan.
- **Husidic, E.**, Wijsen, N., Vainio, R., Poedts, S.: *Modelling Coronal Mass Ejections and Energetic Particle Transport in the Corona and Inner Heliosphere*, Workshop: Particle Acceleration and Transport: from the Sun to Extragalactic Sources, 3–7 February 2025, at the University of Calabria, Rende, Italy
- **Husidic, E.**, Wijsen, N., Jebaraj, I. C., Linan, L., Vainio, R., Poedts, S.: *Modelling of Energetic Particles and Gyrosynchrotron Emission in the Solar Corona*, 22nd Annual International Astrophysics Conference, 7–11 April 2025, in Santiago de Compostela, Spain.

Contributed Talks

- **Husidic, E.**, Lazar, M., Scherer, K., Fichtner, H., and Poedts, S.: *Towards a realistic evaluation of transport coefficients in non-equilibrium plasmas*

from space, EGU General Assembly 2022, in Vienna, Austria, 23–27 May 2022.

- **Husidic, E.**, Lazar, M., Scherer, K., Fichtner, H., and Poedts, S.: *Macroscopic plasma characterisation with the new regularised Kappa distribution*, CmPA retrospective in honour of prof Stefaan Poedts, at KU Leuven, Belgium, 6–9 September 2022.

- **Husidic, E.**, Wijsen, N., Baratashvili, T., Poedts, S., Vainio, R.: *Towards New Insights in Simulations of SEP Events with the PARADISE+Icarus Model*, DPG (German Physical Society) Spring Meeting, Matter and Cosmos section, 20–24 March 2023, Dresden, Germany.

- **Husidic, E.**: *Modelling energetic particle transport with PARADISE*, SEPVAL 2023 (EUROPE) mini-ISWAT workshop, 18–19 November 2023, in Toulouse, France.

- **Husidic, E.**, Wijsen, N., Baratashvili, T., Poedts, S., Vainio, R.: *The novel SEP simulation model Icarus+PARADISE*, AGU Fall Meeting, 11–15 December 2023, in San Francisco, USA.

- **Husidic, E.**, Wijsen, N., Poedts, S., Vainio, R.: *Energetic Particle Transport Modelling with PARADISE*, DPG (German Physical Society) Spring Meeting, Matter and Cosmos section, 26–29 February 2024, in Greifswald, Germany.

- **Husidic, E.**, Wijsen, N., Vainio, R., Poedts, S.: *Particle Transport Modelling in the Inner Heliosphere*, SERPENTINE Seminar & SOLER Workshop, 17–20 June 2024, at the University of Helsinki, Finland.

- **Husidic, E.**, Wijsen, N., Linan, L., Brchnelova, M., Vainio, R., Poedts, S.: *Exploring energetic particle transport in the solar corona with the novel COCONUT+PARADISE model*, COSPAR Scientific Assembly, 13–21 July 2024, in Busan, South Korea.

- **Husidic, E.**, Wijsen, N., Linan, L., Brchnelova, M., Vainio, R., Poedts, S.: *Simulating Energetic Particle Transport in the Solar Corona with COCONUT+PARADISE*, 17th European Solar Physics Meeting ESPM-17, 9–13 September 2024, in Turin, Italy.

- **Husidic, E.**, Wijsen, N., Linan, L., Brchnelova, M., Vainio, R., Poedts, S.: *Modelling Particle Transport in the Solar Corona with COCONUT+PARADISE*, European Space Weather Week, 4–8 November 2024, in Coimbra, Portugal.

- **Husidic, E.**, Wijsen, N., Jebaraj, I. C., Linan, L., Vainio, R., Poedts, S.: *Modelling Energetic Particle Transport in a Solar Coronal Flux Rope CME*, SWATNet Final Conference, 10–14 February 2025, at the University of Helsinki, Finland.
- **Husidic, E.**, Wijsen, N., Jebaraj, I. C., Vourlidas, A., Linan, L., Vainio, R., Poedts, S.: *Modelling Gyrosynchrotron Emission from Energetic Electrons in the Solar Corona*, European Geosciences Union General Assembly 2025 (EGU 2025), 27 April–02 May 2025, in Vienna, Austria.
- **Husidic, E.**, Wijsen, N., Jebaraj, I., Vourlidas, A., Vainio, R., Poedts, S.: *Modelling Type-IV Radio Bursts from (Gyro-)Synchrotron Radiation Emitting Electrons in Coronal Flux Ropes*, Parker Heliophysics Scholars 9th Meeting, 20–22 May 2025.
- **Husidic, E.**, Wijsen, N., Jebaraj, I., Vourlidas, A., Vainio, R., Poedts, S.: *Modelling Gyrosynchroton Radiation from Energetic Electrons in CME Flux Ropes*, Planetary, solar and heliospheric Radio Emissions Conference/Workshop, 11–13 June 2025, at the University of Marseille, France.

Contributed Posters

- **Husidic, E.**, Wijsen, N., Baratashvili, T., Poedts, S., Vainio, R.: *Icarus+PARADISE: Towards new perspectives on SEP event simulations*, European Space Weather Week 2023, 20–24 November 2023, in Toulouse, France.
- **Husidic, E.**, Wijsen, N., Poedts, S., Vainio, R., Linan, L., Baratashvili, T., Brchnelova, M.: *Modelling energetic particle transport with the PARADISE code*, European Geosciences Union 2024 (EGU 2024), 15-19 April 2024, in Vienna, Austria.

Summer Schools

- *Introduction to Space Weather*, SWATNet Summer School, 8–12 November 2021.
- *Python in Heliophysics Summer School*, at European Space Astronomy Centre (ESAC), 30 May–3 June 2022, in Madrid, Spain.
- *Sun-Earth Interactions*, SWATNet Summer School, 26–28 September 2022, at the Academy of Athens, Greece.
- *Space weather and our technology-based society*, SWATNet Summer School, 12–14 June 2023, at ELTE University of Budapest, Hungary.
- *Introductory Course in Solar and Solar-Terrestrial Physics*, 1–6 September 2024, at the University of Sheffield.

Workshops

- *How to successfully communicate science: Posters, Talks and Papers*, SWATNet workshop, 10–11 January 2022.
- *How to write and manage a Research Project: from a one-person scale to large networks*, SWATNet workshop, 15–16 March 2022.
- *Communicate Science to Non-Scientist: Public Outreach*, SWATNet workshop, 20–22 June 2022, at the University of Coimbra, Portugal.
- *Mini-Master of Business Administration (Mini MBA)*, SWATNet workshop, 23–24 March 2023, University of Sheffield, England.
- *Entrepreneurship in Space Physics*, SWATNet workshop, 15–16 June 2023, at ELTE University of Budapest, Hungary.
- *SEPVAL 2023 (EUROPE) mini-ISWAT workshop*, 18–19 November 2023, in Toulouse, France.
- *Careers: Academic vs Non-Academic opportunities*, SWATNet workshop, 10–11 April 2024, at the University of Rome Tor Vergata, Italy.

- *SERPENTINE Seminar & SOLER Workshop*, 17–20 June 2024, at the University of Helsinki, Finland.
- *Particle Acceleration and Transport: from the Sun to Extragalactic Sources*, 3–7 February 2025, at the University of Calabria, Rende, Italy
- *Parker Heliophysics Scholars 9th Meeting*, 20–22 May 2025.
- *Planetary, solar and heliospheric Radio Emissions Conference*, 11–13 June 2025, at the University of Marseille, France.

Postgraduate lectures (examined)

- *Model Reduction and Numerical Simulation with Moment Methods* (2021/2022) at KU Leuven, Belgium
- *Academic Writing for Junior Researchers* (2021/2022) at KU Leuven, Belgium
- *Solar energetic particles* (2022) at University of Turku, Finland
- *Selected Topics in Mathematics II – Scientific Computing and Mathematical Modelling in Space Science* (2022) at KU Leuven, Belgium
- *Science Communication and Outreach* (2022) at KU Leuven, Belgium
- *Space Weather* (2022) at KU Leuven, Belgium
- *Waves and Instabilities* (2022) at KU Leuven, Belgium
- *Computational Methods for Astrophysical Applications* (2022/2023) at KU Leuven, Belgium
- *Ethics of Academic Research* (2024) at University of Turku, Finland

---

Teaching Experience

- *Computational physics* (2017), Chair for Theoretical Physics IV, Ruhr-University Bochum, Germany: Teaching assistant for exercise sessions.
- *Theoretical astrophysics* (2017/2018), Chair for Theoretical Physics IV, Ruhr-University Bochum, Germany: Teaching assistant for exercise sessions and creator of exercises.
- Assisted in preparing lecture notes for the courses *Plasma Dispersion Relations* and *Astroshocks*, held by Dr Klaus Scherer, Chair of Theoretical Physics IV, Ruhr University Bochum, Germany.
- *Theoretical plasma physics* (2019/2020), Chair for Theoretical Physics IV, Ruhr-University Bochum, Germany: Teaching assistant for exercise sessions.
- *Fundamentals of Mechanics* (2020), Chair for Theoretical Physics IV, Ruhr-University Bochum, Germany: Teaching assistant for exercise sessions.
- *Calculus and analysis* (2021/2022), Department of Mathematics, KU Leuven, Belgium: Teaching assistant for exercise sessions.
- *Calculus and analysis* (2022/2023), Department of Mathematics, KU Leuven, Belgium: Teaching assistant for exercise sessions.
- *Calculus and linear algebra* (2024/2025), Department of Mathematics, KU Leuven, Belgium: Teaching assistant for exercise sessions.

Skills

- **Programming**: Python, C++, Fortran, Maple
- **Technical**: Linux, LaTeX, Git, MPI, High-Performance Computing (Vlaamse Supercomputer Centre Tier-1 and Tier-2 architecture in Belgium, and Puhti Supercomputer in Finland)
- **Languages**: German (native), English (fluent), Serbo-Croatian (good command)

FACULTY OF SCIENCE
DEPARTMENT OF MATHEMATICS
CENTRE FOR MATHEMATICAL PLASMA-ASTROPHYSICS
Celestijnenlaan 200B
B-3001 Leuven